

**DEVELOPMENT AND CHARACTERIZATION OF D9 STAINLESS
STEEL - ZIRCONIUM METAL WASTE FORM ALLOYS**

By

LIPIKA RANI BAIRI

Enrolment No: CHEM 02200704001

From

Corrosion Science and Technology Group

Indira Gandhi Centre for Atomic Research, Kalpakkam 603 102

Tamil Nadu, India

*A thesis submitted to the
Board of Studies in Chemical Sciences
In partial fulfillment of requirements*

For the Degree of

DOCTOR OF PHILOSOPHY

of

HOMI BHABHA NATIONAL INSTITUTE

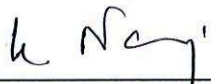


May, 2012

Homi Bhabha National Institute

Recommendations of the Viva Voce Board

As members of the Viva Voce Board, we certify that we have read the dissertation prepared by Lipika Rani Bairi entitled "**Development and Characterization of D9 Stainless Steel - Zirconium Metal Waste Form Alloys**" and recommend that it may be accepted as fulfilling the dissertation requirement for the Degree of Doctor of Philosophy.



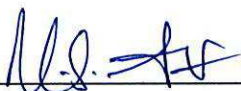
Chairman – Prof. K. Nagarajan

Date: 08/11/12



Supervisor - Convener – Prof. U. Kamachi Mudali

Date: 08/11/12



External Examiner – Prof. V.S. Raja

Date: 08/11/12



Doctoral Committee Member 1 – Prof. K. V. G. Kuty

Date: 08/11/12



Doctoral Committee Member 2 – Prof. C. Mallika

Date: 08.11.12

Final approval and acceptance of this dissertation is contingent upon the candidate's submission of the final copies of the dissertation to HBNI.

I hereby certify that I have read this dissertation prepared under my direction and recommend that it may be accepted as fulfilling the dissertation requirement.

Date: 8.11.2012

Place: IGCAR, Kalpakkam



Supervisor, Prof. U. Kamachi Mudali

**Department of Atomic Energy
Indira Gandhi Center for Atomic Research
Kalpakkam**

Date: 8.11.2012

Certificate

I, **Prof. U. Kamachi Mudali**, certify that all the corrections indicated by the examiners have been incorporated in the thesis entitled "**Development and Characterization of D9 Stainless Steel -Zirconium Metal Waste Form Alloys**" by **Ms. Lipika Rani Bairi**. The thesis in the final form is being submitted to **HBNI** for the award of the degree of **Doctor of Philosophy** to **Ms. Lipika Rani Bairi**.



**Prof. U. Kamachi Mudali
(Supervisor & Convener)**

STATEMENT BY AUTHOR

This dissertation has been submitted in partial fulfillment of requirements for an advanced degree at Homi Bhabha National Institute (HBNI) and is deposited in the Library to be made available to borrowers under rules of the HBNI.

Brief quotations from this dissertation are allowable without special permission, provided that accurate acknowledgement of source is made. Requests for permission for extended quotation from or reproduction of this manuscript in whole or in part may be granted by the Competent Authority of HBNI when in his or her judgment the proposed use of the material is in the interests of scholarship. In all other instances, however, permission must be obtained from the author.



Lipika Rani Bairi

DECLARATION

I, hereby declare that the investigation presented in the thesis entitled "**Development and Characterization of D9 Stainless Steel - Zirconium Metal Waste Form Alloys**" submitted to **Homi Bhabha National Institute (HBNI)**, Mumbai, India for the award of **Doctor of Philosophy in Chemical Science** is the record of work has been carried out by me under the guidance of **Prof. U. Kamachi Mudali**. The work is original and has not been submitted earlier as a whole or in part for a degree / diploma at this or any other Institution / University.



Lipika Rani Bairi

DEDICATIONS

To my parents

Late Mrs. Kajal Rani Bairi

Dr. Bijoy Krishna Bairi

ACKNOWLEDGEMENTS

The thesis work was carried out under the guidance of **Prof. U. Kamachi Mudali**, Associate Director, Corrosion Science and Technology Group (CSTG), Indira Gandhi Centre for Atomic Research (IGCAR). I sincerely thank him for his outstanding guidance, excellent support and motivation. The subject of my Ph.D. work, metallurgy and corrosion were very new to me. He taught me with extraordinary patience which gave me immense confidence to initiate my research work. I have benefitted extremely by his teaching in HBNI course work on the fundamentals of electrochemistry, corrosion and structural materials for nuclear reprocessing plants. He also trained me to write a scientific article. It is a great privilege for me to work with him.

I would like to thank **Dr. Baldev Raj**, former Director, IGCAR, for his support, encouragement and affection to the research scholars which provided us a homely feeling in this institute for pursuing Ph.D.

I acknowledge with thanks **Shri S. C. Chetal**, Director, IGCAR and **Dr. T. Jayakumar**, Director, Metallurgy and Materials Group (MMG) for giving support in my research work.

I want to register my thanks to **Dr. C. Mallika**, Head, Aqueous Corrosion and Surface Characterization Section (ACSCS), CSTG, IGCAR for valuable suggestions and comments while preparing the thesis. She is also a member of my doctoral committee and provided extensive support in my research work with valuable guidance and motivation.

I express my sincere thanks to my doctoral committee members **Dr. K. Nagarajan** and **Dr. K.V.G. Kutty** for their guidance, precious suggestions and constant support.

I would take this opportunity to thank **Dr. V. Ganesan**, Dean Chemical Science for his constant support, guidance and encouragement.

I want to thank **Dr. S. Ningshen** for his technical support and guidance. My sincere thanks to **Dr. Rani P. George**, my friend, philosopher and guide who supported me constantly with affection and guidance.

I take this opportunity to thank Mr. P. Muralidharan, Mrs. R. Sudha, Mr. S. K. Mahato, Dr. G. Panneerselvam, Mrs. S. Kalavati, Mrs. M. Radhika, Dr. M. Kamruddin, Dr. Samima Hussain, Dr. Gopa Chakraborty, Dr. K. Prabhakara Reddy, Mr. M. Sriram, Miss Annapoorany, Mr. P. Vankatesh, Mr. A. Manivannan, Dr. V. Ganesan (INSOT), Mr. K.

Ganapathy, Mr. K. Mohanraj and A. Ramamurthy of IGCAR for their support in experimental work and analysis.

I would like to express my sincere thanks to Dr. G. Balachandran, Dr. G. Gopalakrishnan and Mr. Prabhakar Rao, Defence Metallurgical Laboratory, Hyderabad for alloy casting and to Dr. G. Bhuvaneswari, Vellore Institute of Technology, Vellore for experimental support in leachability studies.

I want to thank my senior Dr. N. Padhy, currently in Max Plank Institute for Iron Research, Duesseldorf, Germany, for his wholehearted support in my early days of research on experimental work, data analysis and valuable discussions.

I am especially grateful to all of my CSTG colleagues for their constant support and caring nature. In this context, I want to take this opportunity to thank Dr. N. Parvathavarthini, Dr. M.G. Pujar, Mrs. S. Girija, Mr. K. Thyagarajan, Mr. A. Ravi Shankar, Dr. B. Anand Kumar, Dr. J. Jayaraj, Mr. Nandagopala Krishna, Dr. R. Priya, Dr. S. C. Vanitha Kumari, Dr. S. Ramya, Mr. R. K. Sole, Mr. T. Nanda Kumar, Mr. Pradeep Samantaroy, Mr. Jagadeesh Sure, Miss K. Indira, Miss Ruth Nithila, Mr. C. Arunchandran, Dr. Vinita Viswakarma, Mrs. Anita Toppo, Mrs. Sivai Bharasi, Mrs. A. Poonguzhali, Mr. R. K. Gupta, Miss K.R. Rashmi, Miss Ezhil Vizhi, Mr. P. U. Jalendran, Mrs. S. Uma, Mr. R. Selvam and Mr. R. Sathish.

I register my acknowledgement to Dr. M. Sai Baba and his colleagues in Resource Management Group for their support.

Finally I would like to acknowledge my father, **Dr. Bijoy Krishna Bairi** and my husband **Mr. Prasanta Jana** whose constant support, encouragement and motivation made me to finish my Ph.D. thesis. I want to thank my other family members, my mother, brother Mr. Parthasarathi Bairi, sisters Ms. Deepika and Ambika and in-laws for their love, understanding and encouragement.

Last, but not the least, I want to thank all my friends for their help, care and support.



Lipika Rani Bairi
May, 2012

CONTENTS

	Page No.
SYNOPSIS	i
LIST OF FIGURES	xii
LIST OF TABLES	xviii
 CHAPTER I	
INTRODUCTION	1
1.1 Spent fuel reprocessing and waste forms	1
1.2 Metal waste form	3
1.3 Nuclear waste disposal	4
1.3.1 Engineered barrier system	5
1.3.1a Waste form and canister	5
1.3.1b Over pack and liner	6
1.3.1c Backfill	6
1.3.1d Drain	6
1.3.1e Cap	6
1.4 Waste disposal issues in geological repository	6
1.5 Aim and objectives of the thesis	8
 CHAPTER 2	
NUCLEAR WASTE IMMOBILIZATION AND METAL WASTE FORM - A REVIEW	10
2.1 Contaminants and hazards	10
2.2 Immobilization of radioactive waste	12
2.2.1 Immobilization in cement matrix	12
2.2.2 Immobilization in bituminous matrix	13
2.2.3 Immobilization in glass matrix	14
2.2.3a Borosilicate glasses	14
2.2.3b Phosphate glasses	15
2.2.3c Glass composites	15
2.2.3d Vitrification technology	16
2.2.4 Crystalline ceramic waste forms	17
2.2.4a Polyphosphate crystalline waste forms (Synroc)	19

	Page No.
2.2.5 Metal matrix immobilization	21
2.3 Development of Metal Waste Form (MWF) alloy	22
2.3.1 Role of Zr in SS-Zr MWF alloys	23
2.3.2 Microstructure of the 304/316 SS-Zr MWF alloys	25
2.3.3 Laves intermetallics in SS-Zr alloy	27
2.3.3a Distribution of noble metals in SS-Zr alloy	28
2.3.3b Distribution of actinides in SS-Zr alloy	30
2.3.4 Corrosion properties	32
2.3.4a Electrochemical corrosion testing	32
2.3.4b Immersion corrosion testing	35
2.3.4c Steam (vapour hydration) corrosion testing	36
2.4 Need for the present study	37

CHAPTER 3

MATERIALS, MEDIA AND METHODS 38

3.1 Material selection and preparation	38
3.2 Media selection and preparation	41
3.2.1 Simulated geological repository media	41
3.2.2 Simulated microbiological media	43
3.2.2a Test organism	43
3.2.2b Microbial culture media	43
3.3 Experimental details	44
3.3.1 Specimen preparation	44
3.3.2 Hardness and density measurements	45
3.3.3 Optical microscopy	47
3.3.4 Scanning electron microscopy	48
3.3.5 X-ray diffraction study	49
3.3.6 Electrochemical corrosion testing	51
3.3.6a Open circuit potential study	51
3.3.6b Potentiodynamic polarization study	53
3.3.6c Electrochemical impedance spectroscopy	55

	Page No.
3.3.7 Immersion corrosion testing	59
3.3.7a Dynamic testing (MCC-5 test)	60
3.3.7b Static testing (MCC-1 test)	60
3.3.8 X-ray photo electron spectroscopy	61
3.3.9 Atomic force microscopy	64
3.3.10 Microbiological studies	66
3.3.10a Bacterial count	66
3.3.10b Epifluorescence microscopic study	66
3.3.10c Surface characterization	67
3.3.10d Microbial induced corrosion study	67

CHAPTER 4

CHARACTERIZATION OF ALLOY METALLURGY OF D9 SS-Zr MWF ALLOYS	68
4.1 Introduction	68
4.2 Experimental	69
4.3 Results and discussion	70
4.3.1 As-cast MWF alloys	70
4.3.1.1 Hardness and density	70
4.3.1.2 Microstructural analysis by SEM	71
4.3.1.3 XRD analysis for phase identification	76
4.3.2 Homogenized MWF alloys	79
4.3.2.1 Microstructure analysis of homogenized MWF alloys by SEM	79
4.3.2.2 XRD analysis for phase identification of homogenized MWF alloys	82
4.3.2.2.1 MWF alloy K2	82
4.3.2.2.2 MWF alloy K4	84
4.3.3 High temperature XRD studies	85
4.3.3.1 MWF alloy K2	85
4.3.3.2 MWF alloy K4	87
4.4 Conclusions	90

CHAPTER 5

CORROSION BEHAVIOUR AND PASSIVE FILM ANALYSIS OF DIFFERENT D9 SS-Zr MWF ALLOYS	92
5.1 Introduction	92
5.2 Experimental	93
5.3 Results and Discussion	94
5.3.1 Electrochemical corrosion study in simulated DM water at pH 1, 5 and 8	94
5.3.1.1 OCP monitoring	95
5.3.1.2 Potentiodynamic polarization study	98
5.3.1.3 Electrochemical impedance spectroscopy	103
5.3.2 Electrochemical corrosion study in simulated KGW and RGW media	108
5.3.2.1 OCP for different MWF alloys in KGW	108
5.3.2.2 Potentiodynamic polarization study on different MWF alloys in KGW	111
5.3.2.3 Electrochemical impedance spectroscopy on MWF alloys in KGW	112
5.3.2.4 OCP monitoring for different repository Environments	114
5.3.2.5 Potentiodynamic polarization study in different simulated repository environments	117
5.3.2.6 Electrochemical impedance spectroscopy with different repository environments	118
5.3.3 Surface morphology after polarization in different simulated media	120
5.3.4 XPS analysis of the MWF passive film	125
5.3.5 AFM topography under different condition	129
5.3.5.1 AFM topography of passivated MWF alloys in different simulated media	129
5.3.5.2 AFM topography of the MWF alloy polarized in different simulated media	130
5.4 Conclusions	133

CHAPTER 6

INVESTIGATION OF SELECTIVE ELEMENTAL LEACHING AND MICROBIAL INDUCED CORROSION BEHAVIOUR OF MWF ALLOYS	135
6.1 Introduction	136
6.2 Experimental	138
6.2.1 Selective leachability testing	138
6.2.2 Microbial induced corrosion study	139
6.3 Results and discussion	140
6.3.1 Selective leachability testing by material characterization Centre	140
6.3.1.1 Leachability by MCC-5 and MCC-1 testing in DM water media	140
6.3.1.2 Leachability by MCC-1 testing in simulated KGW, RGW-1 and RGW-2	143
6.3.1.3 Surface characterization after MCC tests	144
6.3.1.3a SEM and EDS analysis after exposure in DM water	144
6.3.1.3b SEM and EDS analysis after exposure in simulated ground water	150
6.3.1.3c AFM analysis after MCC testing	152
6.3.2 Microbial induced corrosion study	158
6.3.2.1 Evaluation of bacterial density and biofilm morphology	158
6.3.2.2 Electrochemical corrosion testing	162
6.3.2.2a Open circuit potential monitoring and potentiodynamic polarization study	162
6.3.2.2b Electrochemical impedance spectroscopy	167
6.3.2.3 Evaluation of surface morphology after electrochemical studies	170
6.4 Conclusions	172

CHAPTER 7

EFFECT OF NOBLE METAL AND URANIUM ADDITION ON THE BEHAVIOUR OF MWF ALLOYS	174
7.1 Introduction	175
7.2 Experimental	176
7.3 Results and discussion	177
7.3.1 MWF alloys of D9 SS-Zr-NMFP	177
7.3.1.1 Hardness measurements	177
7.3.1.2 Microstructural analysis by SEM	177
7.3.1.3 XRD analysis for phase identification	180
7.3.1.4 Electrochemical corrosion testing	181
7.3.1.4a OCP Monitoring	181
7.3.1.4b Potentiodynamic polarization study	184
7.3.1.4c Electrochemical impedance spectroscopy	189
7.3.1.5 Surface morphology after polarization in different simulated media	193
7.3.1.6 Selective leachability testing	195
7.3.2 MWF alloys of D9 SS-Zr-NMFP-U	198
7.3.2.1 Hardness measurement	198
7.3.2.2 Microstructural analysis by SEM	198
7.3.2.3 XRD analysis for Phase identification	199
7.3.2.4 Electrochemical corrosion testing	200
7.3.2.4a OCP monitoring	200
7.3.2.4b Potentiodynamic Polarization study	201
7.3.2.4c Electrochemical impedance spectroscopy	203
7.3.2.5 Surface morphology after polarization in different simulated media	204
7.4 Conclusions	205

CHAPTER 8**SUMMARY, CONCLUSIONS AND SCOPE FOR FUTURE WORK 207**

8.1	Development of different MWF alloys	207
8.2	Characterization of alloy metallurgy of the MWF alloys	208
8.3	Corrosion and passive film behaviour of MWF alloys	209
8.4	Selective elemental leaching and microbial induced corrosion behaviour	211
8.5	Conclusions	212
8.6	Scope for Future Work	213
8.6.1	Development and characterization of Chrome Moly - Steel – Zirconium MWF alloys	213
8.6.2	Galvanic interaction of MWF alloys with canister materials	213
8.6.3	Microbially induced corrosion	214
8.6.4	Mott-Schottky analysis to evaluate semiconducting nature of passive film	214

REFERENCES 215**PUBLICATIONS, AWARDS AND RECOGNITIONS 228**

SYNOPSIS

Metal waste form (MWF) is the product of metallic waste generated at the end of pyrochemical reprocessing of spent nuclear fuel for final disposal in a geological repository [1]. Pyrochemical reprocessing is a typical spent fuel reprocessing technology wherein electro-refining process plays a key role for the extraction of uranium and plutonium [2]. The prime objective of Department of Atomic Energy, India is to produce 20% of its total energy demand through nuclear energy by 2050 [3]. As the resources of uranium are limited in India, this objective can be realized only through the effective use of the limited uranium by utilising it in Fast Breeder Reactors (FBRs) [3, 4]. In FBRs, breeding of the fertile uranium (U^{238}) produces fissionable plutonium (Pu^{239}) from which heat and energy are generated. Breeding can be enhanced by introducing high fissile atom content metallic fuel, which reduces the doubling time [2-6]. Pyrochemical reprocessing is required for treating the spent metallic fuel discharged from FBRs. This method involves dissolving the spent fuel electrochemically in a molten salt electrolyte followed by deposition of uranium and plutonium on a cathode. The electro-refining operation is carried out in a steel vessel containing a pool of molten cadmium and a mixture of molten chloride (LiCl-KCl) salts [7]. The chopped metallic fuel placed in a basket forms the anode (with respect to the Cd pool as cathode) and is immersed into the salt mixture. The actinides, alkali, alkaline earth metals and rare earth fission products are oxidized at the anode and dissolved in the molten LiCl-KCl eutectic salt. The noble metal fission products (NMFPs), stainless steel (SS) cladding hulls and zirconium (Zr) from the alloy fuel which are not oxidized, remain in the anode basket. Following dissolution, most of the uranium from the fuel is electro-transported (deposited) onto a solid cathode [7, 8]. Pyrochemical reprocessing requires compact space requirement and proliferation related advantages over aqueous reprocessing techniques in addition to reduction in the fuel inventory and fuel cost. This process also offers potential improvements in waste management [2, 9] since the quantity of waste streams generated are low. The flow sheet and the equipment in this process can be developed in such a way that the removal of purified plutonium from the fuel cycle is extremely difficult, thereby reducing the possibility of illegal diversion [7].

Three distinct material streams produced during pyrochemical reprocessing are (a) refined metallic uranium and plutonium, (b) fission products (Cs, Sr, I, Ce, Nd and Pr) and actinides (U, Pu, Np and Am) extracted from the electrolyte salt which are processed into ceramic waste form and (c) metallic waste that are consolidated into metal waste form [1,

10]. Unoxidized metals including SS cladding hulls, NMFPs, Zr from the alloy fuel and contaminated actinide elements which remain in the anode dissolution basket of the electro-refiner are consolidated and melted along with additional Zr to form SS-Zr MWF alloys [10]. The Zr content of the alloy is in the range of 5 to 20 wt.%, the NMFP (Ru, Rh, Pd, Nb, Ag and Tc) content in the range of 0.5 to 4 wt.% and the actinide content varies from 2 to 10 wt.% (mostly in the form of uranium). Both the ceramic wastes as well as metallic waste forms have to be poured inside a canister material, packed as engineered barrier system and finally disposed in geological repositories [1, 10-12].

The objective of geological disposal is to provide protection to mankind and the environment on short and long term basis [13]. As the actinides present in MWF can be up to 10 wt.%, they will retain their radioactivity for more than 10,000 years. Generally, in a geological repository the waste package materials will be subjected to harsh environments such as high temperature, radiation, oxygen, water and other aggressive minerals. Also, owing to natural disasters like volcanic eruption and earth quake, engineered barrier system is prone to failure. Owing to these factors the following issues may arise [14, 15]:

- Presence of heat generating nuclides in the High Level Waste (HLW) will lead to elevated temperatures and provide high levels of radiation. Long-term exposure of materials in such environment could damage materials.
- Exposure to high-temperature gases including oxygen can oxidise the materials resulting in the loss of structural integrity or could promote future oxidation upon exposure of the container to ground water.
- Effects of radiation like radiation hardening and embrittlement, enhanced diffusion and enhanced creep rate must be taken into account since all the materials used for waste package are susceptible to these phenomena.
- The most important issue is the interaction of the waste form with aqueous environment prevailing in repositories leading to corrosion which includes uniform corrosion, localized corrosion, galvanic corrosion, intergranular corrosion and stress-corrosion cracking.
- Most of the actinides have long half lives and have sufficient mobility in ground water [14-16]. Selective leaching of actinide elements from the MWF alloy can occur owing to interactions with the repository environment.

- Microbial induced corrosion (MIC) due to the interaction of waste form with the aqueous environment prevailing in the repository environment. As MWF is heterogeneous in nature, MIC can result from the biofilm formed and leaching of radionuclides due to MIC will be favoured [15, 17, 18].

Since the safety of nuclear-waste management relies mainly on the immobilization of radioactive constituents and long-term isolation of these from the biosphere, materials issues gain importance. The ultimate goal in nuclear-waste management is to develop a highly durable waste package (including the waste form and the surrounding container barriers) that ensures the long-term stability of materials and the isolation of radioactivity. Development of waste forms like SS-Zr is desirable because in the waste package, the waste form represents the first and foremost barrier to retard radionuclides leaching from the nuclear waste disposal site.

The aim of the present work is to develop simulated metal waste form alloys which are the metallic end product of pyrochemical reprocessing of spent nuclear metallic fuel from Fast Breeder Reactor. Alloy D9 SS (15Cr-15Ni-2.5Mo-Ti modified stainless steel) is one of the candidate clad material for the fuel (mixed oxides of uranium and plutonium). Hence, an attempt was made to characterise the MWF alloy to be generated based on D9 SS-Zr alloy. The objectives of the thesis (listed below) are to develop highly corrosion resistant MWF alloys by optimizing Zr concentration and subsequent characterization of microstructure, hardness and phase analysis with emphasis on the assessment of their degradation mechanisms under diverse environmental conditions of the geological repository with respect to corrosion, selective elemental leaching and microbiological induced degradation.

- Development of MWF alloys by casting of D9 SS with different concentrations of Zr in the first phase, with Zr and NMFP in next phase, and with Zr, NMFP and U finally.
- Detailed characterization of the metallurgical aspects of the developed MWF alloys (as cast and thoroughly homogenized condition) with respect to hardness, microstructure and phase analysis.
- Evaluation of the corrosion behaviour and stability of the passive film in different simulated ground water conditions and correlating with MWF composition.
- Assessing the selective elemental leaching behaviour of the MWF alloys in various simulated repository environments.

- Evaluation of the behaviour of the MWF alloy with respect to microbial corrosion in the presence of different biofilm forming bacterial species.

Organization of the chapter in the Thesis

This thesis comprises the eight Chapters. A brief overview of the individual chapters is presented below.

CHAPTER I

Introduction

A brief description about the reprocessing of spent nuclear fuels for the extraction of uranium and plutonium along with an overview of different waste forms generated from reprocessing plants are presented in Chapter I. Metallic fuelled fast breeder reactors (FBRs) are becoming popular owing to safety and better economy. Pyrochemical reprocessing is an essential technique for the treatment of spent metallic fuel of FBRs. Metal waste form generated at the end of pyrochemical reprocessing is consolidated and packed as engineered barrier system for disposal in geological repository. This Chapter deals with the various issues related to development of MWF alloys and the problems which can arise during geological disposal period. Additionally, it focuses on the aim and objectives of the present thesis.

CHAPTER II

Nuclear Waste Immobilization and Metal Waste Form - A Review

The technology and techniques for the development of metal waste form alloys and their characterization are described in this chapter. The development of stainless steel – zirconium metal waste form alloys for the disposal of experimental breeder reactor's (EBR-II) metallic waste by Argonne National Laboratory is discussed in detail. The role of Zr in the composition of MWF alloys was explained with the help of Fe-Zr phase diagram and its microstructure. Distribution of noble metal fission products and actinides in the MWF matrix and their influence in the corrosion behaviour of the MWF alloys in different simulated environment are explained. Chapter II concludes with the significance of the work carried out for this thesis.

CHAPTER III

Materials, Media and Methods

Chapter III describes three different aspects: (i) Proper selection of materials for the development of metal waste form and casting of MWF with different compositions, (ii) Media selection for corrosion testing and their respective compositions and (iii) details about the experimental techniques employed for the metallurgical characterization and evaluation of the corrosion behaviour of the MWF alloys.

D9 SS is a candidate clad material for future FBRs. Hence, the MWF chosen for the present work is D9 SS-Zr based alloys. D9 SS with 5 to 17 wt.% Zr were cast in five heat batches in vacuum arc melting furnace in the first phase, followed by the casting of optimized MWF alloys of D9 SS-10 wt.% Zr along with 1 to 4 wt.% NMFP in the second phase. Casting of D9 SS-10 wt.% Zr-1wt.% NMFP-10 wt.% U was done in vacuum induction furnace. The compositions and designation of the cast alloys are listed in this Chapter. The compositions of the alloys after casting were confirmed by inductively coupled plasma optical emission spectroscopic (ICP-OES) analysis. The different simulated media used for corrosion studies and the composition of Kalpakkam ground water (KGW) and Rajasthan ground water (RGW) are discussed in this Chapter. Preparation of bacterial culture media for microbial exposure studies and description about test organisms for microbial induced corrosion study are presented.

The experimental techniques used for the present thesis are described in this Chapter. Vickers Hardness Tester was used for evaluating hardness; Scanning Electron Microscopy (SEM) was employed for characterizing the microstructures and surface morphology. The compound phases formed in different MWF alloys were characterized using the X-ray diffraction technique. High temperature X-ray diffraction was used to obtain relevant information about high temperature stability of different compound phases present in MWF alloys. Using different electrochemical techniques, the corrosion behaviour of the alloys was evaluated. The open circuit potential (OCP) monitoring aided in understanding the corrosion behaviour of MWF alloys in steady state conditions. Potentiodynamic polarization study helped to understand the passive current density, range of passivation potential and break down potential of MWF alloys. Electrochemical impedance spectroscopy (EIS) was used to analyze the behaviour of hydrated passive film formed in metal solution interfaces in different simulated geological environment. Surface morphological changes after corrosion were examined by optical and scanning electron microscopy. To monitor long term corrosion

behaviour and selective elemental leaching at high temperature conditions, the MWF alloys were subjected to static and dynamic leachability tests as per ASTM standard MCC (Material Characterization Centre) testing. The leachate solutions were analysed by ICP-OES. Atomic force microscopy (AFM), SEM and X-ray photo electron spectroscopy (XPS) techniques were used to analyze the surface of MWF alloys. Total viable count, epifluorescence spectroscopy, SEM and AFM were employed to monitor the attachment of bacterial species on MWF's surface. Corrosion behaviour under bacterial action was also evaluated using different electrochemical techniques mentioned earlier.

CHAPTER IV

Characterization of Alloy Metallurgy of D9 SS-Zr MWF Alloys

Characterization of the MWF alloys with respect to hardness, microstructure and phase analysis is discussed in Chapter IV. Vickers hardness tester, SEM attached with EDS and XRD techniques were employed for this study. Increasing trend in the hardness values was observed with increasing concentration of Zr in MWF alloys. Phase analysis of MWF alloys in the as-cast condition by XRD technique revealed the formation of Ni-Zr and Fe-Zr intermetallic compounds. Microstructural analysis using SEM showed dark Fe based solid solution matrix and brighter Zr rich intermetallic precipitation with the appearance of eutectic network. The MWF alloys were homogenized at 1323 K for 2 h and 5 h and characterized by SEM and XRD. The XRD results showed the presence of NiZr, Ni₂Zr, Ni₇Zr₂, Ni₅Zr, FeZr₂, Fe₂Zr and Fe₃Zr peaks along with austenite. The XRD patterns obtained for most of the compounds were more or less the same in as-cast as well as heat treated alloys. However, the MWF alloy with 17 wt.% Zr exhibited α -ferrite peak only in the as-cast alloy. SEM micrograph indicated agglomeration of intermetallic phases after heat treatment which transformed the eutectic network into isolated islands. The stability of the Zr intermetallic compounds with respect to temperature was established using high temperature XRD technique. It is evident from this study that all the intermetallic phases were stable till 1173 K.

CHAPTER V

Corrosion and Passive Film Behaviour of D9 SS-Zr MWF Alloys

This Chapter compares the corrosion and passive film behaviour of different D9 SS-Zr MWF alloys under simulated repository conditions. DM water at pH 1, 5, 8, simulated KGW and RGW were used to simulate the repository environment. Electrochemical

techniques including OCP monitoring, potentiodynamic polarization study and EIS were employed to monitor the corrosion behaviour of the MWF alloys. The results revealed that in DM water at pH 5 and 8 and in KGW and RGW, the alloys exhibited noble corrosion potential with very low passive current density and wide range of passivation potential indicating excellent corrosion resistance. EIS studies also confirmed the formation of stable passive film. In the highly acidic media (DM water at pH 1), MWF alloys exhibited active corrosion potential with higher passive current density indicating the dissolution of metals due to corrosion. However, EIS studies showed all the alloys to exhibit good stability of passive film at the metal solution interface. In simulated ground water the MWF alloys exhibited very good passive film resistance owing to the formation of hydrated passive film and insoluble $(\text{Ca,Mg})\text{SO}_4$ layer. The corrosion behaviour was also found to depend on the composition of the MWF alloys. MWF alloys with lower concentration of Zr (5 wt.%) revealed noble corrosion potential indicating their resistance against uniform corrosion owing to the availability of Cr_2O_3 on the surface. MWF alloys with Zr concentration more than 8 wt.% showed resistance against breakdown potential due to the formation of amorphous ZrO_2 on the metallic surface. MWF alloys with the composition D9 SS- 8 to 12 wt.% Zr showed excellent corrosion resistance behaviour and passive film stability in the simulated repository environment. XPS studies on DM water passivated MWF surface revealed the formation of ZrO_2 layer below the Cr_2O_3 film. The surface morphologies of the tested samples were studied by optical microscopy, SEM and AFM. After polarization in DM water at pH 1, complete dissolution of passive film was observed without affecting the Zr rich intermetallic phases. After polarization in DM water at pH 5, 8 and in RGW, dissolution of passive film was observed to be negligible. After polarization in KGW, selective salt deposition was found on the surface of the MWF.

CHAPTER VI

Investigation of the Selective Elemental Leaching and Microbial Induced Corrosion Behaviour of D9 SS-Zr MWF Alloys

The selective elemental leaching behaviour of MWF alloys in simulated repository conditions was investigated. Leachability testing was carried out in de-mineralized water under dynamic and static conditions as per ASTM C1220 [19] and ASTM C1308 [20]. Dynamic tests were carried out with a constant flow of water at 90 °C for 260 days while the static tests were carried out at 90 °C and 200 °C for 90 days. The static leachability test was also performed for MWF alloy of D9 SS with 8.5 wt.% Zr at 90 °C for 90 days in simulated

KGW and RGW. Elemental leaching was found to be well below the detection limit of ICP-OES. Surface analysis by SEM/EDS showed the formation of zirconium oxide scale on the exposed surface of MWF. The AFM topographic analysis revealed thicker scale formation after the static test at higher temperature.

The effect of microbial species on MWF alloys in simulated repository environment with different biofilm forming bacteria is also discussed in this Chapter. Two approaches were used to realize the objectives. The first approach involved determining the effect of biocompatibility of zirconium on microbial adhesion. The second was to find out how much damage would result if the microbes are active in the biofilm using electrochemical techniques. MWF alloy specimens were exposed to two most common biofilm formers, *Bacillus* sp. and *Pseudomonas* sp. cultured in simulated Kalpakkam and Rajasthan ground water media to study the bacterial interaction with MWF alloy. The total viable count and epifluorescence microscopic study showed good attachment of bacteria on the MWF surface. Microscopic examination using SEM and AFM on etched MWF surfaces clearly revealed favourable adhesion of bacteria on Zr-rich intermetallic phases. The results of open circuit potential and potentiodynamic polarization experiments showed active corrosion potential and higher current density for biofilmed surface. EIS study indicated the weakening of passive film under the biofilm. The corrosion effect due to *Pseudomonas* sp. is comparatively more than that of *Bacillus* sp.

CHAPTER VII

Effect of Noble Metal and Actinide Addition on MWF Alloy's Behaviour

This Chapter describes the effect of noble metal fission products (NMFP) Ru, Rh and Pd on the behaviour of MWF alloys with respect to microstructure, phase stability, corrosion and selective elemental leaching. Examination of microstructures of as-cast alloys by SEM/EDS revealed that most of the NMFPs segregated at the interfacial boundary between the matrix and intermetallic phases. These NMFPs diffused to the Zr rich intermetallic phase after homogenization at 1323 K for 2 h. Phase identification by XRD did not show any significant peak for noble metals; the peaks obtained corresponded to the typical intermetallic phases Fe-Zr and Ni-Zr. The microstructure was not influenced by the compositional changes of NMFPs. However, the hardness value increased with increase in the concentration of NMFPs. Corrosion results in different simulated ground water media showed noble corrosion potential with good passive film stability. MWF alloys with NMFPs exhibited noble OCP and high impedance, whereas, the passive current density was found to be comparatively

higher than the MWF alloys. Nevertheless, the passive film formed in different media was quite stable and exhibited higher breakdown potential. The metal waste form alloy of D9 SS with Zr, NMFP and uranium was cast in vacuum induction furnace and the effect of uranium on microstructural and corrosion behaviour of MWF alloy is discussed.

CHAPTER VIII

Summary, Conclusions and Scope for Future Work

Summary and conclusions of the work performed for the development and characterization of MWF alloys is provided. This Chapter also includes the work plan for future and the scope for extending this study to other clad materials envisaged for FBRs.

For the development of highly corrosion resistant MWF alloys, initially five alloys of D9 SS with 5 to 17 wt.% Zr (designated as K1 (4.5 wt.% Zr), K2 (8.5 wt.% Zr), K3 (12.2 wt.% Zr), K3B (14.1 wt.% Zr) and K4 (16.8 wt.% Zr)) were cast. A detailed investigation of the microstructural aspects and the corrosion and selective elemental leaching behaviour in simulated ground water showed that the MWF alloys with 8 to 12 wt.% Zr to be superior with respect to corrosion resistance and phase stability. Hence, the MWF alloy K2 (D9 SS with 8.5 wt.% Zr) was selected for further studies. Corrosion testing, selective elemental leaching and microbial corrosion studies were performed with the alloy K2 in simulated KGW and RGW. Subsequently, noble metal fission products (NMFPs) Ru, Rh and Pd were added to D9 SS-10 wt % Zr MWF alloy for further investigations. Three alloys were cast and designated as N1 (1 wt.% NMFPs), N2 (2.5 wt.% NMFPs) and N3 (4 wt.% NMFPs). In the as-cast alloys the NMFPs segregated at the interfacial boundary between the solid solution and intermetallic phases; however, they diffused into the intermetallic phases after homogenization at 1323 K for 2 h. Corrosion testing of these alloys indicated wide range of passivation potential and higher breakdown potential with the formation of stable hydrated passive film on the surface of the alloys.

The MIC study revealed that Zr present in the MWF alloy is biocompatible and susceptible for microbial induced corrosion. To corroborate this observation, rigorous MIC testing of MWF alloys in the presence of noble metals and actinides is planned to be carried out in future.

Prototype Fast Breeder Reactor (PFBR) will be using modified 9 Cr-Mo steel as clad material for metallic fuel in future. Hence, future R&D will be focused on the development of

highly corrosion resistant chrome-moly ferritic steel-Zr MWF alloys and evaluating the microstructure and long term corrosion and leaching behaviour of such MWF alloys.

REFERENCES

1. J.P. Ackerman, T.R. Johnson, L.S.H. Chow, E.L. Carls, W.H. Hannum, J.J. Laidler, Prog. Nucl. Energy, 31 (1997) 141-154.
2. K. Nagarajan, T. Subramanian, B. Prabhakara Reddy, P.R. Vasudeva Rao, Baldev Raj, Nucl. Technol., 162 (2008) 259-263.
3. S.C. Chetal, P. Chellapandi, P. Puthiyavinayagam, S. Raghupathy, V. Balasubramaniyan, P. Selvaraj, P. Mohanakrishnan, Baldev Raj, Energy Proceedia, 7 (2011) 64–73.
4. Baldev Raj, H.S. Kamath, R. Natarajan, P.R. Vasudeva Rao, Prog. Nucl. Energy. 47 (2005) 369-379.
5. Baldev Raj and U. Kamachi Mudali, Prog. Nucl. Energy. 48 (2006) 283–313.
6. Baldev Raj, J. Nucl. Mater., 385 (2009) 142–147.
7. I. Johnson, J. Nucl. Mater., 154 (1988) 169-180.
8. P. Chiotti, S.J.S. Parry, J. Less-Common Met., 4 (1962) 315-337.
9. M.F. Simpson, Nucl. Technol., 162 (2008) 117.
10. D.P. Abraham, J.J. Peterson, H.K. Katyal, D.D. Keiser, B.A. Hilton, Electrochemical corrosion testing of metal waste forms, Report No. ANL/CMT/CP-100737 (2000).
11. D.P. Abraham, S.M. McDeavitt, J. Park, Metall. Mater. Trans., 27A (1996) 2151-2159.
12. D.P. Abraham, Corrosion testing of stainless steel-zirconium metal waste form, Report No. ANL/CMT/CP-97942 (1999).
13. D. Feron, D. Crussel, J.M. Grass, Corros., 65 (2000) 213-223.
14. M.-S. Yim, K. Linga Murthy, J. Metals, 52 (2000) 26-29.
15. ASTM C1174, ASTM International, West Conshohocken, PA, DOI: 10.1520/C1174-07 (2007).

16. S.G. Johnson, D.D. Keiser, M. Noy, T. O'Holleran, S.M. Frank, Microstructure and leaching characteristics of a technetium containing metal waste form, Report No. ANL/NT/CP-96709 (1999).
17. F. King, Corros., 65 (2009) 233-25.
18. B. Little, P. Wagner, Can. J. Microbiol., 42 (1996) 367-374.
19. ASTM, C1308, "ASTM International, West Conshohoken, PA. DOI: 10.1520/C1308-08(2008).
20. ASTM, C1220, ASTM International, West Conshohoken, PA. DOI: 10.1520/C1220-10 (2010).

LIST OF FIGURES

S. No.	Fig. No.	Title	Page No.
1.	Fig. 1.1.	Schematic of a typical engineered barrier system.	5
2.	Fig. 2.1.	Relative toxicity of some materials as a function of time.	11
3.	Fig. 2.2.	Cement encapsulated solid, liquid and slurry LILW in 500 L drums.	13
4.	Fig. 2.3.	Volume of simulated borosilicate glass which is sufficient to hold all the HLW arising from a nuclear reactor generating electricity for a single person of 80 year lifetime.	15
5.	Fig. 2.4.	Microstructure of waste encapsulated GCMs: (a) Synroc-glass with zirconolite crystalline phase; (b) immobilized yellow phase; (c) GCM for immobilizing iodine.	16
6.	Fig. 2.5.	Backscattered electron images of ceramics based on (a) zircon, (Zr, Pu)SiO ₄ , doped with 6.1 wt.% Pu; (b) cubic zirconia, (Zr, Gd, Pu)O ₂ , doped with 10.3 wt.% Pu.	18
7.	Fig. 2.6.	Ceramic waste form with (a) waste phases in solution and (b) ceramic with encapsulated waste phases	20
8.	Fig. 2.7.	Binary phase diagram of Fe-Zr system	24
9.	Fig. 2.8.	Typical microstructure of type 304SS- Zr alloy: (a) 304SS-5 Zr, (b) 304SS-10 Zr, (c) 304SS-15 Zr, (d) 304SS-20 Zr, (e) 304SS-30 Zr, (f) 304SS-40 Zr, (g) 304SS-60 Zr, (h) 304SS-83 Zr and (i) 304SS-92 Zr	26
10.	Fig. 2.9.	Collection of X-ray maps and backscattered electron image of as-cooled SS-15 wt.% Zr-2 wt.% Ru-1.5 wt.% Pd-0.5 wt.% Ag alloy.	29
11.	Fig. 2.10.	Backscattered electron images of Zr-8 wt.% SS-1 wt.% Nb-1 wt.% Ru-1 wt.% Pd-1 wt.% Ag. Enrichment of the noble metal content occurred at Zr phase boundaries in (a) primary and (b) secondary zirconium phases	30
12.	Fig. 2.11.	Representative BSE image of a MWF sample produced from irradiated EBR-II cladding hulls. The dark areas corresponded to the ferrite phase. The actinide-rich areas (marked by arrows) appear as high-brightness regions within the ZrFe ₂ -type intermetallic	31
13.	Fig. 2.12.	Galvanic current measured for SS-15 Zr (SS15ZR17) and SS-15Zr-1Nb-1Pd-1Rh-1Ru (SS15ZR25) specimens coupled to C-22 in J-13 solution	35
14.	Fig. 3.1.	Typical pancake shaped D9 SS-Zr MWF alloy ingot	40
15.	Fig. 3.2.	Typical cast of D9 SS- Zr-NMFP MWF ingot	40
16.	Fig. 3.3.	Typical cast of D9 SS- Zr-NMFP-U MWF ingot	41
17.	Fig. 3.4.	Schematic representation of Vickers hardness indentation	46

S. No.	Fig. No.	Title	Page No.
18.	Fig. 3.5.	Schematic of a typical electrochemical cell for corrosion study	52
19.	Fig. 3.6.	Potentiostatic anodic polarization circuit diagram	54
20.	Fig. 3.7.	Nyquist Plot with Impedance Vector	56
21.	Fig. 3.8.	Simple Equivalent Circuit with One Time Constant	56
22.	Fig. 3.9.	Bode Plot with One Time Constant	56
23.	Fig. 3.10.	The equivalent circuit used for fitting the impedance data (a) with one time constant (b) with two time constant	58
24.	Fig. 3.11.	Soxhlet apparatus used for dynamic leachability study	61
25.	Fig. 3.12.	Schematic representation of the XPS process	62
26.	Fig. 3.13.	Schematic representation of AFM Principle	65
27.	Fig. 4.1.	BSE mode SEM micrographs of D9 SS-Zr MWF alloys	72
28.	Fig. 4.2.	X-ray elemental mapping of the MWF alloy, K3 (D9-12.2 Zr)	75
29.	Fig. 4.3.	X-ray diffraction pattern of different D9 SS-Zr MWF alloys in as-cast condition	76
30.	Fig. 4.4.	Magnified view of X-ray diffraction pattern of different D9 SS-Zr MWF alloys in as-cast condition	78
31.	Fig. 4.5.	Secondary electron mode SEM microstructure of MWF alloy K2 (a) as-cast (b) Homogenized for 2 h at 1323 K (c) Homogenized for 5 h at 1323 K	80
32.	Fig. 4.6.	Secondary electron mode SEM Microstructure of MWF alloy K4 (a) as-cast (b) Homogenized for 2 h at 1323 K (c) Homogenized for 5 h at 1323 K	81
33.	Fig. 4.7.	XRD patterns of MWF alloy K2 of as-cast condition, homogenized at 1323 K for 2 h and 5 h	83
34.	Fig. 4.8.	XRD patterns of MWF alloy K4 in as-cast condition, homogenized at 1323 K for 2 h and 5 h	84
35.	Fig. 4.9.	High temperature XRD patterns of MWF alloy K2	86
36.	Fig. 4.10.	High temperature XRD patterns of MWF alloy K4	89
37.	Fig. 5.1.	Variation of OCP with time for different MWF alloys in DM water at pH 1	96
38.	Fig. 5.2.	Variation of OCP with time for different MWF alloys in DM water at pH 5	97
39.	Fig. 5.3.	Variation of OCP with time for different MWF alloys in DM water at pH 8	97
40.	Fig. 5.4.	Potentiodynamic polarization plot of different MWF alloys in DM water at pH 1	99

S. No.	Fig. No.	Title	Page No.
41.	Fig. 5.5.	Potentiodynamic polarization plot of different MWF alloys in DM water at pH 5	100
42.	Fig. 5.6.	Potentiodynamic polarization plot of different MWF alloys in DM water at pH 8	101
43.	Fig. 5.7.	Electrochemical impedance spectra of MWF alloys in DM water at pH 1	104
44.	Fig. 5.8.	Electrochemical impedance spectra of MWF alloys in DM water at pH 5	105
45.	Fig. 5.9.	Electrochemical impedance spectra of MWF alloys in DM water at pH 8	106
46.	Fig. 5.10.	OCP versus time plot for different MWF alloys in KGW (a) for 1 h, (b) for 24 h	110
47.	Fig. 5.11.	Potentiodynamic polarization plots for different MWF alloys in KGW	111
48.	Fig. 5.12.	Electrochemical impedance spectra of different MWF alloys at KGW	113
49.	Fig. 5.13.	OCP versus time plot of MWF alloy (K2) in KGW, RGW-1 and RGW-2 (a) for 1h (b) for 24 h	116
50.	Fig. 5.14.	Potentiodynamic polarization plots of MWF alloy (K2) in KGW, RGW-1 and RGW-2	117
51.	Fig. 5.15.	Electrochemical impedance spectra of MWF alloy (K2) in KGW, RGW-1 and RGW-2	119
52.	Fig. 5.16.	Optical microscopic images of MWF alloys after polarization at pH 1	121
53.	Fig. 5.17.	Optical microscopic images of MWF alloys after polarization at pH 5	121
54.	Fig. 5.18.	Optical microscopic images of MWF alloys after polarization at pH 8	122
55.	Fig. 5.19.	SEM images of MWF alloys after polarization at pH 1	123
56.	Fig. 5.20.	SEM images and EDS spectra of MWF alloy (K2) after polarization in KGW	124
57.	Fig. 5.21.	The SEM images of MWF alloy (K2) after polarization in RGW media (a) RGW-1, (b) RGW-2.	125
58.	Fig. 5. 22.	Survey spectra of MWF surface after 1 minute and 3 minute sputtering by Ar gun	126
59.	Fig. 5. 23.	De-convoluted XPS spectra for oxygen (a) after 1 minute sputtering (b) after 3 minute sputtering	127
60.	Fig. 5. 24.	De-convoluted XPS spectra for Zirconium (a) after 1 minute sputtering (b) after 3 minute sputtering	128

S. No.	Fig. No.	Title	Page No.
61.	Fig. 5. 25.	De-convoluted XPS spectra for Chromium (a) after 1 minute sputtering (b) after 3 minute sputtering	128
62.	Fig. 5.26.	AFM images of MWF alloy (K2) passivated in (a) DM water at pH 5, (b) DM water at pH 8, (c) KGW (d) RGW	130
63.	Fig. 5.27.	AFM images of the MWF alloy (K2) polarized in (a) DM water at pH 5, (b) DM water at pH 8, (c) KGW and (d) RGW	131
64.	Fig. 5.28.	AFM images of MWF alloy after (a) polarization in DM water at pH 1 and (b) electrochemical etching in 10 % ammonium persulphate solution	132
65.	Fig. 6.1.	The graphical representation of selective leaching of element Fe, Cr, Ni and Zr up to 260 days of MCC-5 testing at 90 °C. The concentration of the element was below the detection limit of the instrument (< 0.25 ppm)	141
66.	Fig. 6.2.	SEM images of MWF alloys surface before leachability testing	145
67.	Fig. 6.3.	SEM images of MWF alloys after 260 days of MCC-5 testing at 90 °C	146
68.	Fig. 6.4.	SEM images of MWF alloys after 90 days of MCC-1 testing at 90 °C	148
69.	Fig.6.5.	SEM images of MWF alloys after 90 days of MCC-1 testing at 200 °C	149
70.	Fig.6.6.	SEM images of MWF alloy (K2) after MCC-1testing at 90 °C for 90 days	151
71.	Fig. 6.7.	AFM images of MWF alloys after 260 days of MCC-5 testing at 90 °C	153
73.	Fig. 6.8.	AFM images of MWF alloys after 90 days of MCC-1 testing at 90 °C	154
74.	Fig. 6.9.	AFM images of MWF alloys after 90 days of MCC-1 testing at 200 °C	155
75.	Fig. 6.10.	AFM images of MWF alloy (K2) after 90 days MCC-1testing in KGW at 90 °C	156
76.	Fig. 6.11.	AFM images of MWF alloy (K2) after 90 days MCC-1testing in RGW-1 at 90 °C	156
77.	Fig. 6.12.	AFM images of MWF alloy (K2) after 90 days MCC-1testing in RGW-2 at 90 °C	157
78.	Fig. 6.13.	Epifluorescence microscopic structure to understand the growth of biofilms on the MWF surface in different geological environment. (a) <i>Bacillus</i> sp. in KGW media (b) <i>Bacillus</i> sp. in RGW media (c) <i>Pseudomonas</i> sp. in KGW media (d) <i>Pseudomonas</i> sp. in RGW media	159

S. No.	Fig. No.	Title	Page No.
79.	Fig. 6.14.	SEM microstructure of the MWF surface exposed in different bacterial and geological environment to understand the preferential sites for bacterial attachment. (a) <i>Bacillus</i> sp. in KGW media (b) <i>Bacillus</i> sp. in RGW media (c) <i>Pseudomonas</i> sp. in KGW media (d) <i>Pseudomonas</i> sp. in RGW media (e) magnified view of <i>Pseudomonas</i> sp. in RGW media	160
80.	Fig. 6.15.	AFM images of etched MWF alloy surfaces exposed to different bacterial culture media (a) <i>Bacillus</i> sp. in KGW media (b) <i>Bacillus</i> sp. in RGW media (c) <i>Pseudomonas</i> sp. in KGW media (d) <i>Pseudomonas</i> sp. in RGW media	161
81.	Fig. 6.16.	OCP variation with time for MWF alloy in KGW media in sterile condition and with presence of different bacterial species.	163
82.	Fig. 6.17.	OCP variation with time for MWF alloy in RGW media in sterile condition and with presence of different bacterial species	163
83.	Fig. 6.18.	Potentiodynamic polarization plots of MWF alloy exposed in KGW media in sterile condition and with presence of different bacterial species	165
84.	Fig. 6.19.	Potentiodynamic polarization plots of MWF alloy exposed in RGW media in sterile condition and with presence of different bacterial species	165
85.	Fig. 6.20.	EIS plots of MWF alloy exposed in KGW media. in sterile condition and with presence of different bacterial species	168
86.	Fig. 6.21.	EIS plots of MWF alloy exposed in RGW media in sterile condition and with presence of different bacterial species	168
87.	Fig. 6.22.	Optical Microscopic images of MWF alloy surface after polarization in different electrolytes. (a) <i>Bacillus</i> sp. in KGW media (b) <i>Bacillus</i> sp. in RGW media (c) <i>Pseudomonas</i> sp. in KGW media (d) <i>Pseudomonas</i> sp. in RGW media	171
88.	Fig. 7.1.	SEM microstructure of different D9 SS-Zr-NMFP MWF alloys	178
89.	Fig. 7.2.	XRD pattern of NMFP added MWF alloys	181
90.	Fig. 7. 3.	Variation of OCP with time for NMFP added MWF alloys in DM water at pH 1	183
91.	Fig. 7. 4.	Variation of OCP with time for NMFP added MWF alloys in DM water at pH 5	183
92.	Fig. 7. 5.	Variation of OCP with time for NMFP added MWF alloys in KGW	184
93.	Fig. 7. 6.	Potentiodynamic polarization plots of different MWF alloys with NMFP and K2 in DM water at pH 1	185

S. No.	Fig. No.	Title	Page No.
94.	Fig. 7.7.	Potentiodynamic polarization plots of different MWF alloys with NMFP and K2 in DM water at pH 5	186
95.	Fig. 7. 8.	Potentiodynamic polarization plots of different MWF alloys with NMFP and K2 in KGW medium	188
96.	Fig. 7.9.	Variation of passive current density with NMFP concentration in different simulated media	189
97.	Fig. 7.10.	EIS plot of NMFP added MWF alloys in DM water at pH 1	190
98.	Fig.7.11.	EIS plot of NMFP added MWF alloys in DM water at pH 5	191
99.	Fig. 7.12.	EIS plot of NMFP added MWF alloys in KGW	192
100.	Fig. 7.13.	Optical microscopic images of NMFP added MWF alloys after polarization at pH 1	194
101.	Fig. 7.14.	Optical microscopic images of NMFP added MWF alloys after polarization at pH 5	194
102.	Fig. 7.15.	Optical microscopic images of NMFP added MWF alloys after polarization in KGW	194
103.	Fig.7.16.	SEM images of NMFP added MWF alloys after 90 days MCC-1 testing at 90 °C	197
104.	Fig. 7.17.	SEM microstructure and EDS composition of U added MWF alloy (a) BSE microstructural image (b) EDS composition of dark phase (c) EDS composition of bright phase	199
105.	Fig.7. 18.	XRD pattern of U added MWF alloy	200
106.	Fig.7. 19.	Variation of OCP with time of U added MWF alloys in DM water at pH 5, simulated KGW and RGW	201
107.	Fig.7. 20.	Potentiodynamic polarization plot of U added MWF alloy in DM water at pH 5, simulated KGW and RGW	202
108.	Fig. 7.21.	EIS plot of U added MWF alloy in DM water at pH 5, simulated KGW and RGW	203
109.	Fig. 7.22.	Optical microscopic images of U added MWF alloys after polarization in different simulated media	204

LIST OF TABLES

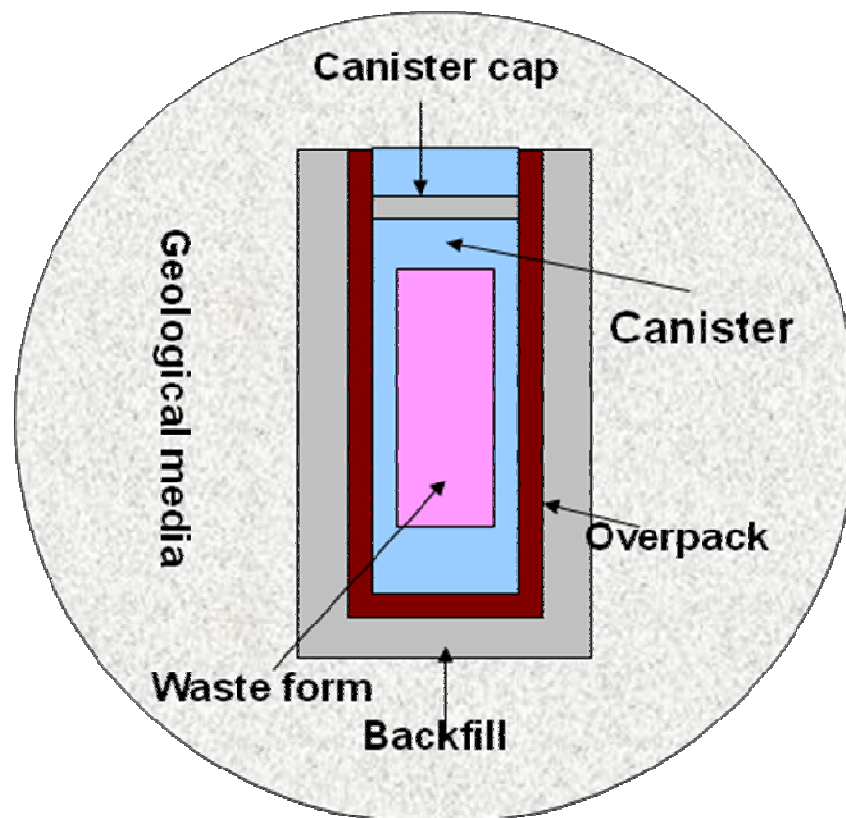
S. No.	Table No.	Title	Page No.
1.	Table 2.1.	Corrosion rates of MWF alloys measured in solutions of pH 2 to 10	32
2.	Table 2.2.	Corrosion rates of MWF alloys containing U and Tc	33
3.	Table 2.3.	Corrosion rates of MWF alloys measured in high chloride solution	33
4.	Table 3.1.	Chemical composition of the D9 SS- Zr MWF alloys	39
5.	Table 3.2.	Chemical composition of D9SS-Zr-NMFP MWF alloys	41
6.	Table 3.3.	Composition of KGW and RGW media	42
7.	Table 3.4.	Morphological and biochemical tests results of bacterial sp.	44
8.	Table 4.1.	Hardness and density values of MWF alloys	71
9.	Table 4.2.	Elemental composition of the MWF alloys at two different regions by EDS	74
10.	Table 4.3.	Elemental composition of as-cast and homogenized MWF alloys in different regions by EDS	82
11.	Table 4.4.	Phases present in the characterization of MWF alloy K2 by HTXRD	87
12.	Table 4.5.	Phases present in the characterization of MWF alloy K4 by HTXRD	88
13.	Table 5.1.	Polarization parameters for different MWF alloys in DM water at pH 1	99
14.	Table 5.2.	Polarization parameters for different MWF alloys in DM water at pH 5	100
15.	Table 5.3.	Polarization parameters for different MWF alloys in DM water at pH 8	101
16.	Table 5.4.	EIS fitted values of different MWF alloys in DM water at pH 1	104
17.	Table 5. 5.	EIS fitted values of different MWF alloys in DM water at pH 5	105
18.	Table 5.6.	EIS fitted values of different MWF alloys in DM water at pH 8	106
19.	Table 5.7.	Polarization parameters for different MWF alloys in KGW	112
20.	Table 5.8.	EIS fitted values for different MWF alloys in KGW	114
21.	Table 5.9.	Polarization parameters for the different MWF alloy (K2) in KGW, RGW-1, RGW-2	118
22.	Table 5.10.	EIS fitted values for MWF alloy (K2) in KGW, RGW-1 and RGW-2	119

S. No.	Table No.	Title	Page No.
23.	Table 6.1.	Weight of MWF alloys before and after 260 days of MCC-5 testing.	142
24.	Table 6.2.	Weights of MWF alloys before and after leachability (MCC-1) testing	142
25.	Table 6.3.	Weights of MWF alloy (K2) before and after MCC-1 testing in simulated ground water	144
26.	Table 6.4.	EDS analysis of MWF alloy specimen after 260 days of MCC-5 testing at 90 °C	147
27.	Table 6.5.	EDS analysis of MWF alloy specimen after 90 days of MCC-1 testing at 90 °C.	150
28.	Table 6.6.	EDS analysis of MWF alloy specimen after 90 days of MCC-1 testing at 200 °C	150
29.	Table 6.7.	EDS analysis for elemental concentration of the MWF alloy (K2) surface after MCC-1 testing in simulated ground water media at 90 °C for 90 days	152
30.	Table 6.8.	Quantitative result of bacterial density by TVC method	158
31.	Table 6.9.	Polarization parameter for MWF alloy in KGW and RGW with different bacterial culture media	166
32.	Table 6.10.	EIS fitted values for MWF alloy in KGW and RGW with different bacterial culture media	169
33.	Table 7.1.	Hardness of MWF with and without NMFPs alloys	177
34.	Table 7.2.	Elemental composition of NMFP added MWF alloys at different regions by EDS	179
35.	Table-7.3.	Polarization parameters of different NMFP added MWF alloys in DM water at pH 1	185
36.	Table-7.4.	Polarization parameters of different NMFP added MWF alloys in DM water at pH 5	187
37.	Table-7.5.	Polarization parameters of different NMFP added MWF alloys in KGW	187
38.	Table 7.6.	EIS fitted values of NMFP added MWF alloys in DM water at pH 1	190
39.	Table 7.7.	EIS fitted values of NMFP added MWF alloys in DM water at pH 5	191
40.	Table 7.8.	EIS fitted values of NMFP added MWF alloys in KGW	193
41.	Table 7.9.	Weight of NMFP added MWF alloys before and after 90 days of MCC-1 testing	195

S. No.	Table No.	Title	Page No.
42.	Table 7.10.	Composition of leachate solution after 90 days of MCC-1 testing at 90 °C along with blank DM water composition	196
43.	Table 7.11.	EDS analysis of NMFP added MWF alloys' surface after 90 days of MCC-1 testing at 90 °C	197
44.	Table 7.12.	Polarization parameter of U added MWF alloy in different simulated media.	202
45.	Table 7.13.	EIS fitted value of U added MWF alloy in different simulated media	204

CHAPTER 1

INTRODUCTION



CHAPTER 1

INTRODUCTION

“Waste form” is an assemblage of unwanted or undesired materials, produced at the end of any kind of treatment (solid materials such as process residues as well as liquid and gaseous effluents). Many times, one’s waste may turn out to be another’s wealth. Reusable plastics and other components in day-to-day household waste are examples of this kind. As radioactive waste emits nuclear radiation, it cannot be reused and may be harmful for environment [1]. Like other industrial activities which generate effluents, nuclear wastes are generated during various steps of nuclear fuel cycle operation such as mining, fuel fabrication, reactor operation and spent fuel reprocessing [2, 3]. The nuclear waste which is generated during the reprocessing of spent nuclear fuel gets worldwide attention [2] because it contains maximum radioactivity. Metal waste form is one of the radioactive waste forms generated from the pyrochemical reprocessing of spent metallic nuclear fuel.

1.1 Spent fuel reprocessing and waste forms

The fuel discharged from nuclear reactors after maximum burn up is referred to as ‘spent fuel’ [1, 4]. The spent fuel contains fission fragments from the spontaneous fission of the fissile elements, uranium and transuranic (TRU) actinides (mainly neptunium, plutonium, americium and curium) by the absorption of neutrons in addition to the un-burnt fuel [2, 5]. Reprocessing of the spent fuel is essential for closing of the fuel cycle by way of recovering the un-burnt fuel material and reducing the radioactivity in the waste [6]. Two types of techniques are mainly available for the reprocessing of spent nuclear fuel, namely aqueous reprocessing and pyrochemical reprocessing. In aqueous reprocessing, combination of solvent extraction and ion exchange separation techniques are employed. The spent fuel is mechanically or chemically de-jacketed from the cladding material and dissolved in nitric acid. The acid solution is subjected to solvent extraction for the removal of fission products in

the first stage and uranium in the second stage. The separated plutonium is further purified by either ion exchange process to plutonium nitrate or precipitation to plutonium oxalate and finally converted to the stable plutonium oxide [7]. The fission products and other actinides are separated and immobilized with various stabilization matrices like borosilicate glass or ceramic systems and finally disposed. This technique is a well established process for the reprocessing of thermal and fast breeder reactor fuels [8-10].

The pyrochemical process is mainly applicable for the reprocessing of mixed oxide and metallic fuel from fast reactors by using electrochemical technique. The key operation in this process is the electrorefining of uranium and plutonium in a molten salt electrolyte. The fuel is electrochemically dissolved and uranium, plutonium and actinide are deposited on a cathode [4]. The electrorefiner (ER) is a steel crucible containing a pool of molten cadmium overlaid with a mixture of molten chloride (LiCl-KCl) salts [8]. The chopped spent fuel along with their clad placed in a basket forms the anode (with respect to the Cd pool) and is immersed into the salt mixture. The alkali, alkaline earth and rare earth fission products are oxidized at the anode and dissolved in the molten LiCl-KCl eutectic salt. Following dissolution, most of the uranium from the fuel is electro-transported (deposited) onto a solid cathode. Subsequently, a smaller Cd pool is introduced into the salt as the cathode. The remaining uranium, TRU and a fraction (~5-10%) of rare earth fission products are electro-transported to the liquid cadmium cathode. The mixture of TRU, uranium and rare-earths is recovered from the solid cathode and Cd cathode by distillation of Cd and salt. The noble metal fission products (NMFs), stainless steel (SS) cladding hulls and Zr from alloy fuel which are not oxidized remain in the anode basket. The separations are obtained by control of the conditions during the oxidation and reduction steps of the process [4, 9]. In the recovery of plutonium and uranium from the mixed oxide fuels of fast reactors, the first step of these

processes involved the reduction of the oxide to metal so that the main separations were achieved by molten-salt-liquid-metal extraction processes [4, 10].

Pyrochemical reprocessing is an advanced technology for achieving the goals of nuclear fuel cycle. It is a dry processing technique in which the spent fuel is electrolytically separated into reusable product and waste stream using high temperature molten salt electrolytes. It can readily be operated remotely because the reagents are highly resistant to radiation damage and can be operated at high temperatures, hence, require minimal cooling of the spent fuel. Compared to aqueous reprocessing technique, pyroprocessing has compact space requirements and operational advantages. This reduces the fuel inventory and therefore, the fuel cost. It also offers improvement in waste management because of the less quantity of waste stream generated [11 - 13]. The chemical processes and the equipment can be designed in such a way that the removal of purified plutonium from the fuel cycle is extremely difficult, thereby reducing the possibility of illegal diversion [4]. Three distinct material streams produced in pyrochemical processing are (a) refined metallic uranium, (b) active and rare earth fission products (e.g., Cs, Sr, I, Ce, Nd and Pr) and actinides (e.g., Pu, Np and Am) extracted from the electrolyte salt which are processed into ceramic waste form and (c) metallic waste that are consolidated into a metal waste form. The salt-borne ceramic wastes are immobilized in zeolite through ion exchange and salt occlusion into a glass-ceramic composite waste form [14-18].

1.2 Metal waste form

The electrochemically noble metals (with respect to U and Pu) which remain inert in the anode dissolution basket after the electrometallurgical treatment are referred to as metallic waste form (MWF). As discussed in Section 1.1, the NMFPs, Zr from the alloy fuel and SS cladding hulls are not oxidized in the pyrochemical reprocessing and hence, remain inert in the anode dissolution basket or in filters along with a residual portion of the actinides. The

anode dissolution basket and its contents are melted together to form a 'metal waste form (MWF)' while the rare-earths and transuranic elements are removed and reintroduced into the electro refiner. Thus a stainless steel-zirconium metal ingot formed by melting the solid metallic waste and the anode basket at 1600°C is known as the metallic waste form [5,14].

The baseline composition of MWF alloy is mainly SS-15wt.% Zr for a stainless steel based clad. However, the zirconium content of the alloy is expected to range from 5 to 20 wt.% [19-22]. The NMFP (Ru, Rh, Pd, Nb, Ag and Tc) content is in the range 0.5 to 4 wt.% and the actinide content varies from 2 to 10 wt.% (mostly in the form of uranium) [23 - 25]. The content of the NMFP, Zr and actinide depends on the type of fuel clad and burn up. Both the ceramic waste forms and metallic waste forms have to be confined inside a canister material, packed as engineered barrier system and finally disposed in geological repositories [3,5,15].

1.3 Nuclear waste disposal

Waste disposal is the final step of waste management and ideally includes placing radioactive waste in a dedicated disposal facility [6]. The concept of geological disposal is to protect human beings and the environment on short and long term basis [15,16]. Hence, all types of radioactive waste need to be carefully managed to keep the public safe, protect the environment and ensure security from accidental or deliberate intrusion. For the safe disposal of radioactive waste in repositories, it is generally packed in a multi-barrier system to isolate the waste from the biosphere. This multi-barrier system typically comprises the natural geological barrier provided by the host rock and an engineered barrier system (EBS). The EBS consists of different components including waste matrix, container or over-pack, buffer or backfill, repository walls and wall linings. The various barriers act in concert, initially to contain the radionuclides and then to limit their release to the accessible environment. The

overall safety and acceptability of such a system is achieved through a sensible balance of these functions [3,6,15,17].

1.3.1 Engineered barrier system

The barriers represent an important component of the safety of the disposal facility from the operational phase through the period of institutional control and ultimately to the possible free release of the site. Assessment of the radiological performance of the disposal facility can provide a key input into the choice of barrier which is the time scale over which the barrier is assumed to function. Figure 1.1 represents a schematic of a typical engineered barrier system. A brief description of its function and the preferred material for use in various parts in the engineered system are listed in the following Section [26].

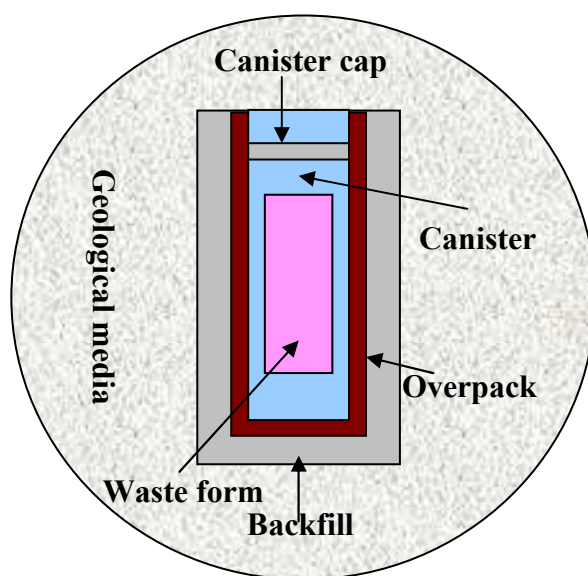


Fig. 1.1. Schematic of a typical engineered barrier system

1.3.1a Waste form and canister

The waste form and canister can provide a barrier to radionuclide migration and certain amount of mechanical strength. The radionuclide barrier function can be provided by low permeability and/or by high sorption capacity. High strength (compressive) and excellent resistance to leachability and corrosion are the important properties of waste form. The

efficiency of the waste form is established based on leach tests. The most preferred materials for canister are Cu and alloy 22 for longer duration [21, 24, 27, 28].

1.3.1b Over pack and liner

Disposal facility structure provides physical stability and containment barrier. Over pack and liners used for disposal facility structure include concrete, reinforced concrete, clay and asphaltic or organic membranes. The key properties required for disposal facility structure are permeability, compressive strength and shear strength [26].

1.3.1c Backfill

Backfills are used for void filling to avoid excessive settlement, limiting the water infiltration, sorption and precipitation of radionuclides, gas control and if necessary to facilitate waste retrieval. Typical materials used either singly or as admixtures include clay, cement grout, rock, soil, etc. [26].

1.3.1d Drain

Drain is designed for water management, particularly during the disposal facility's institutional phase. Typical drainage systems are combinations of clay and gravel blankets, conventional ceramic and concrete drains. The key parameter is volumetric flow [26].

1.3.1e Cap

The purpose of the cap is to facilitate water run-off, limit infiltration of water, provide gas control and to serve as an intrusion barrier and an erosion barrier [19]. Materials used in cap systems include clay, soil/sand, gravel and cobbles, geotextiles, concrete slabs, asphalt and polymeric membranes. The key parameters in selecting the cap design and its components are vertical permeability, water shedding capacity, plasticity, etc. [26].

1.4 Waste disposal issues in geological repository

The actinides, uranium and plutonium present in the MWF alloy may contaminate the environment (as they will be radioactive for more than 100,000 years) though they are

contained in engineered barrier system [5, 17, 18]. Also owing to natural disasters like volcanic eruption and earth quake, engineered barrier system is prone to failure. As physical and chemical stresses arise in the geological site, the following issues can arise [3, 29] during prolonged duration.

- Long-term exposure in a repository could result in significant alterations in materials properties of the EBS during their service life.
- Presence of heat generating nuclides in the high level radioactive waste (HLW) will lead to elevated temperatures and provide high levels of radiation.
- The host media for the repository can be sources of oxygen, water and other species that can be aggressive in altering the nature of the materials used for containment of the waste.
- The physical stresses caused inside the repository owing to high temperature and radiation can degrade the materials of the EBS. Exposure to high-temperature gases containing oxygen can cause oxidation of the materials resulting in loss of structural integrity or could encourage future oxidation upon exposure of the container to ground water.
- Effects of radiation like radiation hardening and embrittlement, enhanced diffusion and enhanced creep rate must be taken into account since all materials are susceptible to these phenomena.
- Corrosion is the most important issue due to the interaction of MWF with aqueous environment which includes uniform corrosion, localized corrosion, galvanic corrosion, intergranular corrosion and stress-corrosion cracking.
- Most of the actinides have long half lives and have sufficient mobility in ground water [3,28,29]. Selective leaching of actinide elements from the MWF alloy can occur due to interaction with the repository environment.

- Microbial induced corrosion (MIC) is one of the major problems in the repository environment. Biofilm formation will be a common phenomenon in the repository environment. As MWF is spatially heterogeneous in nature, localized corrosion can result from the separation of anodic and cathodic processes under the biofilm and leaching of radionuclides due to localized corrosion will be encouraged [28,30,31].

Materials issues are important during the entire process of nuclear-waste disposal period. The performance of the materials used in nuclear waste management determines its safety/hazards. Since the safety of nuclear-waste management relies mainly on the immobilization of radioactive constituents and long-term isolation of these from the biosphere, materials issues are particularly important. Proper selection of materials and quality control of materials manufacturing can lead to a reduction in contamination from nuclear waste. A key consideration in nuclear-waste management is the development of a highly durable waste package (including the waste form and the surrounding container barriers) that ensures the long-term stability of materials and the isolation of radioactivity. Use of durable waste packages is important in the interim storage of nuclear waste also. Development of waste forms like SS-Zr is desirable because in the waste package, the waste form represents the first and foremost barrier to the release of radionuclides from nuclear waste.

Thus, the development of a robust waste form is the first and foremost important task to restrict the release of radionuclides from nuclear waste.

1.5 Aim and objectives of the thesis

The aim is to develop metal waste form alloys which are the end product of metallic waste streams resulting from the pyrochemical reprocessing of spent nuclear fuel from Prototype Fast Breeder Reactor (PFBR), India. Alloy D9 (15Cr-15Ni-2.5Mo-Ti modified stainless steel) is considered as a candidate clad material for mixed uranium and plutonium

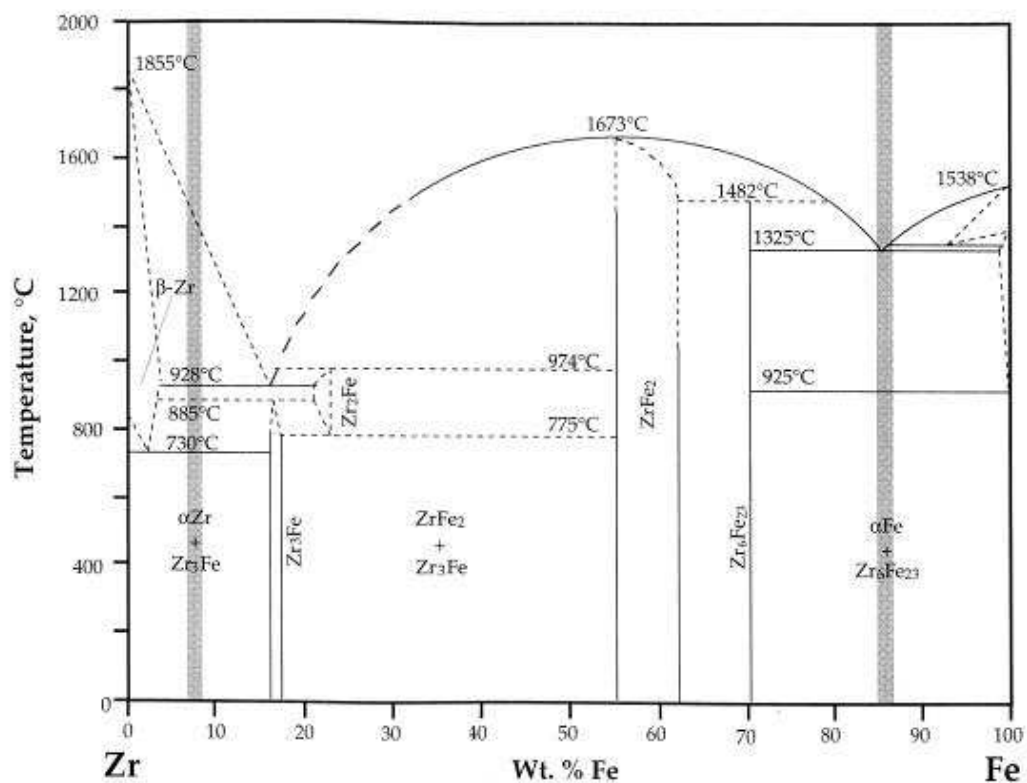
oxide fuel as well as metallic U-Pu-Zr fuel. Hence, the MWF to be generated will be based on D9 SS-Zr alloy [32]. The objectives of the thesis is to (i) develop highly corrosion resistant MWF alloys by optimizing Zr concentration, and (ii) subsequent characterization for detailed alloy metallurgy and physical properties with emphasis on the assessment of their degradation mechanisms under diverse environmental conditions of the geological repository with respect to corrosion, selective leaching and microbiological degradation. Towards this purpose the focus of the present work is to evaluate the performance metal waste form in order to address the following important issues which can arise during nuclear waste disposal.

1. **Microstructure of the MWF:** Is the microstructure beneficial for overcoming the issues discussed in the preceding sections?
2. **Stability of the microstructural phases:** Are the microstructural phases stable and effective in containing the waste form under high temperature conditions?
3. **Corrosion properties:** Does the composition of the MWF alloys influence the corrosion and selective leaching properties?
4. **Environmental condition:** Will the MWF alloys be sensitive towards the geological environmental fluctuation?
5. **Passive film:** How the passive film of the MWF alloys formed under different environmental conditions will behave?
6. **Microbial corrosion:** What will be the effect of microbes present in the geological environment in degrading the MWF alloys?

The present thesis is focused towards providing systematic data and information to clarify these queries without any ambiguity.

CHAPTER 2

NUCLEAR WASTE IMMOBILIZATION AND METAL WASTE FORM - A REVIEW



CHAPTER 2

NUCLEAR WASTE IMMOBILIZATION AND METAL WASTE FORM – A REVIEW

Radioactive waste is defined as the waste material which contains or is contaminated with radionuclides at concentrations or activities greater than the permissible levels prescribed by the regulatory authorities of individual countries and for which no use is foreseen. It will be associated with significant levels of radiation and hence, it requires immobilization and shielding to prevent the radionuclides spreading around the biosphere. The human society has employed different approaches for the management of radioactive waste from the other forms. Immobilization is a technique which reduces the potential for migration or dispersion of contaminants including radionuclides. The International Atomic Energy Agency (IAEA), Vienna defines immobilization as the conversion of a waste into a waste form by solidification, embedding or encapsulation [33, 34].

2.1 Contaminants and hazards

Migration of radionuclide from the waste matrix and redistribution into the surrounding biosphere are the major hazards in waste immobilization. This can happen by three basic processes namely volcanic activity, atmospheric factors and anthropogenic due to the action of living species which cause the rock failure and extraction of the radioactive element into water sources [33]. Hence, if the environment becomes wet and the waste package degrades in future, the radioactive element transport will be rapid which can contaminate the soil, water and air. Figure 2.1 shows the ingestion potential hazard of the high-level radioactive waste (HLW) from the reprocessing of spent fuel for a burn-up of 1 GWd/t in a nuclear power plant as a function of time [6, 35]. The figure indicates that over a

time scale of 100,000 years or so, many of the fission products would have decayed significantly [35, 36].

The relative toxicity of radioactive waste diminishes with time. The spent fuel of a typical pressurized water reactor (PWR) contains about 9 g of actinides (mostly ^{239}Pu) and 35 g of fission products per kilogram of the fuel. The relative toxicity index (RTI) for PWR spent fuel decreases with time and after about 480,000 years, it is the same as that of the natural uranium ore. However, if the nuclear fuel is reprocessed and plutonium is recycled, the toxicity of the waste becomes less than that of natural uranium after 2000 years [6, 36].

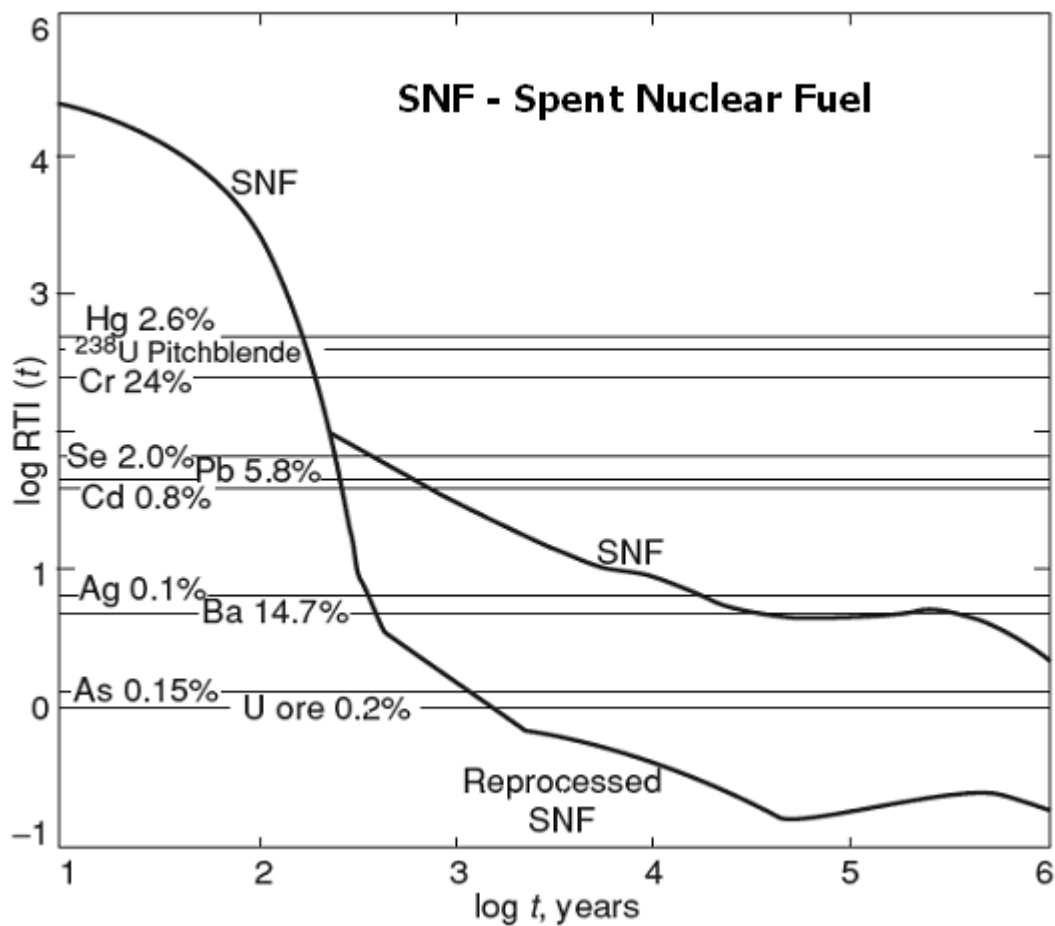


Fig. 2.1. Relative toxicity of some materials as a function of time [3]

2.2 Immobilization of radioactive waste

For long term storage and disposal of radioactive waste, an essential technique to be adopted is waste immobilization. It significantly reduces the potential release of radionuclides into the environment [6]. A variety of matrix materials and techniques are available for immobilization. The proper choice of the immobilization technology depends on the physical and chemical nature of the waste and the acceptance criteria for the long-term storage and disposal facility in which the waste will be disposed. The major immobilization technologies available and have been demonstrated are cementation, bituminization, vitrification in glass matrix and consolidation to metal matrix [6, 35 - 38].

2.2.1 Immobilization in cement matrix

Encapsulation of radioactive waste in ordinary Portland cement was developed during the beginning of the nuclear industry due to its low cost, availability and compatibility with aqueous waste [39]. However, it was realized that some of the wastes interact with the cement and retard the hydration reactions [40]. To overcome the deleterious cement–waste interaction effects, some additives were used and such mixtures are termed as modified cements. The cement modifiers include slaked lime, sodium silicate, natural pozzolans and blast furnace slag. In the presence of water, the extremely high alkalinity of the slaked lime induces a rapid set [41]. Cements are particularly suitable for immobilisation of low and intermediate level radioactive wastes. The low and intermediate level liquid waste (LILW) immobilized via in-lined cementation at the British Nuclear Fuels Limited (BNFL) waste encapsulation plant at Sellafield, UK is shown in Figure 2.2. Most of the transuranic elements were retained well by common cement phases due to the high pH (basic) conditions and the chemical reactions that occur in the matrix [38, 42].



Fig. 2.2. Cement encapsulated solid, liquid and slurry LILW in 500 L drums [42]

2.2.2 Immobilization in bituminous matrix

Immobilization of radioactive waste in bituminous matrix became popular since 1960s. In this process, radioactive wastes are embedded in molten bitumen and the waste matrix is physically encapsulated after cooling. The waste used to be normally in the form of slurry, like aqueous salt concentrates or wet ion exchange resins. Three types of hydrocarbons present in bituminous materials are asphaltenes, resins and oils (aliphatic hydrocarbons) [6]. Immobilisation of radioactive wastes via bituminisation can be carried out as a batch or continuous process. In this process, the waste is continuously introduced into a metered volume of molten bitumen at about 200°C. The mixing vessel is externally heated. Water evaporates and the solid residue particles are mixed with the bitumen [43]. The mixture is stirred while heating to evaporate the residual water and is then discharged into drums or other containers for cooling and solidification [43, 44]. Core samples from the natural Oklo reactor in Gabon contain inclusions incorporating bitumen, which probably acted as a reducing buffer and hydrophobic water shield suppressing the oxidative dissolution of the uraninite cores [44].

The first bituminisation plant in Russia was put into operation at Moscow SIA “Radon” in 1977. It uses an industrial steam heated rotary evaporator as the mixing unit

operating at 135°C while the waste loading is up to 60 wt.%. The bitumen compound is poured into carbon steel containers. The advantage of bituminisation over the cement matrix is that the bitumen matrix can take higher waste loading. However, there will be risk of fire hazards [6].

2.2.3 Immobilization in glass matrix

The advanced technology of waste-immobilization via vitrification in glass matrix was discovered in the 20th century. Immobilization of HLW by vitrification was investigated extensively over the last 40 years in Denmark, Canada, China, Germany, Belgium, Italy, India, Japan, Korea, Russia, the UK and the USA. Vitrification produces smaller waste-form volume (Fig. 2.3), large number of waste elements can be incorporated in the open glass structure and is potentially durable [45]. The high chemical resistance of glass allows it to remain stable in corrosive environments for thousands and even millions of years. The most common glasses used for vitrification of nuclear waste are borosilicate and phosphate which can be processed at lower temperatures (~1000°C) and they form a durable product [46, 47].

2.2.3a Borosilicate glasses

For immobilizing HLW and LILW borosilicate glasses are the best choice of material worldwide. Borosilicate glasses generally have SiO₂ as the major component, relatively high B₂O₃, CaO, MgO, Na₂O and Al₂O₃ content and minor amounts of many other oxides. SiO₂, B₂O₃ and Al₂O₃ are generally network formers because they form strong covalent bonds involving SiO₄, AlO₄ and BO₄ tetrahedra and BO₃ triangles [48]. In waste vitrification, melting should be done in the range ~1100 to 1250 °C to avoid the high temperature volatilization of both radioactive and non-radioactive constituents [45]. Boron concentration below 15 wt.% reduces the thermal expansion coefficient, improves the chemical durability and resistance to mechanical abrasion [48]. Boron in a 3 coordinated position in the

borosilicate glass is a relatively unstable component. Acids easily leach this boron along with sodium bonded to it [49, 50].

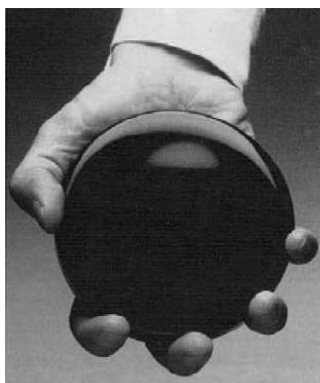


Fig. 2.3. Volume of simulated borosilicate glass which is sufficient to hold all the HLW arising from a nuclear reactor generating electricity for a single person of 80 year lifetime [6]

2.2.3b Phosphate glasses

Novel phosphate glasses are attractive particularly due to their ability to accommodate enhanced amounts of refractory oxides and their high chemical durability [51]. Phosphate glasses have been intensively studied in Russia, at the Eurochemic Corporation at Mol, Belgium, at Oak Ridge National Laboratory and at the University of Missouri-Rolla in the USA [6, 47]. Russia is immobilizing HLW from the nuclear fuel reprocessing plant RT-1 in the Ural region in alumina–phosphate glass since 1987. In contrast to borosilicate glasses, phosphate glasses accommodate significantly larger amounts of corrosion products as well as actinide oxides, molybdates and sulphates. Lanthanides and actinides in the phosphate glasses tend to complex strongly with phosphate ions [6, 48, 49].

2.2.3c Glass composites

Glass composite materials (GCMs) are used to immobilize glass immiscible waste components such as sulphates, chlorides, molybdates and refractory materials requiring unacceptably high melting temperatures [49]. GCMs comprise both vitreous and crystalline components [52] and are produced by dispersing both melted materials and fine crystalline

particles in a glass melt. GCMs can be used to immobilize long-lived radionuclides by incorporating them into durable crystalline phases and the short-lived radionuclides can be accommodated in the less durable vitreous phase [49, 53, 54]. Synroc glass is an example of GCM with Synroc crystalline phases in a vitreous matrix (Fig. 2.4a). Crystalline phases such as zirconolite and perovskite are the hosts for actinides and can accommodate waste loadings up to 50 – 70% by weight with a high durability. France has developed a U–Mo GCM to immobilize Mo-rich HLW. Another example for GCM is the one developed to immobilize sulphur-enriched waste streams in Russia (Fig. 2.4b). This GCM contains conventional borosilicate glass vitreous phase with uniformly distributed particles comprising up to 15% by volume of yellow phase. Its durability is similar to that of conventional waste-form glasses. GCMs are also potential host materials for highly volatile radionuclides such as ^{129}I (Fig. 2.4c). Such GCMs can be produced by sintering an intimate mixture of glass powders and iodine-containing sorbents, probably under applied pressure [6, 55, 56].

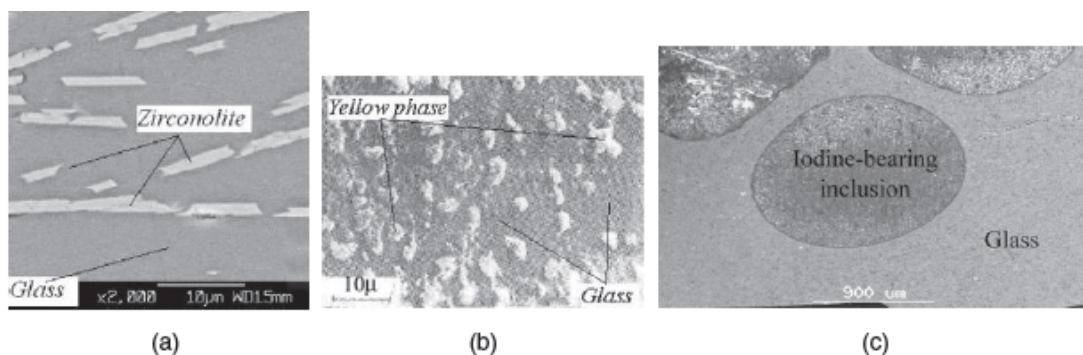


Fig. 2.4. Microstructure of waste encapsulated GCMs: (a) Synroc-glass with zirconolite crystalline phase; (b) immobilized yellow phase; (c) GCM for immobilizing iodine [55]

2.2.3d *Vitrification technology*

Several stages involved in this technology are evaporation of excess water from the liquid radioactive waste, followed by batch preparation, calcination and glass melting and

ending with vitrified waste blocks. One-stage and two-stage vitrification processes were reported by Mazurin et al. [54].

In the one-stage vitrification process, glass forming additives are mixed with concentrated liquid wastes to form a glass forming batch (often in the form of a paste). This batch is fed into the melter (joule heated ceramic melter, JHCM) wherein further water evaporation occurs, followed by calcination and glass melting [53, 54, 57].

In the two-stage vitrification process, the waste concentrate is fed into the calciner. After calcination the required glass-forming additives (usually as a glass frit) together with the calcined waste are fed into the melter [54, 57]. Two streams which come out of the melter are the glass melt containing most of the radioactivity and the off-gas flue, which contains the off-gases and aerosols. The melt waste glass is poured into containers and slowly cooled in an annealing furnace to avoid accumulation of mechanical stresses in the glass. The second stream from the melter goes to the gas purification system, which is usually a complex system that removes not only the radionuclides but also chemical contaminants from the off-gas. Operation of this purification system leads to the generation of a small amount of secondary waste [6, 54].

2.2.4 Crystalline ceramic waste forms

Crystalline materials are generally thermodynamically stable and are capable of accommodating high radionuclide contents which are retained within their structures for more than millions of years. The mechanism by which radionuclides are accommodated varies with species and crystal type, but include direct substitution of isovalent species on particular lattice sites. The following crystal systems have been considered for the purpose of waste fixing [45, 58 - 61]:

Monazite, a phosphate mineral $[(\text{Ce}, \text{La}, \text{Nd}, \text{Th})\text{PO}_4]$ and the major commercial source of Ce, occurring as small heavy crystals in granitic and gneissic rocks and their

detritus (called monazite sands) contains up to 27 wt.% of U and Th oxides. In Brazil, old monazite rock was found to retain radionuclides over two billion years and remains stable. Synthetic lanthanide phosphates exist in several crystalline forms including hexagonal, monoclinic and tetragonal varieties [45, 59].

Zircon, a silicate mineral (ZrSiO_4) is the principal source of Zr. Zircon is widespread as an accessory mineral in acid igneous rocks; it also occurs in metamorphic rocks and in beach sands which is a common heavy mineral in sedimentary rocks. Zircon contains U and Th oxides in concentrations up to 20 wt.%. Plutonium can be substitute directly for Zr in this compound and the pure end-compound PuSiO_4 has been successfully synthesised by cold pressing and sintering or hot pressing [45, 58, 59]. The back scattered electron images of Pu doped zircon are shown in Figure 2.5.

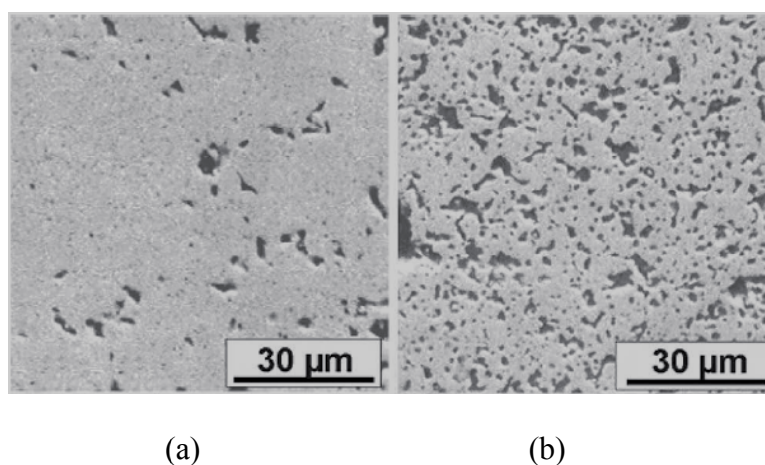


Fig. 2.5. Backscattered electron images of ceramics based on (a) zircon, $(\text{Zr}, \text{Pu})\text{SiO}_4$, doped with 6.1 wt.% Pu; (b) cubic zirconia, $(\text{Zr}, \text{Gd}, \text{Pu})\text{O}_2$, doped with 10.3 wt.% Pu [60].

Zirconolite has the generic formulation $\text{CaZr}_x\text{Ti}_{(3-x)}\text{O}_7$. Natural zirconolite contains up to 20 wt.% of ThO_2 and up to 14% UO_2 . Zirconolite can accommodate lanthanides, Hf and trivalent and tetravalent actinides by insertion into the Ca and Zr sites. Two synthetic processes were developed for zirconolite. The first one is the ceramication process in which

powders are synthesised by the alkoxide process and subsequent air sintering at 1400°C. The second is an oxide melting process using high temperatures (1700 – 1800°C) in a crucible.

The formula $\text{Me}_{10}(\text{XO}_4)_6\text{Y}_2$ [where Me is a divalent cation (Ca^{+2} , Pb^{+2} , Ba^{+2}); XO_4 is a trivalent anion (PO_4 , VO_4 , SiO_4) and Y is a monovalent anion (F^- , Cl^- , OH^- , Br^-)] is assigned to apatites. It crystallises in the hexagonal form. Cesium and iodine have strong affinity for apatite systems. Britholite monosilicate, $\text{Ca}_9\text{Nd}(\text{PO}_4)_5(\text{SiO}_4)\text{F}_2$ is synthesised by solid–solid reaction and sintering in air at 1400°C. Nd can be substituted with the minor actinides since Nd^{+3} simulates the minor actinides Am^{+3} and Cm^{+3} .

Sodium zirconium phosphate (NZP) with the composition $\text{NaZr}_2(\text{PO}_4)_3$ contains three types of crystallographic sites and exhibits great compositional flexibility. Waste loadings up to 20 wt.% have been incorporated into this structure using sol–gel and sintering techniques while maintaining a single phase material. Substitution of Ti with Zr yields sodium titanium phosphate (NTP), which can accommodate up to 60 wt.% waste loadings. Pyrochlores are abundant in nature and over 500 synthetic compositions have been made, including zirconates, titanates and niobates. Pyrochlore structures found in Synroc have been examined as hosts for military Pu [45, 58 - 60].

2.2.4a Polyphosphate crystalline waste forms (Synroc)

Synroc, the short form of “Synthetic Rock” was invented in 1978 by T. Ringwood from the Australian National University. Synroc is the most famous polyphase ceramic for nuclear waste immobilisation. It is made of geochemically stable natural titanate minerals which have immobilised U and Th for billions of years. U/Th containing natural analogues of the basic constituent of Synroc – zirconolites from Sri Lanka dating back 550 million years while amorphised, have nevertheless withstood the alteration processes of their natural environment [45, 61, 62].

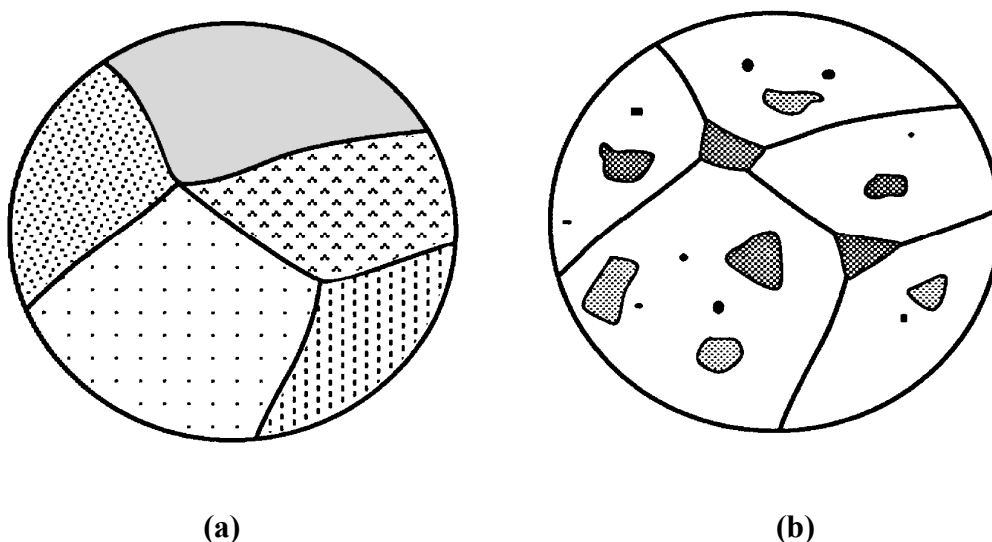


Fig. 2.6. Ceramic waste form with (a) waste phases in solution and (b) ceramic with encapsulated waste phases [45]

Synroc is prepared by a chemical processing route involving the hydrolysis of Ti and Zr alkoxides in the presence of NaOH to form a sodium titanate/zirconate powder. This powder is dried and calcined under reducing conditions and hot pressed at 1100 – 1170°C. Synroc can also be produced via an oxide-melting route in cold crucible melters. Figure 2.6 illustrates the multi-phase microstructure of Synroc manufactured by melting. Synroc can take various forms depending on its specific use and can be tailored to immobilize selective components in the HLW [45]. The original form, Synroc-C was intended mainly for the immobilization of liquid HLW arising from the reprocessing of light water reactor fuel. The major minerals in Synroc-C are hollandite ($\text{BaAl}_2\text{Ti}_6\text{O}_{16}$), zirconolite ($\text{CaZrTi}_2\text{O}_7$) and perovskite (CaTiO_3). Zirconolite and perovskite are the major hosts for long-lived actinides like plutonium [61]. Hollandite principally immobilises caesium (Cs) along with potassium (K), rubidium (Rb) and barium. Synroc-C can hold up to 30 wt.% HLW. Synroc-D contains nepheline ($(\text{Na,K})\text{AlSiO}_4$) instead of hollandite as host for Cs, Rb and Ba [46, 61]. Zirconolite-rich Synroc was developed for the immobilisation of excess plutonium. Pyrochlore-rich Synroc was found to be more efficient for immobilising uranium contained in the waste [47].

Pyrochlore is similar to zirconolite and can incorporate up to 50% by mass of PuO_2 and/or UO_2 [45, 62]. A pilot plant to manufacture Synroc with non-radioactive simulants operates at Lucas Heights in Australia [6]. In 1997, Synroc was tested with active HLW using the technology developed jointly by ANSTO (Australian Nuclear Science and Technology Organisation), Australia and the Argonne National Laboratory, USA [45].

2.2.5 Metal matrix immobilization

Metal matrix immobilization was invented in the 1970s at Mol, Belgium as part of the Pamela HLW vitrification programme. Vitromet is a composite material made of beads of nuclear waste glass dispersed in a metallic (lead) host matrix. It has superior retention properties for radionuclides and is an excellent heat transfer medium for the decaying radionuclides by the metallic host. The slow corrosion rate of lead (less than 1 mm per year) ensures a very low radionuclide leaching rate as well as the absence of environmental contamination [63]. The IAEA recommends metal matrix immobilization for spent sealed radioactive sources (SRS), as other immobilizing materials including glasses are not able to withstand the enhanced radiation doses and heat generation from such highly radioactive sources. In addition, metal matrix immobilization is an excellent method of isolating long-lived SRS for safe storage and disposal [64]. Metal matrix immobilization technology was deployed in the mid-1980s to ensure the safe SRS disposal in borehole-type repositories in Russia and to immobilize the damaged SNF rods from Russian channel-type nuclear reactors (RBMK). Lead is a suitable immobilizing matrix due to its high radiation stability, ability to withstand deformation without loss of integrity, high corrosion resistance, high heat conductivity, effective filling of free space between sources and compatibility with other construction materials. In addition, lead does not contaminate ground water due to its high passivity and slow corrosion. Matrix metal melts are prepared outside of the repository in a special technological unit to minimize the duration of thermal impact on spent SRS. The

prepared melt is fed into the repository by a flexible heat-resistant hose lowered through the SRS loading channel of the borehole. The existing biological protection of the repository functions as an ionizing radiation shield, ensuring an enhanced degree of operational safety. The metal matrix immobilization technology used to immobilize spent SRS in Russia since 1986 is currently being employed in other countries [6, 63, 64].

2.3 Development of Metal Waste Form (MWF) alloy

The stainless steel – zirconium (SS-Zr) based MWF generated at the end of pyrochemical reprocessing need special consideration for its immobilization. The metallic waste from pyrochemical reprocessing consists of SS cladding, NMFP, Zr from alloy fuel and contaminated actinide. However the MNFPs are strong crystal formers in vitrified waste forms, and crystal formation decreases the mechanical integrity of glass [19, 65-69]. Since NMFPs are the primary radioactive constituent of the metal waste form, this problem cannot be avoided. Moreover, vitrification of the metallic waste stream would result in very significant mass and volume increases since the high density metals would be converted into low density oxides and combined with additional glass forming material [69, 70]. Minimizing the waste form volume is important by considering disposal burden. Along with these fundamental issues, some additional practical consideration makes a metal waste form desirable. For example, the electrometallurgical process is very compact and may be contained in a single inert environment cell, which includes a waste form melting furnace. Opting for vitrification would require a large vitrification facility adjacent to the inert cell or transportation of the waste to a separate vitrification facility at an independent location. The electrometallurgical process eliminates the need for these two options.

At Argonne National Laboratory (ANL), stainless steel-zirconium (SS-Zr) metallic waste form alloys were developed for immobilizing radioactive metallic components left at the end of the electrometallurgical treatment for the reprocessing of spent nuclear fuel.

Handling those waste streams is complicated because the metals are covered with clinging salt from the electrorefiner and they must be removed by distillation. The metal waste form alloying process is a very simple and one-step process, though the salt distillation and alloying of the waste components may be accomplished in a high-temperature furnace with a salt recovery mechanism. After salt recovery the MWF alloy can be immobilized by making it consolidated volume by melting at around 1600 °C and can be easily dispose.

2.3.1 Role of Zr in SS-Zr MWF alloys

McDeavitt et al. [21, 71] selected two SS-Zr compositions as baseline waste form alloys: (a) stainless steel with 15 wt.% zirconium (SS-15Zr) for stainless steel-clad fuel and (b) Zircaloy with 8 wt.% stainless steel (Zr-8SS) for Zircaloy-clad fuel [71]. Metal matrix encapsulation was investigated for electrorefiner metal wastes in parallel to the early development of the SS-Zr alloys [22], but alloying was preferred over encapsulation because of the superior behaviour of the waste form. Additionally, Zr metal improves the performance of the final metal waste form in retaining the radioactive isotopes and it produces a low melting alloy [72]. The target composition is stainless steel and 15 wt.% Zr, with acceptable Zr concentration ranging from 5 to 20 wt.% [73]. The charge from the anode dissolution basket is transferred to a yttrium oxide crucible, melted at approximately 1600 °C in the casting furnace in argon atmosphere and is cooled in the crucible and cast into ingots [74]. The physical demands on a waste form are relatively insignificant as compared to the requirements of corrosion resistance and corrosion product retention during immobilization. Waste forms are neither load bearing nor structural materials; they must simply reside in a waste canister for a very long time [21].

The stability of the SS-Zr alloys can be predicted approximately with the aid of Fe-Zr phase diagram reported by Arias et al. [75] and is shown in Figure 2.7.

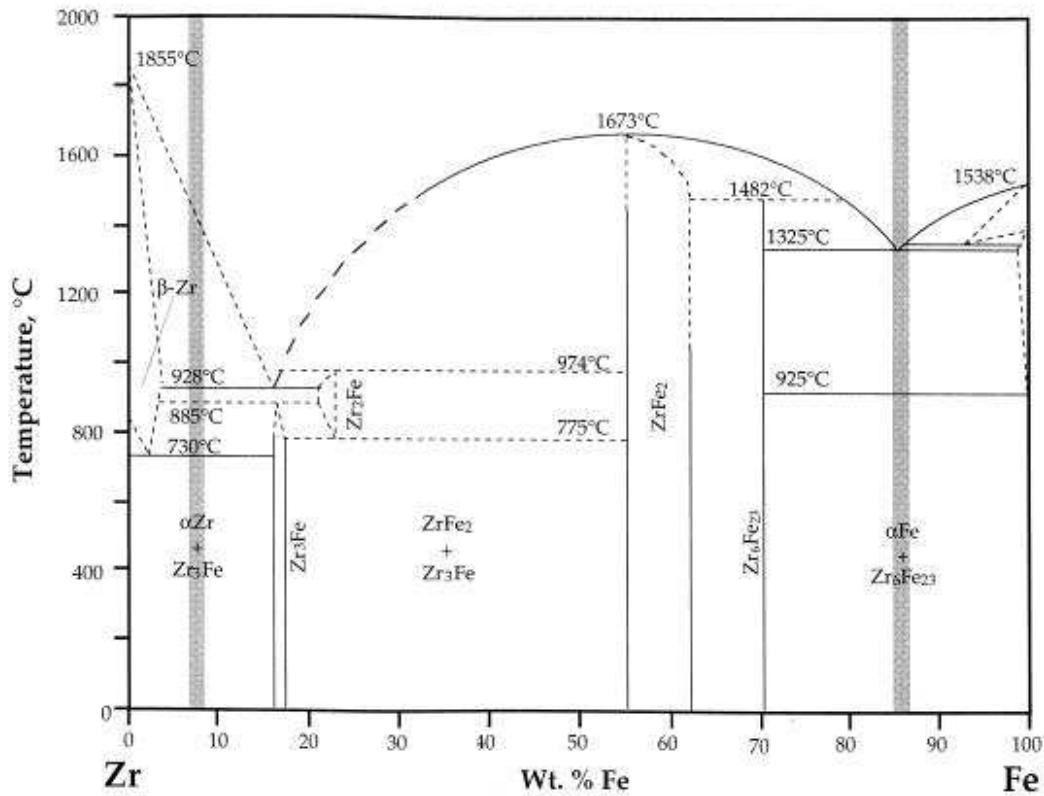


Fig. 2.7. Binary phase diagram of Fe-Zr system [75].

From the phase diagram it is observed that Fe with 15 wt.% Zr shows eutectic behaviour at 1325 °C between Fe and Fe₂Zr. Further addition of Zr increases the melting temperature to 1675 °C [76]. The melting point of pure Zr is 1855 °C. Fe and Zr can form the following four (probably five) distinct intermetallic phases: Fe₃Zr, fcc, isotypic with Mn₂₃Th₆; Fe₂Zr, fcc, MgCu₂ type laves phase; FeZr₂, bcc, tetragonal Al₂Cu type; FeZr₃ and FeZr₄ phases for which the structure is not determined. It is reported that the Zr intermetallic phases are stabilized by impurities [77]. The stable intermetallic phases of the binary system are the cubic and the hexagonal polymorphs of the Fe₂Zr Laves phase and the Zr-rich phases FeZr₂ and FeZr₃. Fe-Zr alloys have wide ranging applications as structural as well as functional materials. In the nuclear industry, the intermetallic phases formed in the Fe-Zr system play an important role. Stainless steel-zirconium alloys have been developed as high-

level nuclear metal waste forms [18, 21, 78 - 80]. The ZrFe_2 -type intermetallics in the stainless steel–zirconium system incorporate and immobilize the highly radioactive and long-lived actinides in the metal waste [78]. The prominent Laves intermetallics in SS–15Zr waste form are responsible for incorporating the highly radioactive and long-lived constituents [71].

The phases of Zr-8SS MWF alloys analogous to those in the Fe–Zr phase diagram (Fig. 2.7) are α -Zr (HCP), Zr(Fe,Cr)_2 and $\text{Zr}_2(\text{Fe,Ni})$. The primary α -Zr phases were surrounded by a complex multi-phase matrix containing secondary α -Zr and $\text{Zr}_2(\text{Fe,Ni})$ along with minor amounts of the Zr(Fe,Cr)_2 Laves phase. This was attributed partly due to the difference in the affinity of Zr for stainless steel and for pure iron [21]. Zirconium-rich SS-Zr alloys exhibit deviations from the Fe-Zr phase system. The phase diagram predicts the presence of primary α -Zr phases in a Zr-8Fe alloy. It also predicts that the matrix intermetallic should be the Zr_3Fe compound instead of the observed multiphase mixture in Zr-8SS; Zr_3Fe is only a very minor constituent (less than 5 vol.%) in the multiphase mixture. Zr_2Fe is a stable, high-temperature phase (above 775°C), but $\text{Zr}_2(\text{Fe,Ni})$ is dominant in the multiphase matrix. Zr_2Ni is a stable compound in the Zr-Ni system. The Laves intermetallic, Zr(Fe,Cr)_2 would not be present in a Zr-8Fe alloy, but it is part of the multi-phase matrix in the Zr-8SS alloy [21].

2.3.2 Microstructure of the 304/316 SS-Zr MWF alloys

Zirconium has very low solid solubility in iron. Addition of zirconium to iron may result in the formation of ZrFe_3 and/or ZrFe_2 intermetallic compounds [81] as shown in Figure 2.7. In the case of stainless steel–zirconium alloys, an equilibrium based explanation is required, considering the effect of nickel on austenite stability. The presence of austenite stabilizing alloying elements gives rise to a peritectic reaction ($L + \delta = \gamma$) during the solidification process, whereas the addition of ferrite stabilizers produces a eutectic reaction [82]. The detailed microstructural characteristics of alloys containing 304 SS with 5 to 92

wt.% Zr was investigated by Abraham et al. [18,70, 71] using scanning electron microscopy (SEM), energy dispersive X-ray spectrum (EDS) and X-ray diffraction (XRD) techniques. Their findings are discussed in detail in the foregoing Section. The microstructures of SS with 5 to 92 wt.% Zr are depicted in Figures 2.8a to 2.8i. The 304 SS exists in austenite phase. The addition of Zr resulted in the formation of an intermetallic phase as well as an increase of ferrite to austenitic ratio.

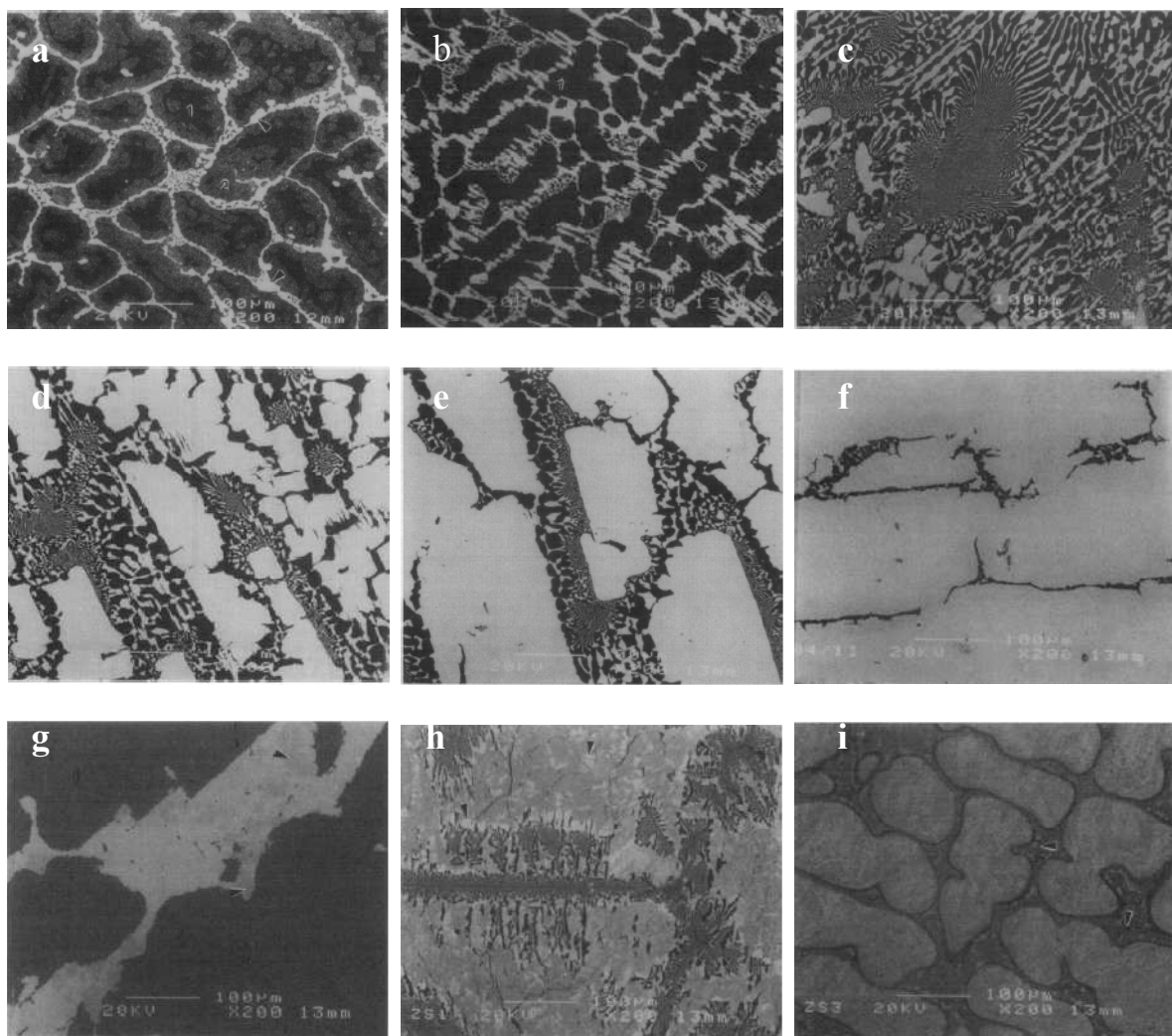


Fig. 2.8. Typical microstructure of type 304SS- Zr alloy: (a) 304SS-5 Zr, (b) 304SS-10 Zr, (c) 304SS-15 Zr, (d) 304SS-20 Zr, (e) 304SS-30 Zr, (f) 304SS-40 Zr, (g) 304SS-60 Zr, (h) 304SS-83 Zr and (i) 304SS-92 Zr [18]

Three distinct phases observed in the 304 SS - 5 wt.% Zr (Fig. 2.8 a) were white intermetallic phase, dark ferrite and gray austenite. The eutectic, which appeared as a form of network is mainly a mixture of austenite and intermetallic. The intensity of brighter intermetallic phases increase with the increase in Zr concentration. In the MWF alloy with 10 wt.% Zr (Fig. 2.8 b) the intermetallic and ferrite phase were dominant and inside the eutectic network the austenite could be observed as a minor phase. In 15 wt.% Zr alloy (Fig. 2.8 c) the intensity of ferrite and intermetallic was more or less equal. The predominant intermetallics were surrounded by the eutectic network in the alloys with 20 and 30 wt.% Zr (Figs. 2.8 d & e). Presence of eutectics in the alloy with 40 wt.% Zr (Fig. 2.8 f) was insignificant when compared to the large intermetallic. From XRD results the intermetallic composition was identified to be $\text{Zr}(\text{Fe,Cr,Ni})_{2+x}$ and was designated as Laves phase [83]. The MWF alloys with higher Zr (45 to 70 wt.%) formed $\text{Zr}(\text{Fe,Cr,Ni})_{2+x}$ in the matrix phase and $\text{Zr}_2(\text{Fe,Ni})$ as the white phase as shown in Figure 2.8 g. The intensity of white phase was found to increase with increase in Zr. With 83 wt.% Zr, 304SS (Fig. 2.8 h) exhibited two regions; eutectics of $\text{Zr}(\text{Fe,Cr,Ni})_{2+x}$ intermetallics with α -Zr and non eutectic regions of $\text{Zr}_2(\text{Fe,Ni})$ mixed with α -Zr. SS with 92 wt.% Zr formed an island of α -Zr with a dark border of $\text{Zr}(\text{Fe,Cr,Ni})_{2+x}$ and $\text{Zr}_2(\text{Fe,Ni})$ intermetallic.

2.3.3 Laves Intermetallics in SS-Zr alloy

The microstructural analysis of MWF alloys revealed the formation of ZrFe_2 type Laves intermetallic, $\text{Zr}(\text{Fe,Cr,Ni})_{2+x}$. In SS-15Zr alloys, $\text{Zr}(\text{Fe,Cr,Ni})_{2+x}$ constitutes about 50% of the microstructure and has a significant effect on waste form properties [84]. Hence, a detailed understanding of laves intermetallic phases is essential. Laves phases are the compounds with the general formula AB_2 and have one of the following crystal structures: C14 (hexagonal, MgZn_2 type), C15 (cubic, MgCu_2 type) and C36 (dihexagonal, MgNi_2 type) [85]. Laves phases occur for the atomic diameter ratios between ~ 1.05 and 1.68. The

occurrence of individual Laves polytypes has also been correlated to electron concentrations (valence electrons per atom) in the compound [82, 86]. Laves intermetallics play an important role in the disposal of metallic waste resulting from the electrometallurgical treatment of spent nuclear fuel.

2.3.3a Distribution of noble metals in SS-Zr alloy

The distribution of noble metals in SS-Zr matrix was studied by McDeavitt et al. [21]. These authors introduced non radioactive metals Ru, Pd, Co, Nb, Ag, Re, Ta and W into SS-15Zr and Zr-8SS systems. No discrete noble metal phase could be identified by them in SS-15Zr alloy. Figure 2.9 portrays a set of X-ray maps highlighting the distribution of major components (Fe, Cr, Zr and Ni) and selected noble metal minor components (Ru, Pd, Ag and Mo) in a SS-15Zr microstructure. For the concentrations examined in this study, the noble metals were observed to dissolve and distribute within the alloy phases; the distribution of these elements among the intermetallic and α -Fe solution phases is as follows: (the concentration ratios (intermetallic : α -Fe solution) expressed in atomic percent are given within parentheses after each element). The elements Si (9:1), Nb (8:1), Pd (10:1), Ag (5:1), Sn (9:1) and Ta (8:1) exhibited a strong preference for the intermetallics, whereas Ru (4:1) exhibited a moderate preference. The elements Mn (1:1), Co (1:1), Mo (1:1), Tc (1:1) and W (1:1) were found in the intermetallic and Fe solution phases without a strong preferential distribution. Hence, elements such as Ru, Pd, Ag, Sn, Nb and Si preferentially distributed in the Laves intermetallic phases rather than distributing in the α -Fe solid solution phase. Nevertheless, the elements like Mn, Mo, Tc and W were distributed throughout the microstructure of the alloys.

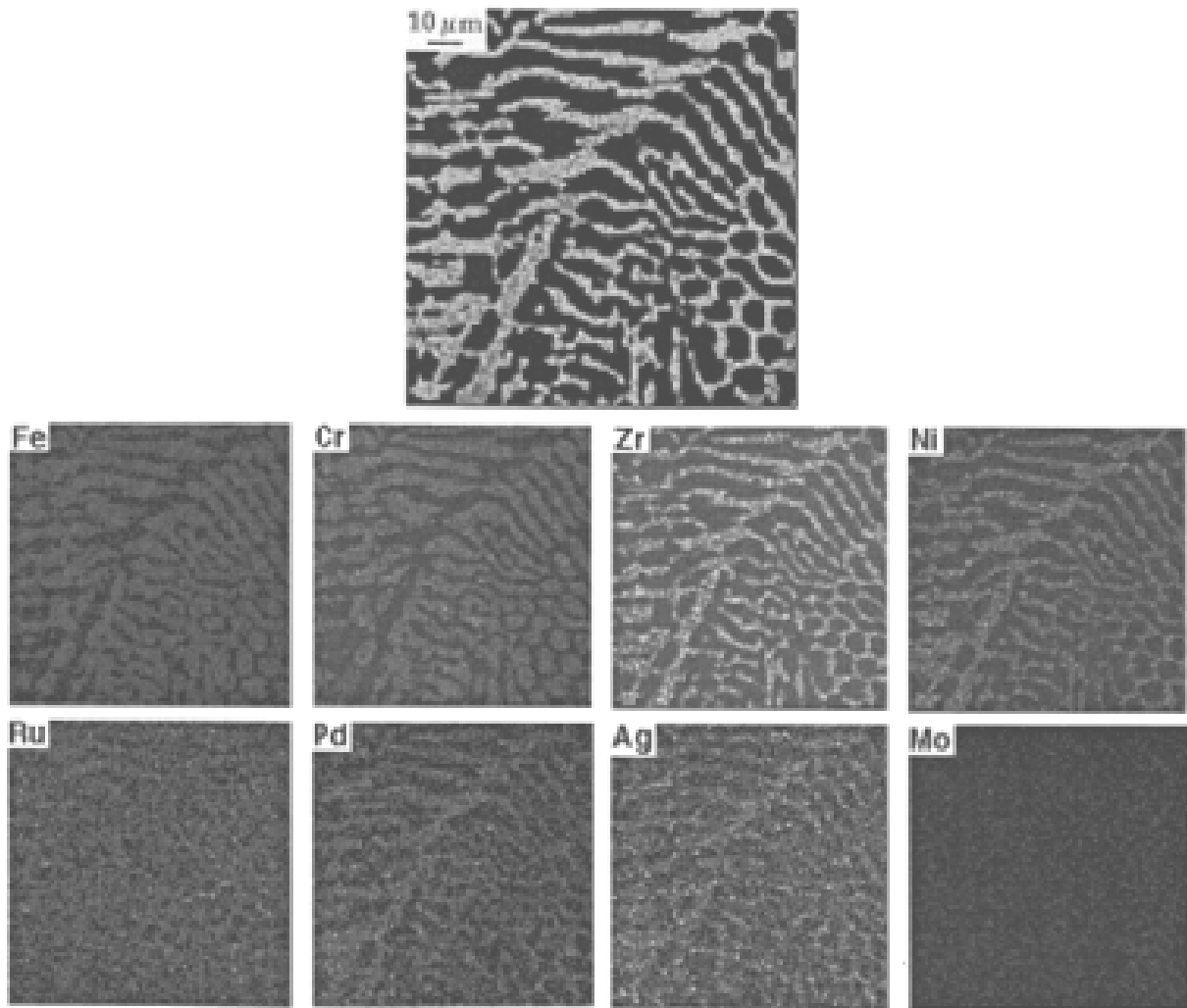


Fig. 2.9. Collection of X-ray maps and backscattered electron image of as-cooled SS-15 wt.% Zr-2 wt.% Ru-1.5 wt.% Pd-0.5 wt.% Ag alloy. The maps highlight the distribution of major (Fe, Cr, Zr and Ni) and minor (Ru, Pd, Ag and Mo) components [21]

Similar behaviour was observed in the study of noble metal (Ru-Pd-Ag-Nb) addition to Zr-8 wt.% SS alloys. The noble metal elements were found to dissolve in the existing phases, but elevated concentrations were observed at α -Zr lath boundaries (Fig. 2.10); lath boundaries are α -Zr phase boundaries within the Zr phases in Zr-8SS.

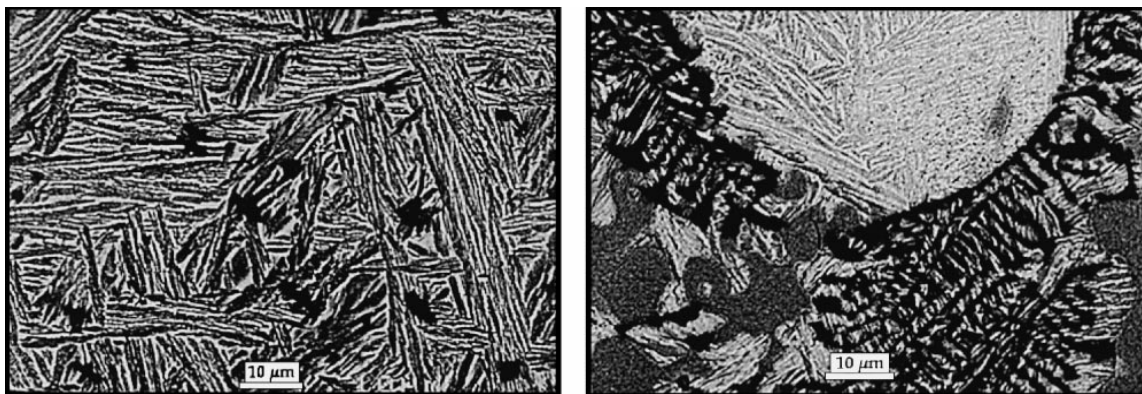


Fig. 2.10. Backscattered electron images of Zr-8 wt.% SS-1 wt.% Nb-1 wt.% Ru-1 wt.% Pd-1 wt.% Ag. Enrichment of the noble metal content occurred at Zr phase boundaries in (a) primary and (b) secondary zirconium phases [21]

2.3.3b Distribution of actinides in SS-Zr alloy

The distribution of actinides and noble metal fission products in SS-Zr MWF alloys was extensively studied by Keiser Jr. et al. [16] and Jenney [87]. Keiser Jr. et al. [16] characterised the MWF alloys of SS-15wt.% Zr with uranium up to 10 wt.% by scanning electron microscopy (SEM), neutron diffraction and transmission electron microscopy (TEM). Neutron diffraction results revealed that addition of uranium to SS-15Zr does not result in the formation of discrete uranium-rich phases. The lattice parameters of the ZrFe_2 -type intermetallics were larger in uranium containing SS-15Zr alloys and are consistent with the substitution of uranium at zirconium sites of the ZrFe_2 lattice. SEM studies (Fig. 2.11) indicated the presence of actinides only in the ZrFe_2 -type intermetallics by the substitution of Zr from the lattice and the formation of white phase. Further, both actinide-rich and actinide-deficient areas were found within the Laves compound. TEM showed the simultaneous presence of multiple Laves polytypes, each with a different preference for uranium atom resulting in uranium concentration gradients which could be observed within the Laves intermetallics [16].

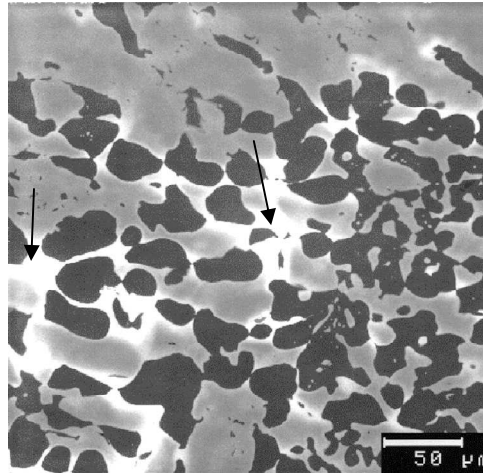


Fig. 2.11. Representative BSE image of a MWF sample produced from irradiated EBR-II cladding hulls. The dark areas corresponded to the ferrite phase. The actinide-rich areas (marked by arrows) appear as high-brightness regions within the ZrFe_2 -type intermetallic [16]

Studies on SS–15Zr alloys containing 2–11 wt.% U, Np or Pu showed the major U- and Pu-bearing materials as Cr–Fe–Ni–Zr intermetallics with structures similar to that of the C15 polymorph of Fe_2Zr , significant variation in chemical compositions and 0 – 20 at.% actinides. An U-bearing material similar to the C36 polymorph of Fe_2Zr had more restricted chemical variability than 0–5 at.% U. Uranium concentrations between 0 and 5 at.% were observed in the materials with $\text{Fe}_{23}\text{Zr}_6$ structure [87].

Actinide distribution in Zr-8SS alloys was investigated by Keiser Jr. and McDeavitt [88]. They observed similar lath morphologies in Zr-8SS alloys containing uranium and plutonium. Elevated U and Pu concentrations were found at α -Zr lath boundaries. This type of structure was formed because the noble metals and actinides have much higher solubility in β -Zr than in α -Zr [89]. During solidification the noble metals segregate at the α -Zr lath boundaries and nucleated within β -Zr grains [90]. The noble metal element Pd also exhibited a strong preference for $\text{Zr}_2(\text{Ni,Fe})$ phase.

2.3.4 Corrosion properties

The corrosion performance of 316SS-Zr MWF alloys with different compositions was studied in detail using different techniques by Abraham et al. [14, 20, 23, 24]. Electrochemical corrosion, immersion corrosion and vapour hydration tests were performed on various alloy compositions to evaluate their corrosion behaviour and resistance to selective leaching of simulated fission products.

2.3.4a Electrochemical corrosion testing

Electrochemical corrosion measurements were conducted at various solution pH values to obtain relative values of corrosion rate for the various MWF alloy compositions. Immersion tests in deionized water and in simulated J-13 groundwater (representative of the proposed Yucca Mountain geologic repository in Nevada) had been performed to evaluate the release of elements (especially fission products) from the alloys. For comparing the corrosion rates, corrosion testing was carried out on the materials 316SS, SS-Zr MWF alloys, NMFP added MWF alloys and actinide added MWF alloys and the results are tabulated in Tables 2.1 to 2.3 [20].

Table 2.1. Corrosion rates of MWF alloys measured in solutions of pH 2 to 10

MWF composition	Room temperature corrosion rate ($\mu\text{m/y}$) at pH value of			
	2	4	9 (J-13)	10
316 SS	3.43	1.93	0.42	0.34
SS-15Zr	4.24	1.85	0.12	0.17
SS-5Zr-2Nb-1Ru-1Pd	8.51	2.78	0.12	0.25
SS-20Zr-2Nb-1Ru-1 Pd	2.51	1.23	0.19	0.23
SS-15Zr-1Nb-1Ru-1Pd-1Rh	3.00	1.57	0.19	0.16
Ni-21Cr-13Mo-4Fe-3W-2Co (C22)	1.04	0.71	0.17	0.27

Table 2.2. Corrosion rates of MWF alloys containing U and Tc

MWF composition	Room temperature corrosion rate ($\mu\text{m/y}$) at the pH			
	2	4	9 (J-13)	10
SS-15Zr-5U-2Tc	5.42	0.43	0.24	0.37
SS- 15Zr-1Nb-1Rh-1Ru-1Pd-2U-1Tc	2.82	0.39	0.32	0.32
SS-15Zr-1Nb-1Rh-1Ru-1Pd-1Tc	0.75	0.41	0.38	0.55
SS-20Zr-1Nb-1Rh-1Ru-1Pd-1Tc	2.09	0.34	0.23	0.40
SS-5Zr-1Nb-1Rh-1Ru-1Pd-1Tc	8.53	0.37	0.37	0.32
SS-15Zr-0.6Ru-0.1Pd-1IU-0.3Tc	9.06	0.66	0.39	0.71

Table 2.3. Corrosion rates of MWF alloys measured in high chloride solution

MWF composition	Room temperature corrosion rate ($\mu\text{m/y}$)		
	1000 ppm Cl^-	10,000 ppm Cl^-	Conc. J-13
316 SS	1.70	2.31	2.18
SS-15Zr	0.91	0.94	0.70
SS-5Zr-2Nb-1Ru-1Pd	0.70	0.75	1.25
SS-20Zr-2Nb-1Ru-1Pd	0.99	2.12	1.80
SS-15Zr-1Nb-1Ru-1Pd-1Rh	0.52	1.53	2.18
Ni-21Cr-13Mo-4Fe-3W-2Co (C-22)	0.56	0.81	0.88

Polarization resistance technique was employed for these alloys at different pH like acidic (pH: 2 and 4) and basic (pH: 10). Testing was also carried out in the simulated J-13 solution which is the probable repository composition for waste immobilization decided by

nuclear regulatory authority of USA. The results of polarization resistance measurements on non radioactive samples given in Table 2.1 showed the corrosion rates of 316SS to be comparable to that of alloy C-22 (which is the candidate canister material for waste disposal). The corrosion rates were also affected by pH; the corrosion rates of MWF alloy in pH 2 were at least one order magnitude higher than the corrosion rates observed in pH 10. The difference in the corrosion performance between U and Tc bearing MWF alloys and non radioactive MWF alloys was not significant (Table 2.2).

Corrosion testing was also carried out in chloride solutions of concentrations 1000 ppm and 10,000 ppm and in simulated concentrated J-13 water solution [20]. The result represented in Table 2.3 which showed that for MWF alloys the corrosion rates were 5 to 10 times greater than the simulated J-13 water as shown in Table 2.2. As per Table 2.3 the corrosion rate of MWF alloys are better than 316 SS and comparable to C-22. The results are provided in the Table 2.3.

Galvanic corrosion measurements were done as a function of time on various MWF specimens coupled with C-22 in J-13 solution. The galvanic potential was found to decrease with time for AISI 1018 since it is electrochemically active than alloy C 22 and finally attained a steady state potential at around -600 mV. For MWF alloys the galvanic potential was increasing with time and finally reached the steady state at the potential around - 60 mV. The initial positive current observed for MWF alloys in the plot of galvanic current versus time shown in Figure 2.12 indicated that waste form specimens were noble with alloy C-22 [14].

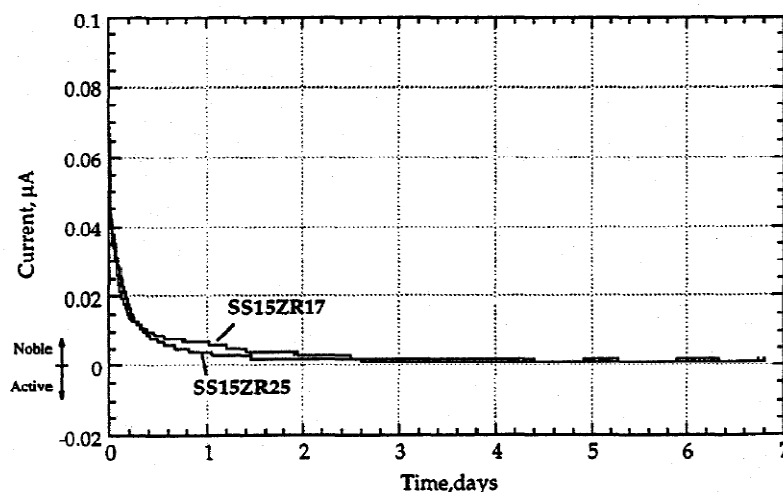


Fig. 2.12. Galvanic current measured for SS-15 Zr (SS15ZR17) and SS-15Zr-1Nb-1Pd-1Rh-1Ru (SS15ZR25) specimens coupled to C-22 in J-13 solution [14].

2.3.4b Immersion corrosion testing

Static immersion tests were conducted at 90°C and 200°C in simulated J-13 water [14, 20] by employing ASTM standard MCC-1 [91]. Immersion tests were conducted on MWF samples of various compositions for durations up to 10,000 h (417 d) at 90°C. Minimal surface corrosion was observed on the test specimens even after 10,000 h; most of the samples retained their as-polished surfaces. The weight changes observed were very small and often within the resolution limit of the balance (± 0.0001 g). Negligible quantities of alloy constituents were present in the test solution, clearly indicating that the alloy samples were highly corrosion resistant. Immersion tests at 200°C were conducted in deionized water solution and sealed in titanium vessels for 28 days. The sample surfaces were examined after completion of the tests. All the specimens exhibited some degree of surface corrosion. The specimens containing 15 and 20 wt.% Zr showed uniform corrosion, whereas the 5 wt.% Zr specimens showed localized attack. The weight changes were small and within ± 0.0001 g. Among the major elements, Ni leaches out the most, followed by Cr, Mn and Fe. The maximum weight loss (1.1 g/m^2) was observed for Ni in the SS-5Zr-2Nb-1Ru-1Pd alloy. The

NMFP elements showed minimum loss; the highest loss was observed for Mo (0.09 g/m^2) in the SS-20Zr-2Nb-1Ru-1Pd alloy.

2.3.4c Steam (vapour hydration) corrosion testing

In a saturated steam environment, tests were conducted to determine the nature and thickness of corrosion layers formed on the metallic alloys. In these tests, monolith specimens were suspended in a sealed stainless steel vessel containing a small pool of de-ionized water beneath the specimen. The water vapourizes and creates a saturated steam environment when the sealed vessel is heated to 200°C . Tests were conducted on pure iron, copper, 316 stainless steel, SS-15Zr, and SS-15Zr-2Ru-1.5Pd-0.5Ag. The oxide scale formed was examined by a combination of techniques including scanning electron microscopy, X-ray diffraction techniques and Raman spectroscopy. Pure iron specimens showed the maximum corrosion and formed a porous, non uniform oxide layer of ~ 10 - $60 \text{ }\mu\text{m}$ thickness within 7 days. The oxide layer thickness did not increase appreciably after this time period, suggesting limited oxygen availability after 7 days. The oxide layers contained hematite (Fe_2O_3), magnetite (Fe_3O_4) and FeO. The oxide layer that formed on the surface of Cu specimens was relatively uniform and increased slowly with time. The average thickness of the oxide layer was $\sim 3 \text{ }\mu\text{m}$ after 7 days and $\sim 12 \text{ }\mu\text{m}$ after 182 days. The copper oxide layers contained both cuprite (Cu_2O) and tenorite (CuO). The oxide layers formed on type 316 stainless steel and SS-15Zr specimens were thin and averaged to $\sim 1 \text{ }\mu\text{m}$ in the 56 day and 182 day tests. The thin corrosion layers made oxide identification difficult. Raman spectroscopy results suggested the presence of Fe_2O_3 , Fe_3O_4 and FeCrNiO_4 in the corrosion products. Sufficient oxygen was available in the sealed vessels to support the oxide growth beyond the $\sim 1 \text{ }\mu\text{m}$ oxide layer observed on the stainless steel and SS-15Zr specimens. However, the protective oxide layers that formed on the stainless steel and SS-15Zr alloys

apparently hindered oxygen diffusion and retarded further oxide growth (known as passivation behaviour).

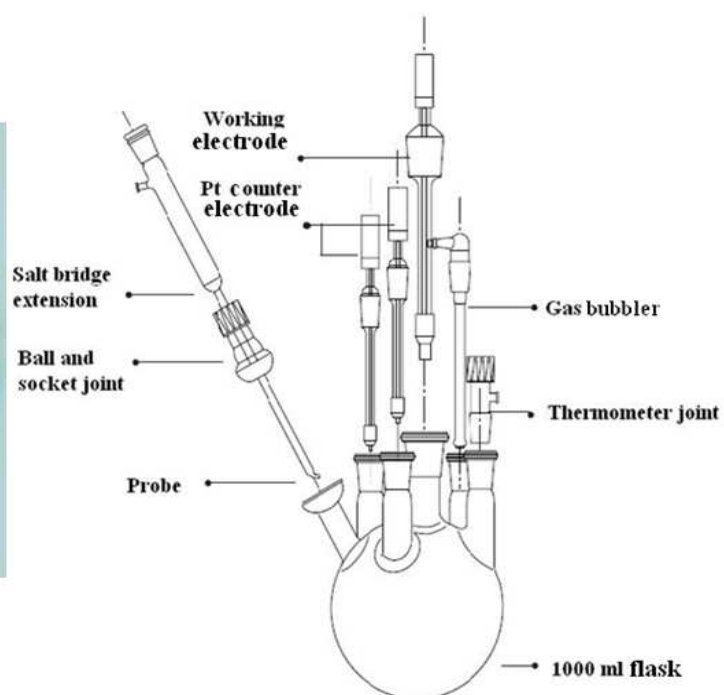
The above studies established that the SS-Zr based MWF alloys exhibit very high resistance from corrosion and selective leaching in all the aggressive media except pH 2. The pH 2 solution represents an extreme condition that may not occur naturally in the repository environment, but is included as an aggressive test for the alloy samples. Despite this, the MWF alloys show superior behaviour than other materials like 316 SS, Cu, Fe etc. Hence, it is concluded that SS-Zr waste forms will be the promising candidate materials for the immobilization and retention of fission products and show the potential for acceptance as high-level nuclear waste forms.

2.4 Need for the present study

The literature review clearly indicates that the MWF alloys are the most appropriate ones for the disposal of high active nuclear wastes in geological repositories. The MWF alloys reported in the literature have been developed based on 316 stainless steel alloys. Since the Prototype Fast Breeder Reactor (PFBR) in India will be using alloy D9 (Ti modified 15Cr-15Ni-2.5Mo stainless steel) as the clad material for mixed oxide fuel, the composition of the MWF to be generated from Indian nuclear power plants will be entirely different from the compositions discussed in this Chapter. Moreover, the geological composition of Indian repository will also vary. Hence, it is strongly desirable to perform further developmental work on the D9SS-Zr based MWF alloys for determining their alloy metallurgy, microstructure, phase evaluation, corrosion and selective leachability in simulated and in actual Indian geological repository solutions.

CHAPTER 3

MATERIALS, MEDIA AND METHODS



Chapter 3

MATERIALS, MEDIA AND METHODS

This chapter describes the selection of materials for the development of metal waste form (MWF) alloy along with their casting and composition. Selection of different simulated repository media and their composition for corrosion testing are presented in this Chapter. The different experimental techniques used for the present investigation are discussed. This chapter is subcategorized based on three different aspects (1) material selection and preparation (2) media selection and preparation and (3) experimental details.

3. 1 Material selection and preparation

Selection of material is one of the foremost important criteria in pursuing a project. In the project “Development and Characterization of MWF alloy” the waste to be considered is the waste that would be generated from the reprocessing of spent nuclear fuels discharging from future prototype fast breeder reactor (PFBR) in India. The fuel strategy of PFBR is that it will use two types of fuels. In the first phase mixed uranium-plutonium oxide (UPuO_2) fuel and in the second phase uranium-plutonium-zirconium metallic fuel will be considered [32]. D9 stainless steel (Ti modified 15Cr-15Ni-2.5 Mo SS) is proposed to be the candidate clad material for mixed oxide fuel and for metallic fuel the clad material will be alloy T91 (modified 9 Cr-1Mo steel) [92]. Metallic waste generated after reprocessing of spent fuel would be made into metal waste form (MWF) alloy. To gain experience in the processing of metal waste and to optimise the process conditions, D9 SS-Zr MWF alloys were developed and characterized for a thorough understanding about the technology to be deployed for future waste management.

In the first phase, MWF alloys of D9 SS with 5 to 17 wt.% Zr were cast in Defence Metallurgical Research Laboratory (DMRL), Hyderabad by using vacuum arc melting

furnace. Casting was done in five batches (around 750 g each) with D9 SS and Zr sponge in a pancake vacuum arc melting furnace (Button Pancake Melting Furnace, Microtorr Vacuum Systems Pvt. Ltd, India). The furnace was evacuated and refilled with high purity Ar at a pressure of 400 mm Hg. The alloys were melted for three time for better homogeneity at applied potential 20 to 28 V potential and 600 to 900 A current. The melt was furnace-cooled to get the pan cake shaped cast as shown in Figure 3.1. The chemical compositions of the different MWF alloys were analyzed by Inductively Coupled Plasma Atomic Emission Spectroscopy (ICP-AES) and the results of the analysis along with that of D9 SS are given in Table 3.1. The MWF alloys were designated as K1 (D9 SS-4.4 wt.% Zr), K2 (D9 SS-8.5 wt.% Zr), K3 (D9 SS-12.2 wt.% Zr), K3B (D9 SS-14.1 wt.% Zr) and K4 (D9 SS-16.8 wt.% Zr) respectively throughout thesis.

Table 3.1. Chemical composition of the D9 SS- Zr MWF alloys (in wt%)

Alloys	D9 SS	K1	K2	K3	K3B	K4
Elements						
Cr	15	12.8	11.8	11.7	11.8	10.8
Ni	15	13.5	12.8	12.8	12.4	12.3
Mo	2.2	1.92	0.71	0.60	1.90	0.31
Si	0.5	0.46	0.5	0.50	0.45	0.52
Ti	0.2	0.12	0.2	0.17	0.12	0.2
Zr	--	4.4	8.5	12.2	14.1	16.8
Fe	67.1	66.8	65.49	62.03	59.23	59.07



Fig. 3.1. Typical pancake shaped D9 SS-Zr MWF alloy ingot

In the second phase, MWF alloys with the addition of ruthenium (Ru), rhodium (Rh) and palladium (Pd) as noble metal fission product (NMFP) were cast to investigate the effect of NMFP on MWF alloy's microstructure and corrosion behaviour. Three alloys (200 g each) were cast with D9 SS-10 wt.% Zr and 1 to 4 wt.% NMFP in the vacuum arc melting furnace in DMRL, Hyderabad as shown in Figure 3.2. The detailed chemical compositions of the alloys are provided in Table 3.2. These alloys are designated as N1 (1 wt.% NMFP), N2 (2.5 wt.% NMFP) and N3 (4 wt.% NMFP).



Fig. 3.2. Typical cast of D9 SS- Zr-NMFP MWF ingot

Table 3. 2. Chemical composition of D9SS-Zr-NMFP MWF alloys (in wt%)

Alloys	D9SS	Zr	Ru	Rh	Pd
N1	89.00	10.00	0.50	0.16	0.34
N2	87.50	10.00	1.25	0.40	0.93
N3	86.00	10.00	2.00	0.64	1.48

In the third phase, the MWF alloy of D9 SS-10 wt.% Zr- 1 wt.% NMFP-10 wt.% U was cast to understand the role of U on the microstructure and corrosion behaviour of MWF alloys. The casting was done in a vacuum induction furnace at 1450°C and the photograph of the ingot is shown in Figure 3. 3 and will be designated as U in the entire thesis.



Fig. 3.3. Typical cast of D9 SS- Zr-NMFP-U MWF ingot

3.2 Media selection and preparation

3.2.1 Simulated geological repository media

The objective of this thesis is to develop MWF alloys for safe disposal in geological repository as mentioned in Section I.3. Hence the performance of the MWF alloys should be evaluated in different geological repository environment. Initially, corrosion and selective

elemental leaching behaviour of different D9 SS-Zr MWF alloys were evaluated in de-mineralized (DM) water because it is aggressive due to lack of mineral in its composition [93]. DM water at pH 1, 5 and 8 were used for electrochemical corrosion investigation to evaluate the influence of pH on the corrosion of MWF alloys. DM water at pH 1 was selected to understand the corrosion behaviour of MWF alloys in highly acidic and most aggressive condition. To understand the corrosion behaviour of the MWF alloys in normal repository environment with little variation of pH towards acidic and basic conditions, DM water with pH 5 and 8 were chosen, respectively. The acidic pH (pH 1 and pH 5) of the media were obtained by the addition of HCl in DM water and basic pH 8 was adjusted by the addition of NH_4OH .

Corrosion and selective elemental leaching behaviour of MWF alloys were evaluated in simulated Kalpakkam ground water (KGW) [94] and Rajasthan ground water (RGW) [95] considering those two locations as probable repository sites in India. Several compositions of KGW and RGW [94, 95] are available in literature. However, a charnokite rocky medium was selected for KGW and two RGW media with a mild (RGW-1) and a hard water (RGW-2) rich in Ca and Mg were selected for the present study. The chemical compositions of the different media along with their measured pH are given in Table 3.3.

Table 3.3. Composition of KGW and RGW media (in ppm) [94, 95]

Medium	pH	Ca^{2+}	Mg^{2+}	Na^+	K^+	Cl^-	SO_4^{2-}	CO_3^{2-}	HCO_3^-
KGW	5.7	196	182	1951	29	2316	830	-	-
RGW-1	9.2	14.03	34.05	200	4.10	204.94	10	30	196
RGW-2	6.7	130.3	126.46	54	2.80	399.87	96.32	-	183

3.2.2 Simulated microbiological media

Biofouling is a major problem in almost all the environments where water is in contact with materials and leading to microbial induced corrosion (MIC). Hence, MIC experiment was carried out in simulated KGW and RGW (RGW-2 was selected as RGW) using two most predominant biofilm former bacteria (organism).

3.2.2a Test organism

Microbial adhesion on MWF alloy was evaluated using a Gram-negative bacterium, *Pseudomonas* sp., and a Gram-positive bacterium, *Bacillus* sp. The reason for the selection of the above genera was that they were identified as major colonizers of the biofilms formed in a fresh water reservoir at Kalpakkam, India [96, 97]. Characterization and identification of the bacteria up to genus level were based on morphological, physiological and biochemical tests as in Bergey's Manual of Systematic Bacteriology [98, 99] and the details are given in Table 3.4.

3.2.2b Microbial culture media

The *Bacillus* sp. and *Pseudomonas* sp. were individually cultured and grown for 24 h in 100 ml nutrient broth solution (sterilized by autoclaving at 120°C for 15 minutes). One ml of the 24 h culture solution was added to 150 ml of simulated KGW and RGW media individually and allowed to grow for 24 h. After 24 h, MWF alloy specimens were suspended for 5 days. Around 1 % glucose was added to the media to maintain the microbes in growing condition.

Table 3.4. Morphological and biochemical tests results of bacterial sp [97].

Properties	<i>Pseudomonas</i> sp.	<i>Bacillus</i> sp.
Gram reaction	Gram-negative	Gram-positive
Morphology	Very small rods	long rods
Pigments	Green fluorescent colony, pigment diffuses into media	off white, rough spreading irregular colonies ,no pigments
Motility	+	+
Catalase	+	+
Oxidase	+	+
<i>Specific reactions</i>		
Anaerobic glucose fermentation	+	+
Nitrate reduction	+	+
Citrate Utilization	+	+
Growth on cetrimide agar	+	-
Indole production	+	-

+ Present, - Absent.

3.3 Experimental details

3.3.1 Specimen preparation

The ingots of MWF alloys ingots were cut into several pieces of dimensions 10 mm × 10 mm × 5 mm. These specimens were mechanically abraded using silicon carbide (SiC) emery paper on all sides up to 600 grit finish and different specimen preparation techniques were employed for the various investigations as mentioned below.

- i. The specimens for hardness, X-ray diffraction (XRD), selective leachability study and monitoring microbial attachment by bacterial density count and epifluorescence microscopic studies were abraded with SiC emery paper up to 1200 grit finish on all sides.
- ii. The specimens for high temperature XRD (HTXRD) study were cut around 2 to 3 mm thickness by SiC wheel and thinned down to 1 mm thickness by mechanical abrading with SiC emery paper. The surface for HTXRD study was abraded up to 1200 grit SiC emery paper.
- iii. The specimens for microstructural analysis by scanning electron microscopy (SEM) and selective microbial attachment by SEM and atomic force microscopy (AFM) study were polished up to 1 μm diamond finish and electrochemically etched with 10 % ammonium persulphate solution (1.8 V, 1.5 minutes).
- iv. The specimens required for the investigation of corrosion behaviour using electrochemical techniques were mounted with epoxy resin connecting a brass rod for electrical connection. The desired surface on the mounted specimens was polished up to 1 μm diamond finish.
- v. For XPS and AFM analysis the specimens were cut around 2 to 3 mm thickness by SiC wheel. Surface finishing was carried out as per the requirement for different experimental conditions. The specimens were polished to 1 μm diamond finish for passive film analysis after polarization and passivation. However for passive film analysis after immersion testing and leachability testing the specimens were used as such.

3.3.2 Hardness and density measurements

Hardness is an important parameter for a solid material for measuring its resistance towards deformation and flow under applied force. There are different types of hardness

measurement techniques including scratch hardness; indentation hardness and rebound hardness are available. For metallic materials indentation hardness is the most viable technique to measure the resistance of the specimen to permanent plastic deformation due to compression load. The common indentation hardness scales are Rockwell, Vickers, Shore and Brinell hardness [100].

The Vickers hardness measurement is simpler than other hardness measurements since the required calculations are independent of the size of the indenter, and the indenter can be used for all materials irrespective of hardness. The Vickers hardness test method consists of indenting the test material with a diamond indenter, in the form of a right pyramid with a square base and an angle of 136° between opposite faces, which is subjected to a load of 1 to 100 kgf. The full load is normally applied for 10 to 15 seconds. The two diagonals of the indentation left in the surface of the material after removal of the load are measured using a microscope and their average calculated as shown in Figure 3.4.

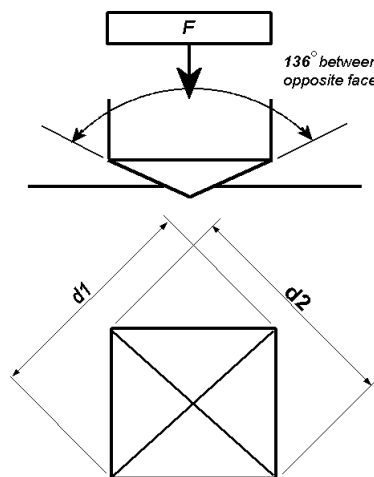


Fig. 3.4. Schematic representation of Vickers hardness indentation [101].

The area of the sloping surface of the indentation is calculated using the following equation [100,101].

$$HV = \frac{2F \sin \frac{136^\circ}{2}}{d^2}; HV = 1.854 \frac{F}{d^2} \text{ approximately}$$

F = Load in kgf

d = Arithmetic mean of the two diagonals, $d1$ and $d2$ in mm

HV = Vickers hardness

In the present investigation the hardness values of different MWF alloys were calculated using Vickers hardness tester (Model No. VM-50, according to ASTM standard E-92) at 10 kg load and 15 second indentation time.

The density of a material is defined as its mass per unit volume. This is also defined as its weight per unit volume and can be expressed as

$$\rho = m / V$$

$$\rho = \text{density (g/cm}^3\text{)}$$

$$m = \text{mass (g)}$$

$$V = \text{volume (cm}^3\text{)}$$

In the present work the density of D9SS-Zr MWF alloys was measure by weight by volume measurement [102].

3.3.3 Optical microscopy

Optical microscope is a conventional and most familiar device for magnifying a small specimen which cannot be directly observed by necked eye. Over the past few decades enormous growth in the application of optical microscope was experienced in field of material characterization in micron level. Generally, in an optical microscope image can be captured by normal light-sensitive cameras to generate a micrograph. Originally images were captured by photographic film, but in modern developments, a combination of

complementary metal–oxide–semiconductor (CMOS) and charge-coupled device (CCD) cameras were allowed to capture digital images. However, nowadays purely digital microscopes are commercially available which is using a CCD camera to observe the specimen and the image can be directly captured on a computer screen without any eyepieces.

In the present work an optical microscope of Leica DMIL was used to observe the surface attack on MWF alloys surfaces after each potentiodynamic polarization experiment in entire simulated media.

3.3.4 Scanning electron microscopy

The scanning electron microscope (SEM) is one of the most advanced imaging tools for microstructural analysis wherein the images of the specimen is formed by scanning it with a high-energy electron beam. The interaction of electrons with the atoms of the specimen produces signals which contain information mainly about the specimen's surface topography and composition. The electron beam is thermionically emitted from an electron gun fitted with a tungsten filament cathode or lanthanum hexaboride (LaB_6) cathodes. The accelerated electron beam of energy around 0.2 to 40 keV is focused by one or two condenser lenses to a spot of about 0.4 to 5 nm in diameter. The accelerated electron beam (primary electron beam) interacts with the specimen surface and the electrons lose their energy by repeated random scattering and absorption within a teardrop-shaped volume of the specimen known as the interaction volume. Secondary electron (SE), back scattered electron (BSE) and absorbed electrons are produced due to energy exchange between the electron beam and the specimen, each of which can be detected by specialized detectors. Various types of electronic amplifiers are used to amplify the signals and are displayed as variations in brightness on a cathode ray tube (CRT). The raster scanning of the CRT display is synchronised with that of the beam on the specimen in the microscope, and the resulting image is therefore a

distribution map of the intensity of the signal being emitted from the scanned area of the specimen. The image can be captured by photography from a high-resolution cathode ray tube, but in modern technology it can be digitally captured and displayed on a computer monitor and saved in a computer's hard disk [103].

A Philips XL 30 SEM (The Netherlands) attached with an energy dispersive spectrometer (EDS) having Beryllium window was used in the present work. The following characterizations were carried out by SEM.

- i. Microstructures of different D9 SS-Zr MWF alloys were characterized in as cast condition, after heat treatment at 1323 K for 2 h and 5 h and the local area elemental composition of different microstructural phases were analyzed by EDS attached with SEM.
- ii. Microstructures of different D9 SS-Zr-NMFP MWF alloys were characterized by SEM and EDS in as-cast and heat treated (1323 K, 2 h) conditions.
- iii. Microstructure of D9 SS-Zr-NMFP-U MWF alloy was characterized by SEM and EDS.
- iv. After polarization in different simulated geological environment, surface morphology of D9 SS-Zr MWF alloys were analyzed by SEM and EDS.
- v. Surface morphological analysis of D9 SS-Zr and D9 SS-Zr-NMFP MWF alloys was carried out by SEM and EDS after selective elemental leaching testing by MCC-1 and MCC-5.
- vi. SEM was also used to understand the selective microbial attachment on the etched surface of MWF alloy.

3.3.5 X-ray diffraction study

X-ray powder diffraction (XRD) is a rapid non-destructive analytical technique used for phase identification of a crystalline material and can provide detailed information about the crystallographic structure of naturally occurring and synthetic materials. XRD is based on

the constructive interference of monochromatic X-rays and a crystalline material. The X-rays are generated by a cathode ray tube, filtered to produce monochromatic radiation, collimated to concentrate and directed towards the specimen. A constructive interference (and a diffracted ray) is produced by the interaction of the incident rays with the specimen by satisfying Bragg's Law ($n\lambda = 2d \sin \theta$). This law relates the wavelength of electromagnetic radiation (λ) with the diffraction angle (θ) and the lattice spacing (d) in a crystalline specimen. The diffracted X-rays are then detected, processed and counted. By scanning the specimen over a range of 2θ values, all possible diffraction directions of the lattice could be obtained due to the random orientation of the powdered material. Conversion of the diffraction peaks to d-spacing allows the identification of the crystalline materials because each material has a set of unique d-spacing. Typically, this is achieved by the comparison of d-spacing with standard reference patterns [104].

In the present work a Philips X'pert MPD XRD system with Cu K α radiation in Bragg- Brentano geometry was used. The XRD pattern was recorded in the two theta range, $30^\circ < 2\theta < 85^\circ$. Calibration of the diffractometer was carried out using powdered silicon and α -alumina standard reference materials. The room temperature XRD pattern of all the alloys of D9 SS –Zr, D9-Zr-NMFP and D9 SS-Zr-NMFP-U were recorded in the as-cast condition. XRD pattern of D9 SS-Zr MWF alloys with 8.5 wt.% Zr (K2) and 17 wt.% Zr (K4) were also recorded after subjecting them to heat treatment at 1323 K for 1 h and 5 h.

The thermal behaviour and intermetallic phase stability of the MWF alloys (K2 and K4) were studied from room temperature to 1373 K using high temperature X-ray diffraction (HTXRD) technique. The HTXRD studies were performed using a Philips-X'pert MPD system, equipped with the Böhler® high vacuum heating stage. Typical instrument related parameters were, operating voltage of 40 kV, current of 30 mA for the X-ray tube; scan speed of $0.02^\circ \text{ s}^{-1}$ with a counting time of 6 s per step and an angular range (2θ) of $30\text{--}85^\circ$. The

heating stage consisted of a thin (80 μ m) resistance heated tantalum foil, on top of which the specimen was placed. Temperature was measured by a W–Re thermocouple, which was spot-welded to the bottom of the tantalum heater. The temperature was controlled to an accuracy of ± 1 K. The diffraction studies were performed using Cu K α radiation in the Bragg-Brentano geometry, at the temperature interval of 50 K from room temperature (298 K) to 1373 K. A heating rate of 1K min⁻¹ and a holding time of 30 min at each temperature of measurement were adopted. The specimen stage was flushed with high purity argon before the start of each experimental run and a vacuum level of about 10⁻⁵ mbar was maintained throughout the experiment. The peak identification and data analysis were performed with the help of JCPDS software.

3.3.6 Electrochemical corrosion testing

3.3.6a Open circuit potential study

Measurement of electrochemical potential is one of the primary steps in electrochemical study. The open circuit potential (also referred to as the equilibrium potential, the rest potential, or the corrosion potential) is the potential of a working electrode relative to the reference electrode when no potential or current is being applied to an electrochemical cell. In the present study an ASTM standard electrochemical cell [105] is used (Fig. 3.5). The working electrode (W.E) is connected to the specimen subjected to corrosion experiment and it represents the anode. Two platinised platinum plates used as counter electrodes (C.E) are connected as cathode and a reference electrode (R.E) of silver/silver chloride (Ag/AgCl, KCl) is used.

The open circuit potential (OCP) is the parameter which determines the tendency of a material towards electrochemical oxidation in a corrosive medium. In general, the potential is generating due to the combination of two half cell reactions in the electrochemical cell. One half cell reactions correspond to oxidation reaction at the anode (W.E) and the other half cell

reaction corresponds to reduction reaction at the cathode (C.E) of the cell. The electrodes are immersed in the electrolyte media, and after allowing sufficient time for equilibration both the half cell potentials stabilize around a stationary value and then measurements can be started. This potential may vary with time due to the changes on the electrode surface arising out of the electrochemical reaction. If the metallic surface (W.E) is subjected to continuous oxidation the potential will move towards cathodic direction (active potential) indicating dissolution of metal (corrosion). However, the cell potential will move to anodic direction (nobler potential) when stable passive film is formed on the metallic surface (W.E) this phenomenon is known as passivation [106]. The OCP is used as a criterion for monitoring the corrosion behaviour in the present study.

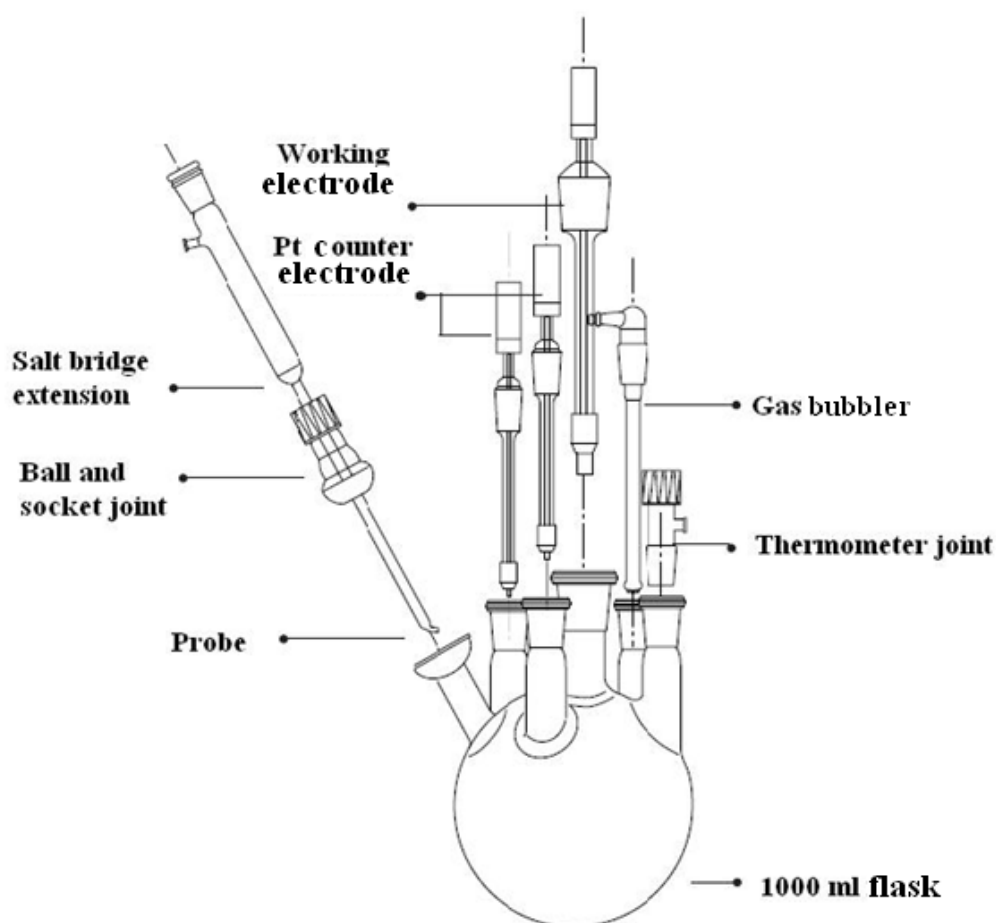


Fig. 3.5. Schematic of a typical electrochemical cell for corrosion study [105]

The OCP versus time was recorded for all the MWF alloy specimens in different simulated media in non stirred and aerated condition. The specimens were exposed to the tested solution for 1 h to attain the steady state potential. The variation of OCP versus time was monitored for (i) different D9 SS-Zr MWF alloys in de-mineralized (DM) water at pH 1, 5 and 8 and simulated KGW for 1 h (ii) D9 SS-8.5 wt.% Zr (K2) MWF alloy in simulated KGW, RGW-1 and RGW-2 for 24 h. (iii) microbial exposed MWF alloy(K2) in simulated KGW and RGW media for 1 h (iv) different D9 SS-Zr-NMFP MWF alloys in DM water at pH 1 and 5 and in simulated KGW for 1 h and (v) D9 SS-Zr-NMFP-U MWF alloys in DM water at pH 5 and simulated KGW for 1 h. OCP was monitored for 1 h to get the immediate response of the MWF alloy in the respective electrolytic environment.

3.3.6b Potentiodynamic polarization study

Potentiodynamic polarization method is a rapid way to measure the corrosion rate of a metal at or near its corrosion potential, E_{corr} in real time corrosion monitoring application. This technique can also be used as a way to rank alloys with respect to their corrosion behaviour. The corrosion rate is determined by extrapolating the linear segment of cathodic and anodic regions which is known as Tafel extrapolation [107]. The intersection of the Tafel lines gives the value of corrosion potential and corrosion current density. A scanning potentiostat is used for potentiodynamic measurements. The schematic of a potentiostatic polarization circuit diagram is illustrated in Figure 3.6. The potentiostat used in this measurement is capable of varying the potential automatically at a constant rate between two preset potentials. This method involves scanning the potential of a working electrode at a fixed rate and recording continuously the current density as a function of potential [106, 108].

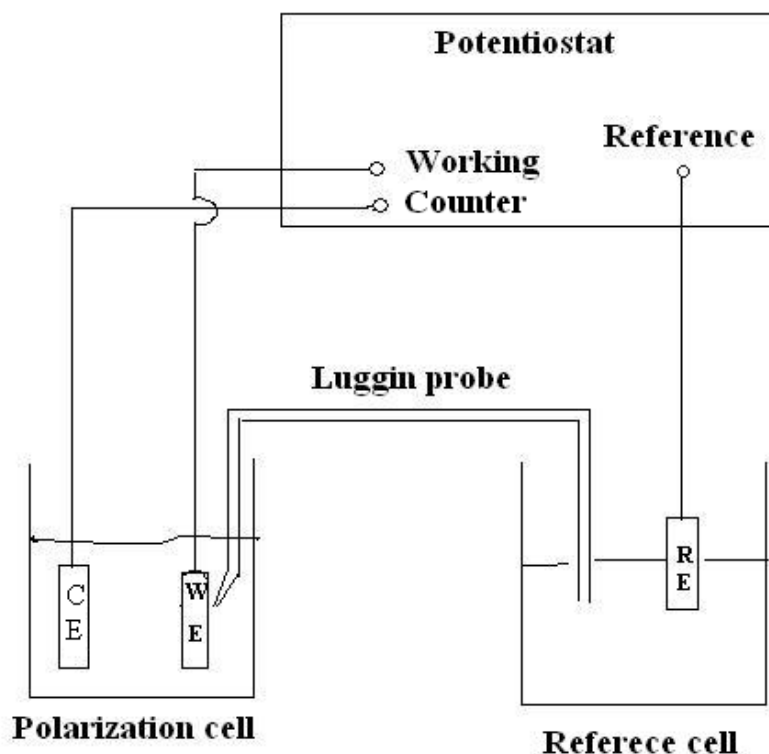


Fig. 3. 6. Potentiostatic polarization circuit diagram

In the present investigation potentiodynamic polarization experiment was carried out with (i) different D9 SS-Zr MWF alloys in DM water at pH 1, 5 and 8 and simulated KGW (ii) D9 SS-8.5 wt.% Zr (K2) in simulated RGW-1 and RGW-2 and after microbial exposure (*Bacillus* and *Pseudomonas* sp.) in KGW and RGW (iii) different D9 SS-Zr-NMFP MWF alloys in DM water at pH 1 and 5 and in simulated KGW and (iv) D9 SS-Zr-NMFP-U MWF alloys in DM water at pH 5 and in simulated KGW at room temperature using the electrochemical cell shown in Figure 3.5. The potentiodynamic polarization experiments were carried out at the scan rate of 10 mV/min using Solartron 1287 electrochemical interface. The polarization was started from -500 mV with respect to OCP and was continued till the breakdown of transpassive potential [109]. Three sets of tests were conducted for each specimen and all the polarization plots were found to be reproducible.

3.3.6c Electrochemical impedance spectroscopy

Electrochemical impedance spectroscopy (EIS) is the most versatile technique for monitoring corrosion rate at metal-electrolyte interfaces in ionically conducting medium. Impedance is defined as the total opposition offered by an electric circuit to the flow of an alternating current of a single frequency and is measured in ohms. It is the combination of resistance and reactance in an electrochemical system [109]. Expression for the reactance employs the complex number j ($= \sqrt{-1}$), and impedance Z , can be expressed in complex number notation as

$$Z = Z' + jZ''$$

where Z' and Z'' represent the real and imaginary components respectively. When the real part is plotted on the X-axis and the imaginary part is plotted on the Y-axis of a graph the plot obtained is known as "Nyquist plot" and is shown in Figure 3. 7. In this plot the Y-axis is negative and each point on this plot representing the magnitude and direction of the impedance vector at a particular angular frequency, ω . It is also observed that the right side of the plot represents low frequency data whereas the higher frequencies are on the left. The impedance can be represented as a vector (arrow) of length $|Z|$ in the Nyquist Plot. The angle between this vector $|Z|$ and the X-axis is known as "phase angle", ϕ . The Nyquist Plot in Figure 3.7 is based on the electrical circuit shown in Figure 3.8. The semicircle is characteristic of a single "time constant". Electrochemical impedance plots often contain several semicircles, however, only a portion of a semicircle is seen often. Another popular method of presenting the data is the Bode Plot in which the impedance is plotted with log frequency on the X-axis and the absolute values of the impedance ($|Z|=Z_0$) and the phase-shift on the Y-axis. The Bode Plot for the electric circuit of Figure 3.8 is shown in Figure 3.9 [110].

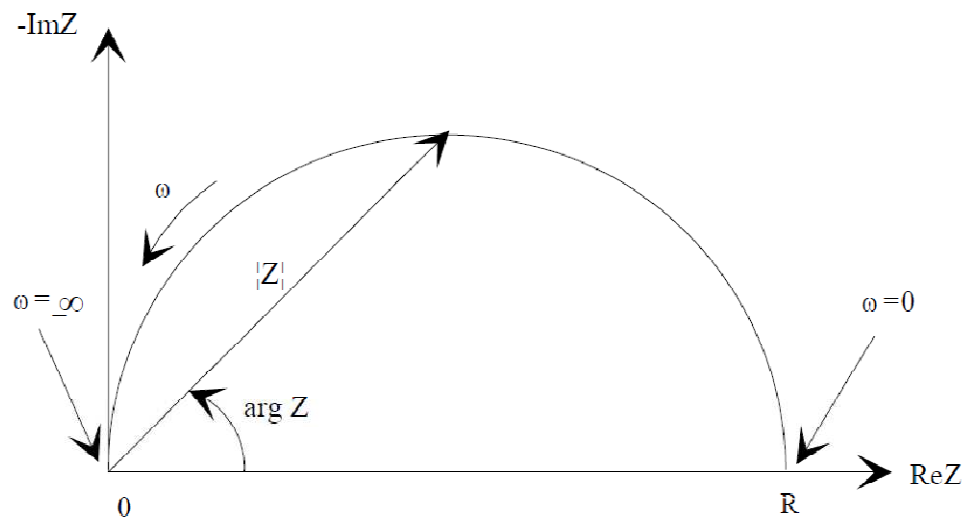


Fig. 3.7. Nyquist Plot with Impedance Vector [110]

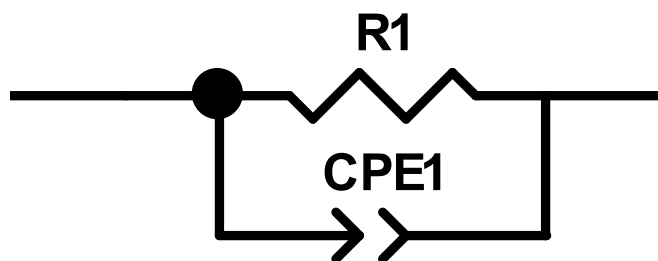


Fig. 3.8 Simple Equivalent Circuit with One Time Constant

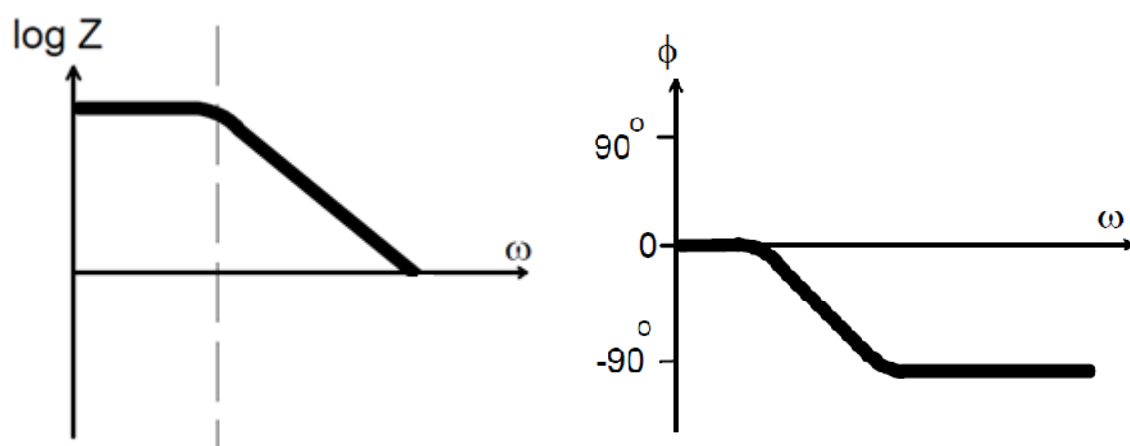


Fig. 3.9. Bode Plot with One Time Constant [110]

In EIS small periodic signals are used to perturb an electrode surface and measure an electrochemical response that can be analyzed to get information about corrosion mechanisms and corrosion kinetics. In corrosion experiments, generally 10 to 50 mV sinusoidal voltage signal is applied to a corroding electrode interface and the current signal resulting at the same excitation frequency is measured. The impedance is measured over a domain of discrete frequencies. At the high-frequency end the interfacial capacitance will dominate and that time only the cell solution resistance will contribute to the impedance. At lower frequencies, interfacial resistances will contribute to the impedance. Electrochemical and diffusional processes associated with corrosion are detected at frequencies in the range 10 to 10^{-6} Hz. However, below the frequency of 10^{-3} Hz, the metallic electrochemical interface will become unstable and reliable measurements may not be possible [109].

For EIS measurements on corroding surfaces usually require (i) a three electrode cell as shown in Figure 3.5 (ii) a potentiostat to control the potential between the working and reference electrodes and measure the current flow between the counter and working electrodes as shown in Figure 3.6 and (iii) a frequency generator to provide the periodic excitation signal. An impedance analyzer is also required to measure the complex impedance. Frequency response analyzers or lock-in amplifiers may be used for this purpose. Integrated systems that contain all the necessary electronic hardware for conducting EIS measurements are commercially available. The data acquisition and analysis of the EIS spectra can be done with the aid of a personal computer [109,111].

In the present investigation EIS measurements were carried out using Solartron 1255 frequency response analyzer and Solartron 1287 electrochemical interface. The experiments were carried out with MWF alloy specimens in the frequency range of 0.01 to 10^6 Hz by superimposing an AC voltage of 10 mV amplitude and were measured under open circuit

potential condition. The EIS results were interpreted using the equivalent circuit shown in Figure 3.10.

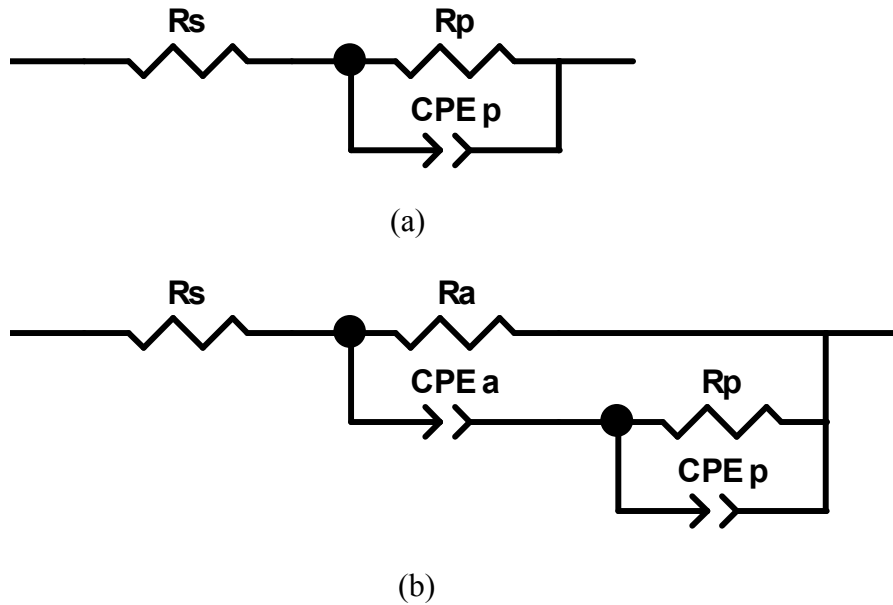


Fig. 3.10. The equivalent circuit used for fitting the impedance data (a) with one time constant (b) with two time constant (R_s - solution resistance, R_a - resistance of adsorbed layer, CPE_a - constant phase element for adsorbed layer, R_p - polarization resistance at electrode electrolyte interface, CPE_p - constant phase element for electrode electrolyte interface).

The selection of this circuit was based on the better and accurate fitting obtained from the experimental impedance data. Zview Version 2.6 (Scribner Inc.) software was used to fit the experimental impedance data. The impedance expression for constant phase element (CPE) is given by $Z_{CPE} = 1/[T(j\omega)^n]$, where T is proportionality constant and n is a fitting parameter. n is defined as $n = 1 - 2\alpha/180$, where α is the depression angle (in degrees) that evaluates the semi-circle deformation or depression. When $n = 1$, CPE describes an ideal capacitor [111-113]. CPE has been used in the present investigation to obtain better fit for the experimental data and this will represent the capacitance of the passive oxide layer. The data derived from the Nyquist plots are used for evaluating the corrosion behaviour of MWF alloys. The EIS measurements were carried out for (i) different D9 SS-Zr MWF alloys in DM water at pH 1, 5 and 8 and simulated KGW (ii) D9 SS-8.5 wt.% Zr (K2) in simulated RGW-

1and RGW-2 and after microbial (*Bacillus* and *Pseudomonas* sp.) exposure in KGW and RGW (iii) different D9 SS-Zr-NMFP MWF alloys in DM water at pH 1 and 5 and in simulated KGW and (iv) D9 SS-Zr-NMFP-U MWF alloys in DM water at pH 5 and simulated KGW.

3.3.7 Immersion corrosion testing

Immersion tests are the important standard testing method designed by American Society for Testing and Materials (ASTM C1220 & ASTM C1308) [91,115] for monitoring the performance of materials in exposed environment for longer duration. In this test the specimen is immersed in the simulated solution for longer duration and the elemental leaching from the material is studied by analyzing the solution. The Materials Characterization Centre (MCC) established by US Department of Energy at Pacific Northwest Laboratory has developed a series of leach tests to simulate materials performance in static, high temperature, low flow rate and dynamic conditions. They are generally referred to as MCC-1, MCC-2, MCC-3, MCC-4 and MCC-5 tests [114]. The present work investigates the release of elements from the simulated MWF alloys in different simulated and aggressive media by using MCC-1 (static or immersion testing) [91] and MCC-5 (dynamic testing) tests [115]. The purpose of both the tests is to assess the release behaviour of the alloying elements from MWF alloys and to determine the extent to which the release of the elements is influenced by the testing conditions. Both the tests provide information on the selective leaching of elements from MWF alloys into the solution. The elemental leaching will be quantified by measuring the changes in specimen mass, analyzing leachate composition and examining the specimen's surface morphology.

3.3.7a Dynamic testing (MCC-5 test)

The MCC-5 test is a convenient method for assessing the leachability of the waste-form under conditions of infinite dilution. This method involves continuous exposure of the specimens to fresh leachant at a given temperature in a Soxhlet apparatus shown in Figure 3.11. All the D9 SS-Zr MWF alloy specimens were introduced into the specimen holder and inserted into the Soxhlet apparatus. Initial weights of the specimens were noted before the experiment. The exposed solution (leachant) used in the present study was demineralised (DM) water. 500ml of the leachant was taken in the round bottomed flask of the Soxhlet apparatus and heated to 90°C. The leachate was sampled at regular intervals of 24 h duration and the total duration of the experiment was 260 days. The weights of the MWF alloy specimens were measured after 260 days. The leachates were analyzed by inductively coupled optical emission spectroscopy (ICP-OES) method.

3.3.7b Static testing (MCC-1 test)

This test method evaluates the relative chemical durability of simulated and radioactive waste forms in various test solutions at higher temperature under low surface area to volume (S/V) ratio conditions. This test can also be used to compare the leaching behaviour of various simulated and radioactive waste forms under a specific condition. In this test the waste form specimens are introduced into a sealed vessel and inserted into a controlled atmosphere furnace for a certain period at a constant temperature. The leachate solution will be analyzed at the end of the exposure period. In the present investigation the MWF alloy specimens were introduced into a Teflon (Polytetrafluoroethylene) container of a high pressure vessel (Teflon lined Parr vessel, model 4748) [29, 91] containing leachant (DM water). The leachability studies were carried out for (i) different D9 SS-Zr MWF alloys at 90°C and 200°C in DM water (ii) D9 SS-8.5 wt.% Zr (K2) MWF alloys at 90°C in simulated KGW, RGW-1 and RGW-2 and (iii) different D9 SS-Zr-NMFP MWF alloys in DM water.

Duration of each experiment was 90 days. The leachates were collected at the end of the experiment and analyzed by ICP-OES method. The weights of the specimens before exposure and after 90 days of exposure were measured.

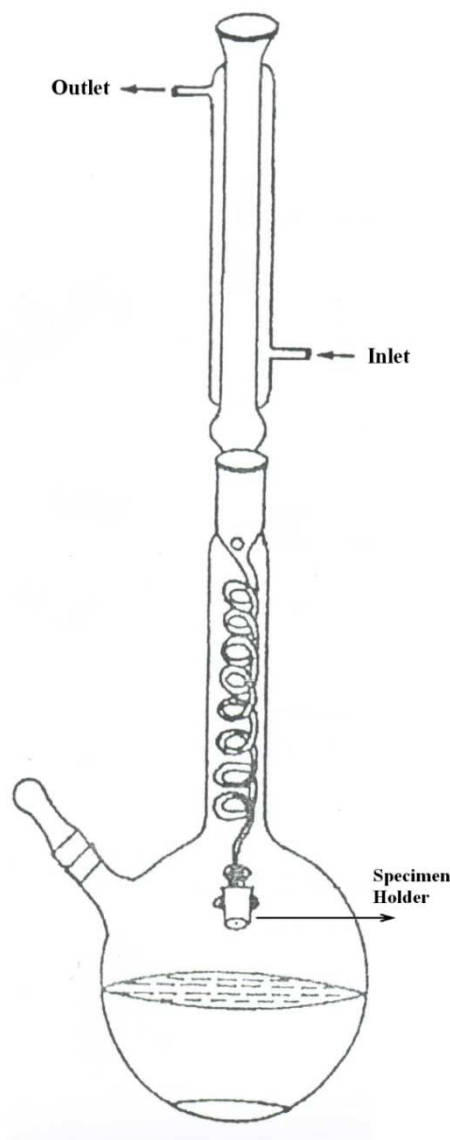


Fig. 3.11. Soxhlet apparatus used for dynamic leachability study

3.3.8 X-ray photo electron spectroscopy

X-ray Photoelectron Spectroscopy (XPS), also known as Electron Spectroscopy for Chemical Analysis (ESCA) is a widely used technique to investigate the chemical composition of surfaces. In XPS, the specimen is irradiated with low-energy (~ 1.5 keV) X-rays, causing photoelectrons to be emitted from the specimen surface. An electron energy

analyzer determines the binding energy of the photoelectrons. From the binding energy and intensity of a photoelectron peak the elemental identity, chemical state and quantity of an element are determined.

The basic principle of XPS is the electron liberation from the specimen as a result of photoemission process. The electron is ejected from an atomic energy level from the specimen surface by an X-ray photon (mostly from an Al-K α , 1486.6 eV or Mg-K α , 1253.6 eV primary source) and its energy is analyzed by the spectrometer. The XPS process is schematically represented in Figure 3.12 for the emission of an electron from the 1s shell of an atom [116].

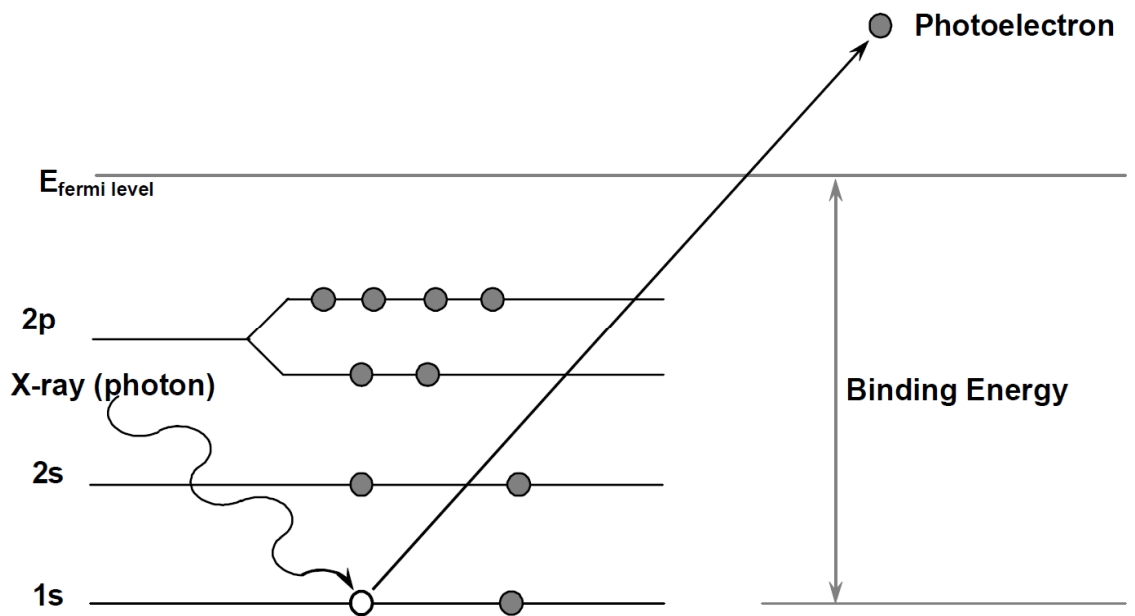


Fig. 3.12. Schematic representation of the XPS process [117]

The experimental quantity that is measured is the kinetic energy of the electron, which depends on the energy ($h\nu$) of the primary X-ray source. The characteristic parameter for the electron is its binding energy. The relation between these parameters is given by

$$E_B = h\nu - E_K - W$$

where E_B and E_K are the binding and the kinetic energy of the emitted photoelectron respectively, $h\nu$ is the photon energy and W is the spectrometer work function. In the first approximation, the work function is the difference between the energy of the Fermi level E_F and the energy of the vacuum level E_V , which is the zero point of the electron energy scale:

$$W = E_F - E_V$$

Each element has a characteristic electronic structure and thus, a characteristic XPS spectrum. In the spectrum, a number of peaks appear on the background. The background originates from photoelectrons which undergo energy changes between photoemission from the atom and detection in the spectrometer. The observed peaks can be grouped into three types: peaks originating from photoemission (*i*) from core levels, (*ii*) from valence levels at low binding energies (0 to 20 eV) and (*iii*) from X-ray excited Auger emission (between 1100 and 1200 eV). The main information comes from the core level peaks and the Auger peaks. The relative intensities are governed by the ionization efficiencies of the different core shells, designated by ionization cross section. The line width, defined as the full width at half-maximum intensity (FWHM), is a convolution of several contributions: the natural width of the core level, the width of the X-ray line and the resolution of the analyzer [116-118].

In the present study XPS was used to investigate the composition of passive film on MWF alloy formed in different simulated media. Measurements were carried out using XPS system (SPECS) that employed monochromatized Al $K\alpha$ radiation as probe and a hemispherical analyzer for energy analysis with pass energy of 20 eV having an optimum energy resolution of 0.6 eV. The passive film was formed electrochemically on MWF alloy in DM water at around 400 mV(Ag/AgCl) potential for 1 h to understand the passive film behaviour in the respective media. Survey scans and high resolution spectra of major alloying elements were acquired to analyze the chemical state of the alloying elements in the above condition. XPS spectra for passivated MWF alloy specimens were obtained after different

sputtering time intervals using 5 keV Ar^+ ion beam with current of $50 \mu\text{A}/\text{cm}^2$ at an incidence angle of 45° , and at a pressure of 1×10^{-5} Pa. The pressure in the analyzer chamber was of the order 1×10^{-7} Pa throughout the measurement.

3.3.9 Atomic force microscopy

Atomic force microscopy (AFM) is one of the advanced versatile tools for imaging and measuring the changes on a material's surface from micrometer to nanometer scale. It can be used in different environments like air, liquid and vacuum and for various types of materials such as conducting, semiconducting and non conducting materials. Three dimensional images also can be obtained by using this technique. AFM is mainly applicable for (i) surface roughness analysis (ii) analysis of thin film deposition (iii) grain size analysis (iv) failure analysis (v) analysis of material properties including surface stiffness, elasticity and adhesion (vi) imaging of biological species and (vii) in situ analysis of topographical variation due to corrosion, change of temperature etc. [119, 120].

The AFM scans the specimen's surface with the help of a tip on a flexible cantilever and measures the forces acting between the fine tip and specimen's surface. The force can be attractive or repulsive depending on the interaction between the tip and the specimen's surface and will create a positive or negative bending of the cantilever. The tip is typically made of Si_3N_4 or Si. A laser beam is reflected from the back side of the cantilever which detects the bending of the cantilever and produces images. A schematic of the principle of a typical AFM is shown in Figure 3.13 [120]. There are three primary modes for AFM imaging (i) contact mode (< 0.5 nm probe-surface separation) (ii) semi contact mode (0.5–2 nm probe - surface separation) and (iii) non contact mode (0.1 – 10 nm probe-surface separation).

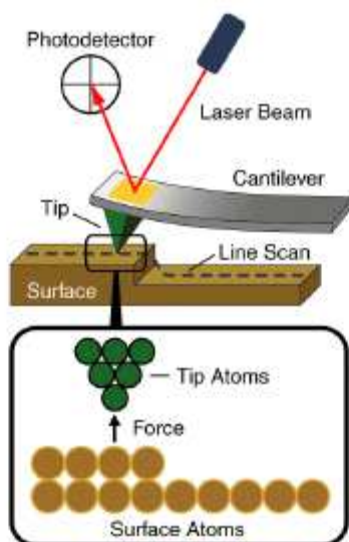


Fig. 3. 13. Schematic representation of AFM Principle [120]

A Molecular Devices and Tools for Nano Technology (NT-MDT) make atomic force microscopy (AFM) (Solver ProEC) was used in this work. The AFM measurements were carried out in contact mode using standard conical Si tip attached to a cantilever having a force constant of 5 nN m^{-1} with a frequency range from 50 to 150 Hz under ambient conditions. The AFM was used to investigate the surface topography of D9 SS-Zr MWF alloys after passivation and polarization in different simulated media. The MWF alloys were subjected to MCC-5 testing and MCC-1 testing in different simulated media for the investigation of its long term selective elemental leaching behaviour. AFM analysis was carried out for the MCC tested specimens to characterize their surface topography. AFM was also used to understand the bacterial topography on etched MWF alloy surface after exposure to bacterial culture. The MWF alloy was passivated electrochemically for 1 h at around 400 mV in DM water at pH 5 and pH 8, simulated KGW and RGW. Likewise, the MWF alloy was polarized in DM water at pH 1, pH 5 and pH 8, simulated KGW and RGW-2. The AFM analysis also carried out for the MWF alloys surface after electrochemical etching of the MWF surface with 10 % ammonium persulphate solution. The image analysis was done with the help of NOVA software.

3.3.10 Microbiological studies

MWF alloy specimens were suspended in *Bacillus* sp. and *Pseudomonas* sp. cultured solutions individually and after 5 days of exposure the specimens were taken out and the following post exposure experiments were carried out

3.3.10a Bacterial count

Quantitative analysis of the total bacterial attachment was done by total viable count (TVC) method [121]. The growth of bacteria in the simulated repository environment was confirmed by doing TVC analysis of the media after 5 days. For each experimental condition two specimens were used for TVC estimation. The specimens were removed from the medium, gently washed to remove loosely adhering cells and the bacterial cells attached on the specimens were dispersed into 15 ml sterile phosphate buffer (0.0425 g KH_2PO_4 and 0.19 g MgCl_2 per litre) by ultrasonication. The duration of sonication for optimum recovery of the cells was found to be 5 min [122]. Serial dilutions of the bacterial cell suspensions were prepared and 0.1 ml of each diluted suspension was plated onto nutrient agar, which supported the growth of both gram-negative and gram-positive bacteria. The plates were incubated for 24 h and the number of colonies were counted. Mean TVC values were calculated for each specimen and the results were expressed as colony forming units per square centimetre (cfu/cm^2).

3.3.10b Epifluorescence microscopic study

One specimen from each exposure condition in the bacterial culture was used for direct microscopic observation. The exposed specimen was gently washed with sterile water, air-dried in a sterile chamber and flooded with acridine orange solution (0.1% in distilled water). After 1 h, the excess stain was drained off and the specimens were washed in sterile water, dried and examine. Acridine orange, a fluorescent nucleic acid dye differentially stains

single stranded RNA and double stranded DNA, as fluorescing orange when intercalated with the former and as green while complexing with the latter [123] when observed under a Nikon Eclipse E600 epifluorescence microscope (excitation filter BP 490; barrier filter O 515).

3.3.10c Surface characterization

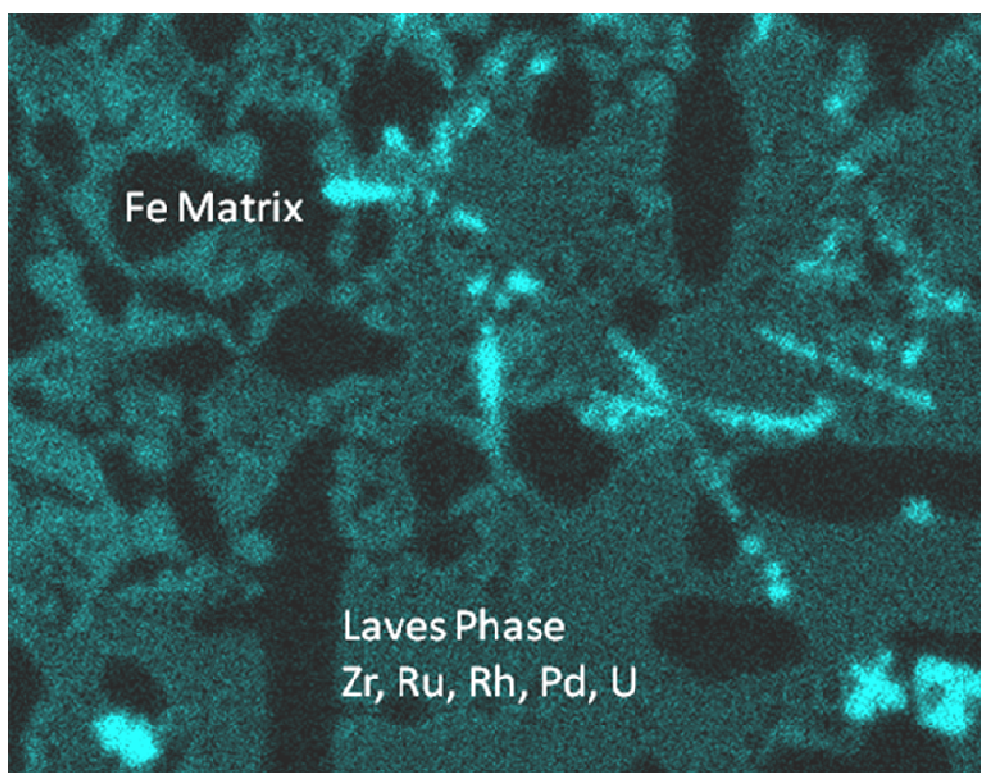
The bacterial morphology on the MWF alloy surface was investigated by SEM and AFM to understand the selectivity of bacterial attachment.

3.3.10d Microbial induced corrosion study

The effect of microbial attachment on the corrosion behaviour of MWF alloys was evaluated by different electrochemical corrosion testing methods including OCP, Potentiodynamic polarization and EIS as explained in section 3. 3.5. The surface morphology after corrosion was investigated by optical microscope.

CHAPTER 4

CHARACTERIZATION OF ALLOY METALLURGY OF D9 SS-Zr MWF ALLOYS



Chapter 4

CHARACTERIZATION OF ALLOY METALLURGY OF D9 SS-Zr MWF ALLOYS

The metallurgical characterization including microstructure, hardness and phase identification of different D9 SS-Zr metal waste form (MWF) alloys was carried out to understand their phase stability and mechanism for their physical performance. Microstructural analysis using scanning electron microscopy (SEM) attached with energy dispersive X-ray spectrum (EDS) showed the formation of two phases, the dark Fe based solid solution matrix and the brighter Zr rich intermetallic precipitates. The intensity of Zr rich intermetallic phases increased with the increase of Zr concentration which increased the hardness of the alloys. The phase identification by X-ray diffraction (XRD) showed the presence of NiZr, Ni₅Zr, Ni₇Zr₂, FeZr₂ and Fe₃Zr intermetallic phases along with austenite Fe based solid solution. Two MWF alloys of D9 SS with 8.5 wt.% Zr (K2) and D9 SS with 17 wt.% Zr (K4) were heat treated at 1323 K for 2 h and 5 h for homogenization. From SEM micrograph it was observed that the Zr rich intermetallic phases were agglomerated to form higher grained precipitation area after heat treatment. The precipitation phase transformed to isolated island after heat treatment for 5 h. The stability of the Zr rich intermetallic compounds was investigated by high temperature XRD. The results showed that all the intermetallic phases were stable up to 1173 K and beyond this temperature most of the Ni-Zr intermetallics were found to dissolve and diffused into Fe based solid solution matrix.

4.1 Introduction

The MWF alloy could remain as radioactive for more than ten thousand years due to the presence of actinides in its composition [124]. In geological repository the waste package

materials will experience high temperature, high level of radiation along with some natural shock like volcanic eruption, earth quake etc. Long term exposure in this environment can destroy the waste package which will allow the waste form to come into contact with repository environment. The integrity of the waste package is affected by high temperature exposure and radiation effects, such as radiation hardening, embrittlement, enhanced diffusion, and enhanced creep rate [3, 15, 28]. These effects will lead to material failure and radionuclide leaching which will be responsible for ground water contamination [3]. Hence, for the development of a new waste form material, detailed investigation of its physical attributes (i.e., microstructure and phase stability) and evaluation of its corrosion behaviour are required in a geologic repository environment. Thus, the prediction of material's performance is essential in the development and use of waste forms.

The objective of this study is to evaluate the basic material properties like hardness, density and microstructure and characterize the different compound phases present in the MWF alloys. It is essential to elucidate the stability of the different compound phases present in the MWF alloys at higher temperature conditions as they can experience high temperature and radiation exposure during disposal period. Hence, high temperature XRD study was carried out.

4.2 Experimental

The different experimental techniques used in this Chapter are listed below (the detailed description of these techniques is provided in Chapter 3):

- (i) Hardness measurements by using PC based Vickers hardness tester with 10 kg load and 15 second indentation time.
- (ii) Densities of the MWF alloys were calculated using weight by volume methods [102].

- (iii) The microstructural investigation was carried out using SEM in the as-cast condition. The local area compositions were analyzed by energy dispersive X-ray spectrum (EDS) unit and X-ray elemental mapping attached to SEM. Two MWF alloys of D9 SS with 8.5 wt.% Zr (K2) and 17 wt.% Zr (K4) were homogenized at 1323 K for 2 h and 5 h and the microstructural changes were studied by using SEM and EDS.
- (iv) Different compound phases present in all the MWF alloys in as-cast condition were studied by X-ray powder diffraction technique (XRD). The XRD patterns were also recorded for the MWF alloys K2 and K4 after heat treating them at 1323 K for 2 h and 5 h.
- (v) The high temperature stability of the intermetallic phases in the MWF alloys K2 and K4 were studied up to 1373 K by high temperature XRD (HTXRD) technique.

4.3 Results and discussion

4.3.1 As-cast MWF alloys

4.3.1.1 Hardness and density

Table 4.1 gives the measured hardness and density values of the MWF alloys along with those of D9 SS and Zr. It was observed that the density of MWF alloys decreases and hardness increases with increasing Zr concentration. However this trend was observed only up to 14.1 wt.% Zr, beyond which the hardness and density values remained unchanged even with increasing Zr concentration. This study showed the opposite trend exhibited by MWF alloys in the hardness and density.

Table 4.1. Hardness and density values of MWF alloys

Alloy sample	Composition	Hardness	Density
	(D9-Zr alloy)	(HV)	(g cm ⁻³)
D9	D9-0 wt.% Zr	295	7.99
Zirconium	Zr	92.08	6.52
K1	D9-4.4 wt.% Zr	213 ± 2	7.67
K2	D9-8.5 wt.% Zr	274 ± 6	7.6
K3	D9-12.2 wt.% Zr	370 ± 15	7.58
K3B	D9-14.1 wt.% Zr	440 ± 5	7.52
K4	D9-16.8 wt.% Zr	440 ± 4	7.52

The decrease in density with the increase in Zr concentration was expected as density of Zr is lower than D9 SS. Moreover, there is a possibility of formation of pores, voids, etc., during the casting of the material which would be responsible for reducing the density. On the contrary, the increase in hardness values with the increase in Zr concentration is indicative of the formation of intermetallic precipitates in the MWF alloy [125, 126].

4.3.1.2 Microstructural analysis by SEM

The back scattered electron (BSE) mode SEM micrographs of the MWF alloys after electrochemical etching are shown in Figure 4.1. The microstructure of the MWF alloys showed the presence of two different phases; the dark phase and the bright phase with appearance of eutectic network. The intensities of the bright eutectic phases were increasing with increasing Zr concentration.

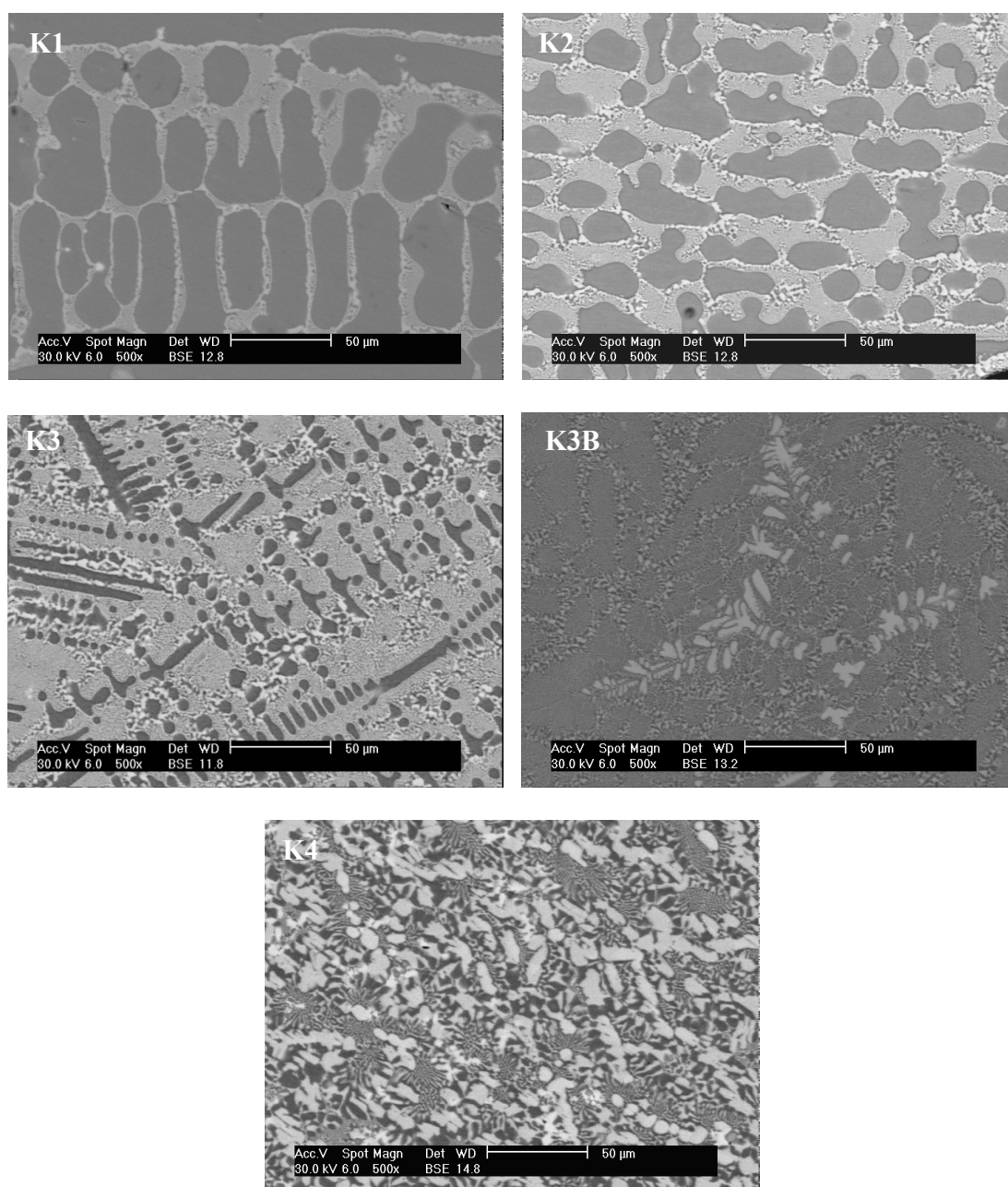


Fig. 4.1. BSE mode SEM micrographs of D9 SS-Zr MWF alloys.

The local area elemental compositions of the different phases were analyzed by EDS attached with SEM and the elemental compositions of the different phases are shown in Table 4.2. From EDS analysis it was found that the dark phase had Fe, Cr, and Ni as major elements

and Si, Mo and Zr as minor elements indicating Fe based D9 SS solid solution phases in the alloy. In the bright phase along with Fe, Cr and Ni, Zr was present as a major element. Nickel concentration was comparatively higher at the bright phase than the dark phase. The concentration of Si, Mo and Ti was more at the bright phases compared to the dark phase. Only exception was alloy K3B wherein an anomalous behaviour could be observed. In this case, the dark phase had sufficient amount of Zr (5.17 wt.%) along with Ti. The X-ray elemental mapping of a typical MWF alloy K3 (D9 SS-12.2 wt.% Zr) over the entire surface shown in Figure 4.2 revealed that at the dark regions presence of Zr was insignificant, whereas the intensities of Fe and Cr was more in the dark phase compared to bright phase. The bright region appeared as Ni and Zr rich phases. Presence of Ti, Mo and Si was nearly uniform in all regions. These results indicate that Ni has higher affinity for Zr and Zr forms a separate phase in the MWF alloys.

The dark phases exhibited Fe based solid solution matrix and the bright phases were Laves-type Zr rich intermetallic phases designated as $\text{Zr}(\text{Fe,Cr,Ni})_{2+x}$ [21]. The formation of these two phases can be explained with the help of Fe-Zr binary phase diagram (Fig. II.7). In the Fe-Zr binary phase diagram it is observed that Fe combines with Zr and forms FeZr_2 type Laves intermetallic compound [75]. It is also reported that Zr combines with iron, chromium, nickel and other elements to form Laves and other intermetallics [72]. These intermetallics are a strong sink for the austenite stabilizer like nickel as well as other impurities [72, 78] and hence, Ni concentration was more in the precipitate phase. The X-ray elemental mapping also revealed the distribution of major components (Fe, Cr, Ni and Zr) and minor components (Mo, Ti, Si) in the MWF microstructure. As expected, X-ray elemental mapping and EDS analysis showed that the elements like Si, Ti, Zr and Ni exhibited strong preference for intermetallic phases. Molybdenum showed moderate preference in both intermetallic and solid solution phases without any

preferential distribution. However, the microstructural investigation of all MWF alloys revealed that with increase in Zr concentration the intensity of intermetallic precipitates increased gradually, whereas in the MWF alloy K3B (D9SS-14 wt.% Zr) a precipitate cloud was formed over the matrix phase. Due to this cloud it was very difficult to focus the electron beam on the matrix phase without the interference of precipitate phase and hence, around 5 wt.% Zr appeared in the matrix phase. In the MWF alloy K4, the precipitates separated from the matrix phases and hence the interference of precipitate was not observed during EDS analysis of the matrix.

Table 4.2. Elemental composition of the MWF alloys at two different regions by EDS

Element	Concentration (wt.%)									
	K1		K2		K3		K3B		K4	
	Dark phase	Bright phase	Dark phase	Bright phase	Dark phase	Bright phase	Dark phase	Bright phase	Dark phase	Bright phase
SiK	0.68	1.68	0.82	1.24	0.53	1.21	0.69	0.85	0.77	2.04
ZrL	0.31	19.53	0.46	26.40	0.43	26.99	5.17	19.80	0.86	30.6
MoL	1.32	2.35	1.79	2.90	2.17	2.56	2.09	2.34	3.23	2.85
TiK	-	0.42	-	0.75	-	0.44	0.36	-	-	0.49
CrK	15.13	8.74	14.94	5.72	15.48	6.71	15.30	10.75	17.85	5.75
FeK	69.50	45.60	70.80	38.40	70.82	42.47	63.62	50.44	70.30	43.99
NiK	13.06	21.68	11.19	24.50	10.56	19.62	12.77	15.82	6.99	14.28

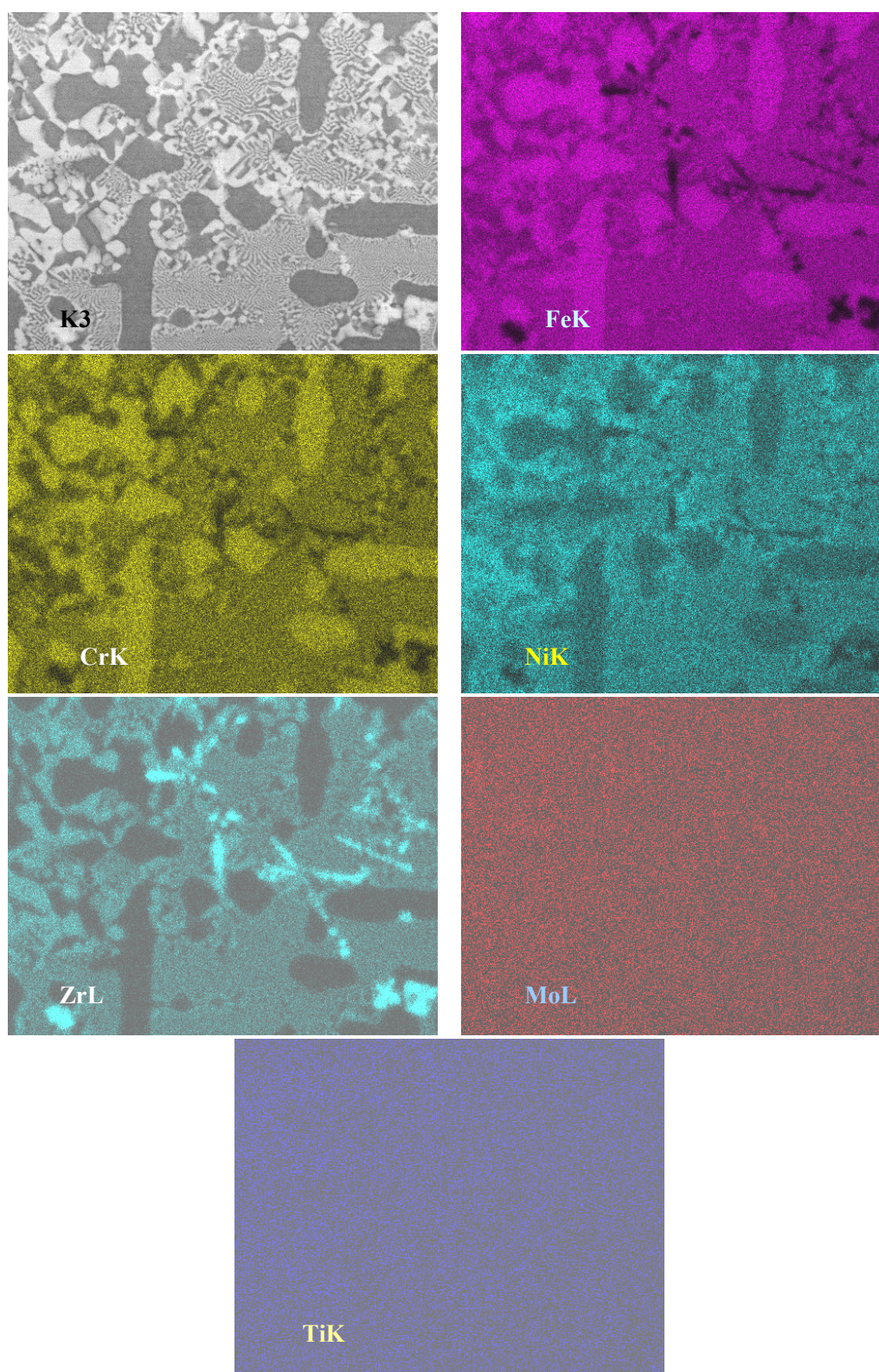


Fig. 4.2. X-ray elemental mapping of the MWF alloy, K3 (D9-12.2 Zr)

4.3.1.3 XRD analysis for phase identification

The intermetallic compounds formed in MWF alloys were characterized by X-ray diffraction (XRD) technique. Figure 4.3 shows the typical XRD patterns of different as-cast D9 SS-Zr MWF alloys and its magnified view is shown in Figure 4.4..

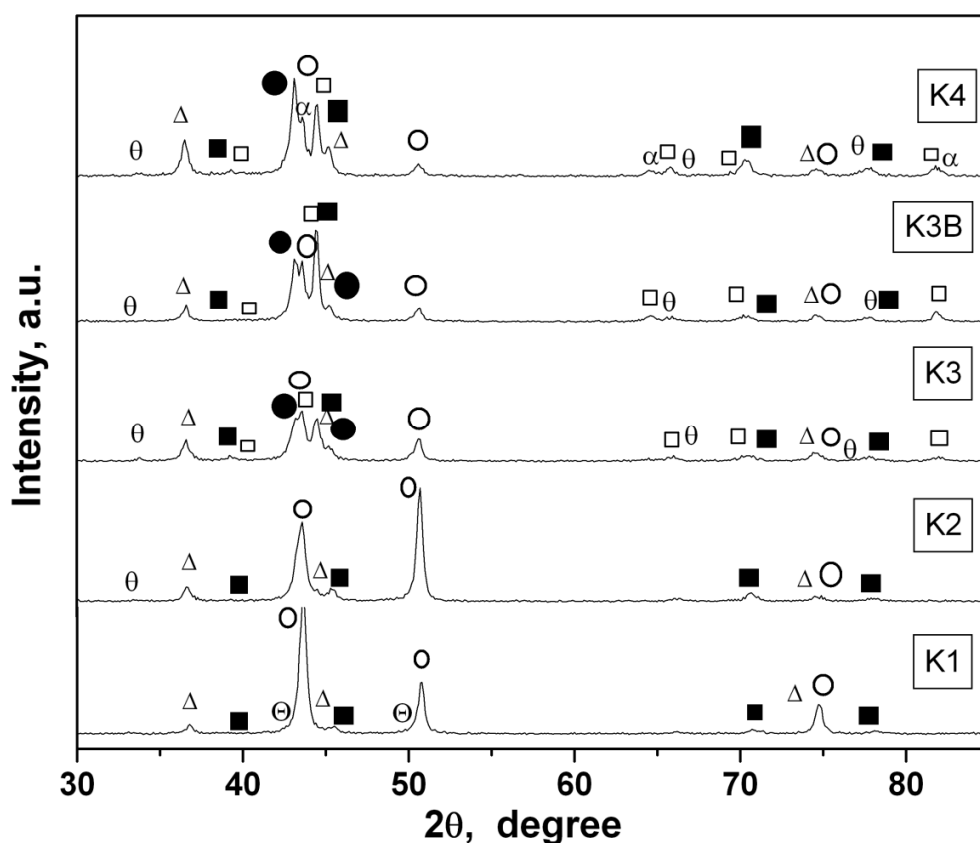


Fig. 4.3. X-ray diffraction pattern of different D9 SS-Zr MWF alloys in as-cast condition (○- fcc Fe based solid solution, θ -FeZr₂, Δ -NiZr, \blacksquare -Ni₅Zr, \bullet - Ni₇Zr₂, \odot - austenite Fe, \square - ferrite Fe)

The phases identified from the XRD pattern were typically fcc Fe based solid solution along with Zr intermetallic compounds like NiZr, Ni₅Zr, Ni₇Zr₂, Fe₃Zr, FeZr₂ etc. The intensities of the peaks were dependent on the composition of MWF alloys. In the MWF alloy K1, the major peaks correspond to austenite Fe based solid solution phase; however, some additional

minor peaks appeared for intermetallic compounds like NiZr, Ni₅Zr and FeZr₂. With increasing Zr concentration the intensity of the intermetallic peaks increased and the austenite Fe based solid solution peak intensity decreased gradually. In addition, with increasing Zr concentration Ni-Zr peaks became more prominent compared to Fe-Zr peaks; and new peaks corresponding to Ni₇Zr₂ and Fe₃Zr could be observed. An interesting feature observed with alloy K1 was the appearance of minor peaks of γ -Fe; and minor peaks of α -Fe for alloy K4 were observed. The XRD analysis did not show any elemental signal for pure Zr metal. The formation of typically Fe-Zr and Ni-Zr type Laves intermetallic compounds by Zr was confirmed from the XRD patterns. The intensity of intermetallic peaks increased with increasing Zr concentration.

Zirconium has very low solubility in Fe (0.16 at.% at 1173 K) [127] and hence, has higher tendency to form intermetallic compound. However, the higher affinity of Ni toward Zr intermetallic phases is due to its higher solubility limit in Zr intermetallic phases. The solubility limit of Fe in Ni-Zr is 1.4 at.% whereas the solubility of Ni in FeZr₂ is 5.6 at.% [128]. According to Fe-Zr phase diagram [75, 76], Fe with 15 wt.% Zr forms α -Fe solid solution, Fe₂₃Zr₆ and Laves type intermetallic phases [86]. McDeavitt et al [21] and Abraham et al. [72] also reported that the predominant phases in MWF alloys were α -ferrite, γ -austenite, Fe₂₃Zr₆, and ZrFe_{2+X} type Laves [86] intermetallic phase. However, in the present study, α -ferrite peak was observed only in the alloy K4 (SS-16.8 wt.% Zr) and the peaks corresponding to Fe₂₃Zr₆ were not observed. Owing to the presence of higher concentration of Ni in the D9 SS-Zr MWF alloys α -ferrite was not formed. The MWF alloys of 316SS with 8 wt.% Ni were used by McDeavitt et al [21] and Abraham et al. [72] as base material during their investigation. Nickel had strong affinity towards intermetallic phases and made the matrix Ni deficient and formed the matrix ferrite. In the present investigation the base material used is D9 SS in which the Ni content is 15 wt.%

which was sufficient to retain the solid solution matrix completely austenite. In the MWF alloy K4 with Zr concentration of around 17 wt.%, the intensity of the Zr intermetallic phases were very high and more Ni was consumed in the Zr intermetallics phase formation. Hence, Ni deficiency occurred in the matrix phase and instead of a completely austenite phase, ferrite peak was observed. Similarly, in alloy K1 with 4.4 wt.% Zr, weak γ -Fe peaks were formed due to lower concentration of Zr intermetallic precipitates

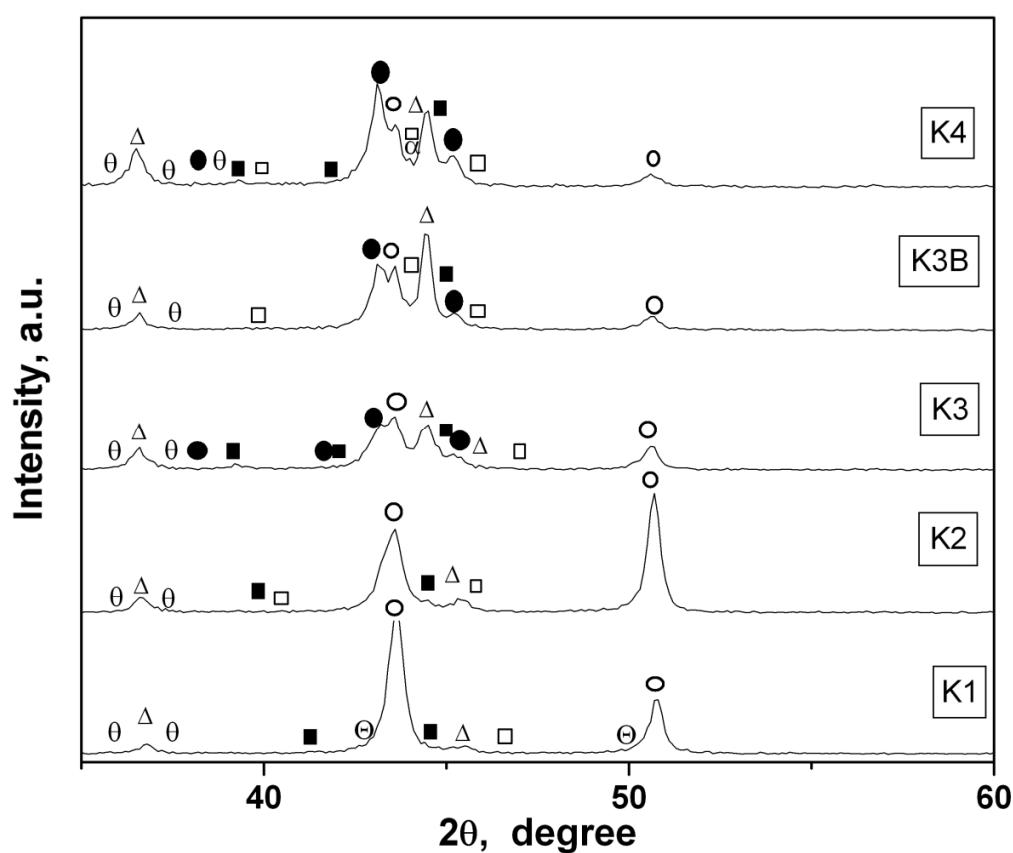


Fig. 4.4. Magnified view of X-ray diffraction pattern of different D9 SS-Zr MWF alloys in as-cast condition (○- fcc Fe based solid solution, θ -FeZr₂, Δ-NiZr, ■-Ni₅Zr, ●- Ni₇Zr₂, ⊖- austenite Fe, α- ferrite Fe)

The existence of the intermetallic Fe₂₃Zr₆ is not reliably reported for Fe-Zr system in the literature. A number of contradictory results are available in which the existence of this phase

has been reported, [129-134] and a few of the reports mention that $\text{Fe}_{23}\text{Zr}_6$ phase is a metastable phase and not an equilibrium phase [77, 128, 133-137]. Based on the discussion of Zhou et al. [128] the experimental studies on the phase diagram of Fe-Zr system by Aubertin et al. [136] and Alekseeva and Korotkova [137] concluded that $\text{Fe}_{23}\text{Zr}_6$ does not exist. Liu et al [135] reported the formation of $\text{Fe}_{23}\text{Zr}_6$ only as a metastable phase. Similarly Stein et al. [77] re-determined Fe-Zr phase diagram and reported the cubic that phase of $\text{Fe}_{23}\text{Zr}_6$ is not an equilibrium phase. Svechnikov et al [130] observed that existence of Fe_3Zr phase instead of $\text{Fe}_{23}\text{Zr}_6$, which is consistent with the observation made in the present study that stable Fe_3Zr phase is formed in the MWF alloys when Zr concentration was more than 12 wt.%.

4.3.2 Homogenized MWF alloys

The MWF alloys K2 (D9 SS-8.5 wt.% Zr) and K4 (D9 SS-16.8 wt.% Zr) were homogenized at 1323 K for 2 h and 5 h, and the microstructural characterization and phase identification were carried out by SEM and XRD analysis respectively in order to find out the changes if any, in microstructure and intermetallic phases present in the MWF alloys after homogenization.

4.3.2.1 Microstructural analysis of homogenized MWF alloys by SEM

SEM micrographs of the MWF alloy K2 in different conditions are shown in Figure 4.5. It was observed that in as-cast condition (Fig. 4.5a) bright phases were not properly distributed; instead they appeared as eutectic network. The microstructure after homogenization at 1323 K for 2 h (Fig. 4.5b) showed the coarsening of the intermetallic grains along with the presence of eutectic network. After homogenization for 5 h, the eutectic network was found to agglomerate to bigger grains and transformed to Zr rich intermetallic island (Fig. 4.5c).

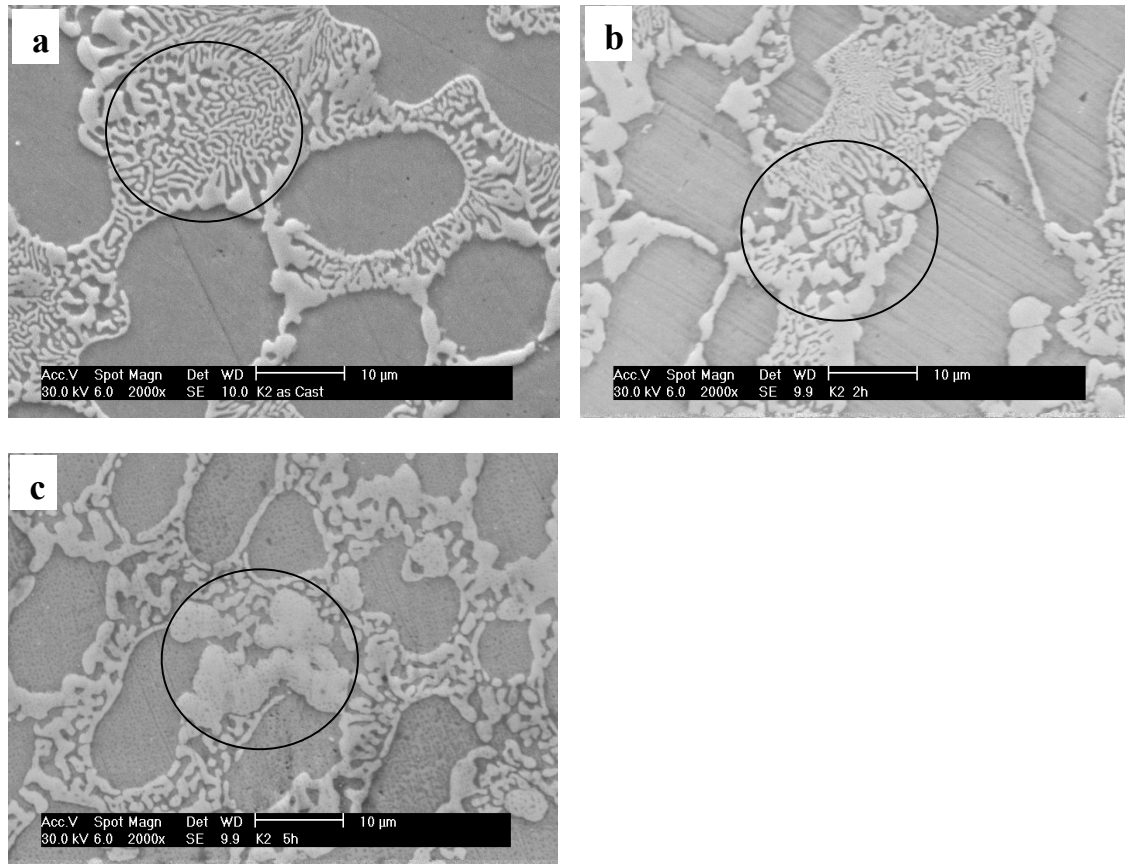


Fig. 4.5. Secondary electron mode SEM microstructure of MWF alloy K2 (a) as-cast (formation of Fe based solid solution along with Zr rich eutectic network) (b) Homogenized for 2 h at 1323 K (coarsening of eutectic intermetallics) (c) Homogenized for 5 h at 1323 K (agglomeration to Zr rich intermetallic island).

Figure 4.6 shows the SEM microstructure of MWF alloy K4 under different conditions. The formation of large grained Zr rich intermetallic phases surrounded by the eutectic network was observed in as-cast condition (Fig. 4.6a). After homogenization at 1323 K for 2 h (Fig. 4.6b) the eutectic networks diminished and the distinct appearance of isolated intermetallic phases (bright) and solid solution phases (dark) could be observed. After homogenization for 5 h at 1323 K (Fig. 4.6c), transformation of eutectic network to isolated island of higher grained Zr rich intermetallic phases took place which was due to high temperature diffusion and thermal ageing.

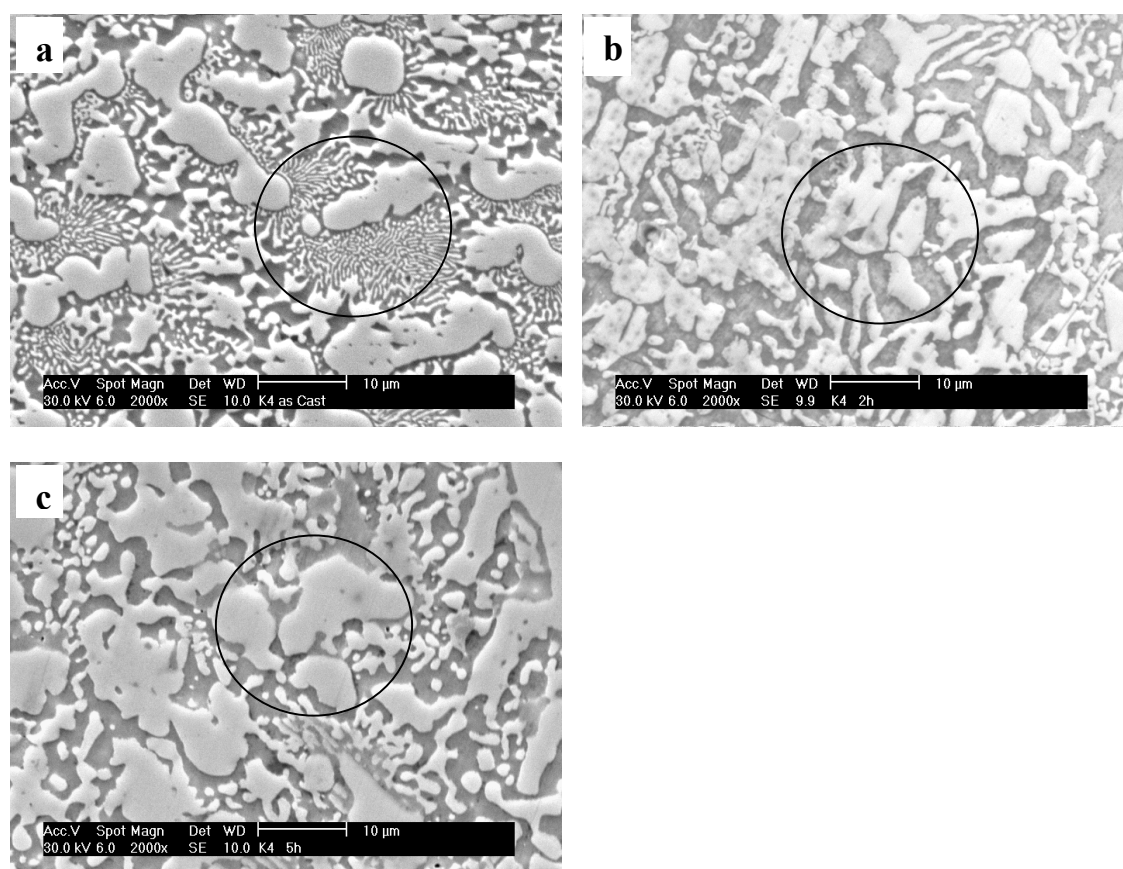


Fig. 4.6 Secondary electron mode SEM Microstructure of MWF alloy K4 (a) as-cast (formation of large intermetallic region surrounded by the eutectic network) (b) Homogenized for 2 h at 1323 K (transformation of eutectic network to isolated Zr rich intermetallic island) (c) Homogenized for 5 h at 1323 K (bigger island due to high temperature diffusion and thermal ageing).

As the Zr concentration in alloy K4 was double than that of alloy K2, the intensity of intermetallic phase was obviously more in alloy K4. In general, the intermetallic phases are the sink for fission products and actinide [72], and hence, due to high temperature diffusion and thermal ageing the intermetallic phases were agglomerated to isolated island with increasing sink size for radionuclides [78]. However, further studies on corrosion behaviour is required to have

higher amount of intermetallic phases as they may show inferior corrosion behaviour leading to leaching of alloying elements.

Table 4.3. Elemental composition of as-cast and homogenized MWF alloys in different regions by EDS

Elements	Concentration (wt.%)							
	K2 (as-cast)		K2 (heat treated)		K4 (as-cast)		K4 (heat treated)	
	Dark phase	Bright phase	Dark phase	Bright phase	Dark phase	Bright phase	Dark phase	Bright phase
SiK	0.82	1.24	---	---	0.77	2.04	---	---
ZrL	0.46	26.4	5.48	43.56	0.86	30.6	23.21	42.46
MoL	1.79	2.90	---	1.56	3.23	2.85	---	1.4
TiK	---	0.75	---	0.44	---	0.49	---	0.45
CrK	14.94	5.72	15.01	4.22	17.85	5.75	11.58	4.37
FeK	70.80	38.4	68	29.9	70.30	43.99	54.01	31.43
NiK	11.19	24.5	11.51	20.32	6.99	14.28	11.19	19.89

4.3.2.2 XRD analysis for phase identification of homogenized MWF alloys

4.3.2.2.1 MWF alloy K2

Different compound phases present in the MWF alloys were identified with the help of XRD technique. Figure 4.7 shows the XRD patterns of alloy K2 in different conditions like as-cast, homogenized at 1323 K for 2 h and homogenized at 1323 K for 5 h. In the as-cast condition presence of intense peak of fcc Fe based solid solution along with peaks of Ni-Zr and Fe-Zr intermetallic phases like NiZr, Ni₅Zr and FeZr₂ was observed.

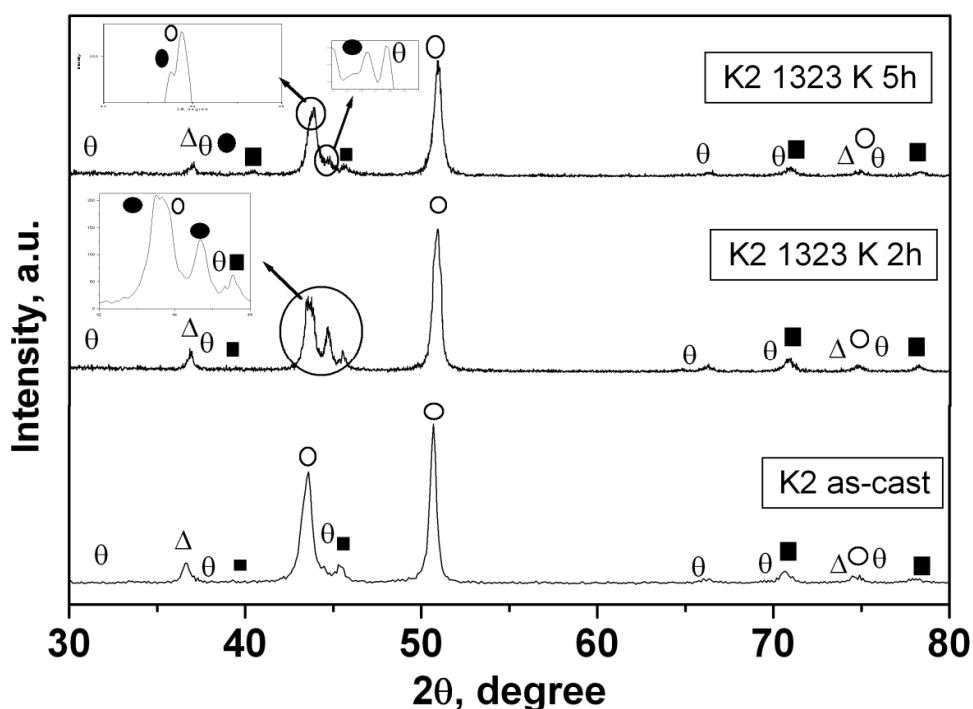


Fig. 4.7. XRD patterns of MWF alloy K2 of as-cast condition, homogenized at 1323 K for 2 h and homogenized at 1323 K for 5 h (○- fcc Fe based solid solution, θ -FeZr₂, Δ -NiZr, ■-Ni₅Zr, ●- Ni₇Zr₂).

After homogenization, the intensity of fcc Fe based solid solution peak decreased and the prominent appearance of intermetallic peaks was observed. Additionally, the new phase, Ni₇Zr₂ appeared after homogenization. The XRD pattern of as-cast MWF alloys given in Figure 4.3 showed the appearance of Ni₇Zr₂ phase when Zr concentration was more than 12 wt.%. After homogenization at 1323 K, the Ni₇Zr₂ peak appeared in the MWF alloys with 8.5 wt.% Zr. The Ni₇Zr₂ is an equilibrium phase and has maximum solubility for Fe, Cr and Ni than the other phases [128]. Additionally its free energy of formation is lower than the other phases [138]. The intensities of peak corresponding to other intermetallics like FeZr₂ and Ni₅Zr increased after homogenization. High temperature diffusion and agglomeration of intermetallic islands took place in the heat treated alloy and hence, the intensity of the intermetallic phases was more when

compared to as-cast alloy. Increase in the intensity of the intermetallic phases was observed in the MWF alloys with increase in annealing time due to higher diffusion at longer equilibration time.

4.3.2.2.2 MWF alloy K4

Figure 4.8 shows the XRD patterns of MWF alloy K4 under different conditions. The XRD pattern of as-cast alloy comprised the peaks of fcc Fe based solid solution, α -ferrite, NiZr, Ni₅Zr, Ni₇Zr₂, FeZr₂ and Fe₃Zr. After homogenization at 1323 K the peak corresponding to α -ferrite was disappeared. The intensity of fcc Fe based solid solution peaks decreased, while those of Fe₃Zr and NiZr increase after homogenization.

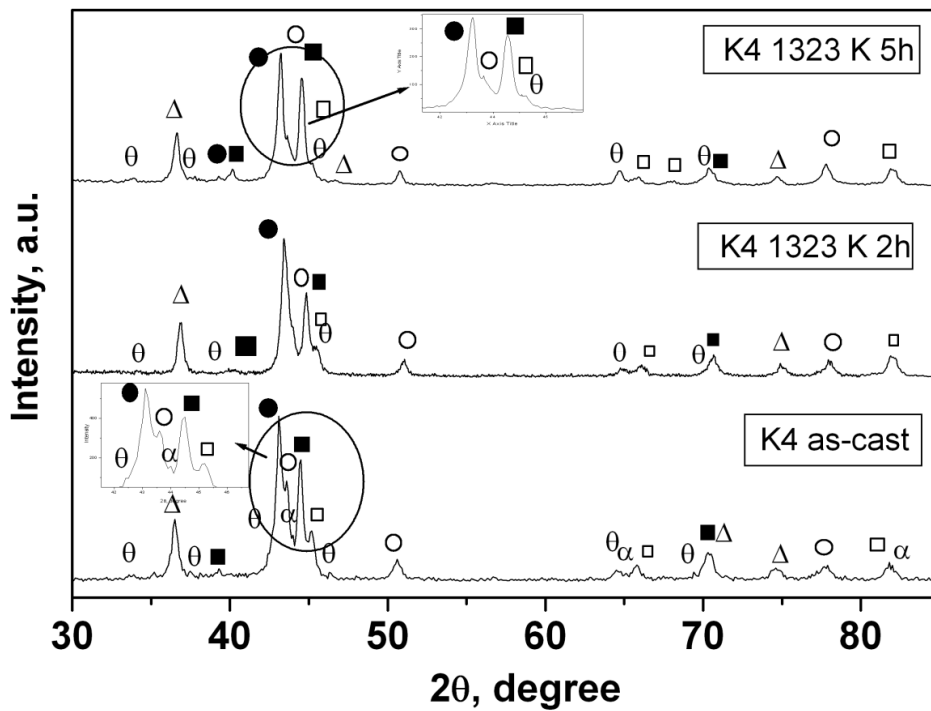


Fig. 4.8 XRD patterns of MWF alloy K4 in as-cast condition, homogenized at 1323 K for 2 h and homogenized at 1323 K for 5 h (\circ -fcc Fe based solid solution, \square -Fe₃Zr, θ -FeZr₂, Δ -NiZr, \blacksquare -Ni₅Zr, \bullet -Ni₇Zr₂, α - α -ferrite).

Table 4.3 shows the EDS elemental composition of the different phases of as-cast and homogenized MWF alloys. In both the conditions the Ni and Zr concentration were higher in the bright intermetallic phases when compared to those in the dark solid solution phases. In the as-cast MWF alloy K4, the Ni content in dark phase was around 7 wt.% whereas in the homogenized alloy the Ni concentration was about 11 wt.%. For maintaining the stainless steel matrix completely in austenite phase a minimum of 8 wt.% Ni was essential [139] and hence, in the as-cast alloy the matrix was deficient of Ni and ferrite phase was appearing. However in the homogenized condition due to high temperature diffusion, sufficient amount of Ni was present in the dark phase to make the whole matrix austenite. The intensity of the intermetallic phases increased due to high temperature diffusion and the transformation of eutectic network to larger grained Zr rich intermetallic phase.

4.3.3 High temperature XRD studies

4.3.3.1 MWF alloy K2

High temperature XRD (HTXRD) study was carried out to determine the stability of different intermetallic phases at high temperature condition. Figure 4.9 shows the HTXRD patterns of MWF alloy K2 and the details about the peaks are given in Table 4.4. The peaks obtained at 573 K such as, fcc Fe based solid solution, FeZr_2 , NiZr , Ni_7Zr_2 and Ni_5Zr were similar to the peaks observed in room temperature XRD (Fig. 4.7). With increasing temperature up to 1073 K only the peak shift towards lower angle was observed due to lattice expansion. At 1173 K, new peaks started to appear at the 2θ values 39.5 degree and 43.03 degree which correspond to Fe_3Zr peak and the intensities of the peaks corresponding to NiZr and Ni_5Zr started to decrease. At 1223 K the peak intensity of Fe_3Zr was increasing and those of NiZr and Ni_5Zr were decreasing. At 1273 K the peaks due to NiZr and Ni_5Zr disappeared and the intensity

of fcc Fe based solid solution peak was increasing. However, the intensities of other peaks corresponding to FeZr_2 , Fe_3Zr and Ni_7Zr_2 remained unchanged.

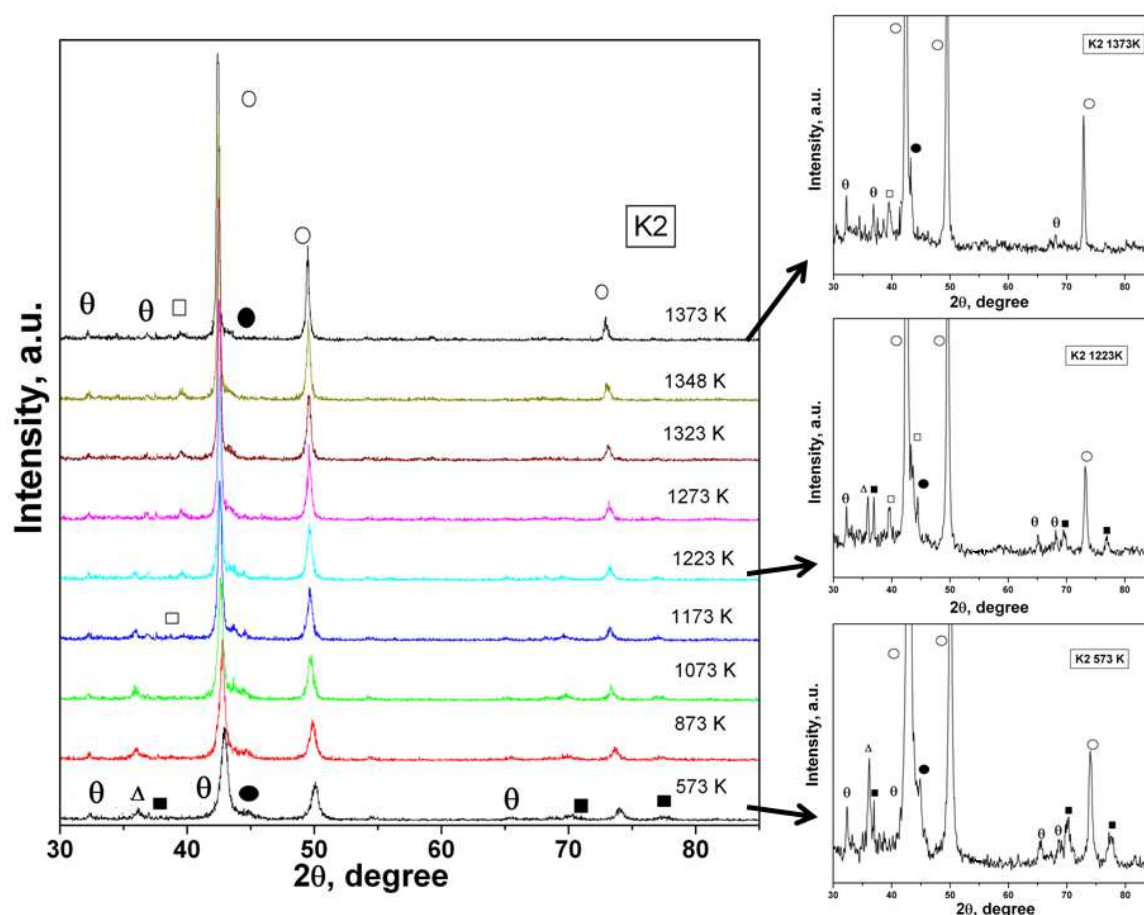


Fig. 4.9. High temperature XRD patterns of MWF alloy K2 (D9 SS- 8.5 %Zr). (○-fcc Fe based solid solution, □ - Fe_3Zr , θ - FeZr_2 , Δ - NiZr , ■- Ni_5Zr , ●- Ni_7Zr_2).

The formation of intermetallic compounds in the brighter phases was evident from SEM/EDS microstructural analysis. The local area composition of the bright phase revealed the Ni and Zr content to be around 20 wt.% and 44 wt.% respectively; therefore the atomic ratio of Ni and Zr was approximately 30 at.% and 70 at.%. In the Ni-Zr binary phase diagram [140] melting point of this composition is 1283 K and the major compounds formed are NiZr , NiZr_5

and Ni_2Zr_7 . As per Fe-Zr-Ni ternary phase diagram at 1173 K reported by Raghavan [141], for the present composition (Fe : Ni : Zr = 30 : 20 : 44) the NiZr phase would dissolve into FeZr_2 matrix. With further increase of temperature, NiZr and Ni_5Zr phases started to dissociate and Ni was diffusing towards the austenite matrix as it is a strong austenitic stabilizer. Hence, the peak intensity of D9 SS increased, and the excess Zr had combined with Fe and formed Fe_3Zr intermetallic compound. The melting point of Ni_7Zr_2 compound is above 1673 K and hence, it remained unchanged at 1373 K. According to the phase diagram of Fe-Zr by Okamoto [76] all the compounds of Fe-Zr system formed in the present study are close to the eutectic point of 1608 K.

Table 4.4. Phases present in the characterization of MWF alloy K2 by HTXRD (✓ Present, ↑ Intensity increasing, ↓ Intensity decreasing, → Appearing, --- Not present)

Phase	fcc Fe based	FeZr_2	Fe_3Zr	NiZr	Ni_7Zr_2	Ni_5Zr
Temperature	solid solution					
Room Temp.	✓	✓	---	✓	✓	✓
573 K	✓	✓	---	✓	✓	✓
873 K	✓	✓	---	✓	✓	✓
1073 K	✓	✓	--	✓	✓	✓
1173 K	✓	✓	→	↓	✓	↓
1223 K	↑	✓	↑	↓	✓	↓
1273 K	↑	✓	✓	---	✓	---
1323 K	↑	✓	✓	---	✓	---
1348 K	↑	✓	✓	---	✓	---
1373 K	↑	✓	✓	---	✓	---

4.3.3.2 MWF alloy K4

Figure 4.10 represents the high temperature XRD patterns of MWF alloy K4. The spectrum at 573 K showed the peaks corresponding to α -ferrite, fcc Fe based solid solution, FeZr_2 , Fe_3Zr , NiZr , Ni_5Zr and Ni_7Zr_2 intermetallics. These peaks were also observed at room temperature (as-cast) spectrum (Fig. 4.8). The details of the peaks observed are given in Table 4.5. Figure 4.10 and Table 4.5 showed that all the peaks were stable up to 1173 K. The peaks corresponding to NiZr , Ni_5Zr and α -ferrite started to decrease from 1223 K onwards, and at 1273 K they disappeared due to Ni diffusion from Ni-Zr intermetallic to Fe-solid solution phase. This observation of disappearance of α -ferrite peak is consistent with the literature data [126] on the transformation of bcc Fe to fcc Fe at 1173 K. Further, due to the lower melting point of NiZr and Ni_5Zr , these compounds disappeared within the austenite matrix and hence, an increase in the intensity of austenite peaks was observed.

Table 4.5. Phases present in the characterization of MWF alloy K4 by HTXRD (✓ Present, ↑ Intensity increasing, ↓ Intensity decreasing, --- Not present).

Phase	fcc Fe based	α -ferrite	FeZr_2	Fe_3Zr	NiZr	Ni_7Zr_2	Ni_5Zr
Temperature	solid solution						
Room Temp.	✓	✓	✓	✓	✓	✓	✓
573 K	✓	✓	✓	✓	✓	✓	✓
973 K	✓	✓	✓	✓	✓	✓	✓
1073 K	✓	✓	✓	✓	✓	✓	✓
1173 K	✓	✓	✓	✓	✓	✓	✓
1223 K	↑	↓	✓	✓	↓	✓	↓
1273 K	↑	---	✓	✓	---	✓	---
1298 K	↑	---	✓	✓	---	✓	---
1323 K	↑	---	✓	✓	---	✓	---

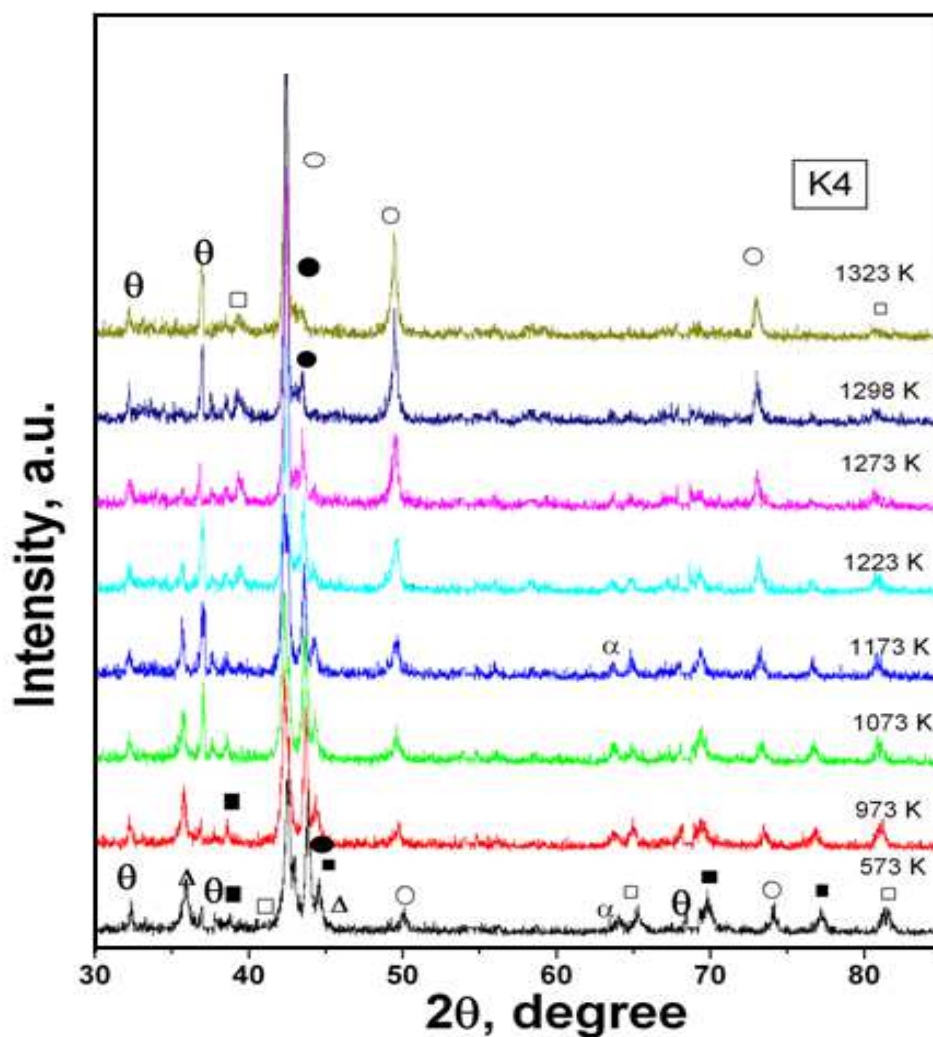


Fig. 4.10. High temperature XRD patterns of MWF alloy K4 (D9 SS- 17% Zr). (○-fcc Fe based solid solution, □ -Fe₃Zr, θ -FeZr₂, Δ-NiZr, ■-Ni₅Zr, ●- Ni₇Zr₂, α- α-ferrite

The present study revealed that owing to homogenization, the intermetallic phases present in MWF alloys agglomerated to form larger grains with the increase in sink size for actinide and fission products. The intermetallic phases were stable up to 1173 K which indicated the excellent stability of the intermetallic phases to resist the high temperature degradation at geological repository environment. Between 1173 K and 1323 K maximum diffusion of the

intermetallic phases was observed and the distribution of intermetallic phases in the solid solution matrix was uniform which is beneficial for hosting the actinide and fission product elements in MWF alloy matrix.

4.4 Conclusions

The following conclusions can be drawn from the study undertaken to evaluate the detailed metallurgical behaviour of MWF alloys with respect to their microstructure and phase stability in different conditions.

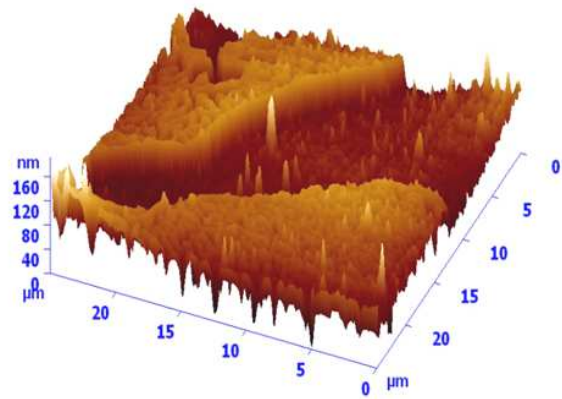
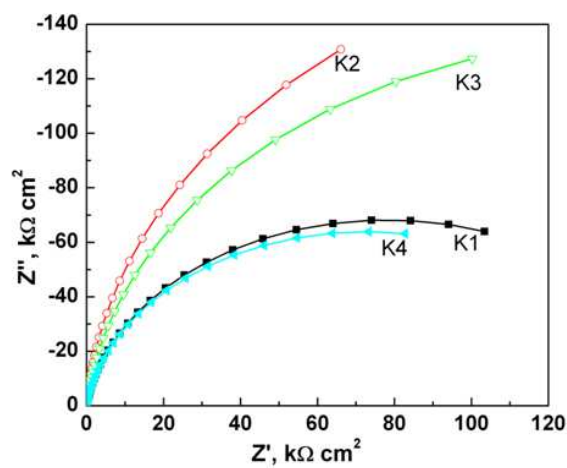
1. The microstructure of different MWF alloys showed the formation of Fe based solid solution matrix and Zr rich intermetallic precipitate phase. The affinity of Ni towards intermetallic phases was more compared to the solid solution phase.
2. Hardness value of the MWF alloys increases with increased in Zr concentration due to the formation of intermetallic precipitation.
3. Homogenization of the MWF alloys at 1323 K leads to agglomeration of Zr rich intermetallic phase due to high temperature diffusion resulting the increase in the grain size of intermetallic precipitate which is beneficial for hosting actinide and fission products.
4. XRD studies revealed that the intensities of intermetallic compounds increased due to heat treatment. The α -ferrite peak observed in the as-cast MWF alloy K4 (D9 SS-17 wt.% Zr) disappeared after heat treatment due to diffusion of Ni into the matrix phase.
5. High temperature XRD studies indicated that most of the Ni-Zr intermetallic phases were stable up to 1173 K and the Ni_7Zr_2 phase was stable till 1373 K.

6. The Fe-Zr phases were stable up to 1373 K and Fe_3Zr was formed at about 1173 K in alloy K2 (D9 SS- 8.5 wt.% Zr), which was not observed at lower temperatures unlike for alloy K4.

The MWF alloys formed Zr intermetallic phases which act as sink for fission product and actinide elements. After homogenization at 1323 K, agglomeration of the intermetallic phases took place, providing better stability. All the intermetallic phases were stable until 1173 K, which is far above the temperature which can be experienced by the waste form during the long term disposal period. Based on the high temperature stability and microstructural data on MWF alloys formed in the present work, these alloys can be considered for accommodating actinide and fission product elements for their disposal at geological repositories.

CHAPTER 5

CORROSION BEHAVIOUR AND PASSIVE FILM ANALYSIS OF DIFFERENT D9 SS-Zr MWF ALLOYS



CHAPTER 5

CORROSION BEHAVIOUR AND PASSIVE FILM ANALYSIS OF DIFFERENT D9 SS-Zr MWF ALLOYS

Corrosion behaviour and passive film stability of metal waste form (MWF) alloys were investigated in de-mineralized (DM) water at pH 1, 5 and 8, simulated Kalpakkam ground water (KGW) and Rajasthan ground water (RGW). The MWF alloys exhibited nobler corrosion potential with low passive current density and wide range of passivation potential in DM water at pH 5 and 8, simulated KGW and RGW indicating appreciable corrosion resistance. The existence of stable passive film was validated by using electrochemical impedance spectroscopy (EIS). In DM water at pH 1 MWF alloys revealed active corrosion potential with higher passive current density indicating dissolution due to corrosion. However, the EIS studies in this medium showed good stability of passive film at the metal - solution interface. The surface morphological analysis by optical microscopy and SEM/EDS showed insignificant surface dissolution after polarization in DM water at pH 5, 8 and RGW. However, after polarization in DM water at pH 1, significant dissolution of passive film was observed, whereas, selective salt deposition was observed after polarization in KGW medium. Passive film analysis by XPS showed Zr rich oxide layer formation below the chromium oxide film. AFM topography of the passivated MWF surfaces revealed the formation of passive film in simulated ground water media which was thicker in KGW due to higher mineral concentration.

5.1 Introduction

The concept of safe disposal of MWF alloy in geological repository is a means of protecting human beings and the environment from radiation for prolong duration [15].

Corrosion is inevitable when water based liquid is in contact with metal. The actinide elements uranium and plutonium present in the MWF alloy will remain radioactive for more than ten thousand years [124]. Aqueous corrosion of MWF alloy is one of the important concerns for isolating the radionuclides from biosphere as it leads to selective radionuclide leaching [3,142]. The geological repository will be a source of water, oxygen and some aggressive minerals [3]. Hence chemical stress may develop due to high temperature, radiation, dissolved oxygen and aggressive minerals present in the ground water. The chemical stress in the ground water environment can cause oxidation of the materials as well as corrosion including uniform corrosion, localized corrosion, galvanic corrosion, intergranular corrosion and stress-corrosion cracking [3]. Therefore, it is necessary to have a good understanding of the corrosion behaviour and passive film stability of the MWF alloys in the ground water medium which will help to predict the performance of the MWF alloy in the repository environment.

The aim and objectives of this chapter are to investigate in detail, the corrosion and passive film behaviour of the MWF alloys in different simulated geological repository environment. This was accomplished by two approaches: (i) the electrochemical investigation of corrosion behaviour and (2) passive film analysis of MWF alloys exhibited in the simulated repository environment after passive film formation and polarization.

5.2 Experimental

In this Chapter the different electrochemical corrosion tests including open circuit potential (OCP), potentiodynamic polarization and electrochemical impedance spectroscopy (EIS) and surface characterization using optical microscope, SEM/EDS, XPS and AFM are dealt with. As the details about the experimental techniques and media are described in Chapter 3, a brief overview of the experimental are listed below:

- (i) Electrochemical corrosion testing including OCP, potentiodynamic polarization and EIS were carried out for all the MWF alloys (K1, K2, K3, K3B & K4) in DM water at pH 1, 5 and 8. The pH of the solution was adjusted by the addition of HCl and NH_4OH in DM water.
- (ii) Electrochemical corrosion behaviour of MWF alloys K1, K2, K3 and K4 was evaluated in simulated KGW medium. The electrochemical corrosion behaviour of the MWF alloy K2 was studied in two different RGW media.
- (iii) Surface morphological changes in the MWF alloys after polarization in different simulated media were investigated using optical microscope and SEM/EDS.
- (iv) The passive film composition of MWF alloy passivated in DM water was analyzed by XPS.
- (v) Passive film topography of MWF alloy (K2) was investigated using AFM after passivation and polarization in different simulated media.

5.3 Results and discussion

5.3.1 *Electrochemical corrosion study in simulated DM water at pH 1, 5 and 8*

The corrosion behaviour of MWF alloys was investigated using different electrochemical techniques in DM water at pH 1, 5 and 8 to simulate the probable environmental condition of geological repository. Assuming the repository to be alkaline in nature pH 8 was selected; pH 5 to simulate its acidic nature and pH 1 was chosen to represent the most aggressive and highly acidic conditions. This study was undertaken as a preliminary step to understand the corrosion behaviour of MWF alloys in simulated geological environment. DM water was chosen as the standard medium as it simulates the aggressive condition due to lack of minerals in its composition [93].

5.3.1.1 OCP monitoring

The OCP versus time plots for different MWF alloys in DM water at pH 1, 5 and 8 are shown in Figures 5.1, 5.2 and 5.3 respectively. In DM water at pH 1 (Fig.5.1), the OCP values for all the MWF alloys appeared in active region compared to the other two media. The OCP values in DM water at pH 1 were approximately in the range -150 to 200 mV(Ag/AgCl) and drifted towards active direction with increasing time. However, in both the media of DM water at pH 5 (Fig.5.2) and 8 (Fig.5.3) the OCP appeared in the range 0 to -100 mV(Ag/AgCl). A steady state OCP was observed in DM water at pH 5 for most of the MWF alloys but in DM water at pH 8 the OCP of the MWF alloys were shifting towards nobler direction with increasing time. No systematic trend could be observed for MWF alloys with variation of Zr concentration in DM water at pH 1 and 5. But in DM water at pH 8 a shift of OCP towards active direction was observed with increasing Zr concentration. Among the entire MWF alloys, alloy K3 (D9SS-12.2 wt.% Zr) exhibited better OCP in all the simulated media.

As shown in Figures 5.1 to 5.3, the variations of OCP values depend not only on the concentration of Zr but also on the pH of the media. The shift in OCP towards more noble values is related to faster growth of passive film and this depends on the nature of passive oxide layer formed on the surface [139, 143]. In DM water at pH 1, the OCP appeared at active region when compared to the other two and was drifting towards more active direction with increasing time. This is attributed to constant dissolution of metal due to higher concentration of HCl which enriched the medium with H^+ and Cl^- species and lowered the passive oxide film stability [139]. The DM water at pH 5 and 8 are nearly neutral media and hence, facilitate to form stable passive oxide film and thus shifting the OCP to nobler region. Moreover, at pH 8, there might be an intense growth of surface scaling with increasing time due to alkaline nature of the medium

which was responsible for OCP shift towards nobler direction; whereas at pH 5, intense growth of surface scaling was not favoured and remained at steady state due to acidic nature. From all the OCP results it was inferred that in acidic media the MWF alloys with 8 to 12 wt.% Zr exhibited better performance compared to the MWF alloys with lower concentration of Zr (4.4 wt.%) and higher concentration of Zr (more than 14 wt.%). Abraham and Deitz [78] have reported that Zr has a tendency to form Zr rich oxide layer below the chromium oxide film slowly which is stable and well adherent in the most aggressive media also. This is consistent with the observation in the present study that the combined effect of zirconium oxide and chromium oxide influenced the MWF alloys (K2 & K3) in exhibiting nobler OCP in the most aggressive media. However, in alkaline media chromium oxide passive film remained stable due to the absence of H^+ and Cl^- ions and showed nobler OCP with lower Zr alloy [139].

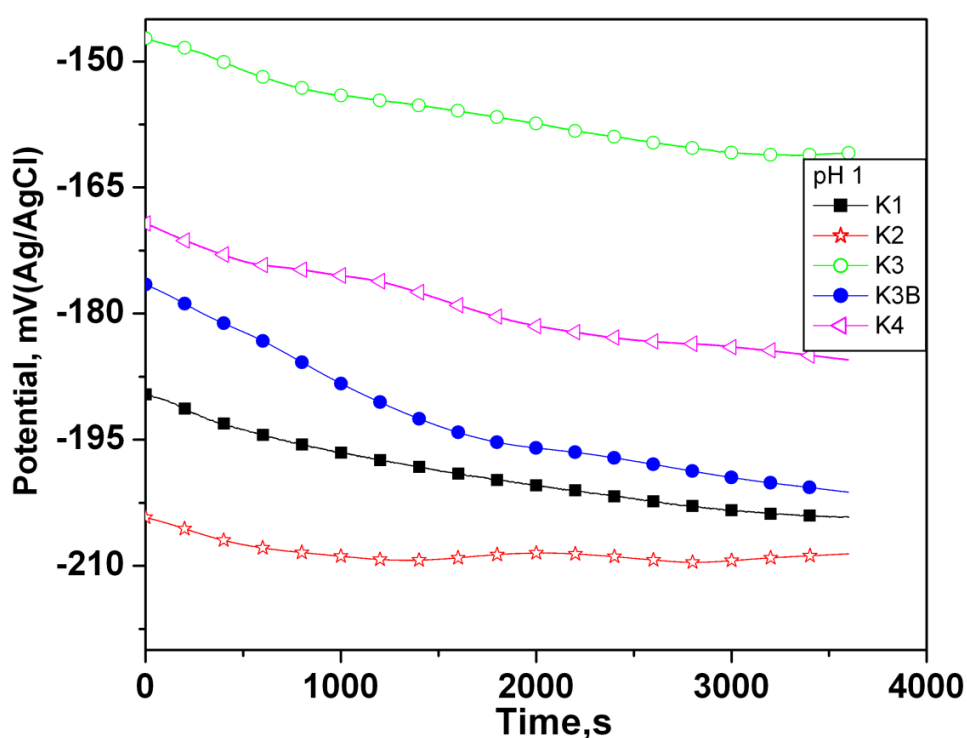


Fig. 5.1. Variation of OCP with time for different MWF alloys in DM water at pH 1

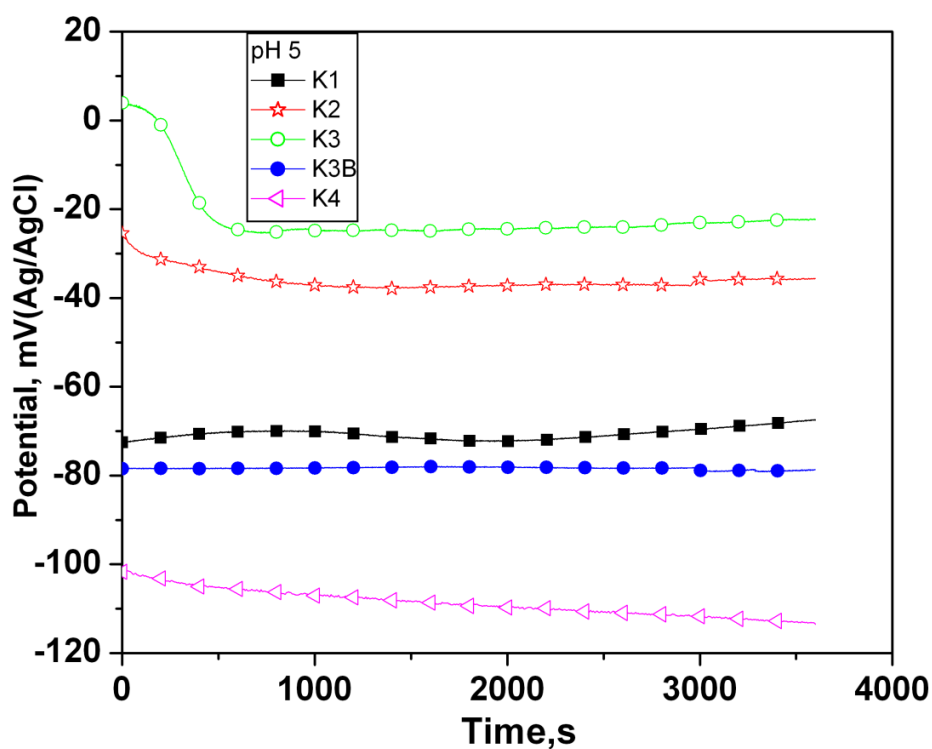


Fig. 5.2. Variation of OCP with time for different MWF alloys in DM water at pH 5

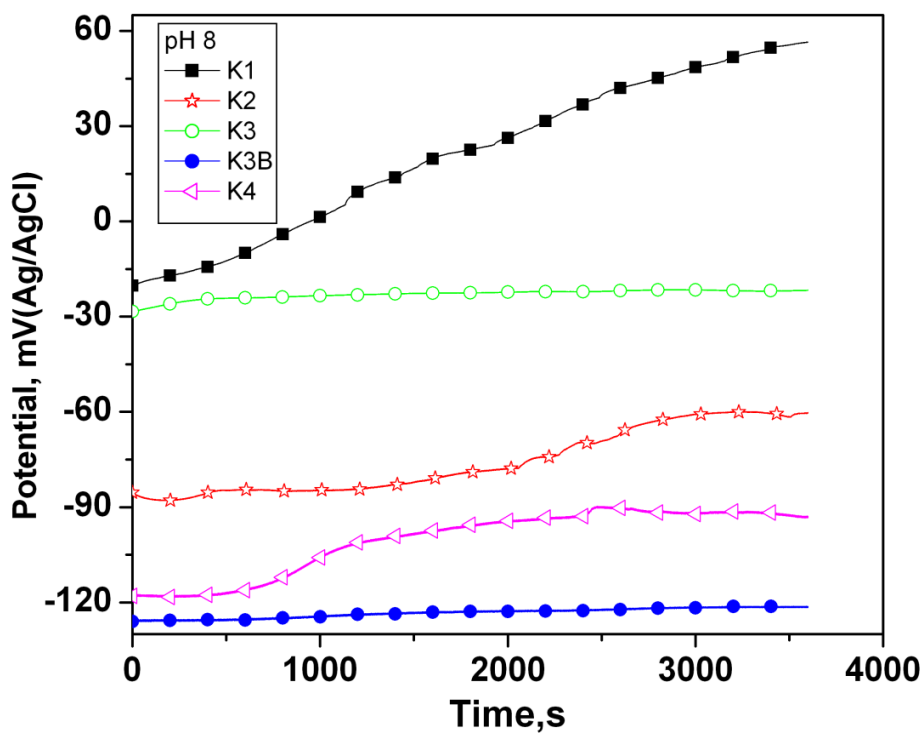


Fig. 5.3. Variation of OCP with time for different MWF alloys in DM water at pH 8

5.3.1.2 Potentiodynamic polarization study

The potentiodynamic polarization plots of different MWF alloys in DM water at pH 1, 5 and 8 are shown in Figures 5.4, 5.5 and 5.6 respectively. The values of corresponding polarization parameters (corrosion potential (E_{corr}), passive current density (i_{pass}) and breakdown potential (E_{BP})) in these media are given in Tables 5.1, 5.2 and 5.3 respectively. The MWF alloys exhibited the most active E_{corr} , lowest E_{BP} and highest i_{pass} in DM water at pH 1. The E_{BP} was below 400 mV(Ag/AgCl) for all the MWF alloys except alloy K2 which exhibited the E_{BP} value higher than 500 mV(Ag/AgCl). The passive current density was in range of 1-5 $\mu\text{A cm}^{-2}$. The polarization results showed that the E_{corr} and E_{BP} values at pH 5 and 8 were in comparable range. The E_{corr} values were in the range 50 to -150 mV(Ag/AgCl) and the E_{BP} values were in the range 1000 to 1400 mV(Ag/AgCl) for the MWF alloys. The i_{pass} values in DM water at pH 5 were marginally higher than the i_{pass} values obtained in DM water at pH 8. The i_{pass} values in DM water at pH 5 were in between 0.1 - 0.2 $\mu\text{A cm}^{-2}$ and in DM water at pH 8 were in between 0.01-0.1 $\mu\text{A cm}^{-2}$. In all the simulated media under consideration the MWF alloy K1 with minimum Zr concentration showed nobler E_{corr} value than the other alloys, but it exhibited higher i_{pass} and lower E_{BP} . Figures 5. 4 and 5. 5 showed existence of an additional noise in the passive region for most of the MWF alloys in DM water at pH 1 and 5.

Table 5.1. Polarization parameters for different MWF alloys in DM water at pH 1

Alloys	E_{corr}	i_{pass}	E_{BP}
	mV(Ag/AgCl)	$\mu\text{A cm}^{-2}$	mV(Ag/AgCl)
K1	-82	4.02	371
K2	-210	1.88	532
K3	-204	4.27	379
K3B	-228	3.79	373
K4	-222	5.36	360

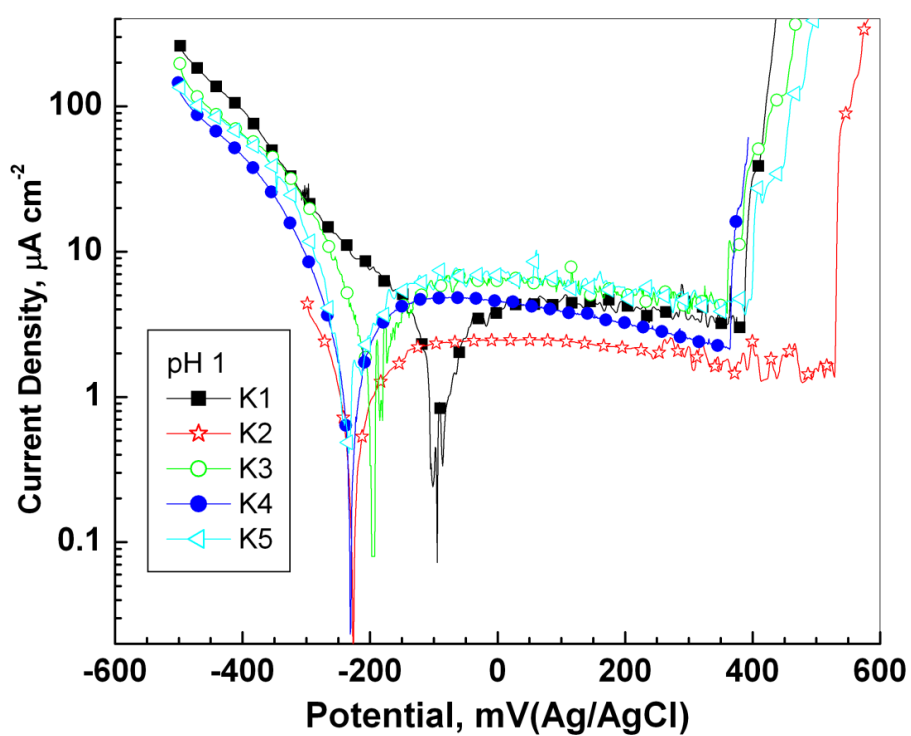


Fig. 5.4. Potentiodynamic polarization plot of different MWF alloys in DM water at pH 1

Table 5.2. Polarization parameters for different MWF alloys in DM water at pH 5

Alloys	E_{corr}	i_{pass}	E_{BP}
	mV(Ag/AgCl)	$\mu\text{A cm}^{-2}$	mV(Ag/AgCl)
K1	-63	0.12	1062
K2	-81	0.10	1167
K3	-63	0.16	1110
K3B	-94	0.12	999
K4	-199	0.20	1148

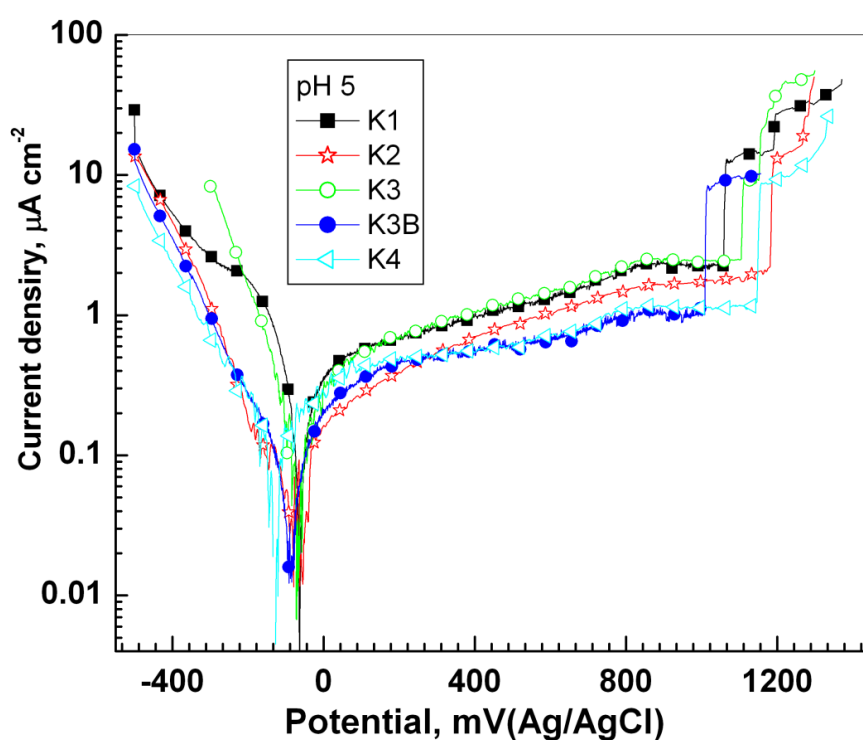


Fig. 5.5. Potentiodynamic polarization plot of different MWF alloys in DM water at pH 5

Table 5.3. Polarization parameters for different MWF alloys in DM water at pH 8

Alloys	E_{corr}	i_{pass}	E_{BP}
	mV(Ag/AgCl)	$\mu\text{A cm}^{-2}$	mV(Ag/AgCl)
K1	43	0.07	1232
K2	-56	0.06	1197
K3	-27	0.12	1281
K3B	-70	0.06	1055
K4	-126	0.14	1240

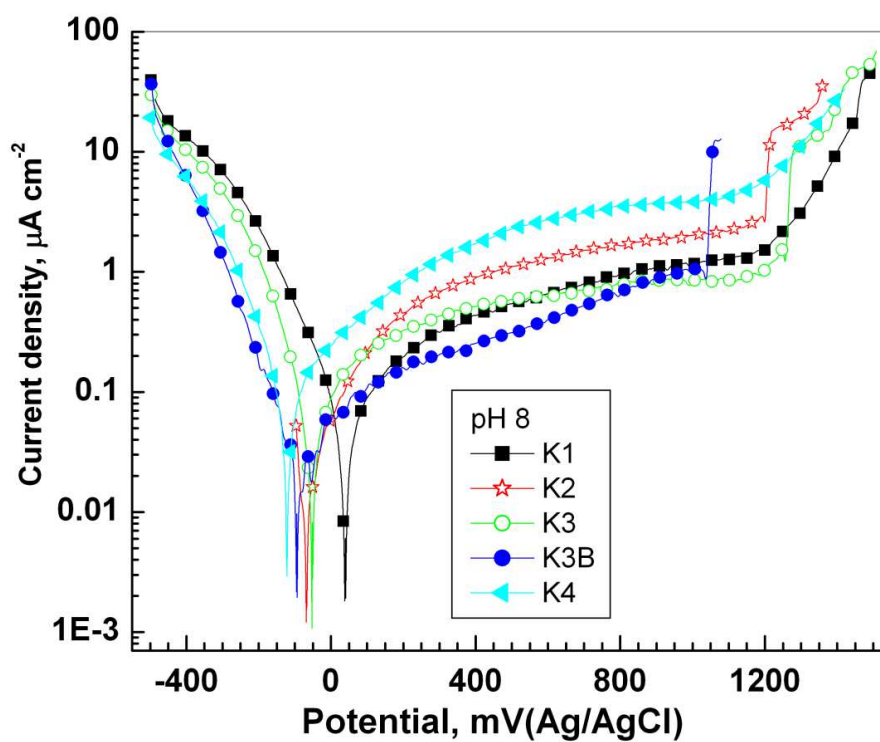


Fig. 5.6. Potentiodynamic polarization plot of different MWF alloys in DM water at pH 8

Potentiodynamic anodic polarization behaviour of MWF alloys in DM water at pH 1 showed active corrosion potential with lower breakdown potentials (E_{BP}). Lower breakdown is attributed due to higher concentration of H^+ and Cl^- ion in the media, which could encourage pitting attack on the specimen surface with increase in current density; this can be referred as pitting potential (E_p) [139,143]. In DM water at pH 5 and 8, mild acidic and mild alkaline conditions prevailed and the transpassive dissolution started after their corresponding E_{BP} of the individual alloy. Owing to the presence of very low concentration of Zr in MWF alloy K1, the chances of forming chromium oxide was more in all environments, thereby protecting the surface against uniform corrosion, and hence nobler E_{corr} value was observed. However, in higher potential and aggressive condition, zirconium oxide formed below the chromium oxide film slowly could play an important role [78]. The MWF alloys K2 and K3 exhibited lower i_{pass} and higher E_{BP} values due to the combined effect of ZrO_2 and Cr_2O_3 . Formation of intermetallic precipitation cloud was observed in the microstructure of MWF alloy with 14 wt.% Zr (K3B) (Fig. 4.1) which was heterogeneous in nature and retarded the formation of stable passive film on the surface and exhibited lower E_{BP} . The microstructure of MWF alloy K4 with 17 wt.% Zr (Fig.4.1) showed the segregation of the intermetallic precipitate and the matrix phase was separated from the precipitation phase. This could have a combined beneficial effect on the formation of chromium oxide and zirconium oxide passive film and showed higher E_{BP} . All the MWF alloys in pH 5 and 8 showed wide range of passivation potential (~ 1.4 V). For comparison, pure Cr exhibited a wide passive range in chloride free solution which is around 1.5 V [144].

The reason for noise in the passive range in DM water at pH 1 and 5 was due to the presence of Cl^- ions in the solution. The Cl^- ions are responsible for the formation of soluble chloride complex within the hydrated passive film and removal of metal ions from the metallic

surface. The vacant site created by the removal of metal ion was filled again by the newly produced passive film [145]. Owing to this phenomenon of breaking and self healing of passive film, the typical noise pattern was observed in the passive region.

5.3.1.3 Electrochemical impedance spectroscopy

The Nyquist plots for all MWF alloys at pH 1, 5 and 8 under OCP conditions are shown in Figures 5.7, 5.8 and 5.9 respectively. The electrochemical impedance data were analyzed by fitting to a model with one time constant corresponding to equivalent circuit shown in Figure 3.10a. The fitting parameters of the impedance spectra in DM water at pH 1, 5 and 8 are given in Tables 5.4, 5.5 and 5.6 respectively. The EIS results obtained in DM water at pH 1 and 5 did not show any systematic trend in R_p values for MWF alloys with the variation of Zr concentration. In DM water at pH 1, MWF alloys K2 and K3 showed maximum polarization resistance followed by K1 and the MWF alloys K3B and K4 with higher Zr content showed low R_p values with higher capacitance. The R_p values obtained in DM water at pH 5 were comparatively higher than the R_p values obtained in DM water at pH 1. The trend shown in the R_p values in DM water at pH 5 was nearly the same with the results in DM water at pH 1. In DM water at pH 5 the MWF alloy K2 with 8.5 wt.% Zr showed the highest R_p and the lowest capacitance followed by K1, K3, K4 and K3B. The EIS results for MWF alloys in DM water at pH 8 exhibited a systematic trend in R_p values with the variation of Zr concentration. The decrease of R_p value with increase in capacitance was observed when Zr concentration was increased. In addition, the R_p values obtained for all the MWF alloys in DM water at pH 8 were very high as could be seen from Table 5.6.

Table 5.4. EIS fitted values of different MWF alloys in DM water at pH 1

Alloy	R_s	R_p	CPE1-T	CPE1-P
	($\Omega \text{ cm}^2$)	($\text{k}\Omega \text{ cm}^2$)	($\text{F cm}^{-2}\text{S}^n$)	
K1	2.15	66.72	9.69×10^{-5}	0.879
K2	2.15	89.95	8.65×10^{-5}	0.859
K3	2.15	91.99	8.65×10^{-5}	0.849
K3B	2.15	31.28	1.20×10^{-4}	0.841
K4	2.15	34.78	1.00×10^{-4}	0.889

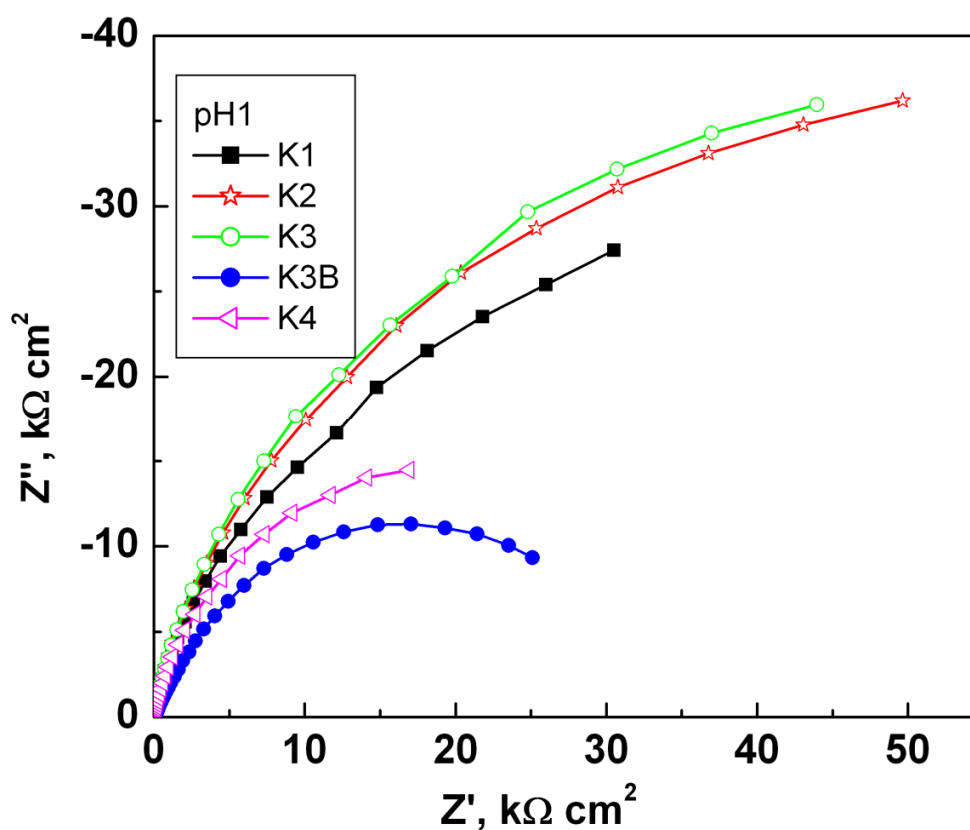


Fig. 5.7. Electrochemical impedance spectra of MWF alloys in DM water at pH 1

Table 5. 5. EIS fitted values of different MWF alloys in DM water at pH 5

Alloy	R_s	R_p	CPE1-T	CPE1-P
	$(\Omega \text{ cm}^2)$	$(\text{k}\Omega \text{ cm}^2)$	$(\text{F cm}^{-2}\text{S}^n)$	
K1	126.1	100.29	4.96×10^{-5}	0.959
K2	126.1	149.95	4.40×10^{-5}	0.958
K3	126.1	82.08	5.20×10^{-5}	0.892
K3B	126.1	56.14	6.12×10^{-5}	0.855
K4	126.1	76.35	5.45×10^{-5}	0.945

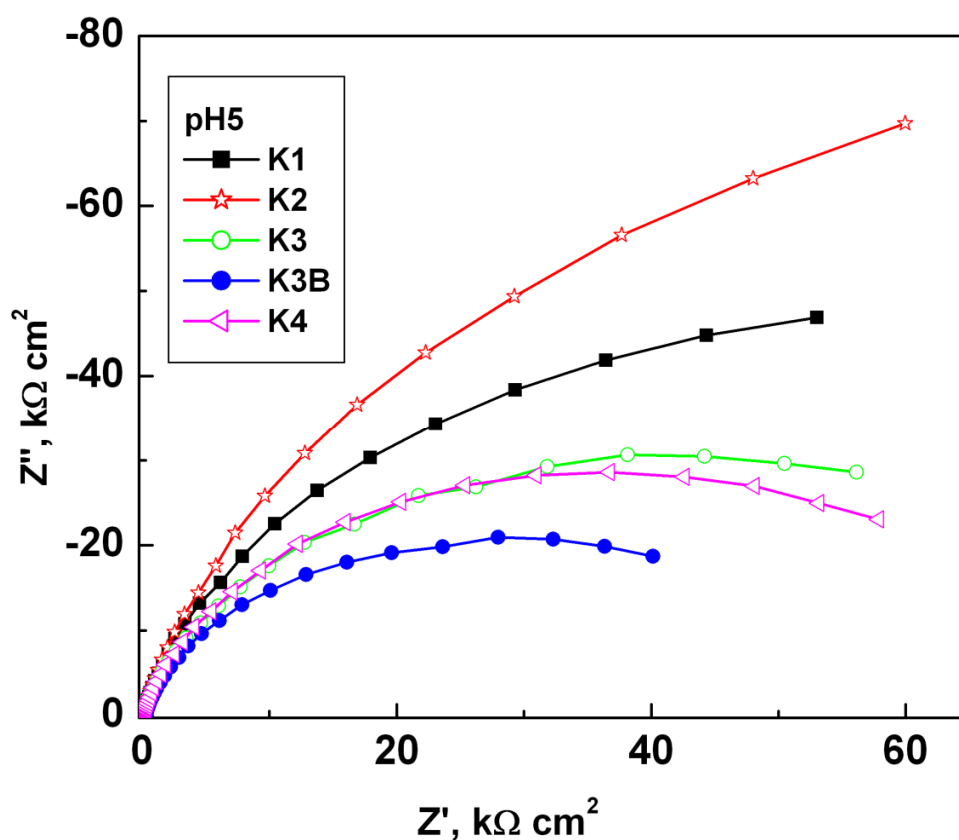


Fig. 5.8. Electrochemical impedance spectra of MWF alloys in DM water at pH 5

Table 5.6. EIS fitted values of different MWF alloys in DM water at pH 8

Alloy	R_s	R_p	CPE1-T	CPE1-P
	$(\Omega \text{ cm}^2)$	$(\text{k}\Omega \text{ cm}^2)$	$(\text{F cm}^{-2}\text{S}^n)$	
K1	675.8	1141.90	5.20×10^{-5}	0.985
K2	675.8	600.19	2.05×10^{-5}	0.985
K3	675.8	400.19	3.55×10^{-5}	0.925
K3B	675.8	375.23	3.78×10^{-5}	0.902
K4	675.8	130.00	3.99×10^{-5}	0.895

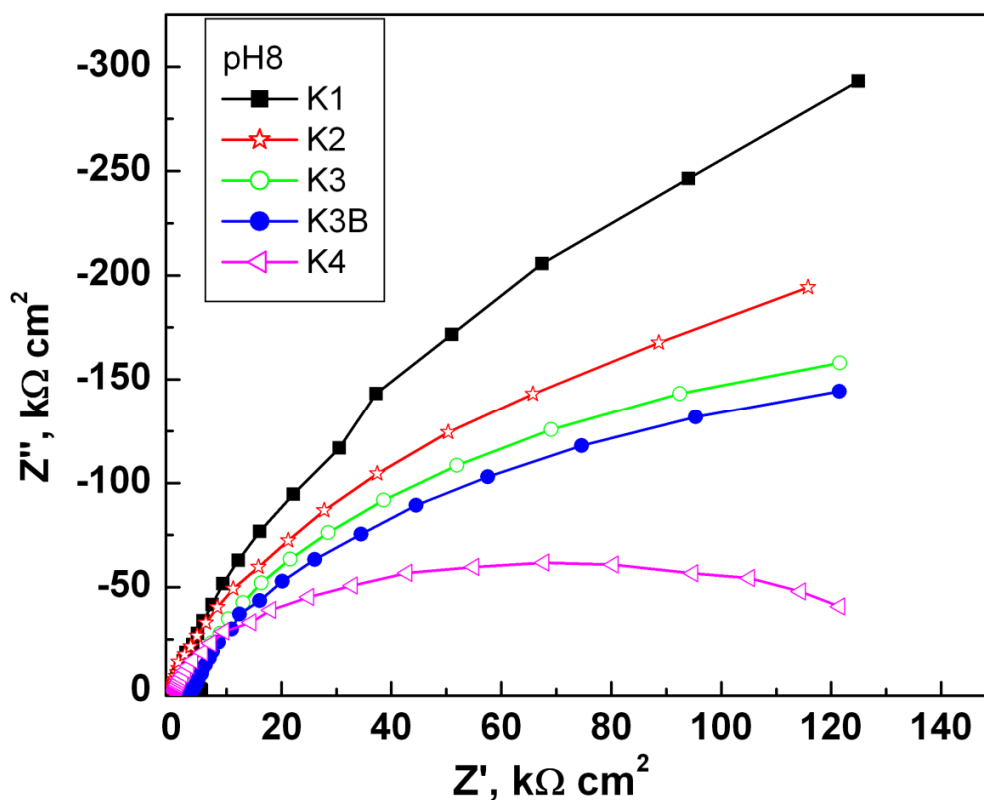


Fig. 5.9. Electrochemical impedance spectra of MWF alloys in DM water at pH 8

At pH 1, the MWF alloys exhibited lower range of R_p values when compared to those at pH 5 and 8 (Tables 5. 4, 5.5 and 5.6). Lower R_p value is indicative of film dissolution due to increasing interfacial charges by pore formation or breakdown in the hydrated passive film. Lower R_p values at pH 1 would also indicate the accelerating oxidation of metal surface due to the formation of soluble chloride bridge inside the hydrated passive film which reduces the stability of the passive film [145]. Higher R_p values shown by the MWF alloys at pH 5 and 8 imply higher passive film stability as well as higher corrosion resistance [146]. The measured capacitive response are generally not ideal (i.e., pure capacitance) in real electrochemical processes and hence the CPE was used in the circuit (Fig. 3.10) in order to account for the non ideal capacitance of the passive film formed. Z_{CPE} is a measure of capacitance of the interface to store charge corresponding to the space charge region developed in the oxide near the film/electrolyte interface. As shown in Tables 5.4, 5.5 and 5.6, capacitance values were high for the different MWF alloys measured at pH 1. Lower capacitance observed for the MWF alloys at pH 5 and 8 revealed higher stability of the passive film due to more protective nature of the passive film. The trend displayed in the Nyquist plots of different MWF alloys in DM water at pH 1 and pH 5 probably due to the role of H^+ and Cl^- ions was similar to that observed during OCP and polarization study. In the DM water at pH 1 and 5, H^+ and Cl^- ions are present in different concentrations which reduced the stability of hydrated passive film [139, 145]. At pH 1 and 5, R_p values increased with increasing Zr concentration up to K3 (D9SS-12 wt.% Zr). With further increase of Zr concentration, in K3B (D9SS-14.1 wt.% Zr) and K4 (D9SS-16.8 wt.% Zr) alloys the R_p values decreased. These results indicated that optimum values of Zr content in the range 8-12 wt.% would impart high corrosion resistance to the MWF alloys. Beyond this range, due to excessive intermetallic precipitation, the passive film stability decreases and hence, leads

to lower corrosion resistance. In pH 8, K1 and K2 alloys showed higher R_p values compared to K3, K3B and K4 alloys. In such a mild alkaline medium like pH 8, all the MWF alloys exhibit higher film stability as well as corrosion resistance and the less intermetallic precipitation in the alloys with low Zr content would provide nearly homogeneous microstructure, thereby showing highest corrosion resistance. Nevertheless, in acidic medium with pH 1 and in near neutral medium with pH 5, the combined effect of ZrO_2 and Cr_2O_3 played a major role in protecting the passive film.

5.3.2 Electrochemical corrosion study in simulated KGW and RGW media

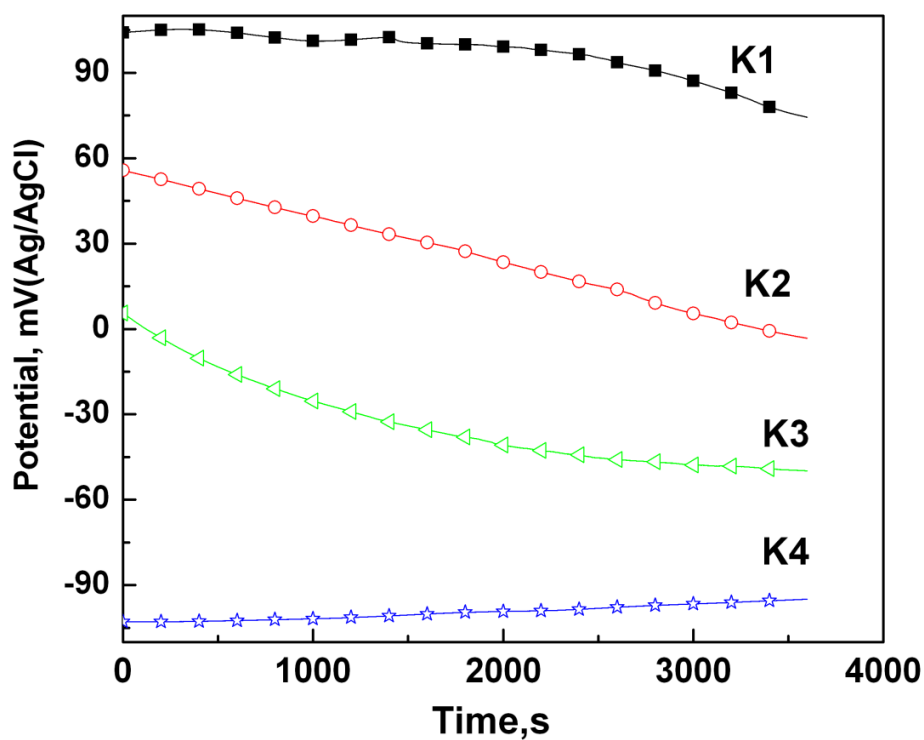
Two probable repository media considered for this study were the Kalpakkam ground water (KGW) at Kalpakkam, Tamilnadu [94] and Rajasthan ground water (RGW) near Thar desert, Jaipur, Rajasthan [95]. Simulated solution these media were prepared in laboratory and used in the present study. An attempted was made to assess the corrosion behaviour and stability of passive film of MWF alloys in simulated repository environment. The evaluation was done in two parts. In the first part four MWF alloys of 5 to 17 wt.% Zr (K1, K2, K3 and K4) were used to predict the role of Zr concentration on the corrosion behaviour in simulated KGW medium and to select a better alloy composition. In the second part this selected alloy was used to determine its corrosion behaviour in two simulated RGW environment for understanding the role of repository environment.

5.3.2.1 OCP for different MWF alloys in KGW

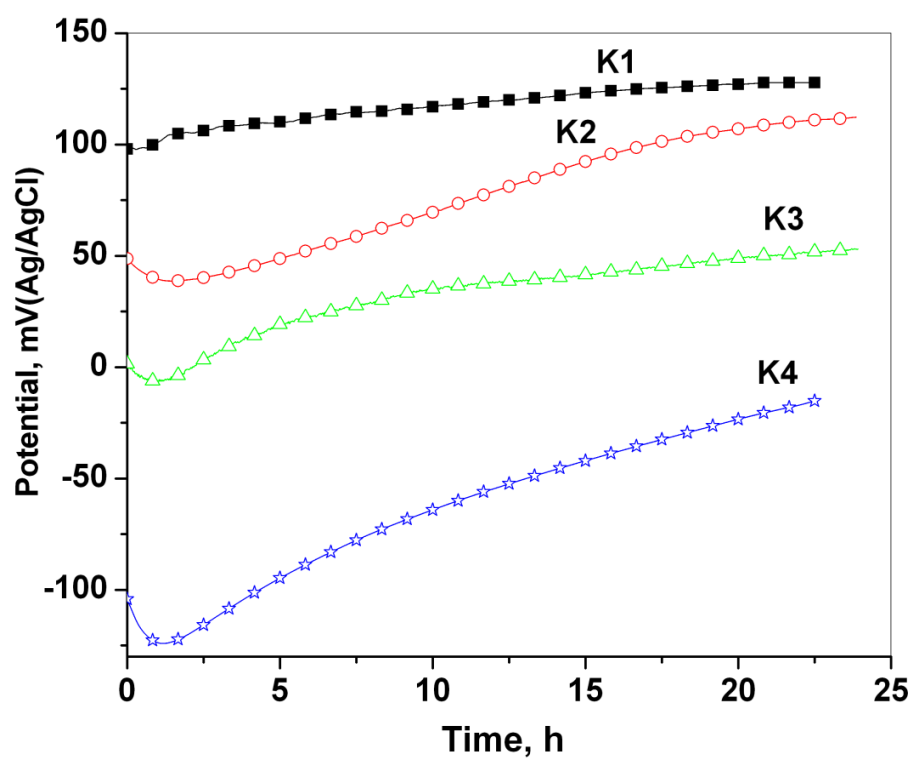
The open circuit potential (OCP) versus time plots of MWF alloys measured in KGW medium for 1 h and 24 h are shown in Figures 5.10a and 5.10b respectively. A systematic trend of OCP shift was observed with the variation of Zr concentration. With increase in Zr concentration the MWF alloys showed OCP shift towards active region. Figure 5.10a shows that

OCP shifts towards active direction with increasing time. However, during long time OCP monitoring an active shift of OCP was observed for 1 to 2 h (Fig. 5.10b) which then gradually shifted towards nobler direction with time in all the MWF alloys. MWF alloys with higher concentration of Zr showed more active shift of OCP initially and then faster shift towards nobler direction.

The shift of OCP towards active region with increase in Zr concentration could be explained with the help of microstructure shown in Figure 4.1. The microstructure of MWF alloys (Fig. 4.1) showed two phases; the dark Fe based solid solution phase and bright Zr rich intermetallic phase. The Zr rich intermetallic phase was typically Fe-Zr and Ni-Zr type Laves compounds which act as host phase for actinide and fission products [72, 78]. In the MWF alloy K1, the intensities of Zr intermetallic phases were less and the chromium oxide film formed easily in all environments exhibited nobler OCP. However, with increasing Zr concentration the intensity of the Zr intermetallic phases increased and the probability for the formation of chromium oxide film was less and initially active OCP was observed [139]. The cations present in the ground water media would have formed stable hydrated passive film slowly on the metallic surface and aided in attaining nobler OCP [145]. As observed in Figure 5.10b, the MWF alloy K4 showed maximum shift of OCP towards nobler direction which could be due to the influence of zirconium oxide formed slowly beneath the chromium oxide film and giving better protection of metallic surface from corrosion dissolution [78].



(a)



(b)

Fig. 5.10. OCP versus time plot for different MWF alloys in KGW (a) for 1 h and (b) for 24 h.

5.3.2.2 Potentiodynamic polarization study on different MWF alloys in KGW

The potentiodynamic polarization behaviour of different MWF alloys in KGW medium is shown in Figure 5.11 and corresponding polarization parameters such as corrosion potential (E_{corr}), passive current density (i_{pass}) and breakdown potential (E_{BP}) are given in Table 5.7. A systematic trend of corrosion potential (E_{corr}) value was observed with increase in Zr content. The MWF alloy K1 with minimum Zr content exhibited nobler E_{corr} value followed by K2 and K3. The MWF alloy K4 with maximum Zr content exhibited the most active E_{corr} . However, the breakdown potential (E_{BP}) was the lowest for the alloy K1, while the alloys K2, K3 and K4 showed higher E_{BP} values. Similarly, the i_{pass} values were found to be increasing with increase in Zr concentration.

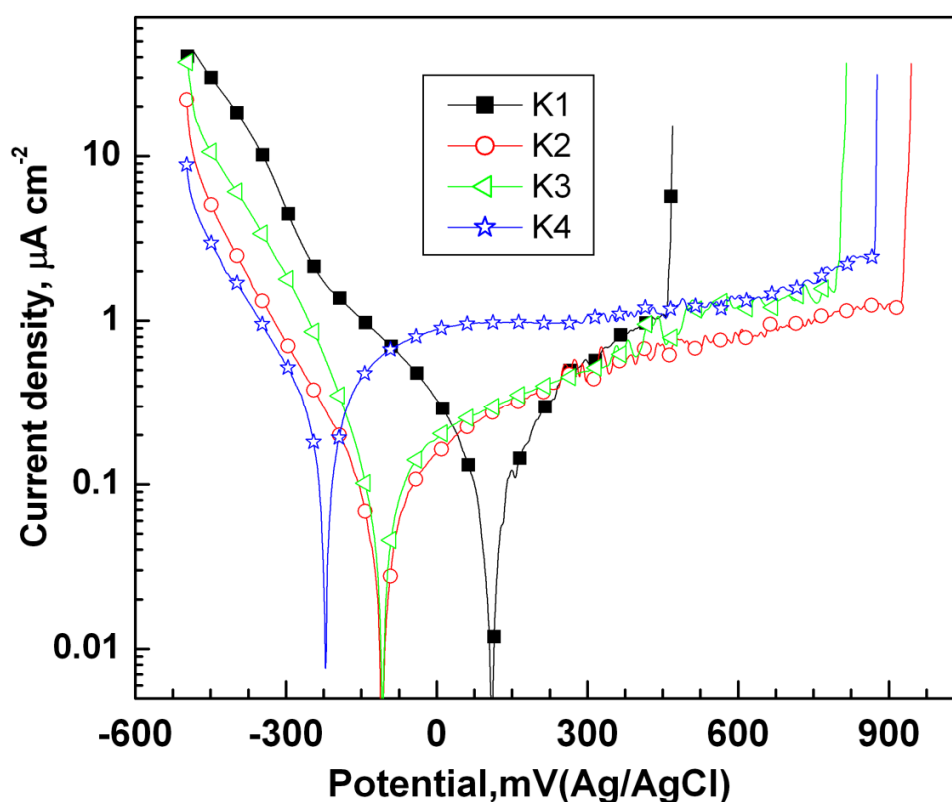


Fig. 5.11. Potentiodynamic polarization plots for different MWF alloys in KGW

Table 5.7. Polarization parameters for different MWF alloys in KGW

MWF	E_{corr}	i_{pass}	E_{BP}
alloys	mV(Ag/AgCl)	$\mu\text{A cm}^{-2}$	mV(Ag/AgCl)
K1	109	0.256	460
K2	-110	0.130	914
K3	-108	0.157	817
K4	-220	0.557	871

The potentiodynamic polarization results validated the trends for corrosion potential (E_{corr}) and passive current density (i_{pass}) due to the microstructural properties as observed during OCP monitoring. The zirconium oxide formed below the chromium oxide and iron oxide films played an important role in increasing the breakdown potential (E_{BP}) with increasing Zr concentration [78]. This zirconium oxide layer formed on the intermetallic surface was thin and adherent. The oxide film formed during the zirconium oxidation is known to be protective [147] as it resists the diffusion of oxygen. According to Abraham and Deitz [78] these oxides are amorphous in nature and hence, enhance the corrosion resistance in two ways: (i) it is more resistant to breakdown than the crystalline oxide [148,149] and (ii) the mobility of ions will be lower in amorphous oxides than in crystalline structures containing defects and grain boundaries [149].

5.3.2.3 Electrochemical impedance spectroscopy on MWF alloys in KGW

The Nyquist plot of impedance spectra for all of the MWF alloys in KGW media (Fig. 5.12) showed unfinished semicircle arc radius. The results obtained from EIS measurements are

interpreted with the help of equivalent circuit as shown in Figure 3.10a and the experimentally fitted impedance values are given in Table 5.8. The results revealed that the MWF alloy K2 shows the highest polarization resistance (R_p) and lowest capacitance value followed by alloy K3. The MWF alloys K1 and K4 showed comparatively lower R_p and higher capacitance value than the alloys K2 and K3.

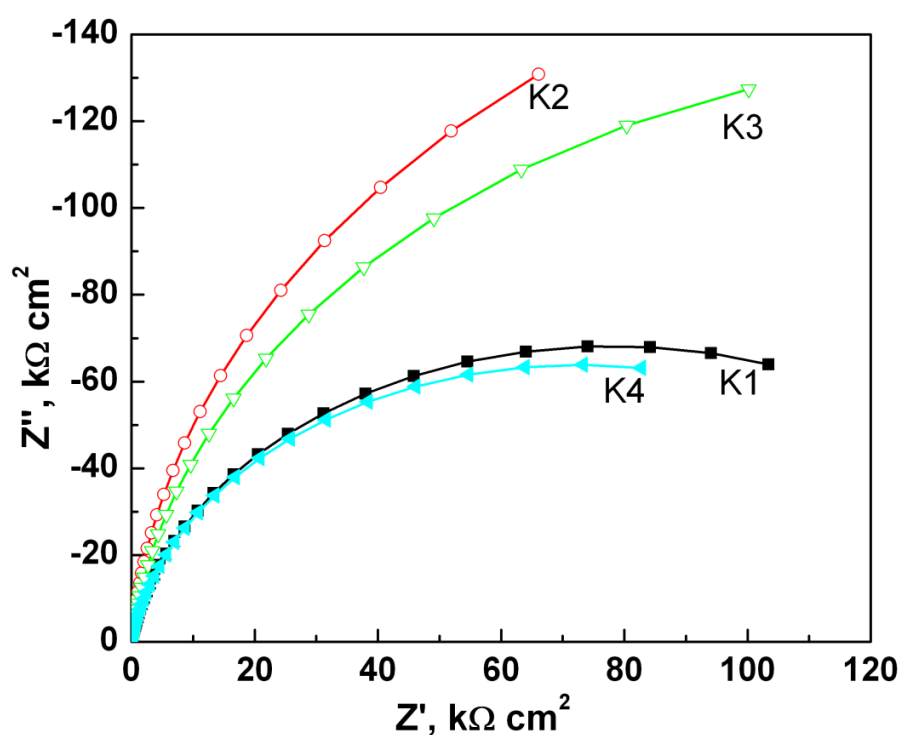


Fig. 5.12. Electrochemical impedance spectra of different MWF alloys at KGW.

The combined effect of both chromium oxide and the zirconium oxide is reflected in the EIS results. From Table 5.8, it is observed that the R_p values for all the MWF alloys were above 100 kΩ cm² which indicated appreciable passive film stability of the MWF alloys in KGW medium. The MWF alloys K2 and K3 wherein Zr concentration was 8.5 to 12 wt.% exhibited still higher passive film stability with high R_p values due to their optimum microstructure. From

the microstructure (Fig. 4.1) of MWF alloys the intermetallic precipitates in the alloys K2 and K3 were present to be an optimum amount. For the alloy K1 the presence of intermetallic precipitation was less and for K4 it was in excess. The stability of the oxide films formed and their adherence due to optimum amount of Zr intermetallic precipitation in the alloy K2 and K3 are in conformity with literature data [72, 78]. In the alloy K1 due to lower concentration of Zr intermetallic phases, the effect of zirconium oxide was less pronounced and for alloy K4 the effect of chromium oxide was minimum due to excess intermetallic phases. Thus it is evident from this study that an optimum amount of Zr (8.5 to 12 wt.%) in MWF alloys is beneficial with respect to corrosion resistance and passive film stability. Based on the foregoing discussion, the MWF alloy K2 with 8.5 wt.% Zr was selected as the candidate alloy for subsequent studies.

Table 5.8. EIS fitted values for different MWF alloys in KGW

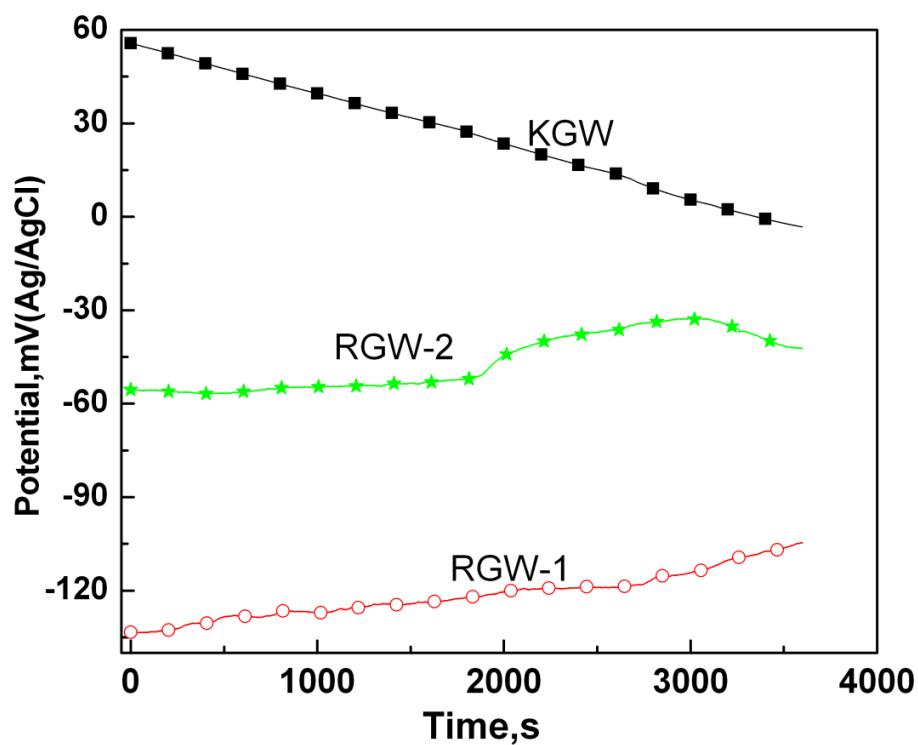
MWF alloys	R_s ($\Omega \text{ cm}^2$)	R_p ($\text{k}\Omega \text{ cm}^2$)	CPE-T ($\text{F cm}^{-2} \text{ S}^n$)	CPE-n
K1	50	120	3.22×10^{-5}	0.904
K2	50	248	2.10×10^{-5}	0.962
K3	50	173	2.13×10^{-5}	0.944
K4	50	104	3.44×10^{-5}	0.917

5.3.2.4 OCP monitoring for different repository environments

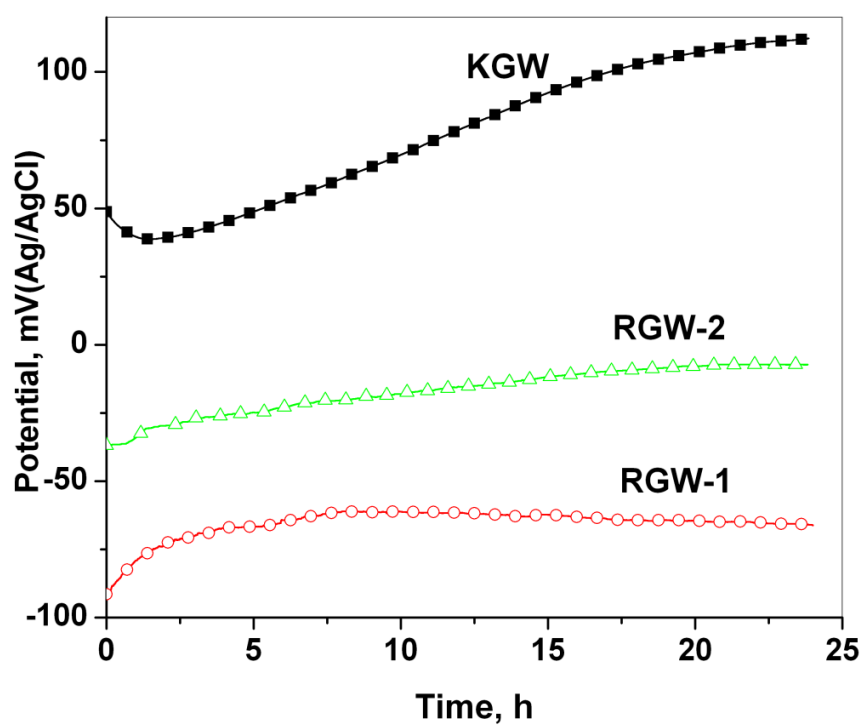
Figures 5.13a and 5.13b show the OCP versus time plots for the MWF alloy K2 in KGW, RGW-1 and RGW-2 for 1 h and 24 h respectively. It was observed that this MWF alloy exhibited nobler OCP in KGW medium than the other two media. The OCP was found to move

towards active direction for 2 h in KGW (Fig. 5.13a and 5.13b) and then shifted towards nobler direction along with time. In both the RGW media initially the OCP moved towards nobler direction for 2 h and attained steady state. However the MWF alloy exhibited nobler OCP value in RGW-2 than in RGW-1.

The ground water contains some minerals in the form of cations and anions (cf.: Table 3). The cations present in the ground water will form hydrated passive film like $\text{H}_2\text{O-M-OH}_2$ and protect the surface of the alloy from metallic dissolution [145]. Calcium, magnesium, sulphate and carbonate ions present in the water could form insoluble $(\text{Ca,Mg})\text{SO}_4$ and $(\text{Ca,Mg})\text{CO}_3$ layer on the surface, which also give surface protection [150]. In KGW, the concentration of these ions was comparatively higher than the values in both the RGW media and hence, nobler OCP was observed in the beginning (Fig.5.13a and 5.13b). However, as the concentration of Cl^- ion was very high in KGW medium, it led to the formation of soluble chloride metal complex [145]. Hence, metallic dissolution was favoured initially, thereby shifting OCP towards active region. But the formation of zirconium oxide beneath the chromium oxide layer could have helped to stabilize the hydrated passive film and to attain nobler OCP at the later stage. As the mineral concentration is very low in RGW-1, the formation of hydrated passive film was not favoured at the beginning which led to active potential. However, with increasing time the hydrated passive film and insoluble sulphate and carbonate layer formation and their stability would be favoured and hence, the potential shifted towards the nobler region. In RGW-2 medium, the concentration of calcium, magnesium, and sulphate ions was relatively higher and the formation of hydrated passive film and insoluble $(\text{Ca,Mg})\text{SO}_4$ layer were faster and showed nobler OCP than RGW-1 medium [139,145,150].



(a)



(b)

Fig. 5.13. OCP versus time plot of MWF alloy (K2) in KGW, RGW-1 and RGW-2 (a) for 1h and (b) for 24 h

5.3.2.5 Potentiodynamic polarization study in different simulated repository environments

The potentiodynamic polarization behaviour of MWF alloy K2 in different ground water media is shown in Figure 5.14 and the polarization parameters determined are listed in Table 5.9. As shown in Figure 5.14, nobler corrosion potential (E_{corr}) was observed in KGW, however, with increasing potential increase in passive current density and lowering of the breakdown potential were observed when compared to RGW media. The changes in the polarization parameters between RGW-1 and RGW-2 were negligible. Among the two RGW media, in RGW-1 medium the MWF alloy exhibited marginally higher passive current density and lower breakdown potential compared to RGW-2 medium.

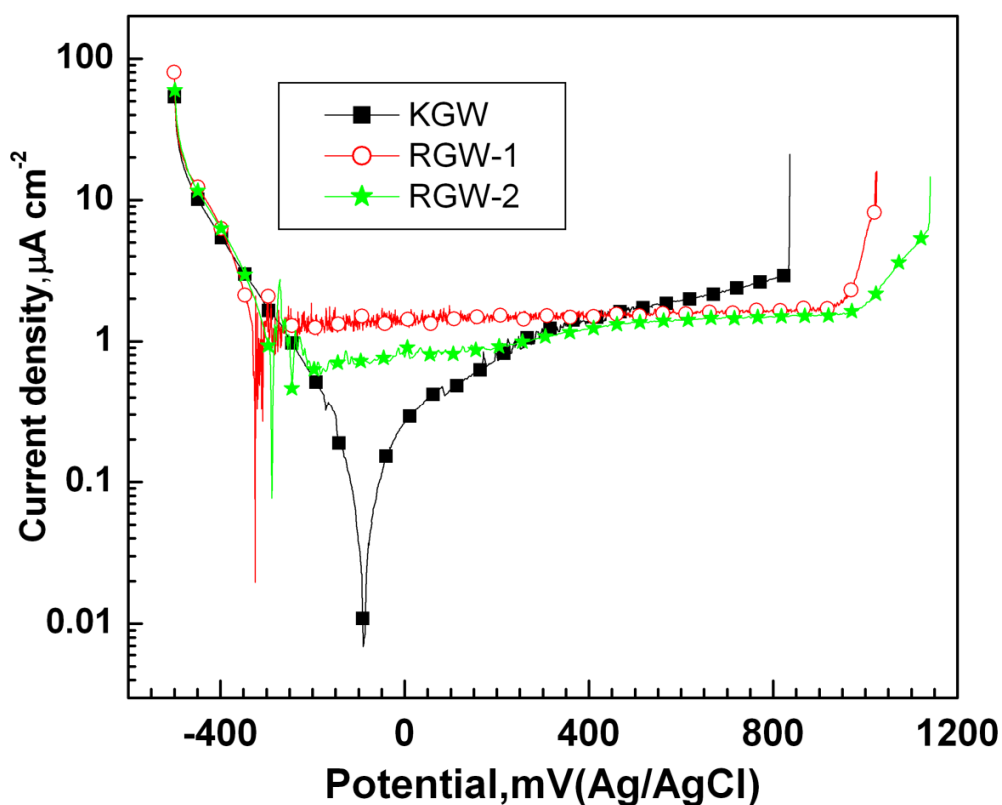


Fig. 5.14. Potentiodynamic polarization plots of MWF alloy (K2) in KGW, RGW-1 and RGW-2

Table 5.9. Polarization parameters for the different MWF alloy (K2) in KGW, RGW-1 and RGW-2

Media	E_{corr}	i_{pass}	E_{BP}
	mV(Ag/AgCl)	$\mu\text{A cm}^{-2}$	mV(Ag/AgCl)
KGW	-110	0.130	914
RGW-1	-308	1.212	984
RGW-2	-289	0.657	1053

The results shown in Figure 5.14 for the MWF alloy in different ground water media upheld the observation made in OCP monitoring. Owing to the formation of thicker hydrated passive film and insoluble sulphate and carbonate layers on the surface of the MWF alloy, nobler E_{corr} and lower i_{pass} were observed in KGW media. However, due to lower mineral concentration, comparatively active E_{corr} and higher i_{pass} values were observed in RGW media. The higher concentration of chloride ions present in KGW medium allowed the passive film to dissolve owing to formation of soluble chloride compounds which resulted in lower breakdown potential when compared to RGW [145,150].

5.3.2.6 Electrochemical impedance spectroscopic measurements with different repository environments

The Nyquist plot of EIS spectra for MWF alloy K2 in different simulated ground water media is represented in Figure 5.15 and the experimentally fitted parameters according to the equivalent circuit represented in Figure 3.10a are given in Table 5.10. In KGW medium lower semicircle arc radius was observed and in the RGW media, the arc radii were marginally higher. It is evident from Table 5.10 that among the three media, the lowest polarization resistance and

highest capacitance value were seen in KGW whereas in RGW-2 highest polarization resistance and lowest capacitance value were found.

Table 5.10. EIS fitted values for MWF alloy (K2) in KGW, RGW-1 and RGW-2

Media	R_s	R_p	CPE-T	CPE1-n
	$(\Omega \text{ cm}^2)$	$(\text{k}\Omega \text{ cm}^2)$	$(\text{F cm}^{-2} \text{ S}^n)$	
KGW	50	248	2.10×10^{-5}	0.962
RGW-1	54	324	2.06×10^{-5}	0.909
RGW-2	99	440	1.85×10^{-5}	0.925

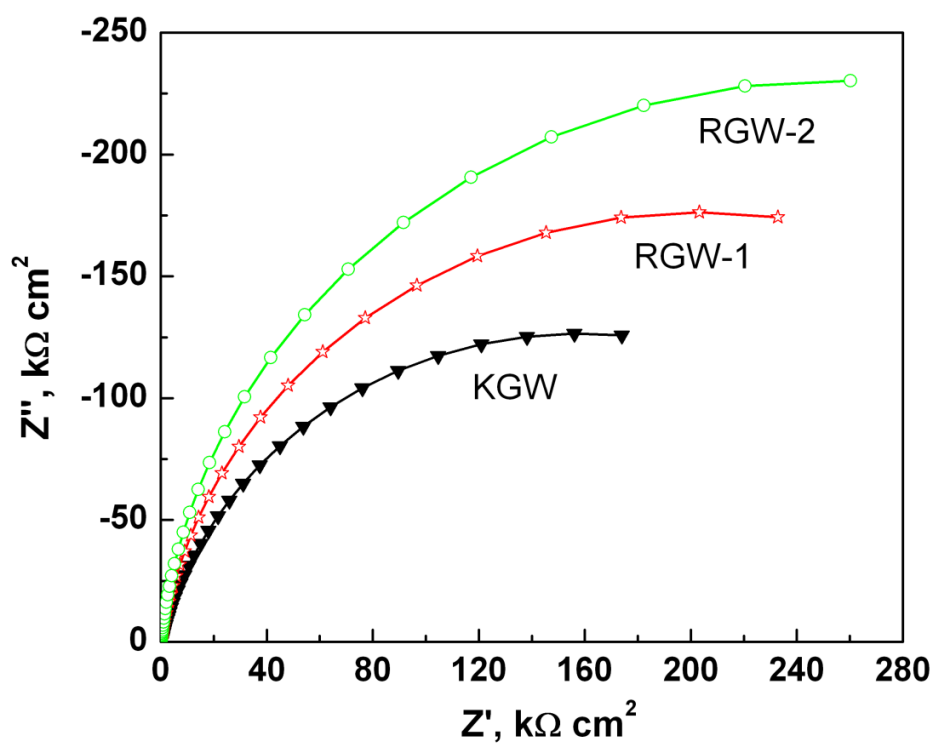


Fig. 5.15. Electrochemical impedance spectra of MWF alloy (K2) in KGW, RGW-1 and RGW-2

The results of EIS in different geological media indicated that the concentration of chloride ions played an important role on the stability of the passive film [145]. It is observed from Figure 5.15 and Table 5.10, that the R_p values for the MWF alloy in all the simulated repository media were quite high. This is due to the formation of hydrated passive film on the MWF surface at the prevailing environment [145,150]. The appearance of higher R_p value for RGW-2 than RGW-1 was obviously due to the higher thickness of the insoluble surface layer formed as a result of higher mineral concentration. Low R_p value in KGW was due to the higher concentration of chloride ions present in this medium.

5.3.3 Surface morphology after polarization in different simulated media

The corrosion damage on the surface of MWF alloys was investigated by optical microscope and SEM after polarisation in different simulated media. The optical microscopic images of the surface of MWF alloys after polarization in DM water at pH 1, 5 and 8 are shown in Figures 5.16, 5.17 and 5.18 respectively. The optical microscopic images given in Figures 5.17 and 5.18 showed no clear contrast which is an indication of insignificant dissolution due to corrosion. However, the optical microscopic images of MWF alloys in Figure 5.16 showed a clear contrast between dark and bright region, indicative of film dissolution due to corrosion in DM water at pH 1. The SEM micrographs of the MWF alloys after polarization in DM water at pH 1 are shown in Figure 5.19. These SEM micrographs showed complete removal of passive film and the appearance of a distinct dark and bright phase which could be observed during electrochemical etching as shown in Figure 4.1. However, neither any localized attack nor a selective segregation at the interface between the matrix and intermetallic precipitation could be observed on MWF alloys' surface after polarization in DM water at pH 1.

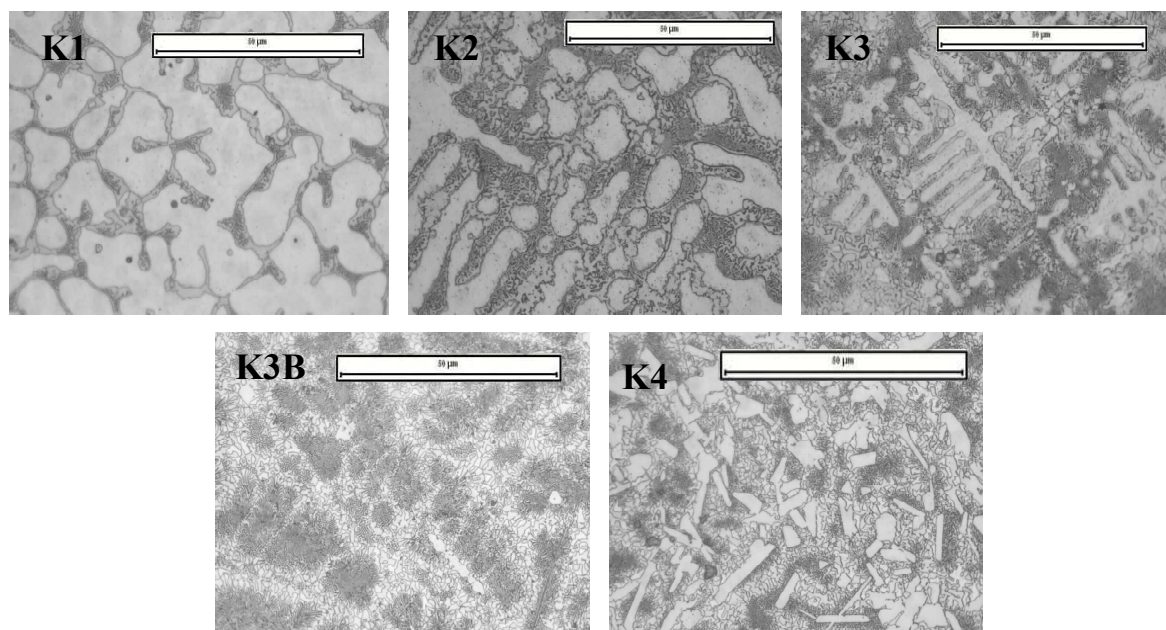


Fig. 5.16. Optical microscopic images of MWF alloys after polarization at pH 1

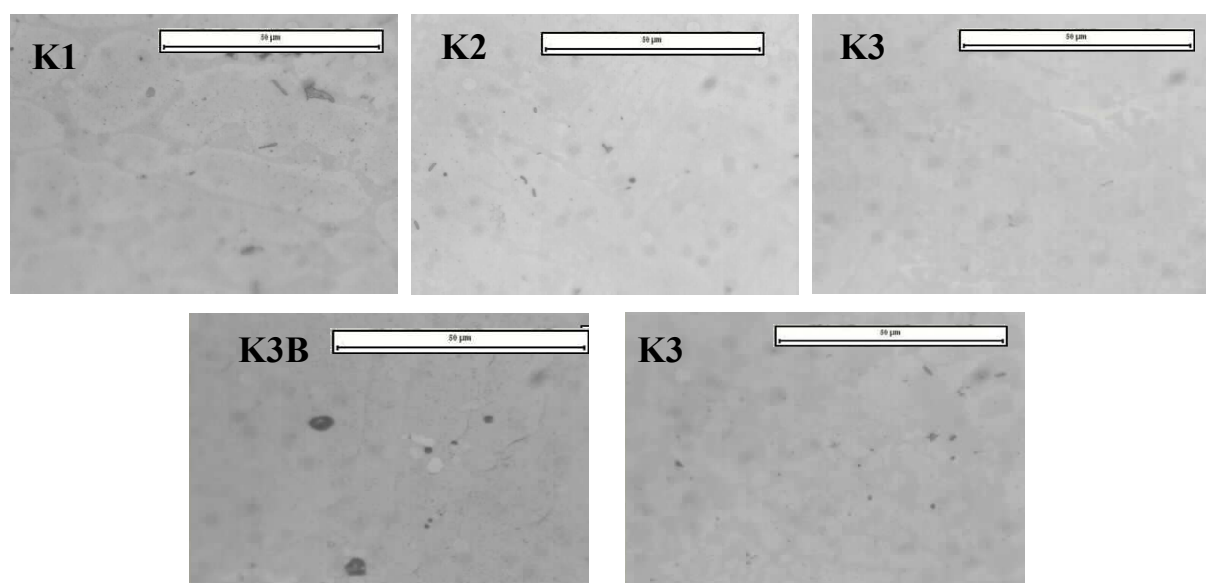


Fig. 5.17. Optical microscopic images of MWF alloys after polarization at pH 5

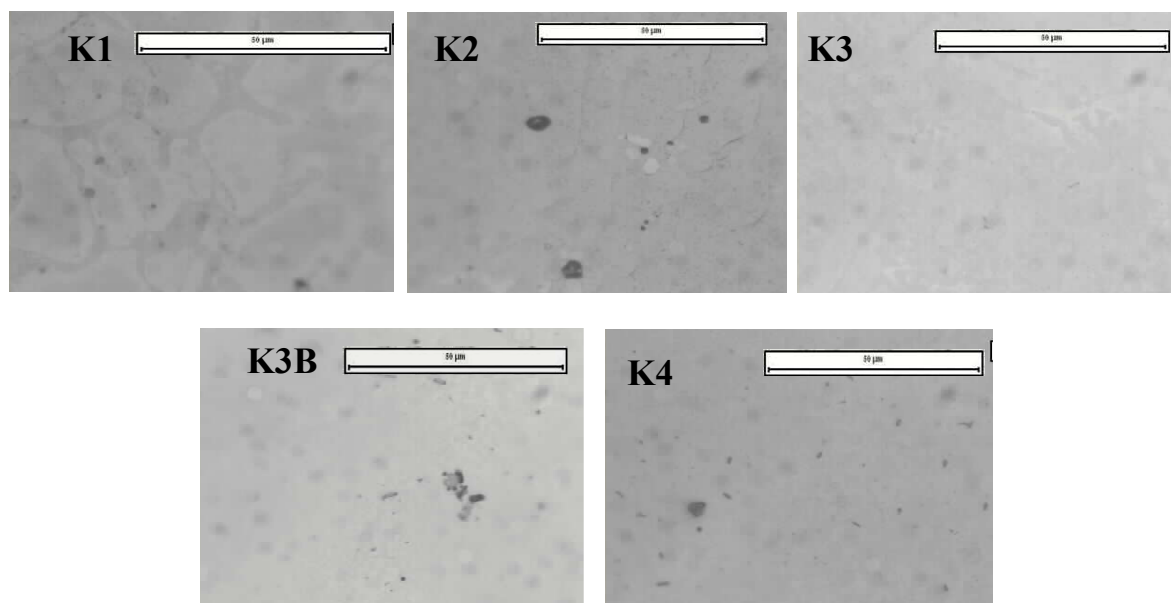


Fig. 5.18. Optical microscopic images of MWF alloys after polarization at pH 8

The surface morphological features clearly revealed the corrosion behaviour of MWF alloys in the respective media. Wide range of passivation behaviour with higher E_{BP} was observed during polarization in DM water at pH 5 and 8. The insignificant corrosion dissolution found in the surface morphological features (Figs. 5.16 and 5.17) validate this observation. During polarization in DM water at pH 1 the MWF alloys exhibited lower E_{BP} and surface morphological features showed significant surface dissolution. However, no localized corrosion was noticed due to the presence of Zr intermetallic phases which protect the alloy surfaces against localized corrosion owing to the formation of stable, adherent and amorphous zirconium oxide film [72, 78]. Abraham and Deitz [78] reported that these Zr intermetallic phases are the sink for actinide and fission products. The present study reveals that Zr rich intermetallic phases possess good resistance against corrosion dissolution even in aggressive media like DM water at pH 1.

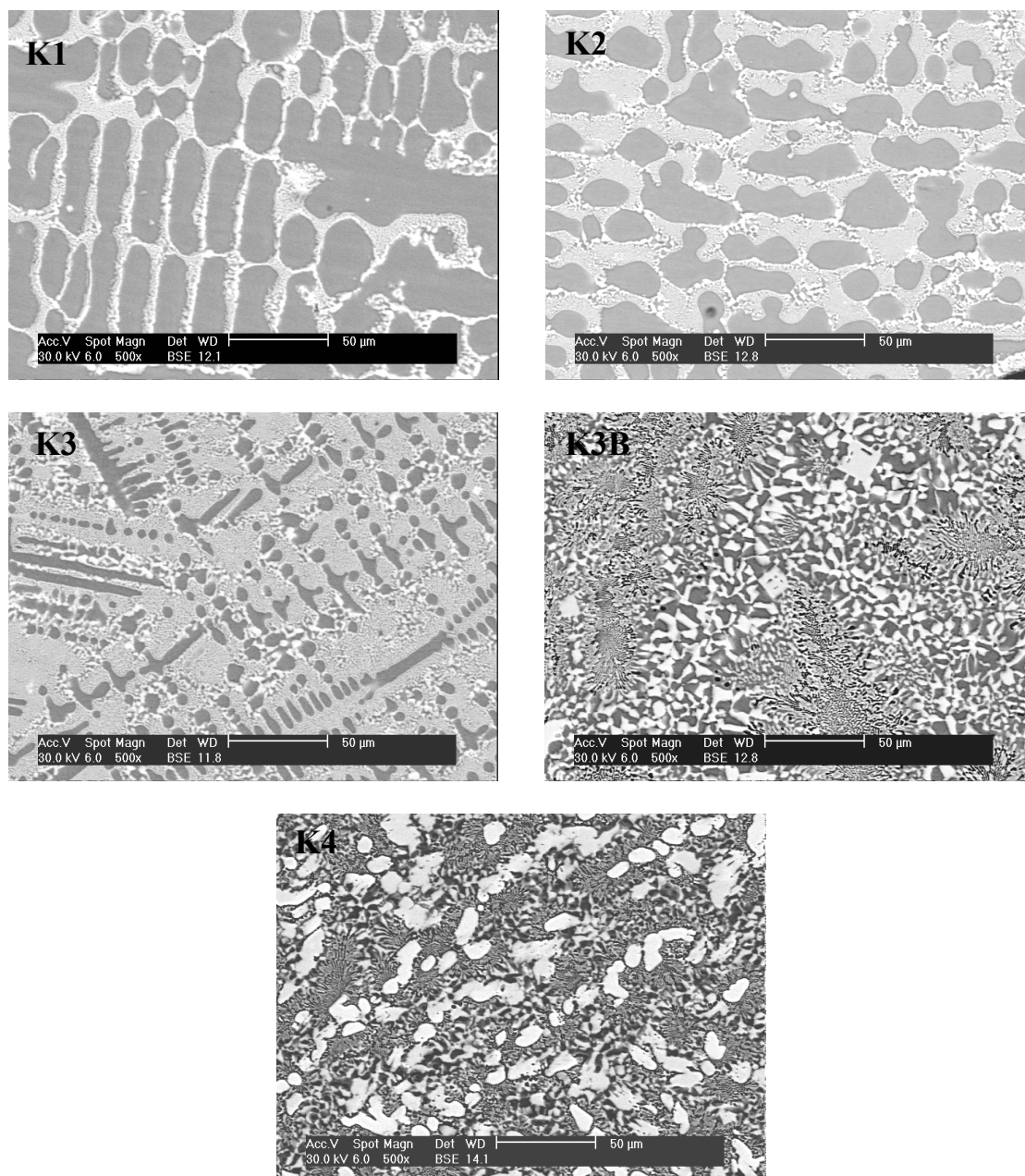


Fig. 5.19. SEM images of MWF alloys after polarization at pH 1

The SEM images along with EDS spectra of the surface of MWF alloy (K2) after polarization in KGW medium are shown in Figure 5.20. The surface morphology did not show

any significant corrosion dissolution but, some dendritic salt deposition was noticed. The magnified view of the surface is shown in Figure 5.20b. EDS scan was carried out at different locations on the surface including the deposited area to analyse the nature of this deposition. Other locations showed the typical composition of MWF alloy (Fe, Cr, Ni and Zr), whereas the deposited area revealed the presence of Na, K, Cl, Ca, Mg along with Fe, Cr, Ni and Zr (Fig. 5.20c).

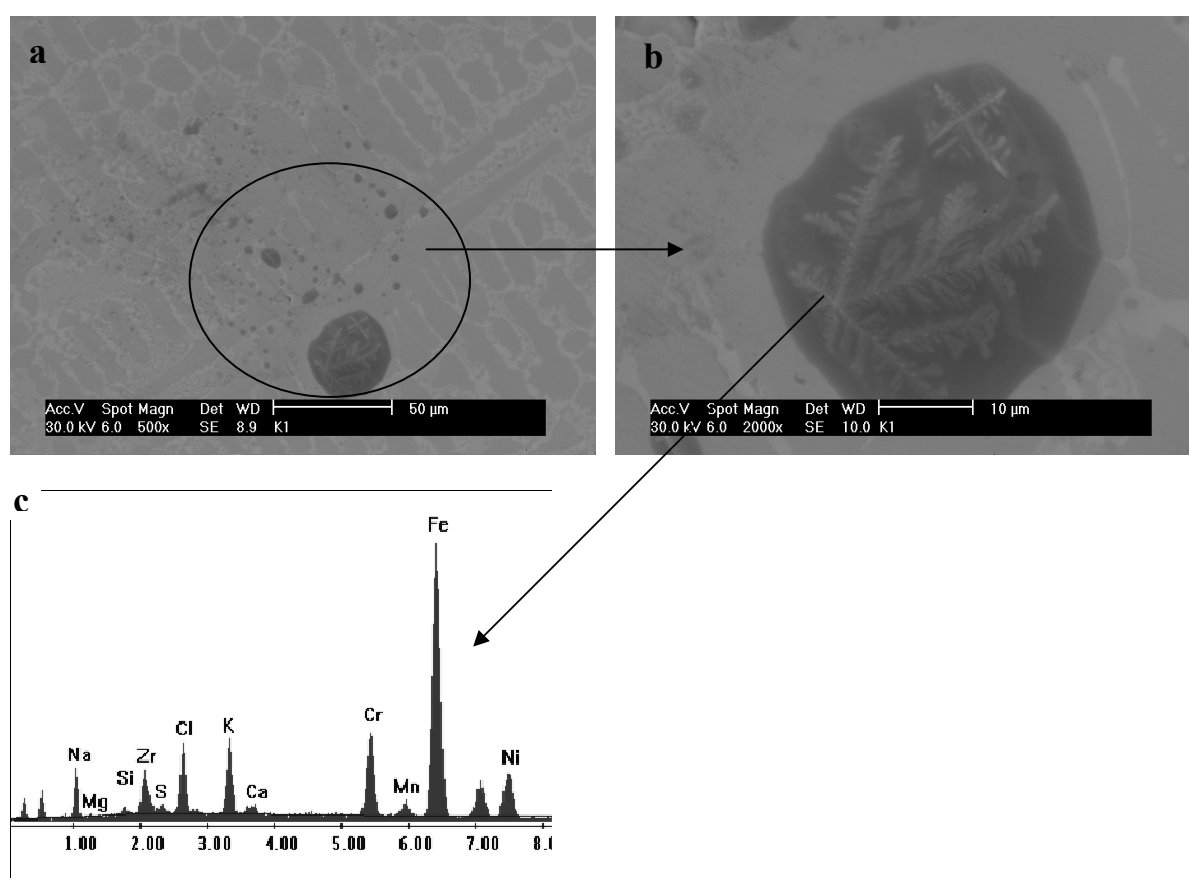


Fig. 5.20. SEM images and EDS spectra of MWF alloy (K2) after polarization in KGW

Figure 5.21 represents the SEM images of MWF alloy surface after polarization in RGW (RGW-1 and RGW-2). Both the images showed insignificant corrosion dissolution and no localized attack like pit formation or salt deposition.

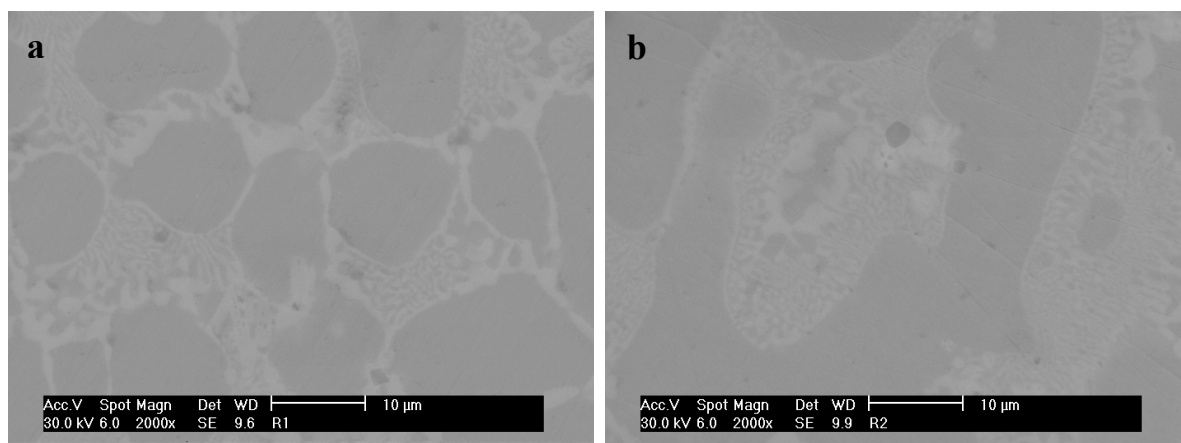


Fig. 5.21. The SEM images of MWF alloy (K2) after polarization in RGW media (a) RGW-1 and (b) RGW-2

The surface morphology after polarization in simulated ground water media revealed the general dissolution behaviour of the alloys in the investigated media. In KGW medium, the presence of excessive minerals led to the formation of dendritic salt deposition on the surface. The EDS analysis at different regions indicated the salt deposition to be not uniform. In both of the RGW media due to lower concentration of Cl^- ions, pit formation and subsequent salt deposition could not be observed. Hence, the chance of any localized corrosion attack or selective salt segregation on MWF alloy will be less in RGW media when compared to KGW medium.

5.3.4 XPS analysis of the MWF passive film

The composition of passive film on MWF alloy (K2) surface formed after passivation in DM water was estimated by X-ray photo electron spectroscopy (XPS). For this purpose, the MWF alloy was passivated in DM water at 400 mV(Ag/AgCl) potential for 1 h. The XPS spectra were recorded after sputtering the surface with Ar gun for 1 minute and 3 minutes respectively.

The survey spectrum of MWF surface shown in Figure 5.22 indicated the presence of Fe, Cr, Ni, Zr and O as the major elements. The high resolution de-convoluted spectra of O, Zr and Cr are presented in Figures 5.23, 5.24 and 5.25 respectively, as these elements are of relevance to the present work in the formation of passive film.

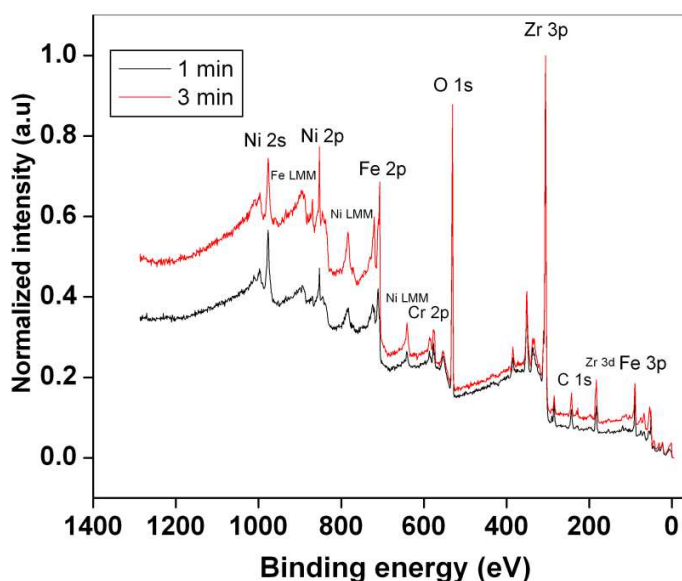


Fig. 5.22 Survey spectra of MWF surface after 1 minute and 3 minute sputtering by Ar gun

Figures 5.23a and 5.23b show the de-convoluted spectra for oxygen after 1 minute and 3 minute sputtering respectively. In these profiles three prominent peaks were observed which corresponded to the intense peak of zirconium oxide and chromium oxide and a smaller peak of hydroxide and adsorbed water. The decrease in the intensity of oxide peaks after 3 minute sputtering indicated the depletion of oxygen with time of sputtering. However, in both the cases the relative intensity of zirconium oxide was higher than that of chromium oxide. Figure 5.24 show the de-convoluted spectra for Zr. It could be seen from Figure 5.24a that after 1 minute sputtering, intense peaks for ZrO_2 appeared along with minor peaks of elemental Zr. However, after 3 minute sputtering the intensity of the peaks for elemental Zr increased and the intensity of

ZrO_2 peak decreased. The de-convoluted spectra for chromium after 1 minute sputtering and 3 minute sputtering are shown in Figures 5.25a and 5.25b respectively. Figure 5.24a showed the presence of both elemental chromium as well as chromium oxide peaks. Whereas, after 3 minute sputtering, the intensity of chromium oxide decreased sharply and the intensity of elemental chromium was found to increase significantly.

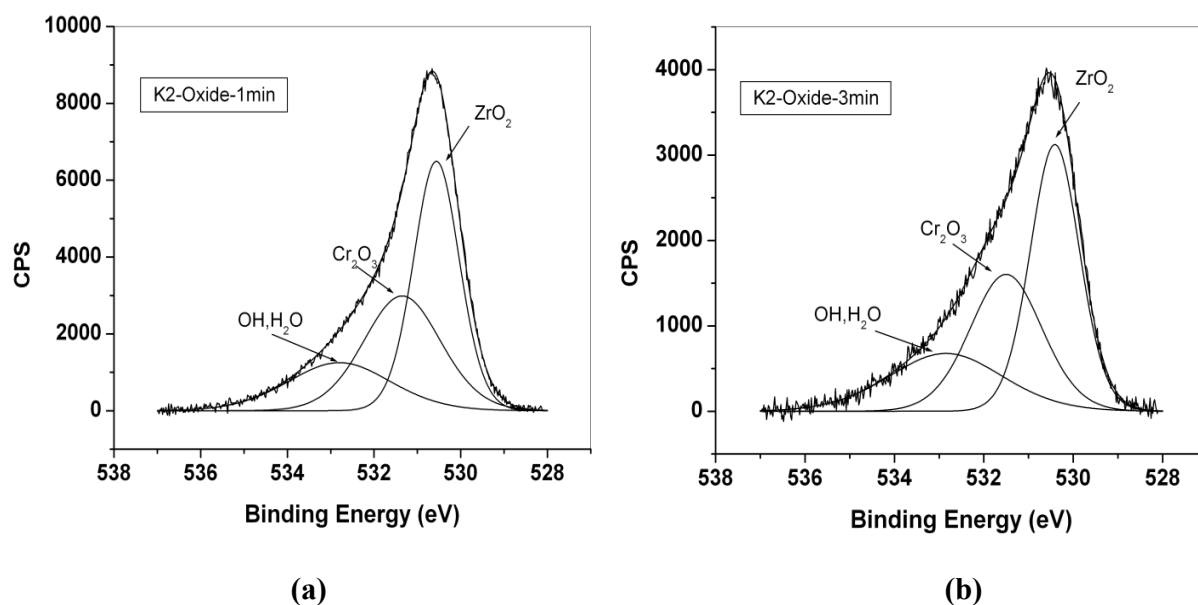


Fig. 5.23 De-convoluted XPS spectra for oxygen (a) after 1 minute sputtering and (b) after 3 minute sputtering.

From the XPS analysis, the formation of intense zirconium and chromium oxides was confirmed. The intensity of oxide peak reduced with the time of sputtering and elemental peak increased. Sputtering time is directly related to the depth of penetration; higher the sputtering time means higher the depth of penetration. The XPS results after 1 minute sputtering indicated composition of the passive film to be very near to the surface and the formation of appreciable amount of oxide film comprising both chromium oxide and zirconium oxide. However, after 3 minute sputtering, the passive film beneath the surface showed the presence of very low amount of Cr_2O_3 , but appreciable amount of ZrO_2 . This observation of Zr forming zirconium rich oxide

film below the Cr_2O_3 layer and protecting the surface from corrosion dissolution is corroborated with the results reported by Abraham and Deitz [78].

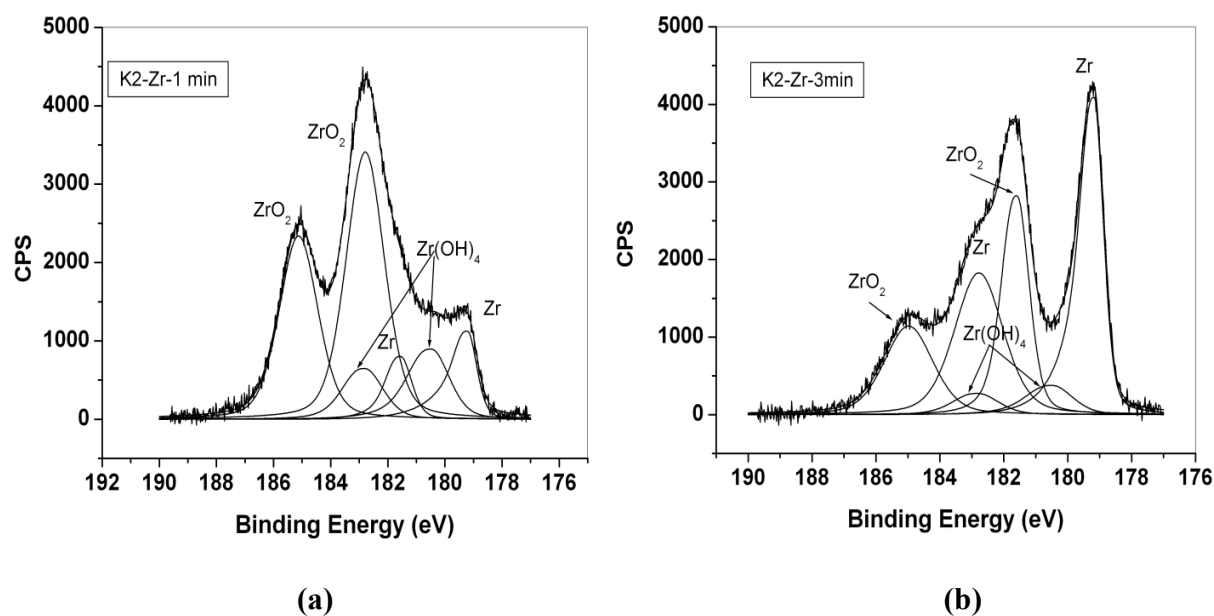


Fig. 5. 24. De-convoluted XPS spectra for zirconium (a) after 1 minute sputtering and (b) after 3 minute sputtering.

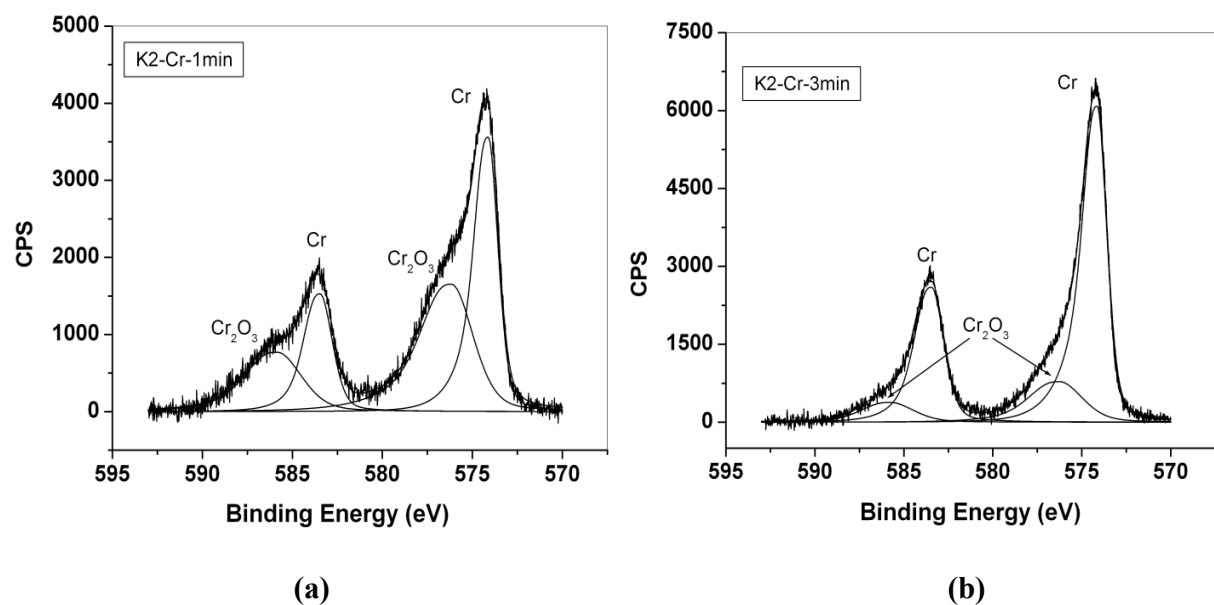


Fig. 5. 25. De-convoluted XPS spectra for chromium (a) after 1 minute sputtering and (b) after 3 minute sputtering.

5.3.5 AFM topography under different condition

The surface topographical features of the MWF alloy surface after passivation and polarization in different simulated media were characterized by AFM.

5.3.5.1 AFM topography of passivated MWF alloys in different simulated media

The MWF alloy (K2) was passivated in DM water at pH 5 and pH 8, simulated KGW and RGW at the respective passivation potentials for 1 h and AFM analysis was carried out. Figure 5.26 show the AFM images of the passivated MWF surface in different simulated media. The surface of the MWF alloy passivated in pH 5 and pH 8 and shown in Figures 5.26a and 5.26b respectively showed smooth topography with minimum surface aggregation. The surface passivated in KGW and shown in Fig. 5.26c revealed the formation of thick salt deposit while the surface passivated in RGW (Fig. 5.26d) showed a thin deposition. The thicker passive film in KGW revealed the presence of higher concentrations of soluble minerals (Table. 3.3) compared to the other media. The deposited layer on the MWF alloy surface acts as thin film insulating layer which prevents leak currents, unspecific adsorption and surface decomposition in aqueous electrolytes [14, 145]. Thicker the deposited layer higher would be the film resistance. In the present study though the film thickness was more in KGW, due to the presence of higher concentration of Cl^- ions, the film became unprotective by the formation of soluble chloride complex and thereby reducing the film resistance when compared to RGW.

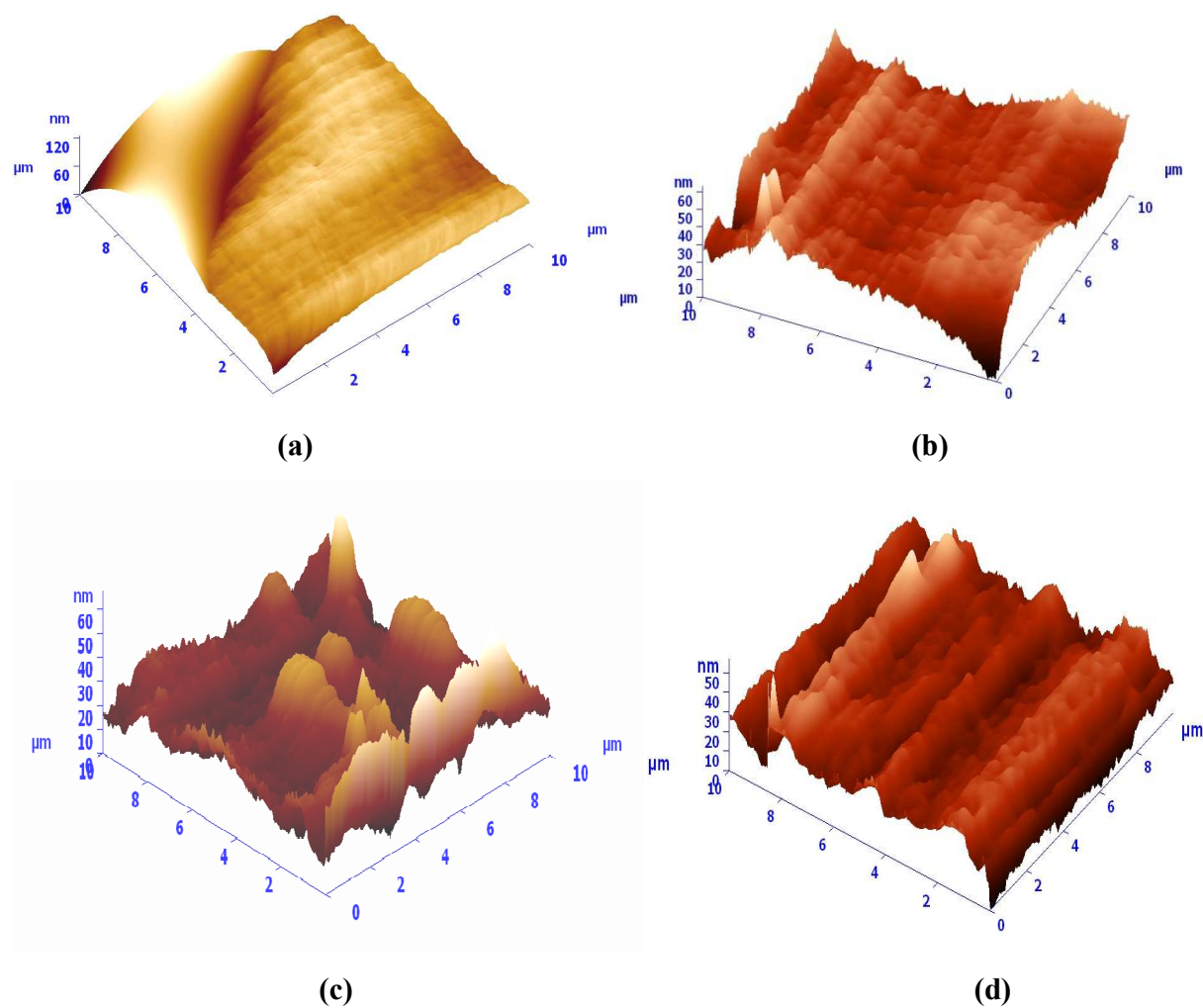


Fig. 5.26. AFM images of MWF alloy (K2) passivated in (a) DM water at pH 5, (b) DM water at pH 8, (c) KGW and (d) RGW.

5.3.5.2 AFM topography of the MWF alloy polarized in different simulated media

AFM images of the MWF alloy surfaces after polarization in DM water at pH 5 and 8, simulated KGW and RGW are shown in Figure 5.27.

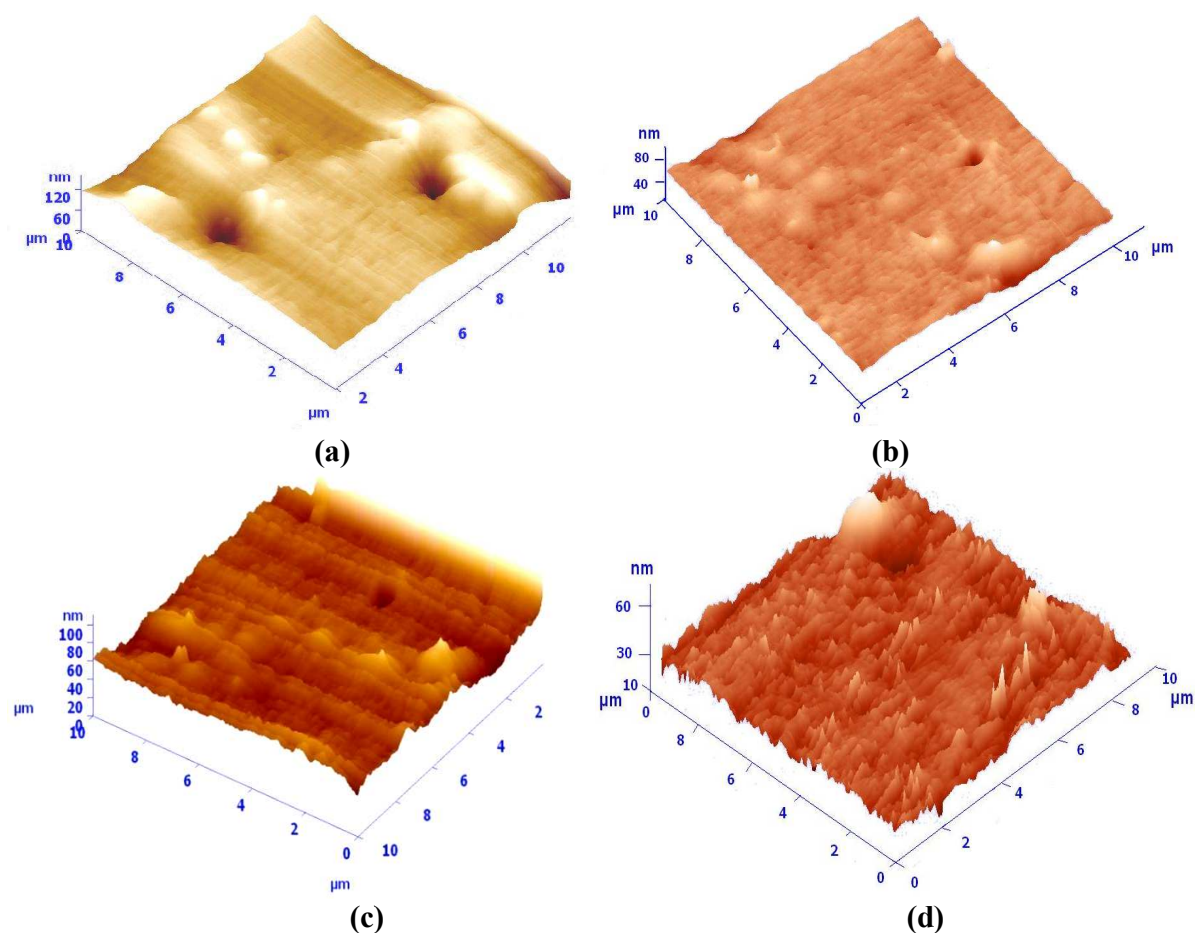


Fig. 5.27. AFM images of the MWF alloy (K2) polarized in (a) DM water at pH 5, (b) DM water at pH 8, (c) KGW and (d) RGW.

All the AFM images after polarization showed the formation of pits on the exposed surfaces. However, surfaces polarised in KGW (Fig.5.23c) showed significant salt precipitation along with pit formation. The surface polarized in DM water at pH 5 and pH 8 (Figs. 5. 27a and 5. 27b) showed pit formation with minimum surface deposition. The surface polarized in RGW showed thinner deposition with minimum pit formation. AFM topography of the MWF alloy after polarization in pH 1 shown in Figure 5. 28a exhibited unique topography with two distinct phases, similar to that observed in Figure 5.28b after electrochemical etching. One phase was at a

higher elevation while the other phase was at a lower valley. The elevated phase in the AFM morphology corresponded to the bright phase obtained in the SEM images and the lower valley corresponded to the dark phase. This indicates that after polarisation in pH 1, the dark phase has higher rate of dissolution compared to the bright phase, since the bright phase is Zr rich intermetallic phase showed lower dissolution and minimum pit formation.

Figure 5. 28 also showed that the Zr intermetallic phases were stable during polarization in DM water at pH 1 and even after electrochemical etching in 10 % ammonium persulphate solution. The present study was aimed at evaluating the MWF alloy's corrosion behaviour in simulated repository environment since corrosion is one of the major mechanism by which radionuclide leaching takes place in geological repository environment. The results of this study established the corrosion resistance of MWF alloy in simulated ground water. Though significant dissolution of the alloy was observed in the highly aggressive condition of DM water at pH 1, the Zr intermetallic phases which are the host matrix for radioactive actinides and fission products did not dissolve significantly.

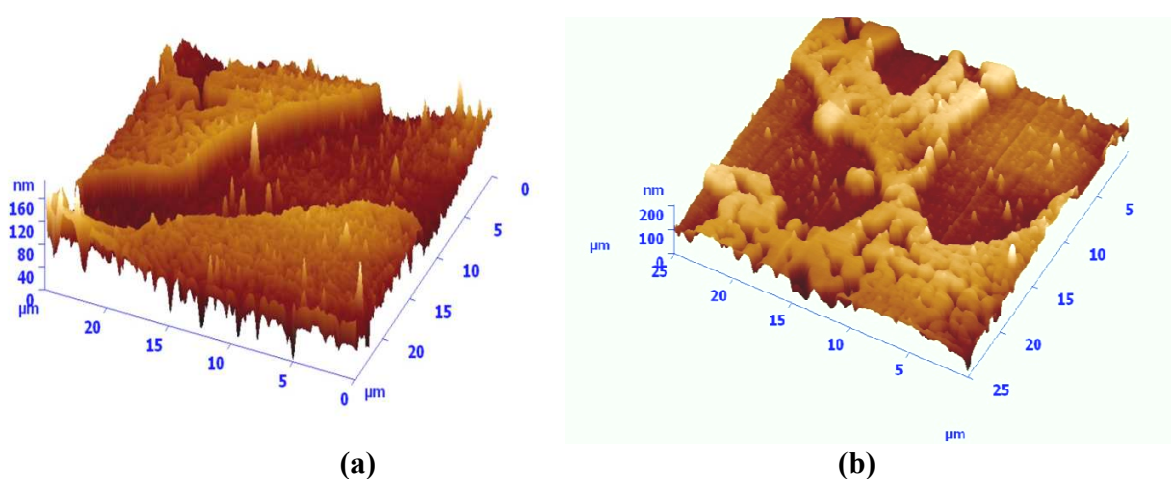


Fig. 5.28. AFM images of MWF alloy after (a) polarization in DM water at pH 1 and (b) electrochemical etching in 10 % ammonium persulphate solution.

5.4 Conclusions

To understand the corrosion behaviour and passive film stability of MWF alloys which would form the host matrix for radioactive solid waste during geological disposal, the present investigation was carried out. The corrosion characteristics with respect to the variation in Zr concentration as well as the behaviour of the MWF alloys in the repository environment were established. The following conclusions were drawn from this study.

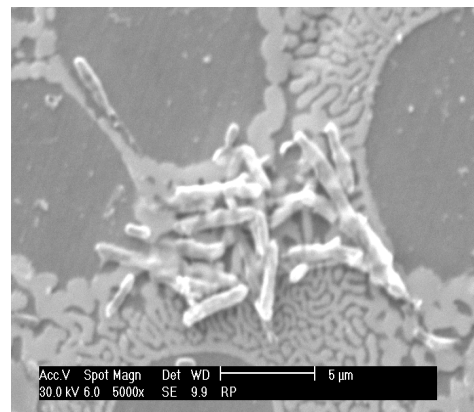
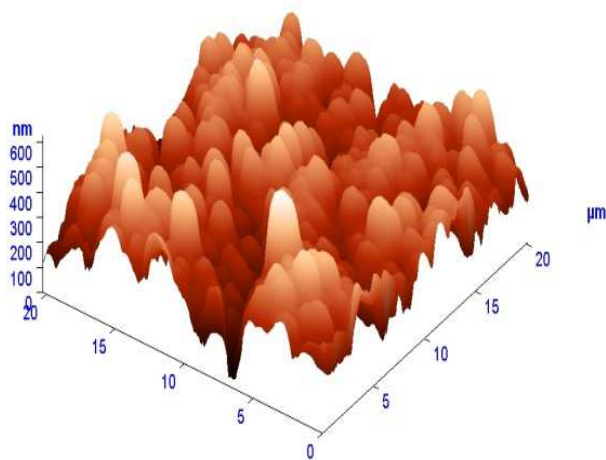
1. OCP and polarization studies revealed that MWF alloys of D9 SS-Zr exhibit excellent resistance against corrosion with wide ranging passivation behaviour in simulated geological media like DM water at pH 5, pH 8, KGW and RGW.
2. The MWF alloys have exhibited higher polarization resistance and formed stable hydrated passive film in metallic interface in simulated media. EIS study indicated that the optimum Zr concentration was about 8 to 12 wt.% for better passive film resistance in most aggressive media (pH 1) due to the combined effect of chromium oxide and zirconium oxide.
3. Surface morphology of the MWF alloys after polarization showed insignificant dissolution in mild media like DM water at pH 5, pH 8 and RGW. After polarization in KGW, corrosion dissolution was not significant but some dendritic salt appearance was noticed. Dissolution of Fe based solid solution matrix was observed after polarization in DM water at pH 1.
4. XPS analysis of passive film composition of MWF alloy surface showed the formation of a thicker oxide scale. The intensity of chromium oxide and zirconium oxide was higher than that for the other elements. Zirconium oxide was present up to sufficient depth below the surface wherein depletion of chromium oxide layer was observed.

5. AFM topography of MWF alloys passivated in simulated media showed passive film formation in KGW and RGW media. Pit formation was observed after polarization in DM water at pH 5 and 8, and in KGW and RGW pits were observed along with salt deposition.
6. MWF alloys showed higher corrosion dissolution in DM water at pH 1. Surface analysis indicated that the corrosion dissolution occurs only on Fe based solid solution matrix. The Zr rich intermetallic phase which is the host phase for actinide and fission product was stable even after polarization in the aggressive media like DM water at pH 1.

It is evident from this study that the MWF alloys exhibit good corrosion resistance with the formation of stable passive film in simulated geological environment. Though significant corrosion dissolution was observed in the aggressive media like DM water at pH 1, the actinide and fission product bearing intermetallic phases continued to remain stable in all circumstances. Based on the corrosion behaviour of MWF alloys reported in this study, MWF alloys with Zr in the concentration range 8-12 wt.% are recommended to be the appropriate host matrix for long term disposal of solid metallic wastes in geological repository.

CHAPTER 6

INVESTIGATION OF SELECTIVE ELEMENTAL LEACHING AND MICROBIAL INDUCED CORROSION BEHAVIOUR OF MWF ALLOYS



CHAPTER 6

INVESTIGATION OF SELECTIVE ELEMENTAL LEACHING AND MICROBIAL INDUCED CORROSION BEHAVIOUR OF MWF ALLOYS

Long term corrosion performance of MWF alloys was evaluated through selective elemental leaching and microbial induced corrosion behaviour in simulated geological repository environment. The selective elemental leaching study was carried out in de-mineralized (DM) water under dynamic and static conditions by following ASTM standard material characterisation centre (MCC) procedure. The dynamic tests were carried out in constant flow of water at 90 °C for 260 days while the static tests were carried out at 90 °C and 200 °C for 90 days. Selective elemental leaching of MWF alloy K2 with 8.5 wt.% Zr was investigated in simulated KGW and RGW under static condition at 90 °C for 90 days. The composition of the leachate solutions was analyzed by inductively coupled plasma optical emission spectroscopy (ICP-OES) and the result showed insignificant elemental leaching from MWF alloys. Whereas, SEM/EDS morphology showed that, after long term exposure in high temperature condition a protective zirconium oxide rich scale was formed on the MWF surface. AFM topographic analysis showed that the thickness of surface scale was higher during static testing and was increasing with the increase of testing temperature.

Microbially induced corrosion (MIC) behaviour of MWF alloy was evaluated in simulated KGW and RGW media. MWF alloy specimens were exposed in Bacillus sp. and Pseudomonas sp. cultured in simulated KGW and RGW media to study the bacterial interaction with MWF alloy. Total viable count and epifluorescence microscopy were carried out to monitor microbial attachment on MWF alloy and the results showed good bacterial attachment on MWF surface. SEM and AFM were used to understand the preferential phases

for bacterial attachment and the result on etched MWF surfaces showed preferential bacterial adhesion on Zr-rich intermetallic phases. Results of electrochemical corrosion studies showed active corrosion potential and higher current density for biofilmed surface indicating high corrosion probability. Electrochemical impedance spectroscopy showed instability of passive film due to the biofilm formation. The corrosion effect of Pseudomonas sp. was comparatively higher than that of Bacillus sp.

6.1 Introduction

Selective leaching of alloying elements from MWF alloys due to long term exposure in geological repository can be a major problem [3] as this can lead to ground water contamination due to radionuclide leaching. Corrosion can enhance or resist the leaching depending upon the chemistry of the corrosion product formed on the MWF alloy's surface. Generally, the radioactive waste disposal site will be a repository with stable rock structure [28]. However, the aqueous environment that may be in contact with the waste package is expected to be hot and multi-ionic system. Long term exposure in such repository environment could result in significant degradation of waste package materials. Due to failure of waste package material, the MWF alloy will be exposed to the geological repository environment. The interaction of waste form and repository environment will encourage selective leaching of actinide elements [3] which will be responsible for ground water contamination. Most of the actinide elements have long half life and sufficient mobility in ground water [29]. Additionally biofouling is a major problem in almost all circumstances where water based environments are in contact with materials. For engineering structural materials, virtually all forms of microbiologically influenced corrosion (MIC) reported in literature are associated with localized corrosion underneath a biofilm which will be responsible for radionuclide leaching [30, 151]. Though it was observed from Chapter 5 that the MWF alloys showed good corrosion resistance with long range of passivation potential

due to the formation of zirconium oxide below the chromium oxide film, it is also well reported in literature that zirconium metal has excellent biocompatible property [152, 153]. Hence, microbes in natural water of the repository environment can favor biofilm formation on D9SS-Zr MWF alloy. The biofilms are mostly patchy in nature and initiate concentration cells at the metal biofilm interface [31, 154]. Therefore, localized corrosion can favor under the biofilm [31, 151, 154] which can encourage leaching out of radionuclides and pose an environmental threat [28, 155].

Therefore radionuclide leaching can be possible due to prolonged exposure of MWF alloys in geological environment. This can be possible either by long duration high temperature exposure or by microbially induced corrosion in the geological environment. Thus, the behaviour of MWF alloys must be evaluated by exposure in high temperature aggressive condition and with microbial species across the full range of repository relevant environments [28].

The aim and objectives of this study is to assess the long term behaviour of MWF alloys with respect to selective elemental leaching in high temperature condition as well as microbial induced corrosion behaviour in simulated repository environment. The present work carried out in two different approaches. The first approach involved the evaluation of elemental leaching from the D9 SS-Zr MWF alloys in DM water and in simulated KGW, RGW-1 and RGW-2 using ASTM standard materials characterization centre (MCC) testing procedures [114]. In this study the investigation of selective elemental leaching was carried out in two different methods, MCC-5 (dynamic testing) and MCC-1 (static or immersion testing) [91,115]. After the tests the changes in specimen mass, leachate composition and surface morphology was evaluated. The second approach was to monitor the microbial attachment and its corrosion effect on MWF alloy in KGW and RGW-2 media using two predominant biofilm formers; Bacillus sp. and Pseudomonas sp. [96,97]. This study

involved (i) determining the effect of biocompatibility of zirconium by bacterial count and microscopic observation and (ii) the effect of bacterial damage was assessed by using different electrochemical techniques.

6.2 Experimental

A brief description of different experimental techniques used in this chapter is given below (the detailed description of these experiments were provided in Chapter 3).

6.2.1 Selective leachability testing

The selective leachability testing was carried out in two different methods as per ASTM standard material characterization centre (MCC) procedure at high temperature condition as describe below.

1. The dynamic leachability testing as per MCC-5 test was carried out for all the MWF alloys (K1, K2, K3, K3B and K4) in DM water at 90 °C for 260 days. The leachate solution was sampled at regular intervals of 24 h and analyzed by ICP-OES. The weight changes of the MWF alloy specimens were measured after 260 days of leachability testing.
2. The static leachability testing as per MCC-1 procedure was carried out for all the MWF alloys in DM water at 90 °C and 200 °C for 90 days in Teflon Parr vessel. The MCC-1 testing of MWF alloy K2 with 8.5 wt.% Zr was carried out in simulated KGW, RGW-1 and RGW-2 at 90 °C for 90 days. The weight changes of the MWF specimen was measured after the MCC-1 testing and the leachate solution was analyzed by ICP-OES method.
3. The surface morphological changes of the exposed MWF alloy specimens after dynamic and static leachability testing were examined by SEM and the elemental composition of the surface layer was characterized by EDS attached with SEM. The

corresponding surface topography of the MWF alloys was analyzed by AFM in contact mode using standard conical silicon tip attached to a cantilever.

6.2.2 Microbial induced corrosion study

The bacterial culture of *Bacillus* sp. and *Pseudomonas* sp. was cultured and grown for 24 h individually in 100 ml nutrient broth solution (sterilized by autoclaving at 120 °C for 15 minutes). One ml of the 24 h culture solution was added to 150 ml of simulated KGW and RGW-2 (mentioned as RGW) solution individually and allowed to grow for another 24 hours. Seven MWF specimens (2 for corrosion monitoring, 2 for viable count, 1 for epifluorescence study for visualising bacterial density and 2 for surface characterization by SEM and AFM) were suspended in that culture for 5 days. One weight percent of glucose was added to the medium to maintain the microbes in growing conditions for 5 days. With these microbial exposed specimens the following post exposure experiments were carried out.

1. The total bacterial attachment on MWF alloy's surface and in culture media was investigated by total viable count (TVC).
2. The bacterial morphology on MWF alloys specimen's surface was directly observed by epifluorescence microscopy.
3. The detailed bacterial attachment on different microstructural phases (solid solution / intermetallic) of etched MWF surface was observed by SEM and AFM study.
4. The microbially induced corrosion of MWF alloy in respective media was evaluated using different electrochemical corrosion testing including OCP-time, Potentiodynamic polarisation and EIS. All the experiments were carried out in the following electrolytes, (i) KGW (sterile) (ii) KGW + *Bacillus* sp. (iii) KGW + *Pseudomonas* sp. (iv) RGW(sterile) (v) RGW + *Bacillus* sp. (vi) RGW + *Pseudomonas* sp.

5. Surface attack after potentiodynamic polarization on different bacterial exposed MWF alloy specimens was observed by optical microscopy.

6.3 Results and discussion

6.3.1 Selective leachability testing

The long term corrosion investigation was carried out in DM water and in simulated KGW, RGW-1 and RGW-2. DM water was selected for this study because it is most aggressive leachant due to lack of minerals in its composition [93]. Hence maximum leaching was expected in this medium and can give a better insight into the long term disposal experience. The KGW and RGW were selected for this experiment by considering probable repository environment for waste disposal site in India. The effect of different aggressive minerals and ions can be monitored in KGW and RGW which will give more confidence for waste disposal experience.

6.3.1.1 Leachability by MCC-5 and MCC-1 testing in DM water media

The quantitative elemental leaching from MWF alloys after long term exposure in DM water at high temperature condition was evaluated by measuring the weight changes of the of the MWF alloy specimens. The weights values of different MWF alloy specimens (K1, K2, K3, K3B and K4) before exposure and after 260 days of MCC-5 testing at 90 °C are provided in Table 6.1. It was observed that the difference in weights of all the MWF specimens before and after the MCC-5 test were within the resolution limit of the balance. The selective leaching of alloying elements from the MWF alloys was investigated by ICP-OES analysis of the leachate solutions. The ICP-OES results of leachate solutions are shown in Figure 6.1 which is a graphical representation of elemental concentration of the leachant collected at a regular interval. The results showed that for the MWF alloys the concentration of alloying element (Fe, Cr, Ni and Zr) in the leachate solution was less than 0.25 ppm even after 260

days of exposure. Same concentration of alloying element (< 0.25 ppm) was observed in blank DM water medium (day = 0) also. This concentration value was actually below the detection limit of the instrument. Hence, appreciable selective elemental leaching from MWF alloys during MCC-5 testing was not observed.

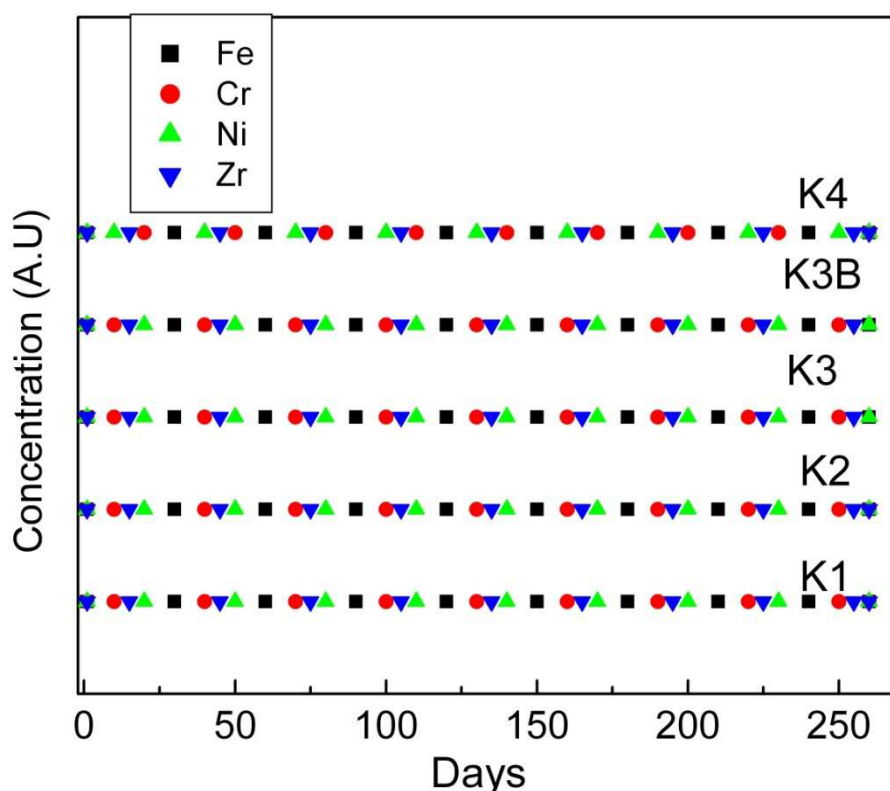


Fig. 6.1. The graphical representation of selective leaching of element Fe, Cr, Ni and Zr up to 260 days of MCC-5 testing at 90 °C. The concentration of the element was below the detection limit of the instrument (< 0.25 ppm).

Weight changes of all MWF alloys specimens after the completion of 90 days MCC-1 testing at 90 °C and 200 °C is given in Table 6.2. The result showed negligible weight loss after 90 days of MCC-1 testing carried out at 90 °C and 200 °C. This result indicated insignificant materials loss due to long term corrosion and selective leaching at high temperature static condition.

Table 6.1. Weight of MWF alloys before and after 260 days of MCC-5 testing at 90 °C.

MWF Alloys	Weight (g)	
	Before exposure	After exposure
K1	8.5085	8.5087
K2	9.1371	9.1373
K3	12.8517	12.8515
K3B	7.5862	7.5861
K4	9.0073	9.0070

Table 6.2. Weights of MWF alloys before and after leachability (MCC-1) testing.

MWF alloys	Weight (g)			
	90 °C		200 °C	
	Before exposure	After exposure	Before exposure	After exposure
K1	7.5516	7.5516	7.5021	7.5021
K2	7.1740	7.1739	8.4711	8.4711
K3	10.5316	10.5316	10.3150	10.3149
K3B	7.7973	7.7972	6.6705	6.6705
K4	4.9484	4.9483	5.1604	5.1602

The leachate solutions were analyzed by ICP-OES at the end of MCC-1 testing. The ICP-OES analysis of leachate solution obtained from both the testing condition at 90 °C and 200 °C showed that the concentration of alloying elements were below the detection limit of

instrument (< 0.25 ppm). This result also indicated that there was negligible elemental leaching from MWF alloys specimens at high temperature static condition (MCC-1).

In general the leachability tests were carried out in DM water because of its aggressive nature [78, 93]. After the removal of minerals and other dissolved substances, pure water becomes very unstable. The aggressive demineralised water attacks the water distribution pipe and storage tanks, leading to leaching of metals and other materials [93]. In the present study, significant selective leaching from the alloy specimens was expected. However, from the results of ICP-OES analysis negligible elemental leaching was observed. The probable reason for this negligible elemental leaching could be correlated with the microstructure of MWF alloys shown in Figure 4.1. The presence of secondary phase of Zr intermetallic precipitation acted as sink for impurity elements which improved the resistance to localized corrosion as well as selective leaching [72,78,87]. It was also reported by Abraham and Deitz [78] that during immersion testing at $90\text{ }^{\circ}\text{C}$, the corrosion layer formed on ZrFe_2 intermetallic particles was typically uniform, amorphous and well adherent to metallic surface. The layer was rich in amorphous zirconium oxide with Fe, Cr and Ni.

6.3.1.2 Leachability by MCC-1 testing in simulated KGW, RGW-1 and RGW-2

The MWF alloy K2 (D9SS-8.5 wt.% Zr) was selected for further leachability study in simulated ground water to understand the effect of aggressive minerals and ions on the MWF alloys during long term disposal in geological environment. The MWF alloy specimens were exposed in simulated solution of KGW, RGW-1 and RGW-2 individually for 90 days at $90\text{ }^{\circ}\text{C}$ for MCC-1 testing. The leachate solution was analyzed at the end of exposure period and the result showed that the concentration of the alloying elements were below the detection limit of the ICP-OES. The changes of the specimens weight is shown in Table 6.3. However, the results did not show any significant weight change after 90 days of MCC-1 testing in simulated ground water media. These results revealed that the corrosion effect on MWF

alloys due to long term exposure in ground water system at high temperature condition was negligible.

Table 6.3. Weights of MWF alloy (K2) before and after MCC-1 testing in simulated ground water.

Leachant	Weight (g)	
	Before exposure	After exposure
KGW	2.1191	2.1191
RGW-1	0.9594	0.9597
RGW-2	1.8018	1.8020

6.3.1.3 Surface characterization after MCC tests

6.3.1.3a. SEM and EDS analysis after exposure in DM water

The SEM images of the MWF alloy surfaces before exposure to MCC test are shown in Figure 6.2. The SEM images of the exposed MWF alloys surfaces after 260 days of MCC-5 testing at 90 °C are shown in Figure 6.3, showed the formation of surface scaling. The EDS compositions of MWF surface after MCC-5 testing are shown in Table 6.4. The EDS results showed presence of O along with Fe, Cr, Ni and Zr. In the composition of MWF alloys (Table 3.1), the presence of O was not observed. Hence the presence of O indicated the formation of oxide scale on the exposed MWF alloys surfaces. The concentration of Zr in the MWF alloys (K1, K2, K3, K3B and K4) was in the range of 4.5 wt.% to 17 wt.% (Table 3.1). However, after exposure of MWF alloys in present experimental condition, the concentration of Zr increased to the range of 15 wt.% to 23 wt.% (Table 6.4). This observation suggested that Zr and O rich oxide layer was formed with the presence of Fe, Cr and Ni on the MWF surface after 260 days of MCC-5 testing. Moreover, intensities of the Zr and O were increasing with increase of Zr concentration in the MWF alloy.

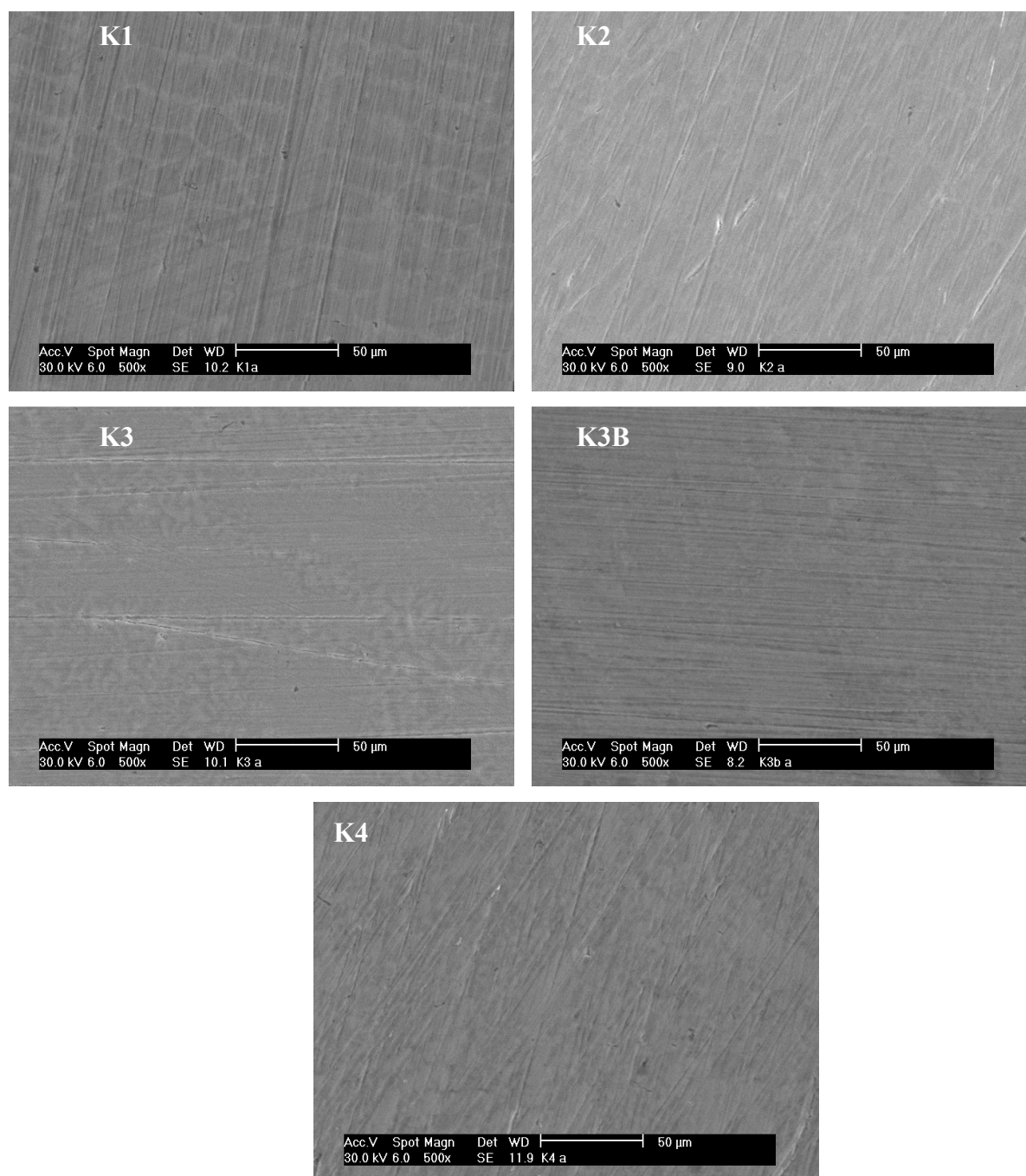


Fig. 6.2. SEM images of MWF alloys surface before leachability testing.

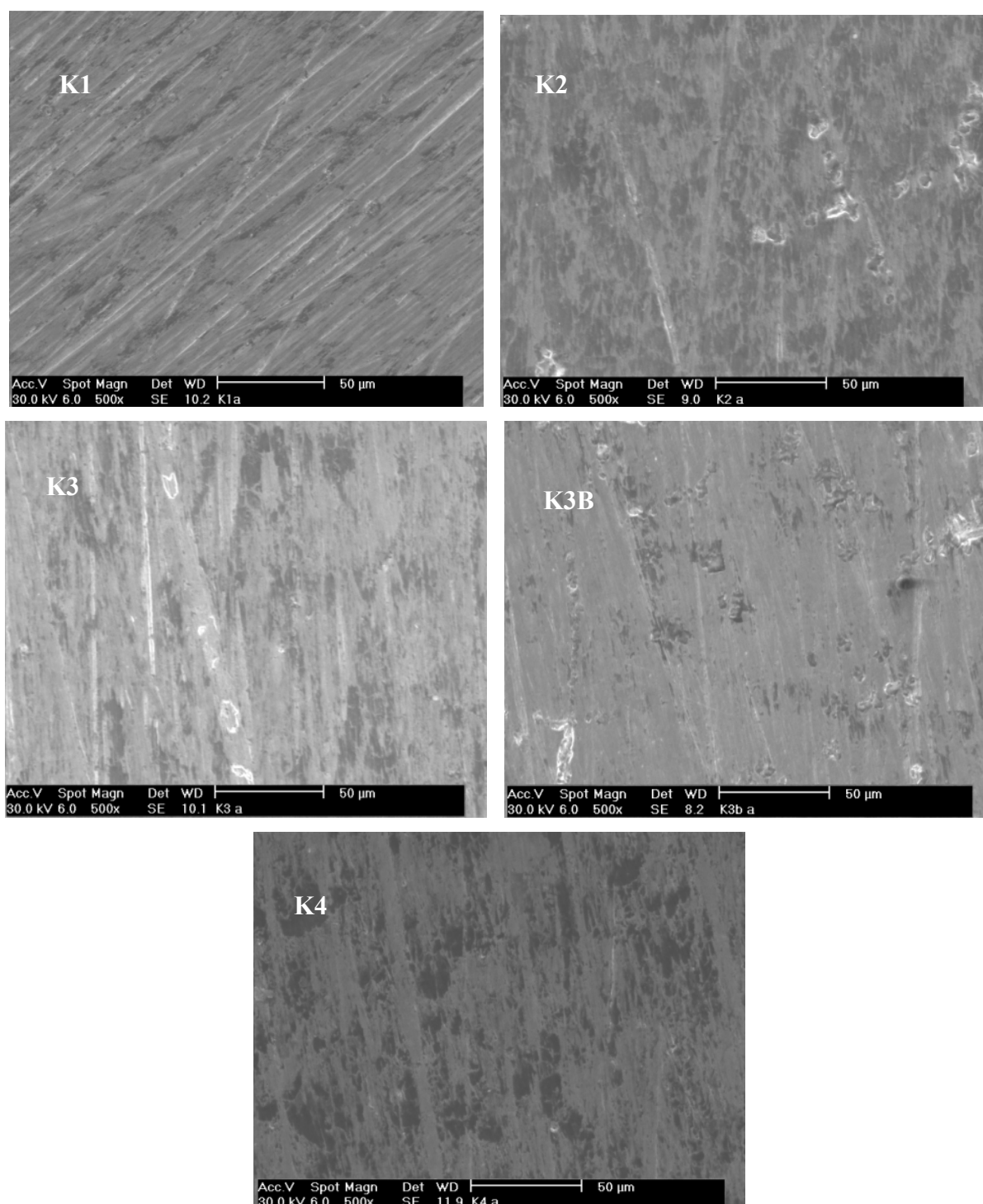


Fig. 6.3. SEM images of MWF alloys after 260 days of MCC-5 testing at 90 °C.

Figure 6.4 represents the SEM images of MWF alloys surfaces after 90 days of MCC-1 testing at 90 °C. Significant scale formation was observed on the MWF alloys surfaces. The EDS compositions of the corresponding surfaces are given in Table 6.4. Formation of Zr and

O rich corrosion layer was observed on the MWF surface similar to that as observed in MCC-5 testing. The SEM images of MWF alloys surfaces after MCC-1 testing at 200 °C is shown in Figure 6.5. The surfaces as shown in Figure 6.5 suggested that the thickness of the surface scaling was comparatively higher. As expected, the EDS composition (Table 6.6) for these specimens showed formation of Zr rich oxide scale. The concentration of O was found comparatively higher than the other two conditions. This result also supported the thicker oxide scale formation during MCC-1 testing at 200 °C. Moreover the presence of Mo and Ti was not observed on the surfaces after MCC-1 testing at 200 °C (Table 6.6) unlike MCC-5 and MCC-1 testing at 90 °C (Table 6.4 and 6.5) indicating higher thickness of zirconium rich oxide scale.

Table 6.4. EDS analysis of MWF alloy specimen after 260 days of MCC-5 testing at 90 °C

MWF		Elements (wt.%)					
alloy	Cr	Fe	Ni	O	Zr	Ti	Mo
K1	11.4	46.3	19.5	6.5	14.7	0.3	1.3
K2	11.2	45.3	16.1	7.4	17.7	0.2	2.1
K3	9.6	44.2	15.6	8.6	20.0	0.3	1.7
K3B	9.0	43.5	12.6	10.5	22.3	0.3	1.8
K4	9.3	42.7	11.2	11.4	23.2	0.2	2.0

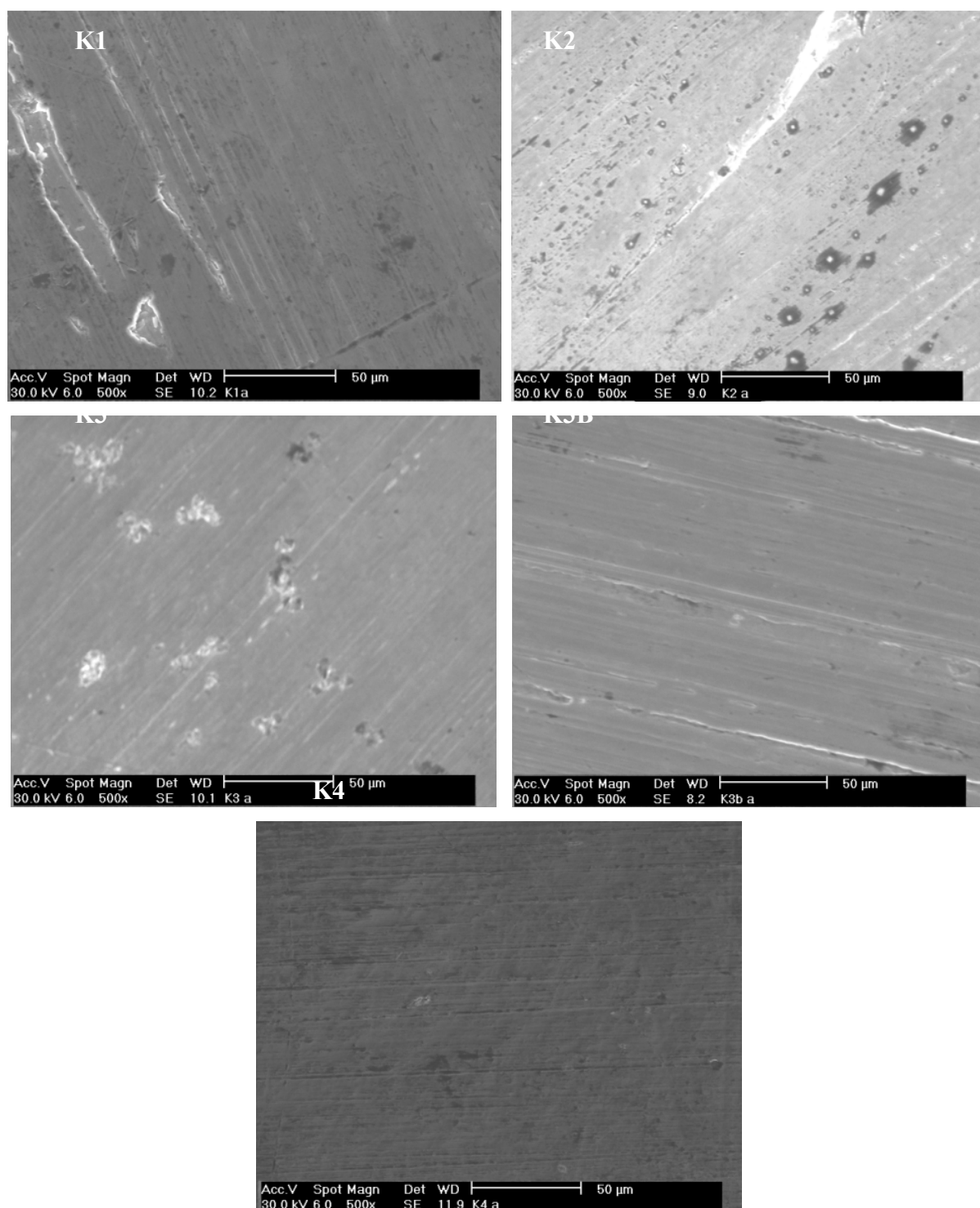


Fig. 6.4. SEM images of MWF alloys after 90 days of MCC-1 testing at 90 °C.

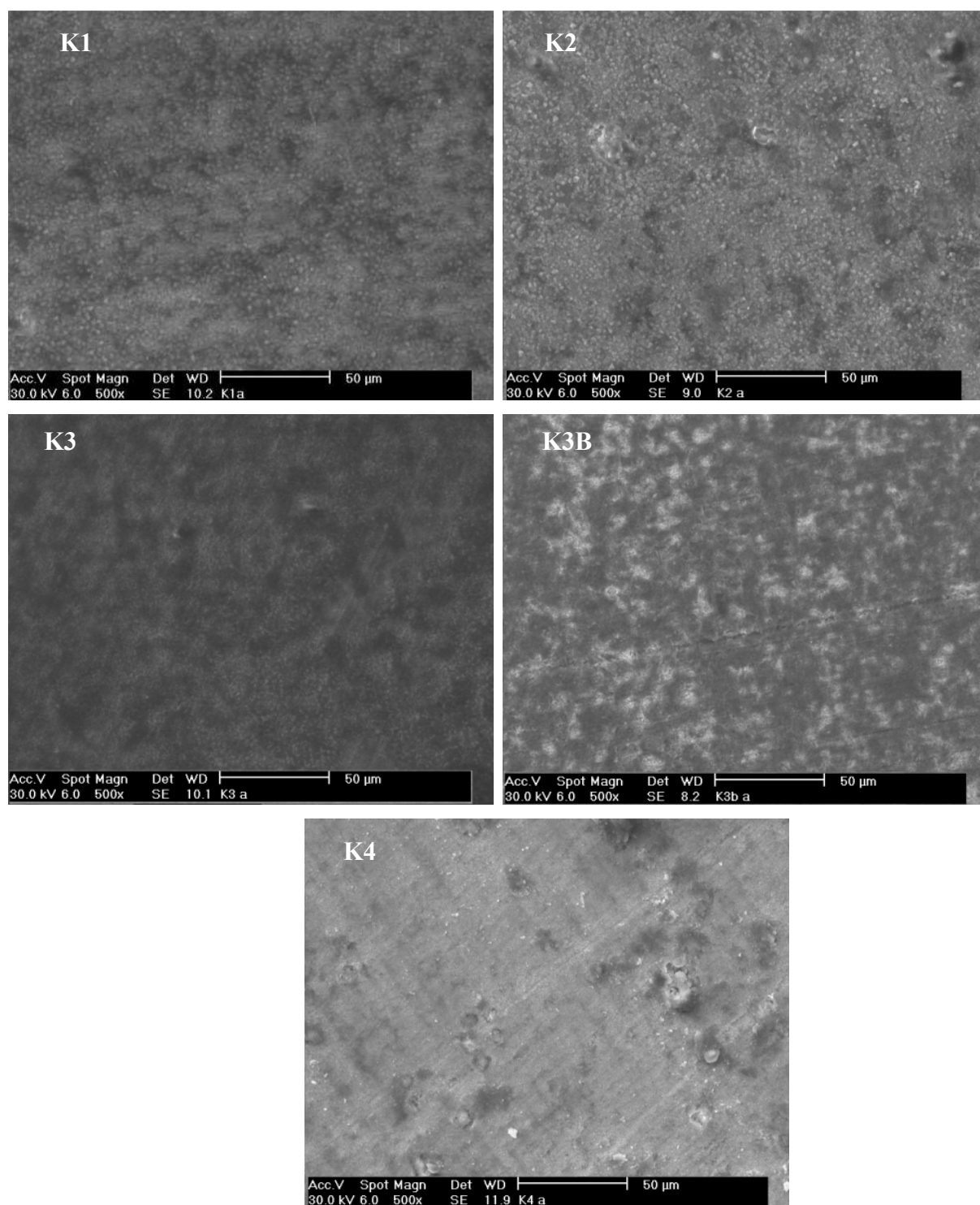


Fig.6.5. SEM images of MWF alloys after 90 days of MCC-1 testing at 200 °C.

Table 6.5. EDS analysis of MWF alloy specimen after 90 days of MCC-1 testing at 90 °C.

MWF	Elements (wt.%)						
alloy	Cr	Fe	Ni	O	Zr	Ti	Mo
K1	13.7	58.2	12.7	4.3	9.5	0.2	1.4
K2	12.4	52.7	15.7	5.0	12.4	0.3	1.5
K3	10.5	51.5	11.8	7.0	17.9	0.2	1.1
K3B	11.8	45.5	12.4	8.6	19.9	0.3	1.5
K4	10.0	42.2	10.8	12.5	22.5	0.3	1.7

Table 6.6. EDS analysis of MWF alloy specimen after 90 days of MCC-1 testing at 200 °C.

MWF	Elements (wt.%)					
alloy	Cr	Fe	Ni	O	Zr	
K1	11.0	44.7	13.5	21.5	9.3	
K2	9.1	40.9	13.0	21.4	15.6	
K3	9.7	35.7	9.6	25.8	19.2	
K3B	8.8	32.8	9.3	30.0	19.1	
K4	9.1	29.9	7.1	31.2	22.7	

6.3.1.3b. SEM and EDS analysis after exposure in simulated ground water

The SEM images of MWF (K2) alloy's surface after exposure in KGW, RGW-1 and RGW-2 is shown in Figure 6.6. The result showed the formation of a few localized pits which could have formed due to material loss from MWF surface. Inside the pit whitish deposition was observed and this deposition was also observed along the polishing lines. This localized

attack was prominent in KGW and RGW-2. The average area EDS analysis of the MWF surface (Table 6.7) showed the formation of zirconium rich oxide layer. The EDS investigation was also carried out on the white spot and the result (Table 6.7) showed that the intensity of Zr and oxygen was comparatively higher in these places.

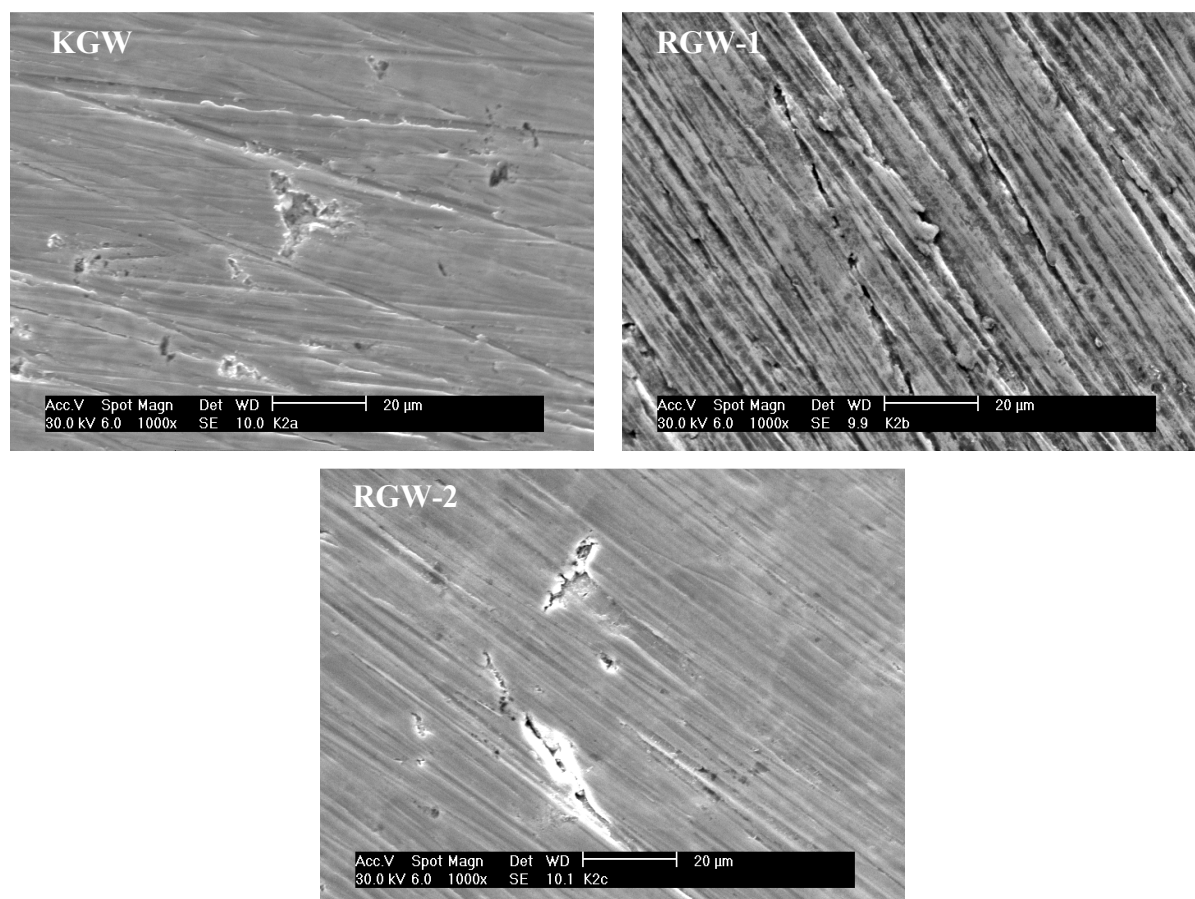


Fig.6.6. SEM images of MWF alloy (K2) after MCC-1 testing at 90 °C for 90 days.

The composition of the ground water as shown in Table 3.3 contain chloride ion which was responsible to damage the hydrated passive film at the metal leachate interface due to the formation of soluble chloride complex [145]. Hence localized corrosion could take place. But the Zr in the MWF alloy forms Zr rich oxide film at these sites and protected them from further dissolution. The attack was observed comparatively higher in KGW due to

higher concentration of chloride in its composition. Though localized material loss was observed in the surface morphological images, the solution analysis result did not show the presence of alloying element in its composition. This observation suggested that either the material loss was insignificant or the material remained on the surface and made it protective by the deposition of the corrosion product.

Table 6.7. EDS analysis for elemental concentration of the MWF alloy (K2) surface after MCC-1 testing in simulated ground water media at 90 °C for 90 days.

Leachant		Elemental Concentration (wt.%)					
		Cr	Fe	Ni	O	Zr	Si
KGW	Average area	9.6	47.3	15.6	5.5	20.6	1.4
	White spot	8.1	40.5	14.0	7.3	27.9	2.2
RGW-1	Average area	12	58.8	12.9	4.3	10.5	1.5
	White spot	10.7	51.2	11.5	6.4	18.1	2.1
RGW-2	Average area	12.5	59.8	12.2	3.9	10.2	1.4
	White spot	11.3	53.9	11.2	5.8	16.3	1.5

6.3.1.3c AFM analysis after MCC testing

Significant oxide scale formation was observed from SEM/EDS study. The AFM analysis was carried out to get a clear idea about the thickness and topographic features of these oxide scales. The AFM topographies of the MWF alloys surfaces after leachability testing in different conditions are shown in Figures 6.7 to 6.12. The surface topographies of MWF alloys exposed during MCC-5 and MCC-1 testing at 90 °C (Fig. 6.7 and Fig. 6.8) showed formation of surface scale with the presence of polishing lines. The thickness of the surface scaling was varying from 150 nm to 300 nm. Whereas, in Figure 6.8, the surface

topographies of MWF alloys after 90 days of MCC-1 testing at 200 °C showed thick scale formation with the appearance of globular oxide particles. The thickness of the oxide scale was varying from 300 to 600 nm (Fig. 6.8).

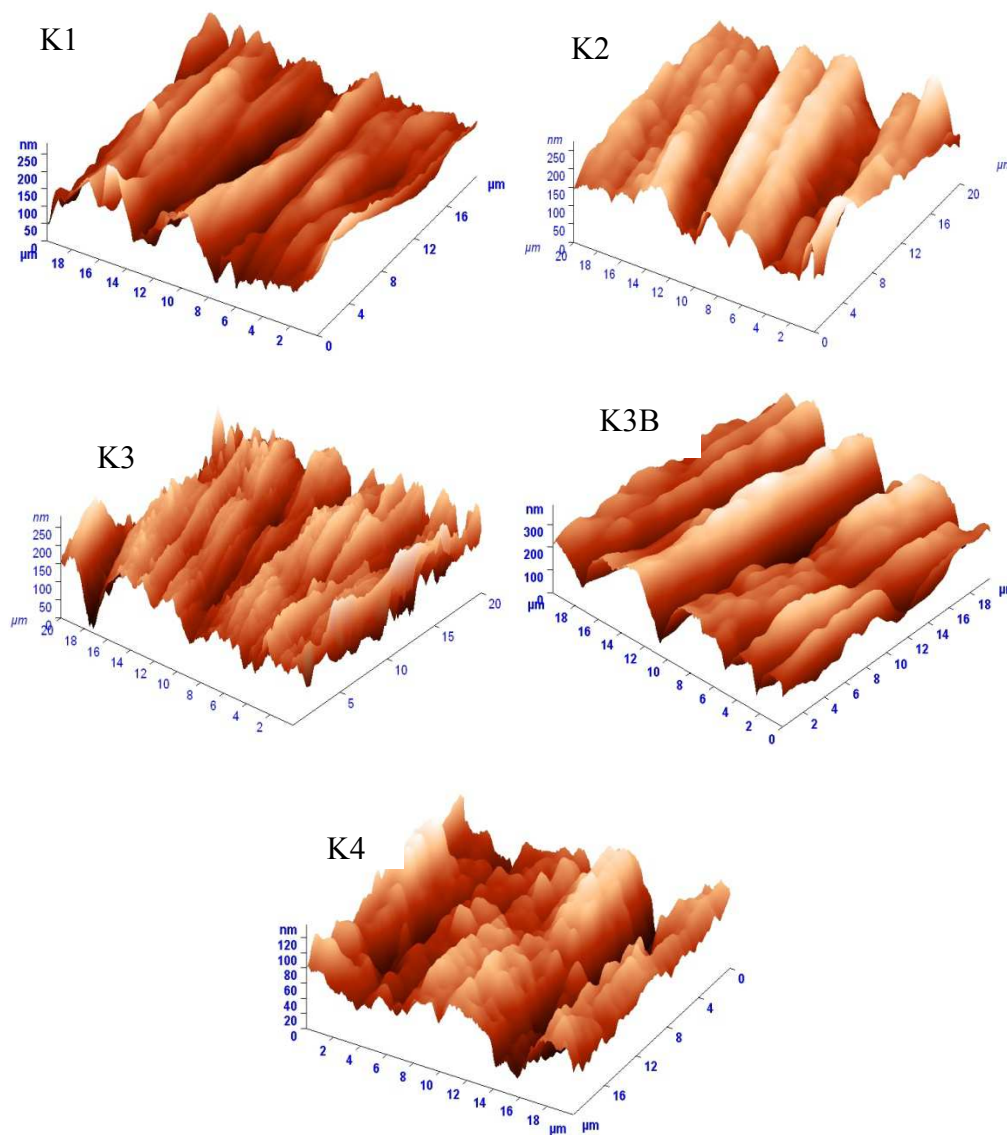


Fig. 6.7. AFM images of MWF alloys after 260 days of MCC-5 testing at 90 °C.

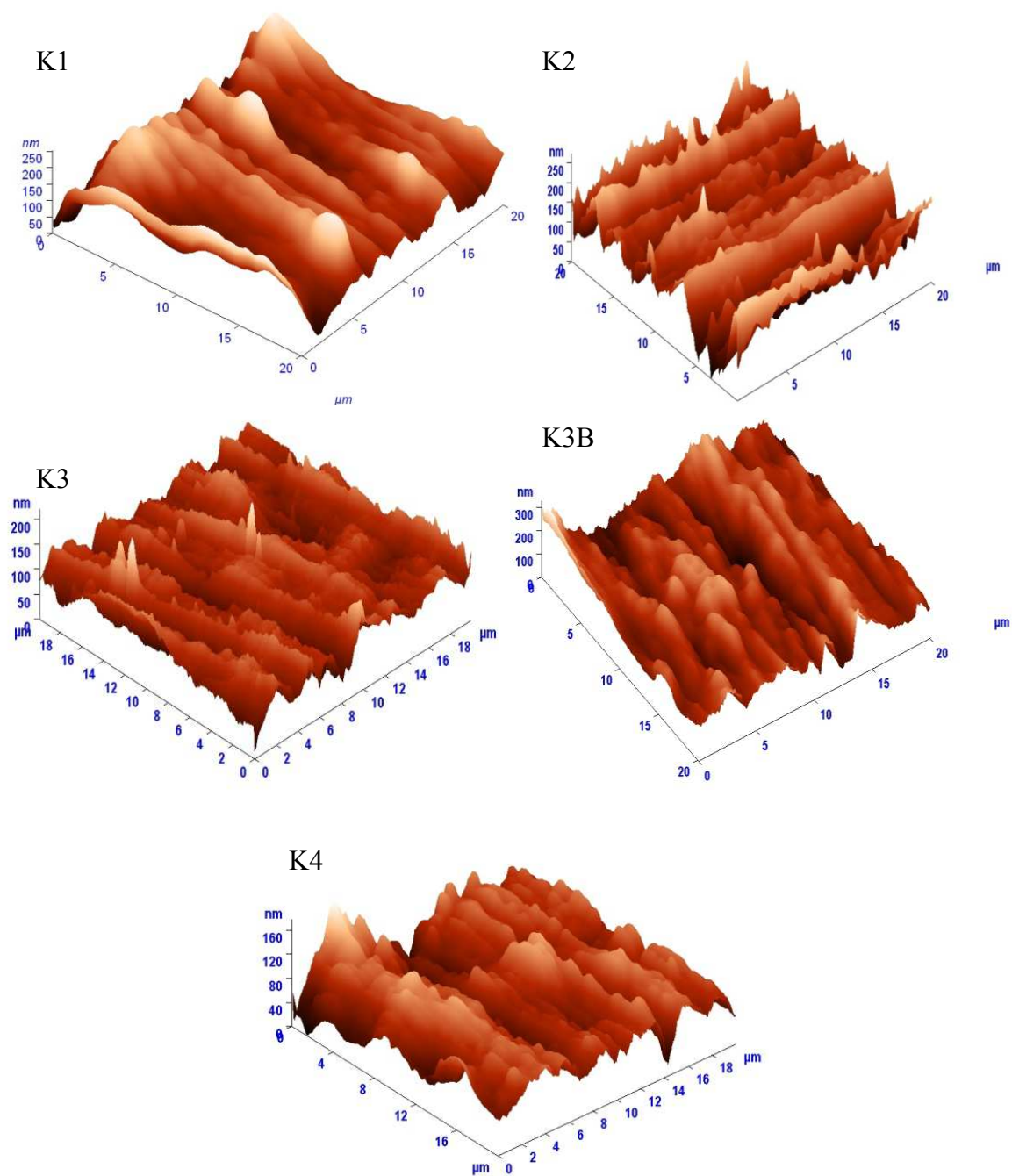


Fig. 6.8. AFM images of MWF alloys after 90 days of MCC-1 testing at 90 °C.

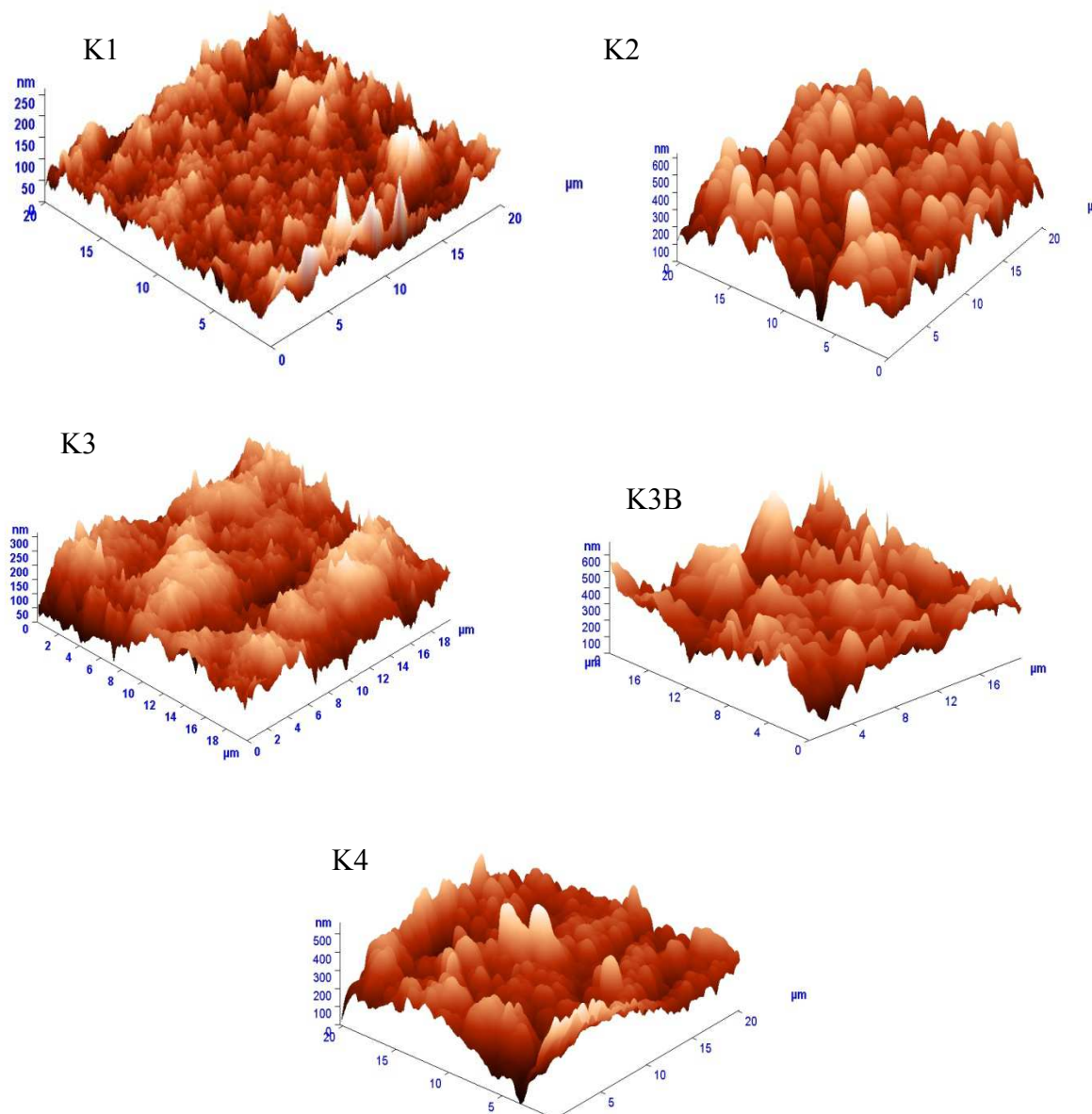


Fig. 6.9. AFM images of MWF alloys after 90 days of MCC-1 testing at 200 °C.

The AFM topographies of MWF alloy K2 after exposure in KGW, RGW-1 and RGW-2 are shown in Figures 6.10, 6.11 and 6.12 respectively. In these figures the left side images showed two dimensional representations where as right side images showed three dimensional representations. The topography of the whitish zirconium rich oxide deposition observed in SEM morphology was clearly seen from AFM analysis also. Around 100 to 200 nm thick deposition was observed on the MWF surface and intensity of the deposition was more along the edges of polishing lines.

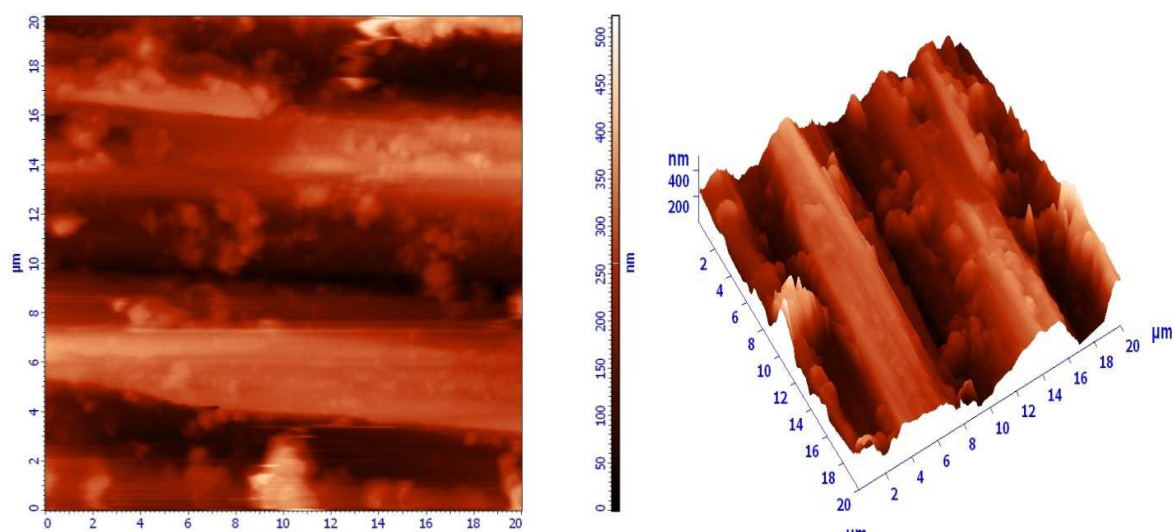


Fig. 6.10. AFM images of MWF alloy (K2) after 90 days MCC-1 testing in KGW at 90 °C.

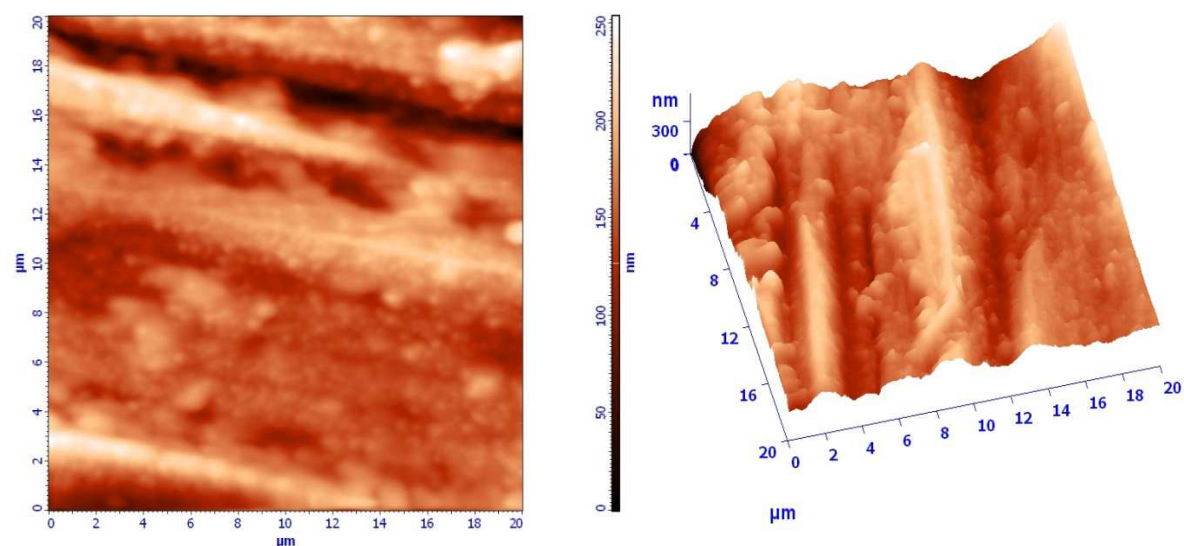


Fig. 6.11. AFM images of MWF alloy (K2) after 90 days MCC-1 testing in RGW-1 at 90 °C.

From the surface morphology, formation of surface scaling was observed and from the EDS analysis, it was confirmed that the scale formed was rich in zirconium oxide. The zirconium oxide thus formed, acted as protective film and resisted selective leaching. It is reported that if the corrosion products remain on the sample surface, it is difficult to detect them by solution analysis, though the leachant is aggressive [73, 156]. Hence, as expected the zirconium oxide rich corrosion product formed on the MWF surface was well adherent and

protected the MWF surface from selective leaching. Generally during steam corrosion testing at 200 °C on 316 SS-Zr MWF alloy by Abraham and Deitz [78] the formation of hematite (Fe_2O_3) layer on the zirconium oxide film was observed. However, during immersion testing at 200 °C the Fe_2O_3 layer was not detected, which could have spalled off into the test environment, and hence only zirconium oxide was found on the top layer. The thickness of the surface deposition as well as the intensity of oxygen (Table 6.6) were comparatively higher at higher temperature in static condition indicating formation of thicker film on the MWF alloys surface.

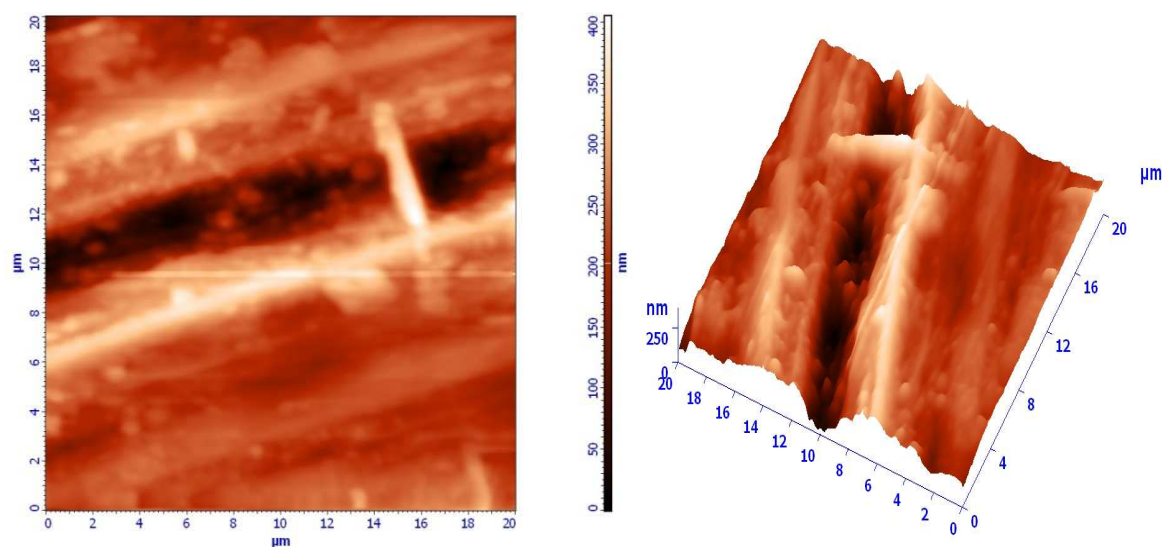


Fig. 6.12. AFM images of MWF alloy (K2) after 90 days MCC-1 testing in RGW-2 at 90 °C.

This investigation confirmed the formation of stable passive film under this test environment to protect the MWF alloys from corrosion and selective elemental leaching. Moreover, intensity of the zirconium and oxygen in the oxide film was found to be more for the MWF alloys with higher concentration of Zr, which makes the alloys more resistant towards selective leaching.

6.3.2 Microbial induced corrosion study

The main objective of this study was to monitor the formation of biofilm on MWF alloy surface and to assess the corrosion behaviour under these biofilm in the repository environment. Exposure studies in microbe cultured simulated Rajasthan and Kalpakkam ground water was adopted and evaluation of microbial attachment was done by TVC, epifluorescence microscopy, SEM and AFM studies. Corrosion behaviour was evaluated by using different electrochemical corrosion testing and the surface morphological analysis.

6.3.2.1 Evaluation of bacterial density and biofilm morphology

Bacterial density in the culture media and on the MWF surface was evaluated by using TVC count method and the results are shown in Table 4. TVC results confirmed that the growth of *Bacillus* sp. and *Pseudomonas* sp. in RGW and KGW media were in the range of 1×10^6 cfu ml⁻¹ to 5×10^6 cfu ml⁻¹. TVC results showed that the attachment of *Bacillus* sp. on the MWF alloy surface in KGW was around 1.3×10^5 cfu cm⁻² and in RGW was 1.4×10^5 cfu cm⁻². The attachment of *Pseudomonas* sp. on MWF alloy on both media was higher (in KGW 2.4×10^5 cfu cm⁻², in RGW 3.2×10^5 cfu cm⁻²).

Table 6.8. Quantitative result of bacterial density by TVC method

Solution	Bacterial growth in culture media		Bacterial growth on MWF surface	
	<i>Bacillus</i> Sp.	<i>Pseudomonas</i> Sp.	<i>Bacillus</i> Sp.	<i>Pseudomonas</i> Sp.
	(cfu/cm ²) $\times 10^6$	(cfu/cm ²) $\times 10^6$	(cfu/cm ²) $\times 10^5$	(cfu/cm ²) $\times 10^5$
KGW	2.5 ± 0.5	4.8 ± 0.3	1.3 ± 0.3	2.4 ± 0.1
RGW	3.1 ± 0.4	5.1 ± 0.5	1.4 ± 0.2	3.2 ± 0.2

Figure 6.13 shows the epifluorescence microscopic images for bacterial attachment on the MWF surface. All the images supported the trend of TVC count as shown in Table 6.8. The microbial cells were attaching and surviving on the alloy surface. However it was observed that the density of *Bacillus* sp. was less when compared to *Pseudomonas* sp. The *Pseudomonas* sp. exhibited a tendency to form dense biofilm on the MWF surface.

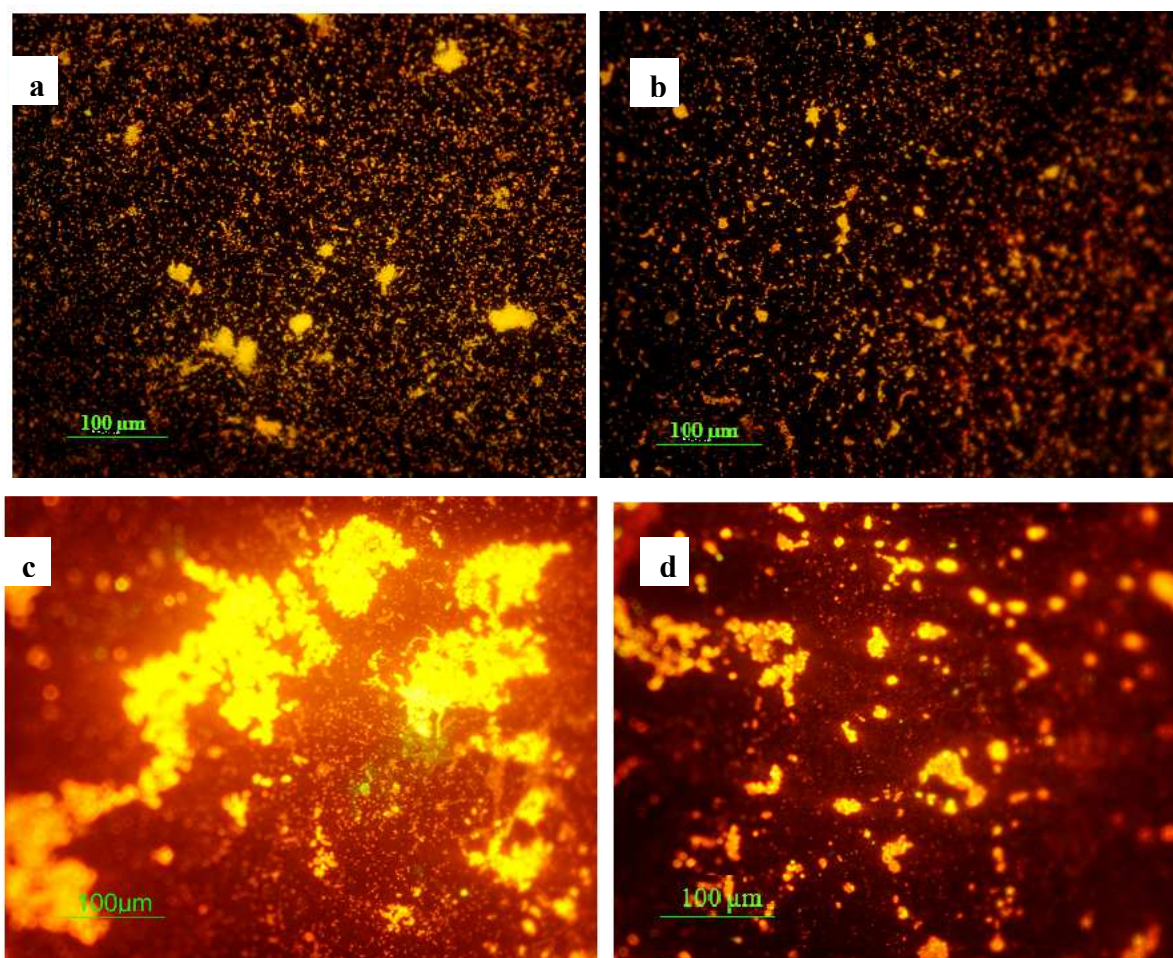


Fig. 6.13. Epifluorescence microscopic structure in different geological environment. (a) *Bacillus* sp. in KGW media (b) *Bacillus* sp. in RGW media (c) *Pseudomonas* sp. in KGW media (d) *Pseudomonas* sp. in RGW media.

6.14 shows the SEM morphology of the biofilm on the etched MWF alloy exposed in *Bacillus* sp. and *Pseudomonas* sp. culture media in KGW and RGW. The microstructure of the MWF alloy showed two different phase formation; the dark phase with D9 SS solid solution matrix and bright phase with Zr rich intermetallic compounds (Fig.4.1). In all the

images it was observed that the microbes were aggregating on bright phases of Zr intermetallics. Figure 6.14 also showed that the density of *Pseudomonas* sp. cells was comparatively higher and preferentially aggregating on Zr- intermetallic site.

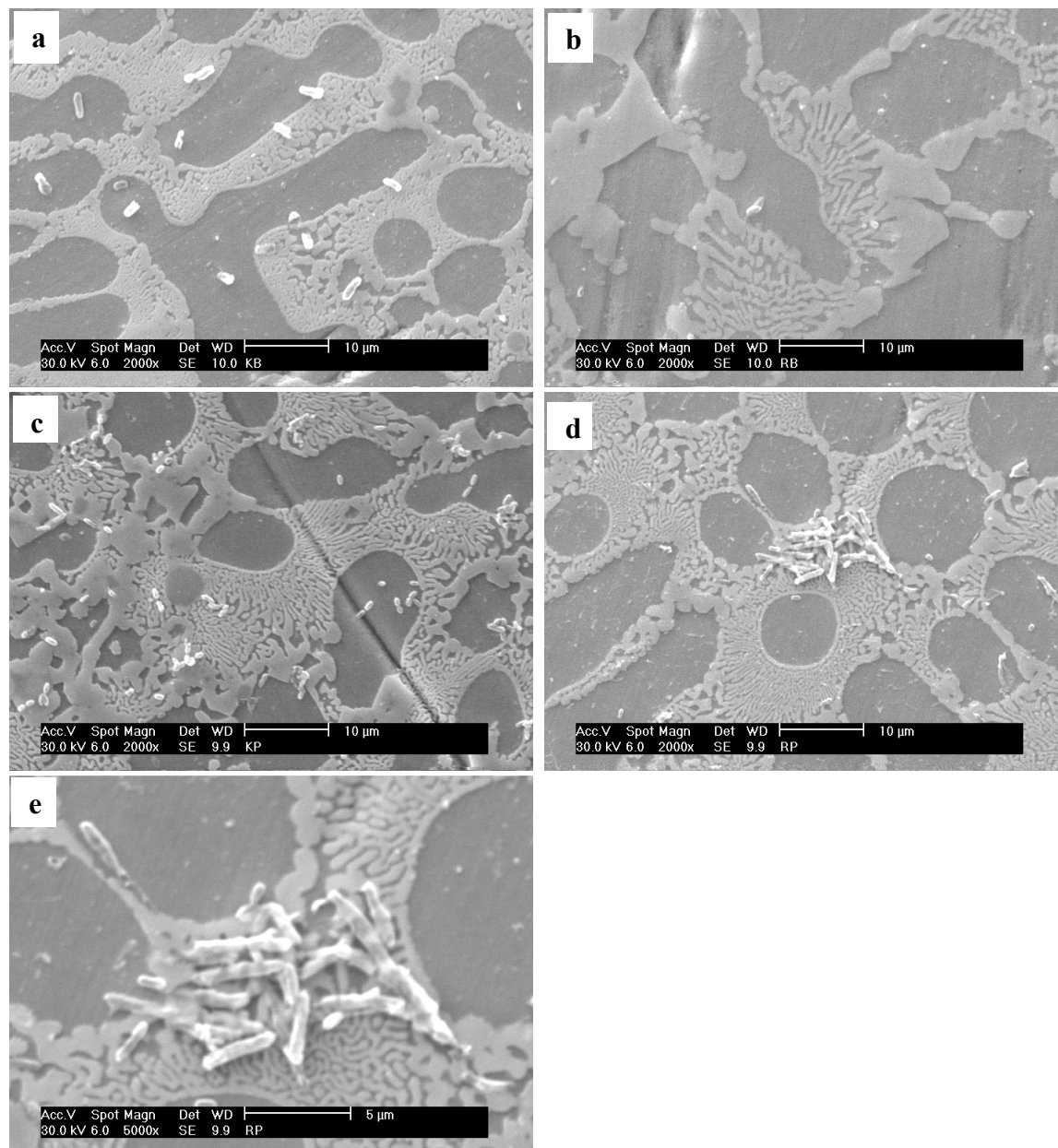


Fig. 6.14. SEM microstructure of the MWF surface exposed in different bacterial and geological environment. (a) *Bacillus* sp. in KGW media (b) *Bacillus* sp. in RGW media (c) *Pseudomonas* sp. in KGW media (d) *Pseudomonas* sp. in RGW media (e) magnified view of *Pseudomonas* sp. in RGW media

The AFM surface topographical images (Fig.6.15) also showed similar features as seen in SEM images. From AFM topography the attachment of bacteria on the Zr intermetallic phases was easily confirmed. Additionally AFM images showed slime formation for *Pseudomonas* sp. which was not observed for *Bacillus* sp. The *Bacillus* sp. was attached in a scattered manner. Wider area was selected to observe the *Bacillus* sp. (100 μm by 100 μm) compared to *Pseudomonas* sp. (40 μm by 40 μm).

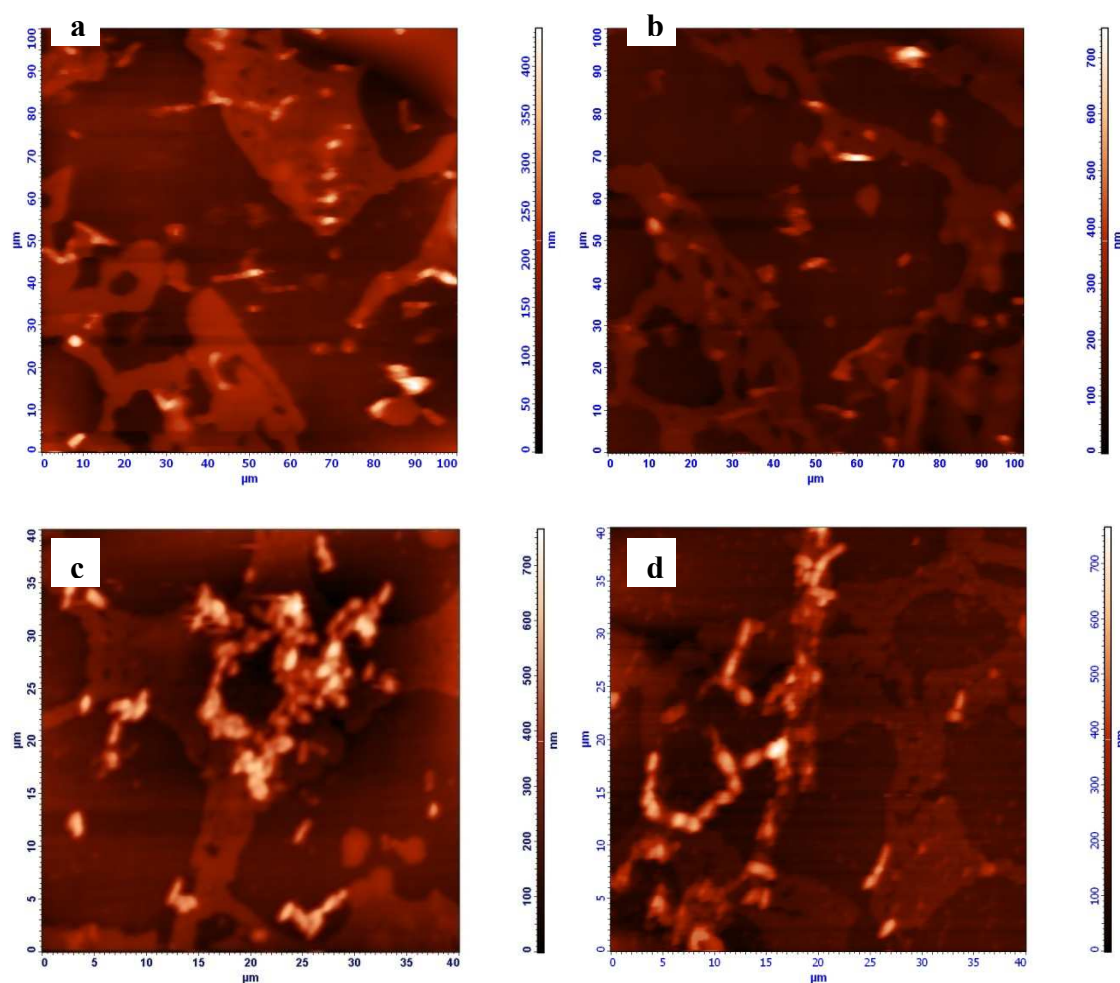


Fig. 6.15. AFM images of etched MWF alloy surfaces exposed to different bacterial culture media (a) *Bacillus* sp. in KGW media (b) *Bacillus* sp. in RGW media (c) *Pseudomonas* sp. in KGW media (d) *Pseudomonas* sp. in RGW media

TVC count showed good growth of microbes on MWF alloy surface in both the simulated geological environments. However, in both the environments, density of

Pseudomonas sp. was higher on MWF alloy surface compared to *Bacillus* sp. Epifluorescence microscopy, SEM and AFM images showed dense biofilm of *Pseudomonas* sp. and scattered cells of *Bacillus* sp. *Pseudomonas* sp. has higher tendency to form dense biofilm due to slime formation on the metal surface [157] which was clearly observed from the AFM images. Bacteria generally attach on the surface for better survival conditions like more nutrients, protection from biocides and predators [31, 158]. However for their nutrient requirement bacteria favoured adhesion on MWF alloy. SEM and AFM morphologies showed higher bacterial adhesion on the brighter Zr rich phase and lesser adhesion on dark matrix contains Fe solid solution phase where Zr is minimum [159,160] and this could be due to the biocompatible nature of Zr [153].

6.3.2.2 Electrochemical corrosion testing

6.3.2.2a Open circuit potential monitoring and potentiodynamic polarization study

The OCP - time and potentiodynamic polarization study was carried out to study the corrosion behaviour of MWF alloy in bacterial environment. All the electrochemical studies were carried out in bacterial culture and the results were compared with the result obtained in sterile media. Figures 6.16 and 6.17 show the OCP versus time plots of MWF alloy in KGW and RGW media with and without bacterial species respectively. From both the figures it was observed that the OCP of the MWF alloy moved towards active direction in bacterial exposed solution. Though there was not a significant difference between the OCP of the MWF alloy in *Bacillus* sp. and *Pseudomonas* sp. culture solutions, the solution with *Bacillus* sp. exhibited relatively nobler OCP than *Pseudomonas* sp.

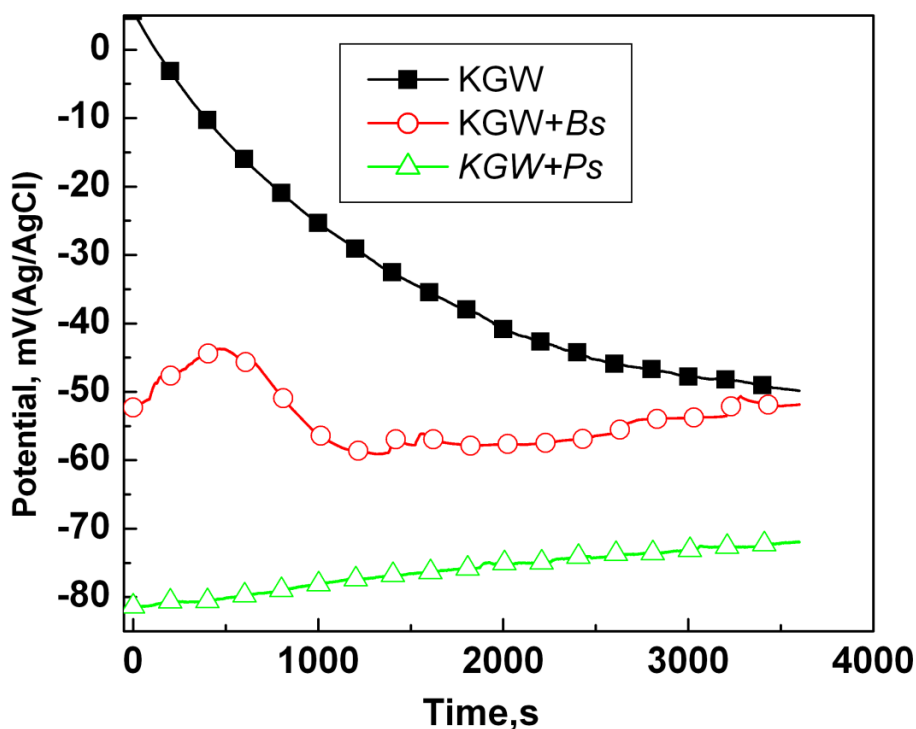


Fig. 6.16. OCP variation with time for MWF alloy in KGW media in sterile condition and with presence of different bacterial species. (*Bs*-*Bacillus* sp., *Ps*-*Pseudomonas* sp.).

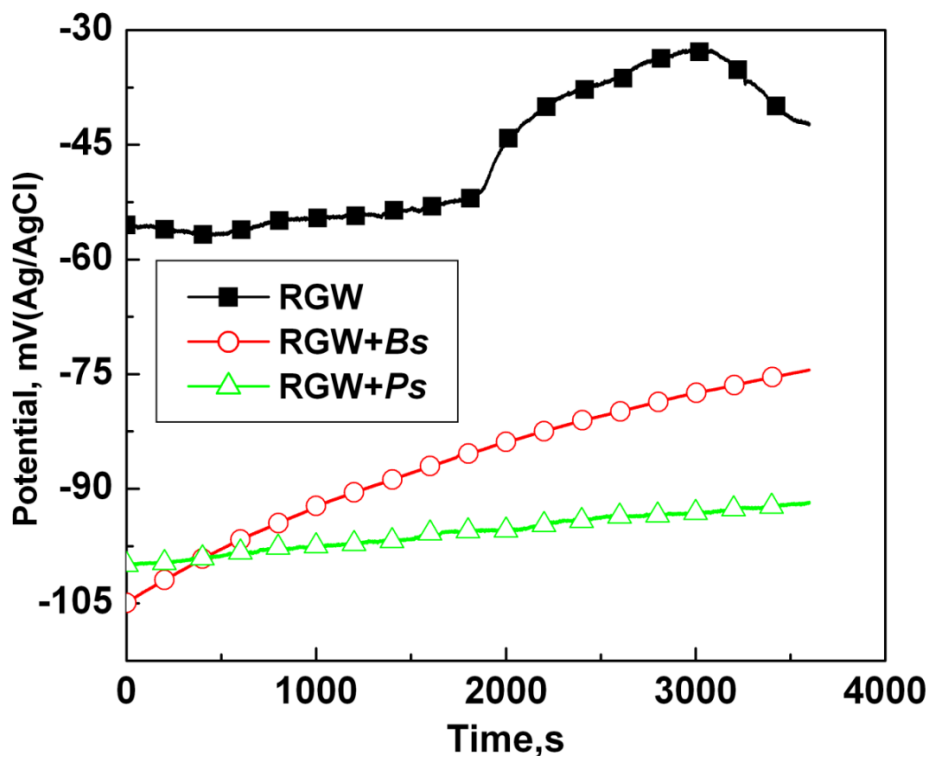


Fig. 6.17. OCP variation with time for MWF alloy in RGW media in sterile condition and with presence of different bacterial species (*Bs*-*Bacillus* sp., *Ps*-*Pseudomonas* sp.).

The potentiodynamic polarization curves obtained for MWF alloy exposed in *Bacillus* sp. and *Pseudomonas* sp. grown in KGW and RGW media are shown in Figures 6.18 and 6.19. The potentiodynamic polarization curves of MWF alloy in sterile culture were also performed to get comparative results. The values of corresponding electrochemical parameters (corrosion potential E_{corr} , passive current density i_{pass} and breakdown potential E_{BP}) are given in Table 6.9. The corrosion potential (E_{corr}) of MWF alloy in sterile KGW was -110 mV(Ag/AgCl). However, the E_{corr} value of the MWF alloy after exposing in *Bacillus* culture for 5 days was -464 mV(Ag/AgCl) and in *Pseudomonas* sp. culture was -560 mV(Ag/AgCl). Similarly in RGW, the E_{corr} values in sterile media was -289 mV(Ag/AgCl), in *Bacillus* sp. culture media was -472 mV(Ag/AgCl) and in *Pseudomonas* sp. culture was -643 mV(Ag/AgCl) respectively. Similarly their passive current density also increased in respective manner. In KGW the E_{BP} for the MWF alloy was 927 mV(Ag/AgCl) in sterile media, 616 mV(Ag/AgCl) in *Bacillus* sp. culture and 681 mV(Ag/AgCl) in *Pseudomonas* sp. culture respectively. In RGW media E_{BP} was 1004 mV(Ag/AgCl) in sterile media, 685 mV(Ag/AgCl) with *Bacillus* sp. culture and 1070 mV(Ag/AgCl) with *Pseudomonas* sp. culture media respectively.

According to Pope and Morris [155], micro-organisms like *Bacillus* sp. and *Pseudomonas* sp. form colonies on metal surfaces. The microbial colonies create sticky polymers which tend to attract and aggregate other biological and non biological species [158] and thus form patchy biofilms. Microbial metabolic products like oxygen, acids etc., create differential environment at the biofilm metal interface from the surrounding environment. Crevices can form below these patchy biofilm where metallic dissolution will be encouraged and corrosion will proceed [155, 161, 162].

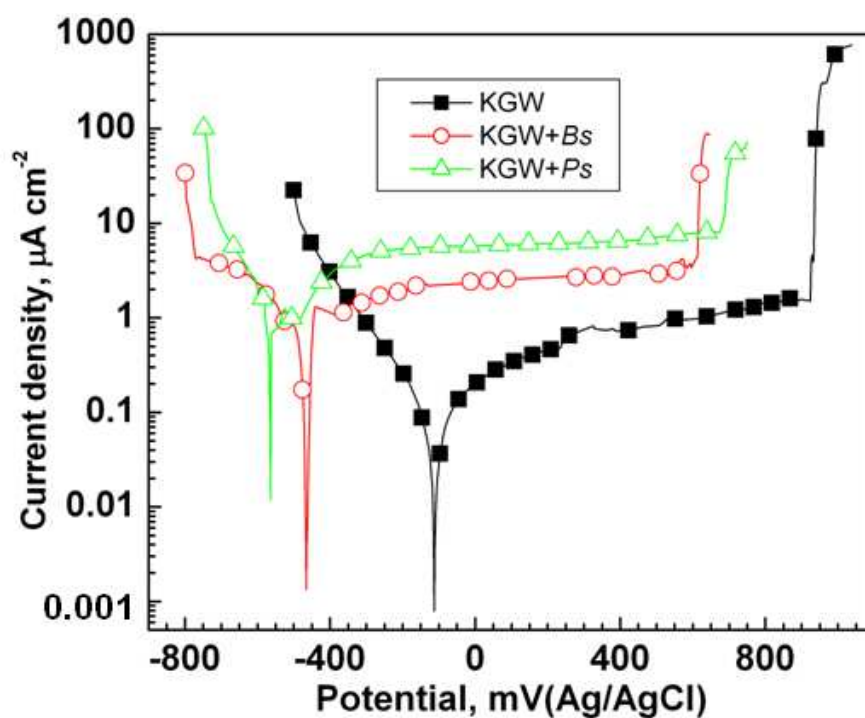


Fig. 6.18. Potentiodynamic polarization plots of MWF alloy exposed in KGW media in sterile condition and with presence of different bacterial species (*Bs*-*Bacillus* sp., *Ps*-*Pseudomonas* sp.).

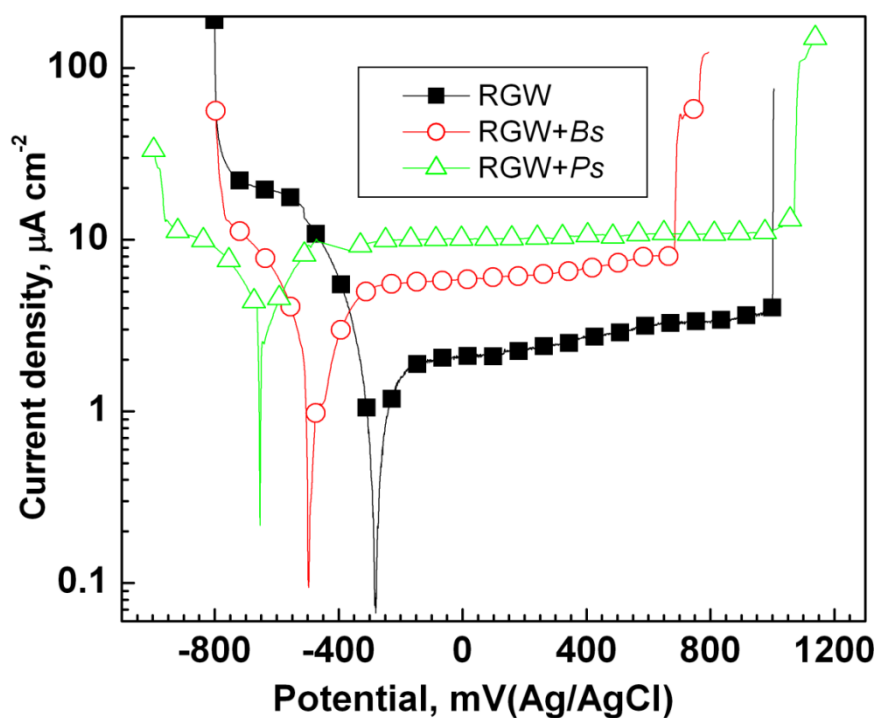


Fig. 6.19. Potentiodynamic polarization plots of MWF alloy exposed in RGW media in sterile condition and with presence of different bacterial species (*Bs*-*Bacillus* sp., *Ps*-*Pseudomonas* sp.).

Table 6.9. Polarization parameter for MWF alloy in KGW and RGW with different bacterial sp.

Culture media	E_{Corr}	i_{Pass}	E_{BP}
	mV(Ag/AgCl)	$\mu\text{A cm}^{-2}$	mV(Ag/AgCl)
KGW	-110	0.4	927
KGW+ <i>Bacillus</i> sp.	-464	1.8	616
KGW+ <i>Pseudomonas</i> sp.	-560	4.5	681
RGW	-289	2.2	1004
RGW+ <i>Bacillus</i> sp.	-472	5.6	685
RGW+ <i>Pseudomonas</i> sp.	-643	9.6	1070

In both the ground water condition formation of crevices below the biofilm might be responsible for active E_{corr} , as observed from potentiodynamic polarization plot. From epifluorescence microscopy, SEM and AFM images it was observed that the density of *Pseudomonas* sp. attached on the metallic surface was more and hence responsible for more active potential compared to *Bacillus* sp. It was also reported by the earlier investigators [78, 159, 160] that Zr intermetallic phases are resistant to corrosion and selective leaching by the formation of stable and adherent Zr rich oxide layer on the surface [78]. However, the present study showed preferential bacterial attachment on Zr rich intermetallic phases. The respiration of these aerobic bacterial species causes depletion of oxygen under their aggregations. This was responsible for the formation of oxygen concentration cell and weakening of the Zr oxide layer leading to significant passive film dissolution and higher passive current density. The densely attached *Pseudomonas* sp. were responsible for more active corrosion potential and higher passive current density (Table 6.9). During polarisation with *Pseudomonas* sp. biofilm on MWF alloy higher breakdown potential was observed compared to that in *Bacillus* culture.

The probable reason might be the formation of slime on the surface, which was protecting the surface from transpassive dissolution.

6.3.2.2b Electrochemical impedance spectroscopy

EIS study was carried out to evaluate the passive film behaviour of the MWF alloy in the microbial cultured environment. The EIS spectra of the MWF alloy after 5 days immersion in different bacterial culture solution recorded in OCP condition are presented in Figures 6.20 and 6.21 for KGW and RGW respectively. The corresponding fitting parameters according to the equivalent circuit (Fig.3.10a) are provided in Table 6.10. It was observed that all the experimental plots were appearing as single unfinished semicircle arc with different radius indicating similar passivation mechanism. In both the cases of sterile KGW and RGW, the MWF alloy exhibited highest R_p and lowest capacitance value. After 5 days exposure in bacterial solution the R_p values decreased in all cases. In KGW the R_p value in sterile solution was $248 \text{ k}\Omega \text{ cm}^2$, in solution with *Bacillus* sp. it was $169 \text{ k}\Omega \text{ cm}^2$ and in solution with *Pseudomonas* sp. it was $149 \text{ k}\Omega \text{ cm}^2$. However, in RGW medium the R_p values decreased sharply with the addition of bacterial species. The R_p value in sterile solution was $440 \text{ k}\Omega \text{ cm}^2$, with *Bacillus* sp. it was $130 \text{ k}\Omega \text{ cm}^2$ and with *Pseudomonas* sp. it was only $3.2 \text{ k}\Omega \text{ cm}^2$. With the *Pseudomonas* sp. depression of the semicircle arc was also observed (Fig. 6.21).

The EIS results (Fig. 6.20 and 6.21) showed a decreasing trend in the R_p values for the specimens exposed to bacterial culture, corroborating with the results of potentiodynamic polarization experiments (Fig. 6.18 and 6.19). An extraordinary decrease of R_p value of around 100 fold was observed under *Pseudomonas* sp. biofilm in RGW media indicating corrosion initiation.

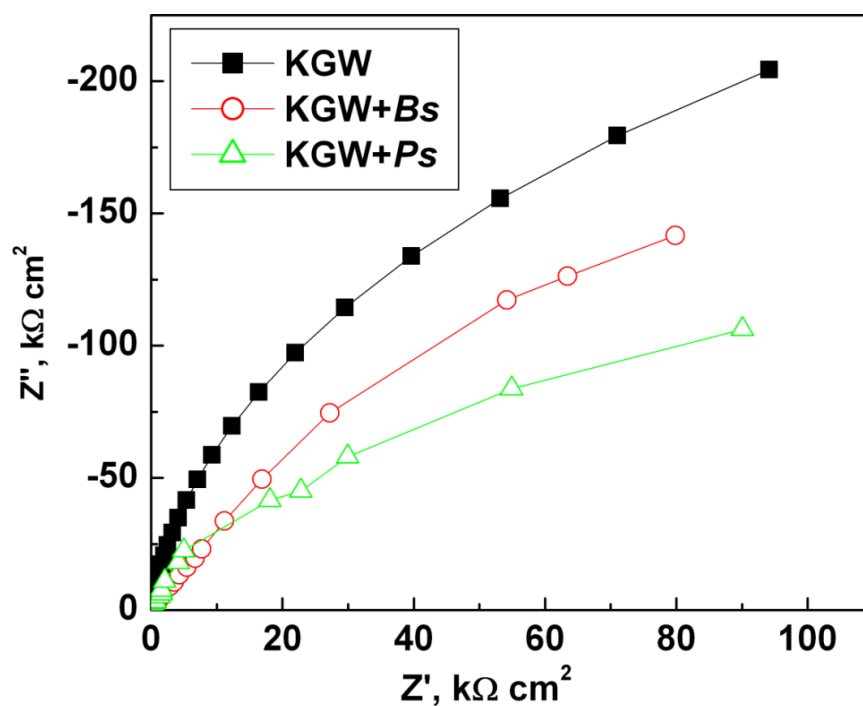


Fig. 6.20. EIS plots of MWF alloy exposed in KGW media. in sterile condition and with presence of different bacterial species (*Bs*-*Bacillus* sp., *Ps*-*Pseudomonas* sp.).

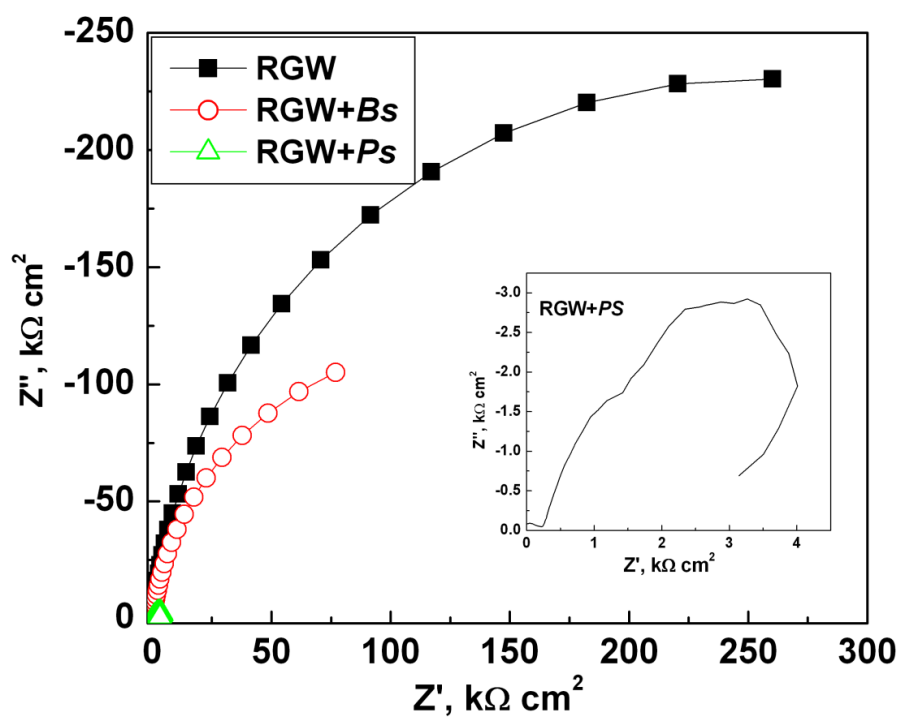


Fig. 6.21. EIS plots of MWF alloy exposed in RGW media in sterile condition and with presence of different bacterial species (*Bs*-*Bacillus* sp., *Ps*-*Pseudomonas* sp.).

Table 6.10. EIS fitted values for MWF alloy in KGW and RGW with different bacterial sp.

Culture media	R_s	R_p	CPE-T	CPE1-n
	($\Omega \text{ cm}^2$)	($\text{k}\Omega \text{ cm}^2$)	($\text{F cm}^{-2}\text{S}^n$) $\times 10^{-5}$	
KGW	50	248	2.1	0.96
KGW+ <i>Bacillus</i> sp.	238	169	2.4	0.93
KGW+ <i>Pseudomonas</i> sp.	40	149.4	5.4	0.91
RGW	99	440.8	1.8	0.92
RGW+ <i>Bacillus</i> sp.	245	130	3.1	0.93
RGW+ <i>Pseudomonas</i> sp.	25	3.2	20.2	0.76

The EIS is an important tool for characterizing the passive film stability. The key process involved in the impedance is the charge transfer at the metal/electrolyte interface which relates to the surface passive film property in the experimental environment [109,163]. In this technique the impedance was measured with scanning frequency from higher range to lower range. At high frequency the solution resistance will dominate for impedance and with decrease in frequency the interfacial resistance and the reactance will contribute to the impedance. At frequency below 10^{-3} Hz, corrosion will start and instability of the metal surface will be seen with the decrease of resistance value [109]. However in the present study, frequency was scanned till 10^{-2} Hz. Almost in all the experiments at the frequency 10^{-2} Hz the interfacial resistance played a major role. In RGW media (Fig. 6. 21) due to the formation of dense biofilm of *Pseudomonas* sp. on MWF surface and lower mineral concentration, surface corrosion started in the current frequency range and the depression of semicircle was observed. In sterile RGW media (Fig. 6. 21) the R_p value was $440 \text{ k}\Omega \text{ cm}^2$ representing very high polarization resistance with excellent passive film stability. Table 6.10 shows that in sterile condition the MWF specimen in RGW solution acquired higher R_p compared to that of

the KGW. From Table 3.3, the compositions of KGW and RGW media, higher concentration of cations in KGW could form a hydrated passive film like $\text{H}_2\text{O-M-OH}_2$ and protect the surface of the alloy [145]. However the higher concentration of Cl^- ion in KGW media could have lowered the film stability [139,145]. The presence of Cl^- ion could replace the water molecules and such replacement might form soluble chloride metal complex [150]. In RGW media the Cl^- concentration was very low. Hence the hydrated passive film especially the insoluble (Ca, Mg) SO_4 layer formed in the media will be more stable due to lack of chloride ion [160]. However in bacterial cultured solution especially with *Pseudomonas* sp. the bacteria can prevent the formation of insoluble layer on the surface. Moreover, there was a chance that, the minerals like Ca, Mg and S can be consumed by bacteria as their nutrient [31] and prevent the formation of the protective layer. Also, due to formation of bacterial biofilm and microbial metabolism [154], oxygen deficiency can appear on the metallic surface which could make the passive film weak and the metallic dissolution occurred resulting in lower R_p and higher i_{pass} .

6.3.2.3 Evaluation of surface morphology after electrochemical studies

Figure 6.22 shows the optical microscopic images of MWF alloy surfaces after polarization in respective electrolytes. The polarized MWF alloy surface in *Bacillus* sp. cultured in KGW and RGW showed a few micro pit formation (Fig. 6.22a & b). The polarized MWF alloy surface in *Pseudomonas* sp. culture in KGW media showed the formation of crevice and passive film dissolution (Fig. 6.22c). Higher dissolution comparable to electrochemical etching and crevices were observed on surface polarized in *Pseudomonas* sp. (Fig. 6.22d) cells in RGW.

From the optical microscopic images after polarization it was observed that, due to lesser attachment of *Bacillus* sp. the corrosion damage was less. However due to the higher attachment of *Pseudomonas* sp., the dissolution of passive film was higher under these

biofilms leading crevice corrosion [139]. Moreover in RGW the *Pseudomonas* sp. did not allow the formation of passive film, which was confirmed by the image (Fig. 6.22d) showing passive film removal and the surface appearing as etched surface.

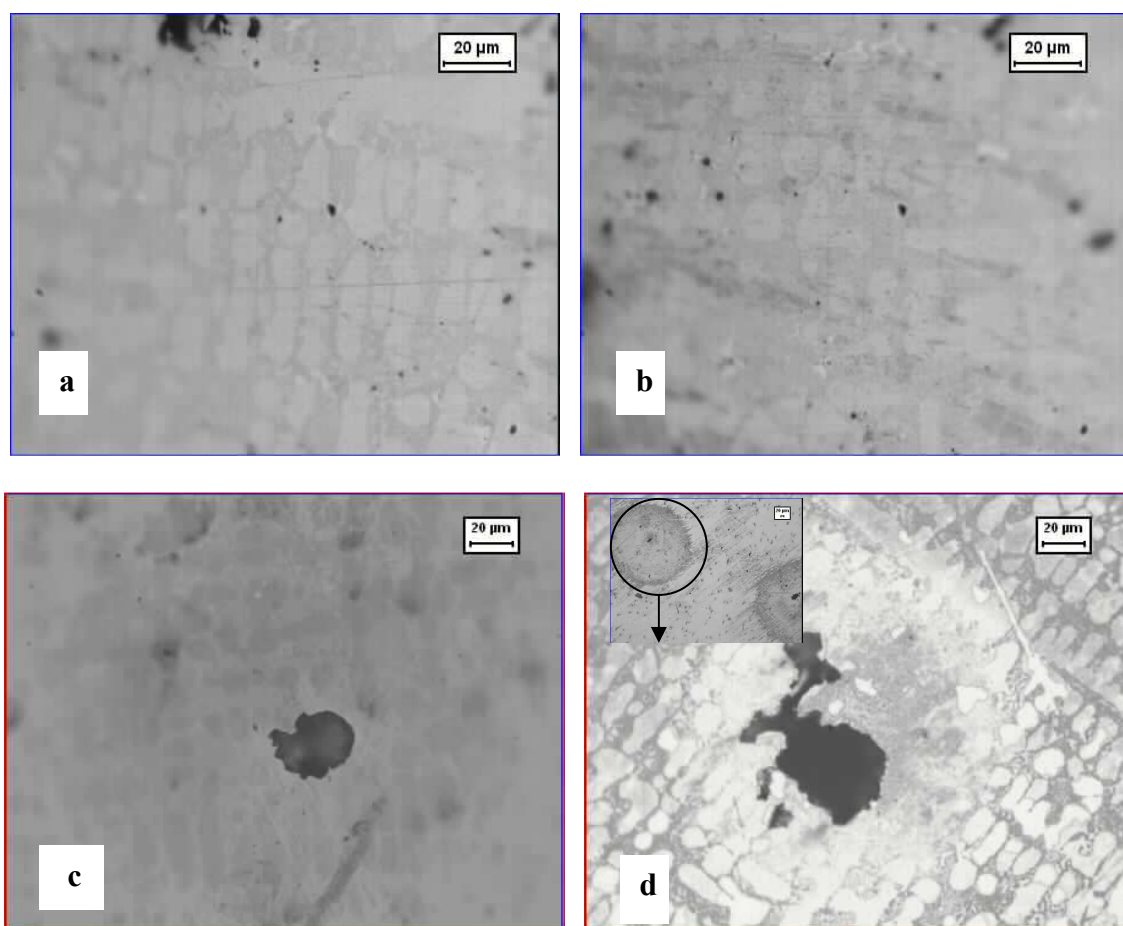


Fig. 6.22. Optical Microscopic images of MWF alloy surface after polarization in different electrolytes. (a) *Bacillus* sp. in KGW media (b) *Bacillus* sp. in RGW media (c) *Pseudomonas* sp. in KGW media (d) *Pseudomonas* sp. in RGW media

Due to microbial corrosion, lifetime of waste container will reduce and the waste form will come to contact with geological environment [30]. The present study clearly showed that the bacterial adhesion can pose severe threat on MWF alloy due to higher corrosion dissolution on Zr- rich intermetallic phases which are the host phases for actinide elements

[72,78,87]. Hence the actinide elements can leach out towards geological environment during long term storage and lead to ground water contamination.

6.4 Conclusions

The long term disposal issues in geological repository environment with respect to selective radionuclide leaching and microbial induced corrosion on MWF alloys have been discussed in this chapter. In order to understand the long term corrosion behaviour and selective elemental leaching the leachability tests was carried out in de-mineralized water and simulated ground water. The MIC was carried out using gram-positive *Bacillus* sp. and gram-negative *Pseudomonas* sp. in simulated geological environments. Based on the results obtained the following conclusions could be drawn.

1. Insignificant weight loss was observed for MWF alloys after different MCC testing which revealed negligible material loss during long term exposure in geological environment.
2. The ICP-OES analysis of the leachate solution revealed that leaching of elements was negligible at higher temperature and in most aggressive media like DM water. This was attributed due to the presence of secondary Zr intermetallic phases which possess improved resistance against both corrosion and selective leaching of elements.
3. The SEM/EDS analysis of MWF alloys' surface after leachability testing revealed the formation of Zr rich oxide layer. The intensity of zirconium oxide increased with increase in Zr concentration. The zirconium oxide layer was uniform and well adherent to metallic surface and enhanced the resistance to selective leaching.
4. The AFM topographical analysis after leachability testing showed that during MCC-1 and MCC-5 testing a uniform and thicker oxide scale was formed on the surface. The

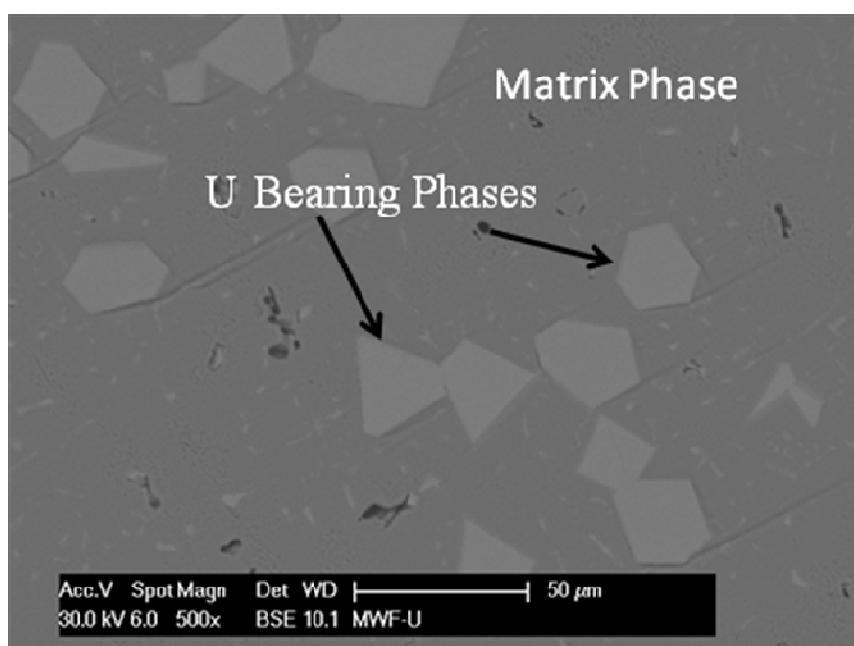
thicknesses of the surface scaling were in the range of 150 nm to 600 nm. It also showed that at higher testing temperature the thickness of oxide film was comparatively higher.

5. During long term exposure in simulated ground water media localized material loss was observed due to presence of chloride ion. However, the formation of zirconium rich oxide scaling protected the alloys from further leaching.
6. From microbial exposure study it was observed that there was considerable growth of microbial sp. in simulated geological environment and significant attachment on the MWF alloy surface. Compared to *Bacillus* sp. *Pseudomonas* sp. were more densely attached on the MWF alloy surface.
7. Both the microbes exhibited higher affinity towards the Zr rich intermetallic phases. *Pseudomonas* sp. formed thicker biofilm on the metallic surface, and created crevices on the surface.
8. Due to the formation of bacterial crevices active dissolution of the metal was observed. This leads to active E_{corr} , higher i_{pass} , and lower R_p .

Hence, the present investigation suggested that the simulated D9 SS-Zr MWF alloys exhibited very good resistance against corrosion and selective elemental leaching by the formation of adherent zirconium oxide layer in most aggressive DM water environment as well as with the presence of aggressive chloride ion. However, it was also observed that the presence of microbes will pose a threat for MWF alloy though they were resistant to corrosion and selective leaching in geological environment. Due to microbially induced corrosion, the radiation contamination of ground water system is a possibility which will be harmful for future generation. Hence, it is strongly recommended to perform further detailed study to develop some methods to make the surface of MWF alloy antibacterial for geological disposal.

CHAPTER 7

EFFECT OF NOBLE METAL AND URANIUM ADDITION ON THE BEHAVIOUR OF MWF ALLOYS



CHAPTER 7

EFFECT OF NOBLE METAL AND URANIUM ADDITION ON THE BEHAVIOUR OF MWF ALLOYS

Metal waste form alloys with the addition of noble metal fission products (NMFP) and uranium were cast and characterized to understand the influence of NMFP and U on the microstructure and corrosion behaviour of MWF alloys. The SEM analysis of NMFP added MWF alloys showed the formation of two phases, the dark Fe based solid solution matrix and the brighter Zr rich intermetallic precipitate similar to that of D9 SS-Zr MWF alloys. In the as-cast alloys the NMFPs remained at the interfacial boundary between the solid solution and precipitation phases. These NMFPs diffused into the Zr rich intermetallic phases after homogenization at 1323 K for 2 h. XRD study revealed that the NMFP added MWF alloys also formed Fe based solid solution matrix and different Ni-Zr and Fe-Zr type intermetallic phases and no discrete phases containing NMFP was observed. The SEM microstructure of NMFP and U added MWF alloys showed the formation of separate U bearing Zr-rich intermetallic phases and Fe based solid solution matrix. Phase analysis by XRD confirmed that the various compound phases formed in the U added MWF alloys were typically UZrO_2 , fcc Fe based solid solution and small amount of Fe-Zr and Ni-Zr intermetallic phases. Corrosion studies on NMFP added MWF alloys showed wide range of passivation potential with higher breakdown potential and polarization resistance indicating the formation of stable passive film in the geological media which would protect the alloys from corrosion dissolution. Long term leachability experiment with NMFP added MWF alloys indicated negligible leaching of the alloying elements with insignificant surface attack. The corrosion behaviour of U added MWF alloys showed nobler corrosion potential and wide range of passivation potential in DM water at pH 5 and in RGW, but pit formation was observed in

KGW media. EIS studies in all the simulated media exhibited higher polarisation resistance due to the formation of stable passive film at the metal solution interfaces.

7.1 Introduction

The objective of developing MWF alloys is mainly to immobilise the noble metal fission products (NMFP) such as Ru, Rh and Pd etc. and the radioactive actinide U, which are present in the anode dissolution basket of pyrochemical reprocessing. Vitrification of nuclear waste in glassy matrix is a well established technique, but the NMFPs are strong crystal formers which decrease the mechanical integrity of the vitrified glassy waste form and make it undesirable. The primary radioactive actinide, U present in metal waste stream is also incompatible to vitrified glassy matrix [65-70]. Hence, the chemical state of both NMFPs and U are the important deciding factor in the development of MWF alloys for geological disposal of pyrochemically reprocessed metallic waste. Though the NMFPs and U are expected to be compatible to metal matrix immobilisation, it is essential to understand their role in MWF alloys with respect to microstructure, phase composition and corrosion behaviour. Essentially, both NMFPs and U constitute the radioactive component in the MWF alloys which will be contaminating the ground water. Hence, understanding of their phase stability, corrosion and leaching behaviour in simulated ground water media are important and need to be studied.

In this chapter the distribution of NMFPs and U in the microstructure of the MWF alloys and their influence on the corrosion and selective leaching behaviour in the simulated repository environment is addressed. This study was carried out in two stages. In the first stage three MWF alloys of D9 SS-Zr-NMFP was cast (Table-3.2) and investigations on microstructure, phase analysis, corrosion and selective elemental leaching behaviour were carried out. In the second stage, MWF alloy of D9 SS-Zr-NMFP-U was cast and was characterised as per the sequence followed in stage I. As the

composition of MWF alloy with the Zr concentration of 8.5 wt.% (K2) exhibited the least corrosion and leachability behaviour in all the simulated ground water media (cf: Chapter 5 and 6) this alloy was selected for evaluating the influence of NMFPs and U on the corrosion behaviour of MWF alloy.

7.2 Experimental

A brief overview of the different experimental techniques adopted in this Chapter is given below (the details of each techniques are provided in Chapter 3)

- (i) Hardness values of different D9 SS-Zr-NMFP (the wt.% of NMFP taken were 1, 2.5 and 4 % and are denoted as N1, N2 and N3 respectively) and D9 SS-Zr-NMFP-U (U content 10 wt.%) MWF alloys were determined using PC based Vickers hardness tester with 10 kg load and 15 second indentation time.
- (ii) The microstructural investigation of the different D9 SS-Zr-NMFP and D9 SS-Zr-NMFP-U MWF alloys was carried out by SEM and EDS. For N1, N2 and N3, the microstructure was evaluated in the as-cast and heat treated (1323 K, 2 h) conditions and for the MWF alloy with U, the microstructure was evaluated in the as-cast condition only.
- (iii) Different compound phases present in these MWF alloys were identified by XRD.
- (iv) The corrosion behaviour of the MWF alloys N1, N2 and N3 was investigated in DM water at pH 1 and 5 and in simulated KGW using different electrochemical techniques including OCP, potentiodynamic polarization and EIS. The electrochemical corrosion behaviour of the MWF alloy with U was evaluated in DM water at pH 5 and in simulated KGW and RGW.
- (v) Optical microscopic examination was carried out after polarization in different simulated media to examine the corrosion attack on the surface of MWF alloys.

- (vi) The selective elemental leaching behaviour of the MWF alloys N1, N2 and N3 was evaluated by static leachability testing as per ASTM standard MCC-1 testing procedure in DM water at 90 °C for 90 days. The weight changes in the MWF specimen were measured after the MCC-1 testing, the leachate solution was analyzed by ICP-OES method and the surface morphology was examined by SEM/EDS.

7.3 Results and discussion

7.3.1 MWF alloys of D9 SS-Zr-NMFP

7.3.1.1 Hardness measurements

Table 7. 1 lists out the hardness values of MWF alloys N1, N2 and N3 along with that of MWF K2. The results showed that addition of NMFP increased the hardness of the MWF alloys and the hardness value increased with increase in NMFP concentration.

Table 7.1. Hardness of MWF alloys with and without NMFPs

MWF alloys	K2	N1	N2	N3
Hardness value (HV)	274 ± 6	304 ± 15	312 ± 13	324 ± 14

7.3.1.2 Microstructural analysis by SEM

The SEM microstructures of different NMFP added MWF alloys are shown in Figure 7.1 and the EDS analysis of the composition of the different microstructural phases are given in Table 7.2. Similar to D9 SS-Zr MWF alloys, these NMFP added MWF alloys also formed the dark Fe based solid solution and bright Zr rich intermetallic phases. In the MWF alloys N2 and N3 where NMFP concentration was 2.5 wt.% and 4 wt.% respectively, the Ru, Rh and Pd were present in the bright intermetallic phases. In the MWF alloy N1 where NMFP

concentration was about 1 wt.%, Ru and Rh were found neither at the matrix phase nor at the precipitation phase, but they remained at the interfacial boundary between the matrix and precipitation except Pd, which was present in both the phases. After heat treatment at 1323 K for 2 h, Ru, Rh and Pd were found to diffuse completely at the intermetallic phases in all the alloys. However, no significant changes could be observed in the microstructural features with the variation of NMFP concentration or after heat treatment.

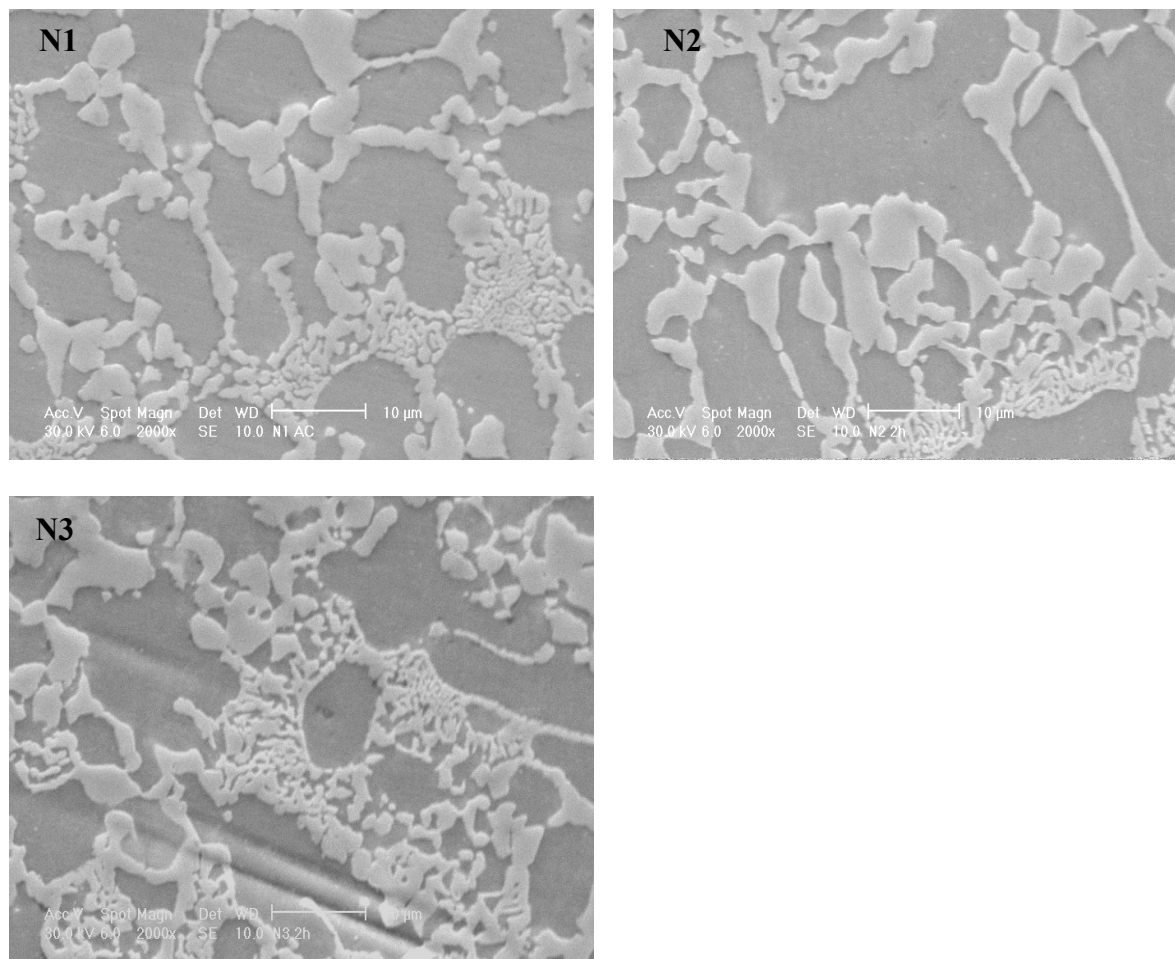


Fig. 7.1. SEM microstructure of different D9 SS-Zr-NMFP MWF alloys

Table 7.2. Elemental composition of NMFP added MWF alloys at different regions by EDS (in wt%) (AC- as-cast, HT- heat treated)

Alloy	Region		Si	Cr	Fe	Ni	Zr	Ru	Rh	Pd	Mo	Ti
N1	Matrix	AC	0.45	19.51	57.38	15.83	5.46	----	----	1.38	----	----
		HT	0.51	19.81	61.71	11.45	3.12	0.92	----	----	1.18	----
	Ppt	AC	1.00	5.14	33.76	21.14	34.94	----	----	2.64	1.39	----
		HT	0.85	5.05	33.17	22.02	31.65	1.84	0.80	1.90	1.15	0.57
	Bdy	AC		7.37	46.93	21.17	14.77	3.93	1.44	4.05	----	0.33
		HT	0.76	7.84	47.89	20.47	17.24	1.90	0.57	1.71	1.12	0.50
	Matrix	AC		17.63	65.83	8.61	3.56	3.83	0.20	0.30	----	----
		HT	0.20	18.54	67.65	8.84	3.18	0.45	----	----	1.28	----
N2	Ppt	AC	1.35	5.61	35.50	17.37	33.96	1.62	0.40	1.64	1.15	0.60
		HT	1.76	5.90	35.28	21.30	29.83	1.84	0.43	1.67	1.21	0.80
	Bdy	AC	0.87	12.09	53.61	13.42	16.38	1.16	0.43	0.59	1.46	----
		HT	0.83	7.52	45.29	18.03	23.55	1.43	0.61	1.72	1.02	
	Matrix	AC		17.02	68.76	10.87	2.74	----	----	----	----	0.61
		HT		18.72	65.89	8.68	2.19	----	----	----	1.32	0.82
	Ppt	AC	1.36	5.06	33.83	17.44	31.36	3.05	1.98	4.55	0.97	0.39
		HT	0.71	4.55	32.86	18.84	30.07	2.95	0.86	3.51	1.02	0.45
N3	Bdy	AC		16.71	60.58	11.98	5.82	----	1.30	1.21	2.20	0.20
		HT	0.64	7.97	42.77	16.99	26.65	1.71	0.53	2.74	----	----

Ppt- precipitation, Bdy- boundary, AC- as-cast, HT- heat treated.

The SS-Zr MWF alloys form Fe-based solid solution matrix and Zr-rich Laves type intermetallic phases [72]. The Laves intermetallic phases act as strong sink for impurities and fission products [78] and these phases are stable until 1173 K and are highly resistant to corrosion and selective elemental leaching (Chapters 4 to 6). The MWF alloys with NMFPs also showed the same behaviour in forming Fe based solid solution matrix and Laves type Zr rich intermetallic phases. The Zr rich Laves intermetallic phases hosted the NMFPs except alloy N1 in which NMFPs got selectively accommodated at the interfacial boundary between the matrix and intermetallic phases. However, after heat treatment at 1323 K for 2 h, all the NMFPs were found to diffuse in to the Zr rich Laves intermetallic phases.

7.3.1.3 XRD analysis for phase identification

Figure 7.2 shows the XRD pattern of different NMFP added MWF alloys. The typical compound phases formed in these alloys were almost identical to those phases formed in D9 SS-Zr MWF alloys. The major peaks corresponded to NiZr, Ni₅Zr, NiZr₂, Ni₇Zr₂, Fe₃Zr, FeZr₂ and austenite Fe based solid solution phases. There were no discrete phases for NMFPs including compounds of Ru, Rh and Pd and no systematic trend could be observed in the XRD pattern with respect to the concentration of NMFPs. The intensities of peaks corresponding to intermetallic and solid solution phases were almost the same for all the alloys. This observation is corroborated by the SEM microstructure which also did not show any significant microstructural difference among the alloys.

From the XRD results it is inferred that the NMFP elements dissolved and got distributed within the alloy phases. The SEM microstructure confirmed this observation that the NMFPs are soluble in the Zr rich Laves intermetallic phases. McDevitt et al. [21] reported that the NMFPs are soluble in the MWF alloy phases and preferentially in Zr(Fe,Cr,Ni)_{2+X} type Laves intermetallic phases. Hence, it is evident that the Zr rich intermetallic phases have a significant role in immobilizing the fission products. The SEM observation revealed the

segregation of NMFPs, probably at the interfacial boundary but these were also Zr rich phases.

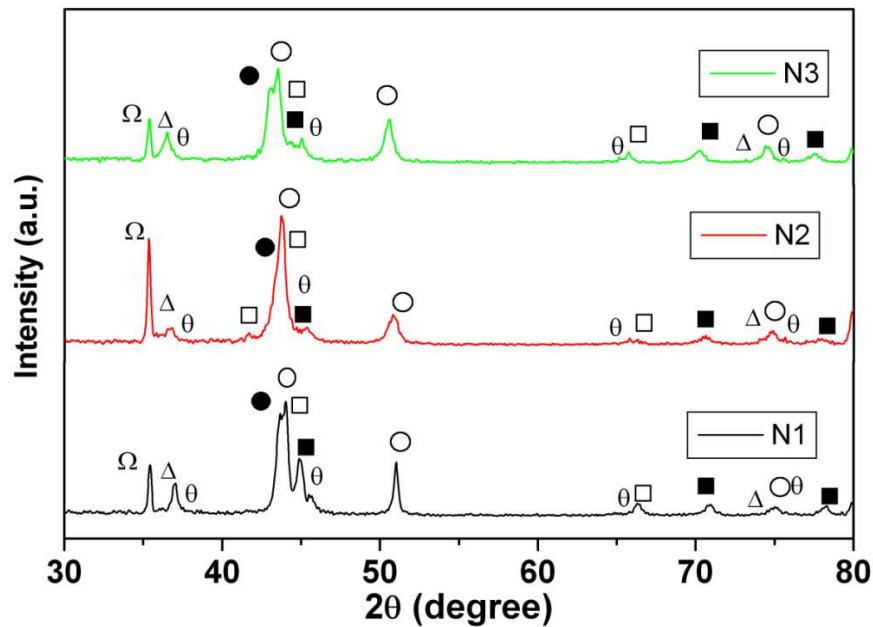


Fig. 7.2. XRD pattern of NMFP added MWF alloys (○-fcc Fe based solid solution, □ -Fe₃Zr, θ -FeZr₂, Δ-NiZr, ■-Ni₅Zr, Ω- NiZr₂, ●- Ni₇Zr₂)

7.3.1.4 Electrochemical corrosion testing

Different electrochemical techniques were used to evaluate the corrosion behaviour of the NMFP added MWF alloys. Electrochemical studies including OCP, potentiodynamic polarization and EIS were carried out in different simulated media such as DM water at pH 1 and 5 and in simulated Kalpakkam ground water (KGW).

7.3.1.4a OCP monitoring

To determine the equilibrium potential of the alloys in different simulated media, OCP was monitored for 1 h in non stirred and aerated condition. The OCP versus time plots for different NMFP added MWF alloys in various simulated geological media are shown in Figure 7. 3 to Figure 7.5. The OCP behaviour of MWF alloy, K2 (D9 SS-8.5 wt.% Zr) was

also plotted in Figures 7.3 to 7.5 for the sake of comparison. In simulated DM water media at pH 1 and pH 5, the NMFP added MWF alloys N1, N2 and N3 exhibited nobler OCP when compared to MWF alloy with 8.5 wt.% Zr (K2), and these OCP was shifting towards nobler direction with increase in time. This behaviour indicated the stability of the metallic surfaces against corrosion dissolution. The OCP versus time behaviour of MWF alloys N1, N2 and N3 in KGW shown in Figure 7.5 revealed that the OCP of N2, N3 and K2 are in comparable range whereas the alloy N1 exhibited comparatively active OCP. However, it was moving towards nobler direction with increasing time. The shift of OCP towards nobler region with increasing NMFP concentration indicates the stability of the MWF surface in the entire geological environment [139].

The MWF alloys without NMFP showed active OCP in aggressive media like DM water at pH 1 due to the dissolution of passive film [159]. However, the MWF alloys with the addition of NMFP showed nobler OCP in the aggressive medium like DM water at pH 1. This observation indicates the possible role of noble metals Ru, Rh and Pd in forming stable oxide film by the which have appreciable stability in the aggressive media also. At pH 5 (very mild medium) nobler potential was obtained as expected. In KGW medium the effect of NMFP observed was insignificant. These results are in accordance with the literature report [145] that the presence of higher concentration of minerals in the media form hydrated passive film on the metallic surface and thus most of the alloys showed stability of the metallic surface. However, with increase in time insoluble scale is formed on the surface and a protective oxide of ZrO_2 below the Cr_2O_3 film [78] which shifted the OCP towards nobler direction and made the alloys resistant to corrosion dissolution.

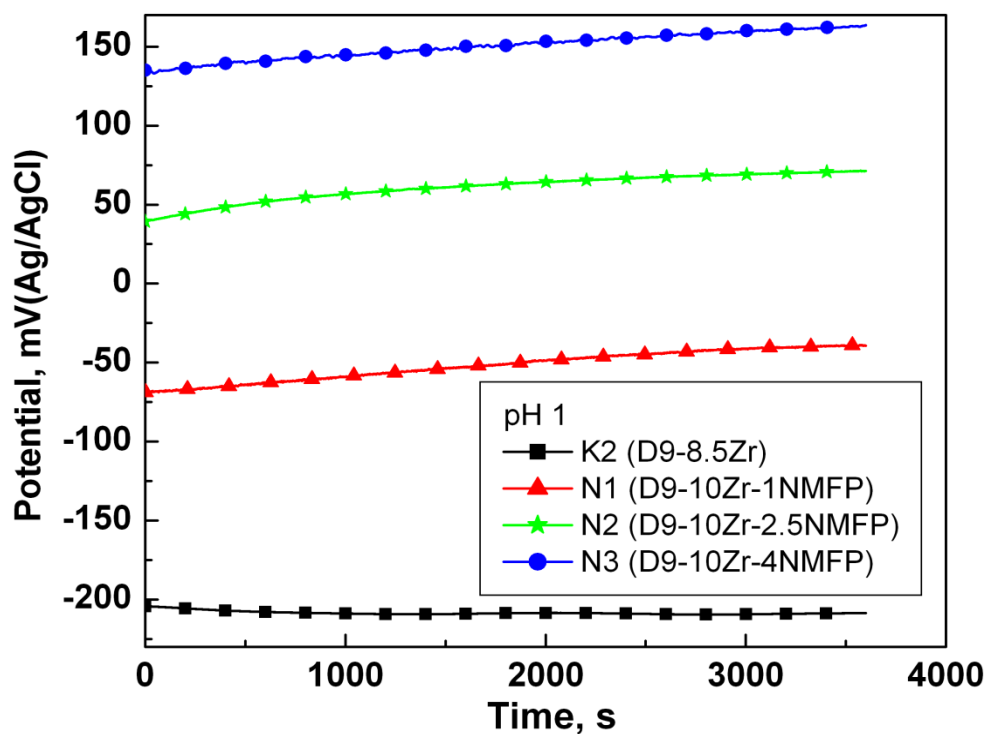


Fig.7. 3. Variation of OCP with time for NMFP added MWF alloys in DM water at pH 1

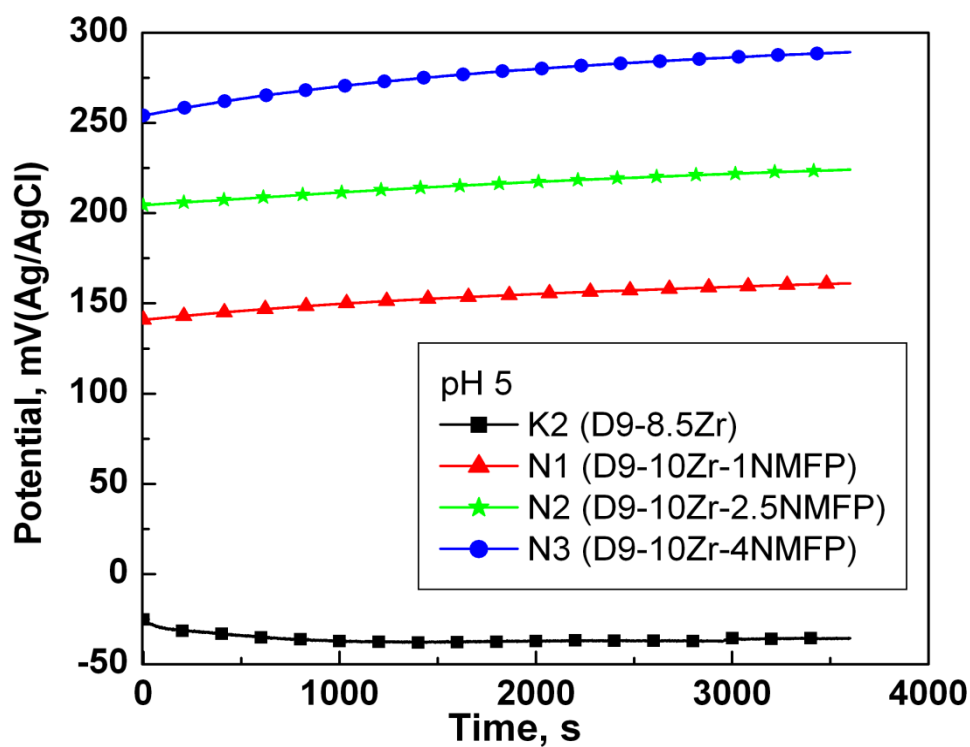


Fig.7. 4. Variation of OCP with time for NMFP added MWF alloys in DM water at pH 5

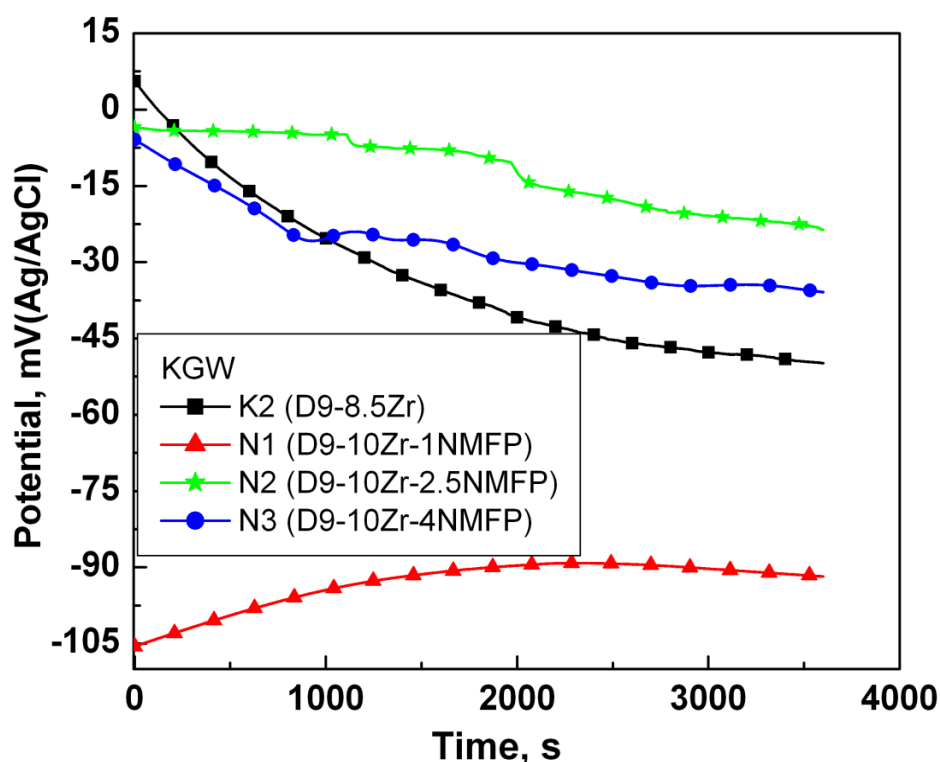


Fig.7. 5. Variation of OCP with time for NMFP added MWF alloys in KGW

7.3.1.4b Potentiodynamic polarization study

The potentiodynamic polarization plots for the MWF alloys with NMFPs N1, N2 and N3 and the MWF alloy with 8.5 wt.% Zr (K2) in different simulated media are shown in Figures 7. 6 to 7. 8. The polarization plot of the MWF alloys in DM water at pH 1 is given in Figure 7.6 and the polarization parameters including E_{corr} , i_{pass} and E_{BP} are given in Table 7.3. The MWF alloys with NMFP exhibited active corrosion potential (E_{corr}) with higher passive current density (i_{pass}) when compared to the respective values for the MWF alloy K2. However, the NMFP added MWF alloys exhibited a steady and wide ranging passivation potential with higher breakdown potential (E_{BP}) indicating stable passivation behaviour. The E_{corr} did not vary significantly with respect to NMFP concentration. However, minor shift of E_{corr} towards nobler direction was noticed with increasing NMFP concentration. The i_{pass} and E_{BP} were increasing with increase in NMFP concentration. The noise observed at the passivation region in this medium is attributed to the presence of Cl^- and H^+ ion which have a

tendency to form soluble bridge in the hydrated passive film and are responsible for breaking and self healing of the passive film [139, 145].

Table 7.3. Polarization parameters of different NMFP added MWF alloys in DM water at pH

1

Alloys	E_{corr}	i_{pass}	E_{BP}
	mV(Ag/AgCl)	$\mu\text{A}/\text{cm}^2$	mV(Ag/AgCl)
K2	-210	1.88	532
N1	-344	22.9	789
N2	-331	32.7	881
N3	-328	41	1050

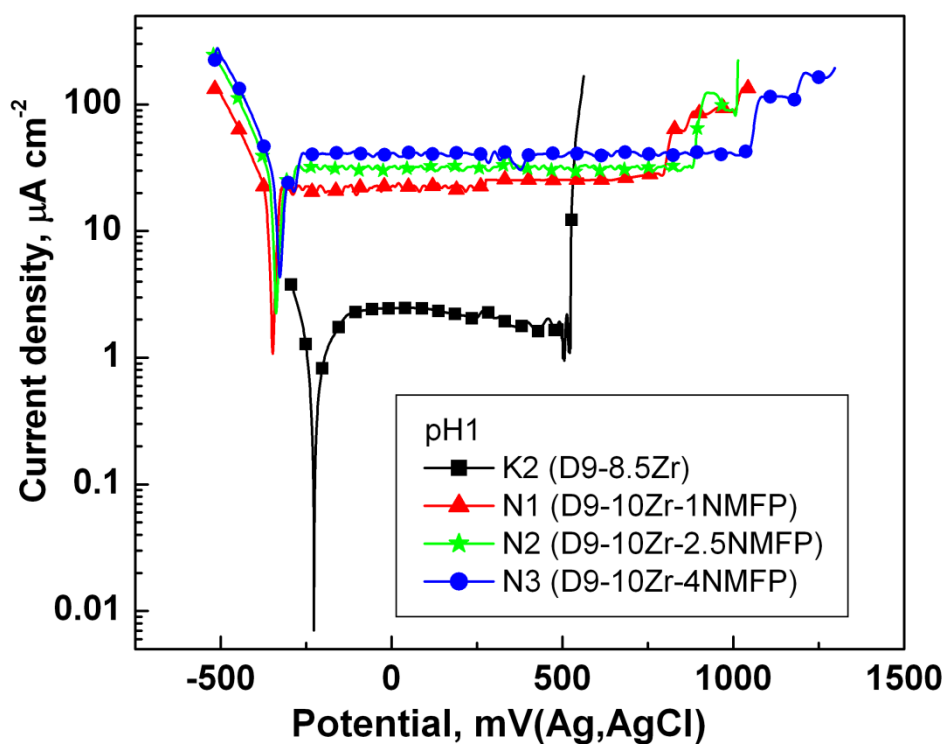


Fig. 7. 6. Potentiodynamic polarization plots of different MWF alloys with NMFP and K2 in DM water at pH 1

The polarization behaviour of NMFP added MWF alloys in DM water at pH 5 are shown in Figure 7. 7 and their corresponding polarization parameters are given in Table 7. 4. Active corrosion potential and higher passive current density were also observed in this medium compared to the MWF alloy, K2. The breakdown potential for NMFP added MWF alloys were found to be higher which indicated wide range of passivation potential. DM water at pH 5 is a mild medium and the alloys showed appreciable corrosion resistance with wide range of passivation behaviour.

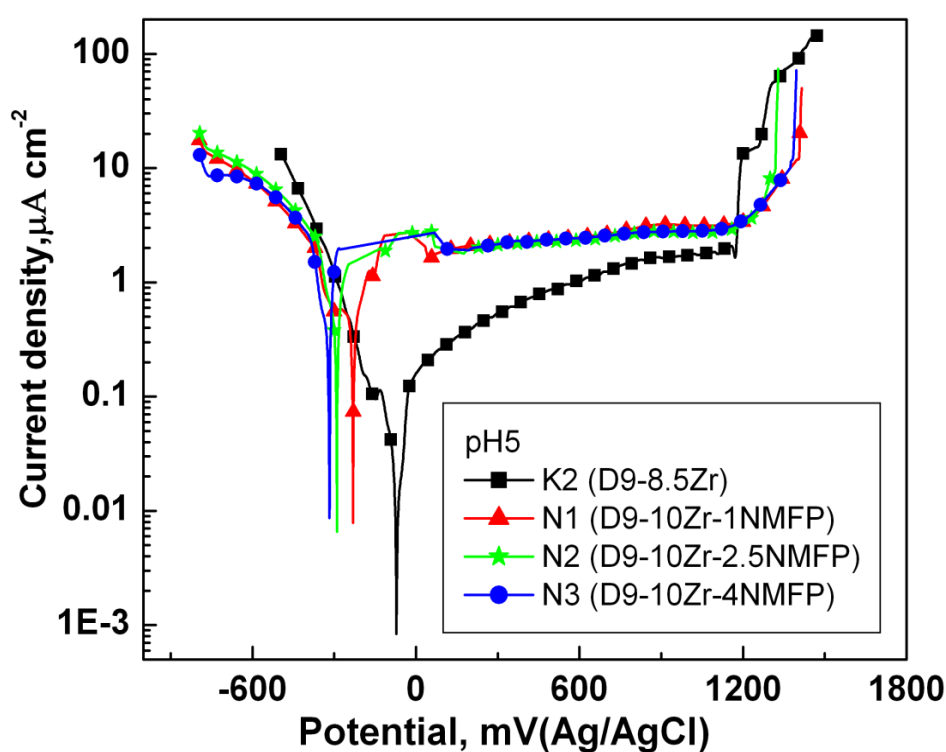


Fig. 7. 7 Potentiodynamic polarization plots of different MWF alloys with NMFP and K2 in DM water at pH 5

Figure 7.8 depicts the potentiodynamic polarization plots of N1, N2, N3 and K2 alloys in KGW medium and the different polarisation parameters are given in Table 7.5. Similar to the trend in other media, in this medium also the NMFP added MWF alloys showed active corrosion potential with higher passive current density when compared to the

MWF alloy without NMFP. However, the higher breakdown potential exhibited by these alloys indicated that the passive film formed in this medium is stable and exhibited prolonged corrosion resistance. The KGW medium is rich in chloride content wherein the MWF alloys would have a tendency to form pit on the surface. However, in the present study the NMFP added MWF alloys revealed the existence of stable passive film with higher E_{BP} and the E_{BP} was observed to increase with increase in NMFP concentration without any pitting attack.

Table-7.4. Polarization parameters for different NMFP added MWF alloys in DM water at pH 5

Alloys	E_{corr}	i_{pass}	E_{BP}
	mV(Ag/AgCl)	$\mu A/cm^2$	mV(Ag/AgCl)
K2	-81	0.10	1167
N1	-230	2.0	1267
N2	-301	1.8	1276
N3	-337	1.95	1316

Table-7.5. Polarization parameters for different NMFP added MWF alloys in KGW

MWF	E_{corr}	i_{pass}	E_{BP}
alloys	mV(Ag/AgCl)	$\mu A/cm^2$	mV(Ag/AgCl)
K2	-110	0.130	914
N1	-415	6.96	965
N2	-359	15	1124
N3	-409	19	1080

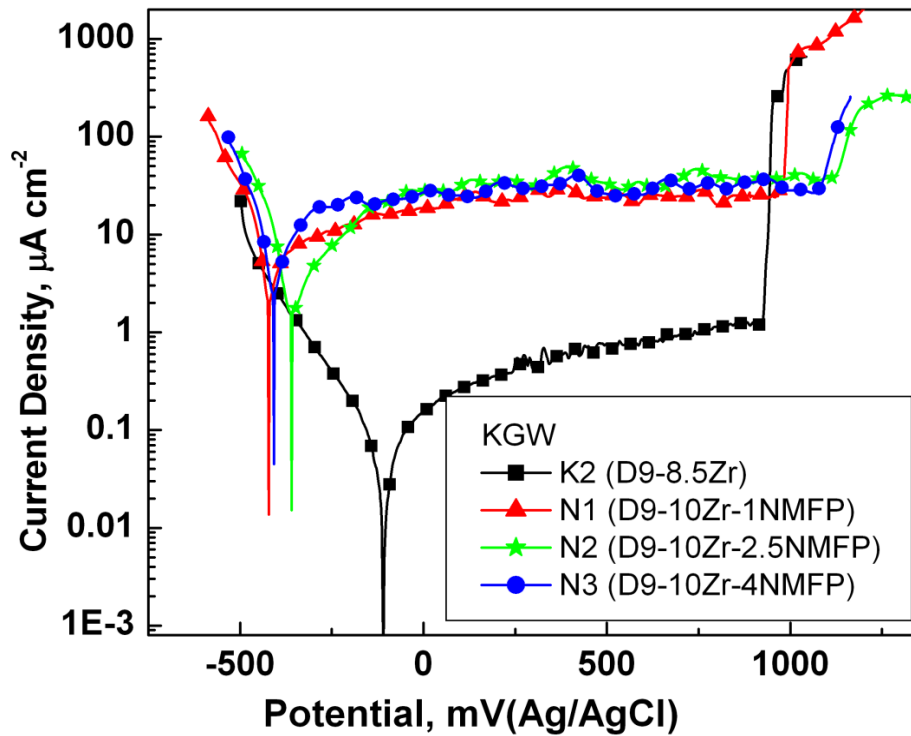


Fig. 7. 8. Potentiodynamic polarization plots of different MWF alloys with NMFP and K2 in KGW medium

Naturally, the addition of NMFP in the MWF alloy's composition had created microstructural heterogeneity, which could have resulted in more active E_{corr} and higher i_{pass} [139]. The Fig. 7.9 shows the variation of passive current density with respect to NMFP concentration. In the entire investigated media it was observed that the passive current density increases with the increase in NMFP concentration. This is attributed to the following explanations: (i) the passive film formed on the Fe based SS surface is generally semiconducting in nature. Addition of noble metal increases the point defects in the semiconducting film which is equivalent to doping and hence increases the local electronic conductivity as well as the passive current density [164], (ii) the noble metal can also increase the crystallinity of the passive film which also responsible for the higher electronic conduction and revealed higher passive current density [149].

However, both the above phenomenon provided long range stability of the passive film and was responsible for higher breakdown potential. The stability of the passive film can also be confirmed by the EIS study in the later section.

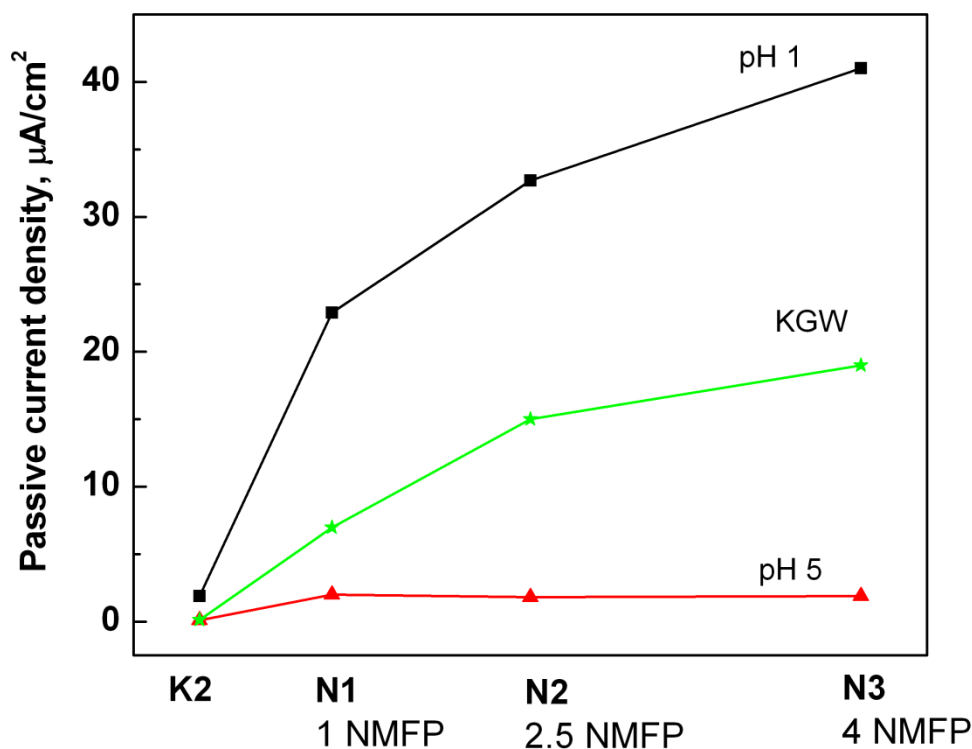


Fig. 7.9. Variation of passive current density with NMFP concentration in different simulated media

7.3.1.4c Electrochemical impedance spectroscopy

Electrochemical impedance spectra of different MWF alloys with NMFP N1, N2 and N3 and MWF alloy with 8.5 wt.% Zr (K2) in different simulated media are shown in Figures 7. 10 to 7.12. The EIS results obtained for NMFP added MWF alloys were fitted with the help of equivalent circuit shown in Figure 3.10b. The circuit consists of two time constants and this circuit model was considered for accurate and best fitting results. The EIS fitted values for N1, N2 and N3 in DM water at pH 1 and 5 and in simulated KGW are given in Tables 7. 6, 7.7 and 7.8 respectively. The EIS results of MWF alloy without NMFP were fitted accurately with simple equivalent circuit of one time constant as shown in Figure 3.10a

wherein the circuit arrangement was $(R_s(CPE_p||R_p))$. The alloys of NMFP added MWF showed one more constant due to the influence of additional adsorbed layer formed on the MWF surface and the circuit arrangement became $(R_s(CPE_a||R_a(CPE_p||R_p)))$ [111].

Table 7.6. EIS fitted values for NMFP added MWF alloys in DM water at pH 1

Alloy	R_s ($\Omega \text{ cm}^2$)	R_a ($\Omega \text{ cm}^2$)	CPE_a-T ($F/\text{cm}^2\text{S}^{-n}$)	CPE_a-n	R_p ($k\Omega \text{ cm}^2$)	CPE_p-T ($F/\text{cm}^2\text{S}^{-n}$)	CPE_p-n
K2	2.15	-----	-----	-----	89.95	8.65×10^{-5}	0.859
N1	2.7	90.1	4.19×10^{-8}	0.98	209.2	4.6×10^{-5}	0.93
N2	2.0	70.5	9.9×10^{-8}	0.99	341.3	3.2×10^{-5}	0.93
N3	2.2	82.4	9.2×10^{-8}	0.99	409	2.8×10^{-5}	0.929

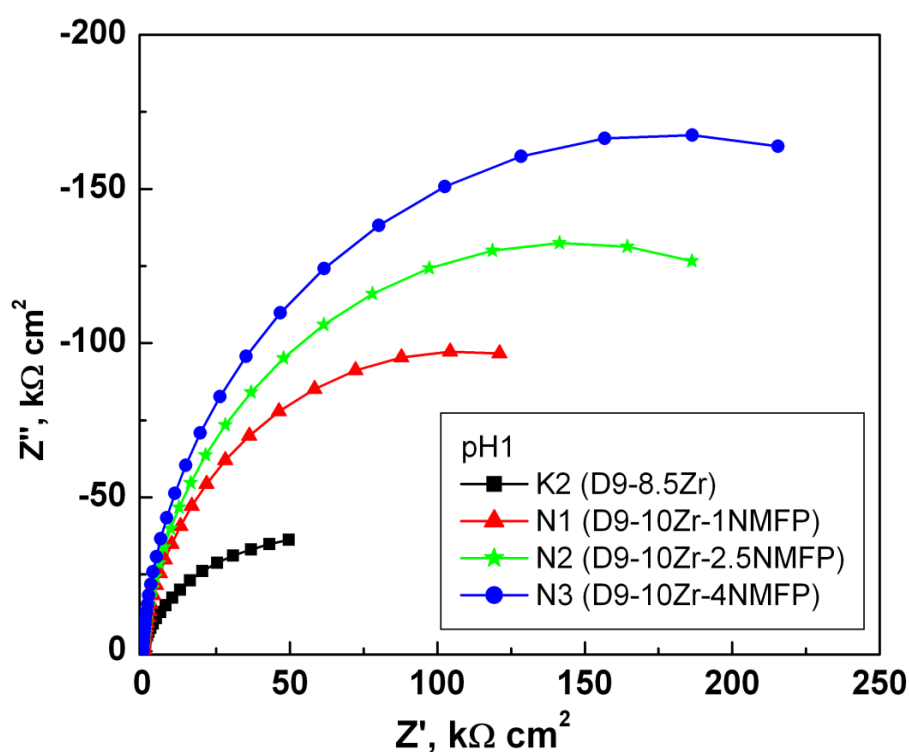


Fig. 7.10. EIS plot of NMFP added MWF alloys in DM water at pH 1

Table 7.7. EIS fitted values of NMFP added MWF alloys in DM water at pH 5

Alloy	R_s	R_a	$CPEa-T$	$CPEa-n$	R_p	$CPEp-T$	$CPEp-n$
	($\Omega \text{ cm}^2$)	($\Omega \text{ cm}^2$)	($F/\text{cm}^2\text{S}^{-n}$)		($k\Omega \text{ cm}^2$)	($F/\text{cm}^2\text{S}^{-n}$)	
K2	126	-----	-----	-----	149.95	4.40×10^{-5}	0.958
N1	1300	22500	2.8×10^{-10}	0.781	725.5	1.99×10^{-5}	0.803
N2	1500	23913	7.2×10^{-10}	0.751	770.5	1.5×10^{-5}	0.820
N3	1280	21770	5.2×10^{-9}	0.738	828.9	1.48×10^{-5}	0.840

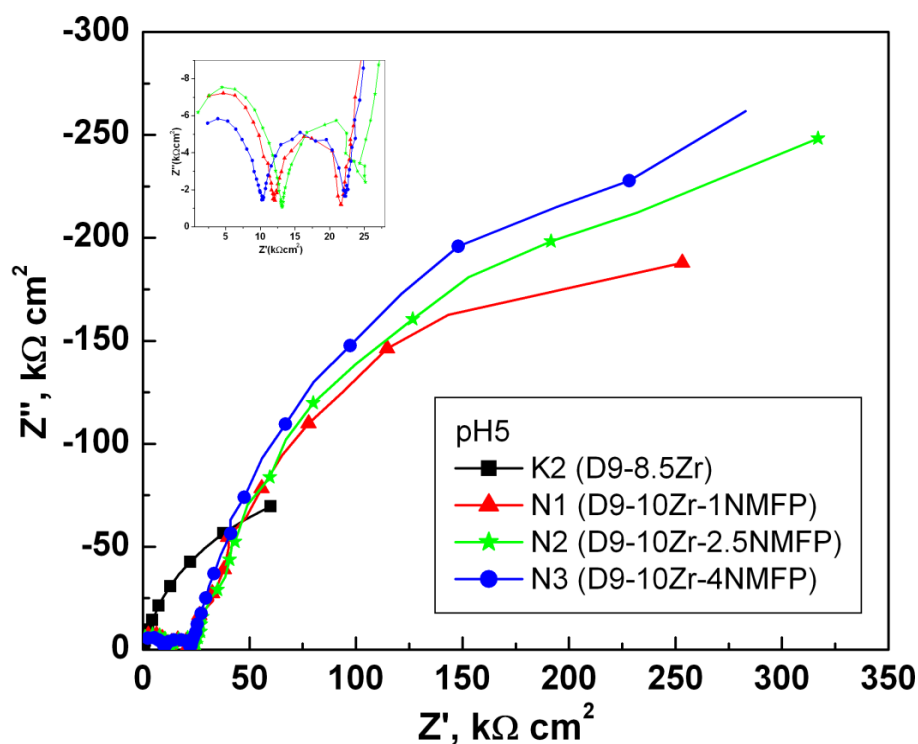


Fig.7.11. EIS plot of NMFP added MWF alloys in DM water at pH 5

In all the simulated media, the R_p values obtained from the EIS study were higher for MWF alloys with NMFP compared to the MWF alloys without NMFP. The polarization resistance values increased with the increasing concentration of NMFP. The polarisation resistance values in highly acidic media, viz. DM water at pH 1 were in the range 200 to 400

$\text{k}\Omega \text{ cm}^2$ and in highly chloride rich KGW medium, the values were around 300 to 500 $\text{k}\Omega \text{ cm}^2$. In DM water at pH 5 which represents a near neutral medium without any aggressive minerals the R_p values were more than 700 $\text{k}\Omega \text{ cm}^2$. This observation upholds the findings in the previous sections that the NMFP added MWF alloys exhibit very stable passive film in all kind of environment even in very aggressive media. The polarization resistance values recorded were several folds higher than the MWF alloys without NMFP. The higher resistance could be due to the formation of an adsorbed layer on the metallic surface which had acted as an additional barrier for charge transfer from the metallic surface. Hence, a protective and adherent passive layer could be formed at the metal solution interface which protected the surface from charge transfer as well as from corrosion dissolution [109].

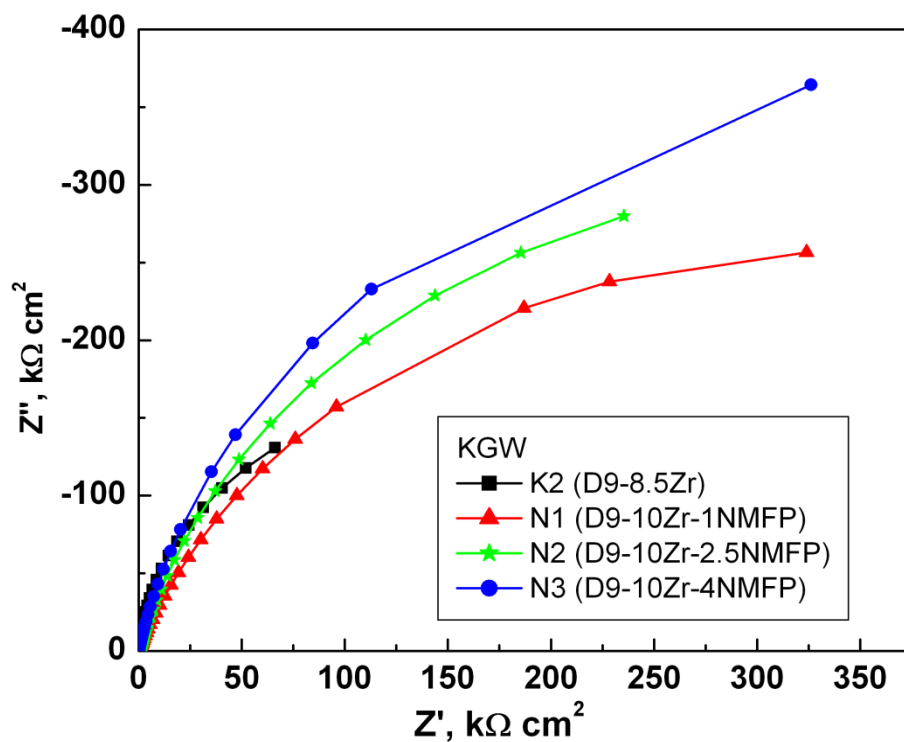


Fig.7.12. EIS plot of NMFP added MWF alloys in KGW

Table 7.8. EIS fitted values of NMFP added MWF alloys in KGW

Alloy	R_s	R_a	$CPEa-T$	$CPEa-n$	R_p	$CPEp-T$	$CPEp-n$
	$(\Omega \text{ cm}^2)$	$(\Omega \text{ cm}^2)$	$(F/\text{cm}^2\text{S}^{-n})$		$(k\Omega \text{ cm}^2)$	$(F/\text{cm}^2\text{S}^{-n})$	
K2	676	-----	-----	-----	248	2.10×10^{-5}	0.962
N1	8.9×10^{-5}	183	5.2×10^{-8}	0.99	243.7	3.1×10^{-5}	0.86
N2	6.1×10^{-5}	220	1.9×10^{-8}	0.98	295.5	2.9×10^{-5}	0.91
N3	7.3×10^{-5}	166	1.6×10^{-8}	0.96	486.8	2.6×10^{-5}	0.89

7.3.1.5 Surface morphology after polarization in different simulated media

The surfaces of MWF specimens were examined by optical microscope after potentiodynamic polarization study to understand the corrosion damage in different simulated media. The optical microscopic image of MWF alloys N1, N2 and N3 after polarisation in DM water at pH 1 and pH 5 and in simulated KGW are shown in Figures 7.13 to 7.15 respectively. The optical microscopic images did not reveal any significant surface dissolution. However, after polarisation in DM water at pH 1, pits were formed on the MWF surface (Fig. 7.13). Insignificant surface dissolution and minimum pit formation were observed on the NMFP added MWF alloys' surfaces after polarisation in DM water at pH 5 and in KGW. On the contrary, the results reported in Chapter 5 for the MWF alloys without NMFP showed the complete dissolution of passive film with the appearance of dark solid solution matrix and bright Zr rich intermetallic phases after polarisation in DM water at pH 1 (Fig. 5.16). Moreover, significant salt deposition was also observed on the metallic surface after polarisation in KGW (Fig. 5.20). Neither any significant dissolution of passive film nor any salt segregation could be observed on the surface of MWF alloys with NMFPs after polarisation in DM water at pH 1 or in KGW. This observation confirms the role of NMFP

addition in preserving the integrity of the MWF alloy's surface which acts as a protective barrier from any selective dissolution or any unwanted deposition.

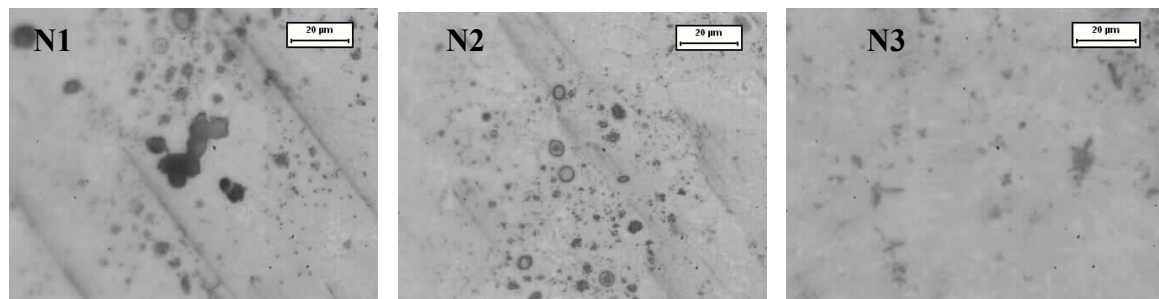


Fig. 7.13. Optical microscopic images of NMFP added MWF alloys after polarization in DM water at pH 1

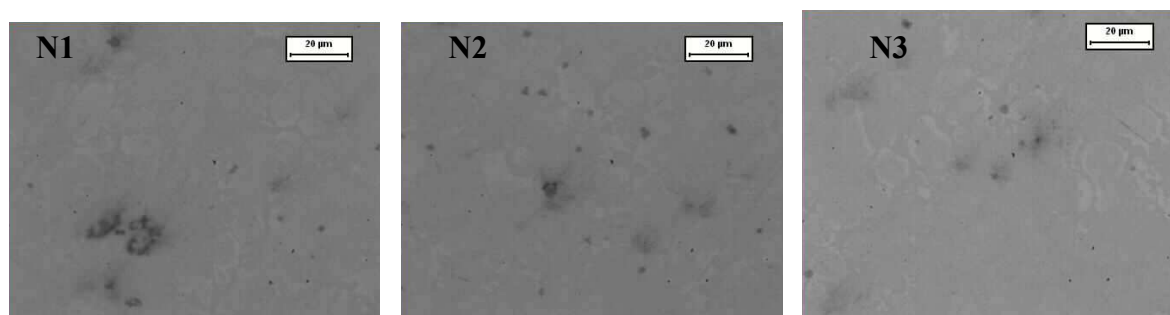


Fig. 7.14. Optical microscopic images of NMFP added MWF alloys after polarization in DM water at pH 5

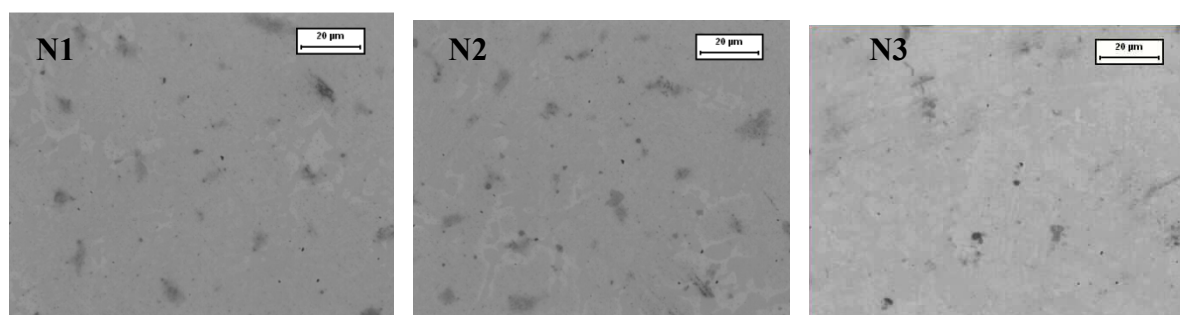


Fig. 7.15. Optical microscopic images of NMFP added MWF alloys after polarization in KGW

7.3.1.6 Selective leachability testing

Immersion corrosion testing as per ASTM standard material characterization centre (MCC) was carried out on NMFP added MWF alloys to understand their selective elemental leaching behaviour. Static leachability testing known as MCC-1 [91] was performed on these MWF alloys at 90 °C for 90 days in DM water medium. The weight changes in the MWF alloys N1, N2 and N3 after 90 days of MCC-1 testing in DM water at 90 °C given in Table 7.9 shows that there was absolutely no change in the weights of the specimen. All the weights were within the resolution limit of the balance. The ICP-OES composition of the leachate solution after 90 days of MCC- 1 testing along with blank DM water composition are given in Table 7.10. This Table indicates that the presence of alloying elements in the leachate solution is below the detection limit of the instrument. Incidentally, the elemental composition in blank DM water medium analyzed by ICP-OES is also similar to that of the leachate solutions. Hence, the composition of the leachate solution was presumed to be the concentration of the representative elements in the DM water medium and it is concluded that there was no leaching of any alloying element from the NMFP added MWF alloys.

Table 7.9. Weight of NMFP added MWF alloys before and after 90 days of MCC-1 testing

MWF Alloys	Weight (g)	
	Before exposure	After exposure
N1	8.4604	8.4605
N2	7.8687	7.8687
N3	8.0798	8.0798

Table 7.10. Composition of leachate solution after 90 days of MCC-1 testing at 90 °C along with blank DM water composition

Element	Bulk (ppm)	N1(ppm)	N2(ppm)	N3(ppm)
Fe	< 0.4	< 0.4	< 0.4	< 0.4
Cr	< 0.4	< 0.4	< 0.4	< 0.4
Ni	< 0.4	< 0.4	< 0.4	< 0.4
Zr	< 0.4	< 0.4	< 0.4	< 0.4
Ru	< 0.4	< 0.4	< 0.4	< 0.4
Rh	< 0.4	< 0.4	< 0.4	< 0.4
Pd	< 0.4	< 0.4	< 0.4	< 0.4

The surface morphology of the MCC-1 tested NMFP added MWF alloys was analysed by SEM and the images are shown in Figure 7.16. The EDS analysis of their composition is given at Table 7.11. The SEM morphology of the MWF surface showed no significant changes after 90 days of MCC-1 testing at 90 °C. The EDS composition of the alloys' surface revealed the typical composition of the MWF alloys. No oxide deposition was observed on the surface unlike the oxide scale formation observed during the leachability studies of MWF alloys without NMFP (Chapter-6). Hence it is inferred that the addition of NMFP in MWF alloys make them to resist from the selective leaching of alloying element during long term high temperature exposure. NMFPs also protected the surface of the MWF alloys from any localized attack or scale formation. Hence, these alloys with NMFPs can prevent the leaching out of radioactive fission products from their matrix even after very long term exposure under high temperature conditions.

Table 7.11. EDS analysis of NMFP added MWF alloys' surface after 90 days of MCC-1 testing at 90 °C.

MWF	Elements (wt.%)					
alloy	Fe	Cr	Ni	Zr	Ru	Pd
N1	60.4	11.3	14.2	14.1	-----	-----
N2	62.3	13.4	13.9	10.5	-----	-----
N3	58.5	11.8	13.9	13.7	1.1	1.0

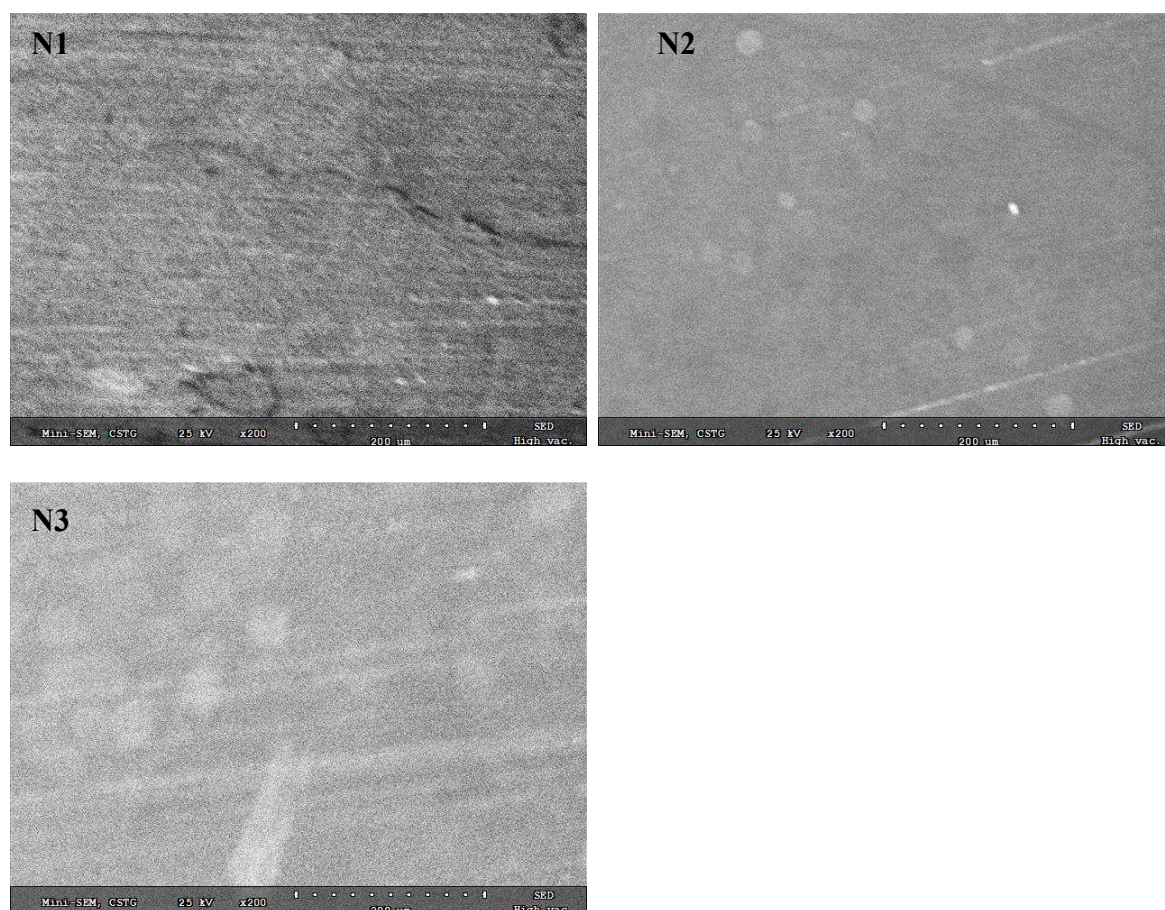


Fig. 7.16. SEM images of NMFP added MWF alloys after 90 days MCC-1 testing at 90 °C.

7.3.2 MWF alloys of D9 SS-Zr-NMFP-U

The corrosion behaviour and the leaching characteristics of the MWF alloy D9 SS-10Zr-NMFP in various simulated repository environments were evaluated using electrochemical techniques and surface characterisation methods in Section 7.3.1. As it is desirable to investigate the effect of actinides on the corrosion aspects of MWF alloys, in this section MWF-1NMFP alloy with the addition of 10 wt.% U was cast and was characterized to understand the effect of uranium on the microstructure and corrosion behaviour of MWF alloys. The composition of the alloy used in this study contains 1 wt.% NMFP and 10 wt.% Zr (D9 SS-10Zr-1NMFP-10U).

7.3.2.1 Hardness measurement

The hardness value of the U added MWF-1NMFP alloy was measured to be 455 ± 12 HV. This result shows that the hardness value increases with the addition of U.

7.3.2.2 Microstructural analysis by SEM

The microstructure of the U added MWF-1NMFP alloy was investigated using SEM and the local area composition of its different microstructural phases was analyzed by EDS attached with SEM. The SEM microstructure along with EDS composition of the U added MWF alloy shown in Figure 7.17 reveals that this alloy also forms two phases. However, unlike D9 SS-Zr and D9 SS-Zr-NMFP MWF alloys, the U added alloy formed a brighter isolated island on the matrix phase. The EDS composition of the matrix phases showed the presence of Fe, Cr and Ni as major elements and represents Fe based solid solution matrix phase and the brighter isolated island to be Zr rich intermetallic islands comprising Zr as the major elements with little amount of Fe, Cr and Ni. Uranium was present in these brighter Zr rich intermetallic phases and it was not found in the Fe based matrix phase or as any separate phase. This observation indicates that the Zr rich intermetallic phases also hosted U, in

addition to accommodating NMFPs within the matrix. Moreover, the alloy did not allow U to form any separate phase outside the Zr intermetallics.

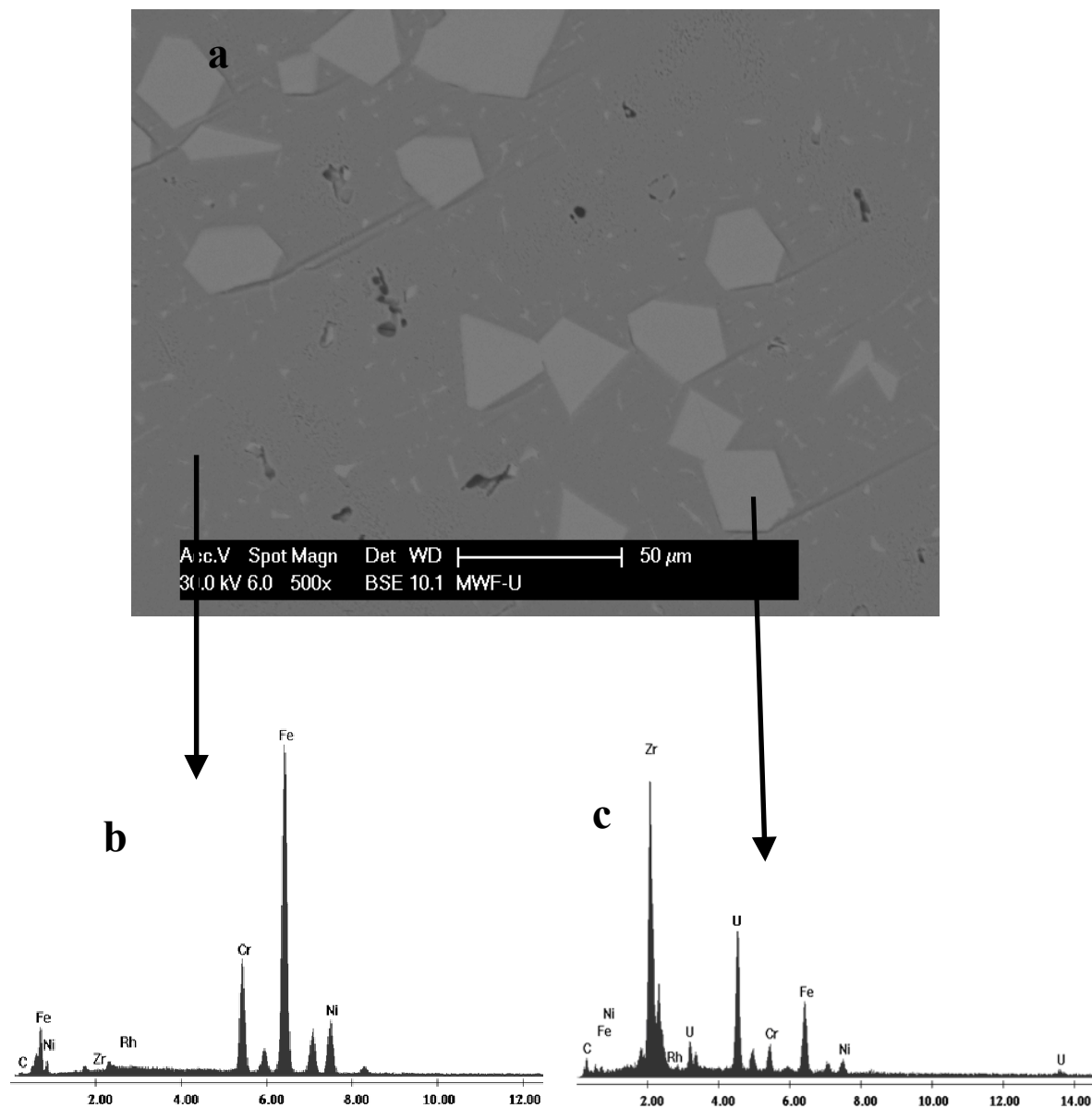


Fig.7.17. SEM microstructure and EDS composition of U added MWF alloy (a) BSE microstructural image, (b) EDS composition of dark phase and (c) EDS composition of bright phase containing U.

7.3.2.3 XRD analysis for Phase identification

The typical XRD pattern of U added MWF-1NMFP alloy is shown in Figure 7.17. The different compound phases identified from the XRD pattern were austenite Fe based

solid solution, Fe-Zr and Ni-Zr type intermetallic phases like NiZr, Ni₇Zr₂, Fe₃Zr and U based UZrO₂ and Ni₂U. Phase analysis by XRD confirmed the formation of stable compounds by U with Zr and Ni.

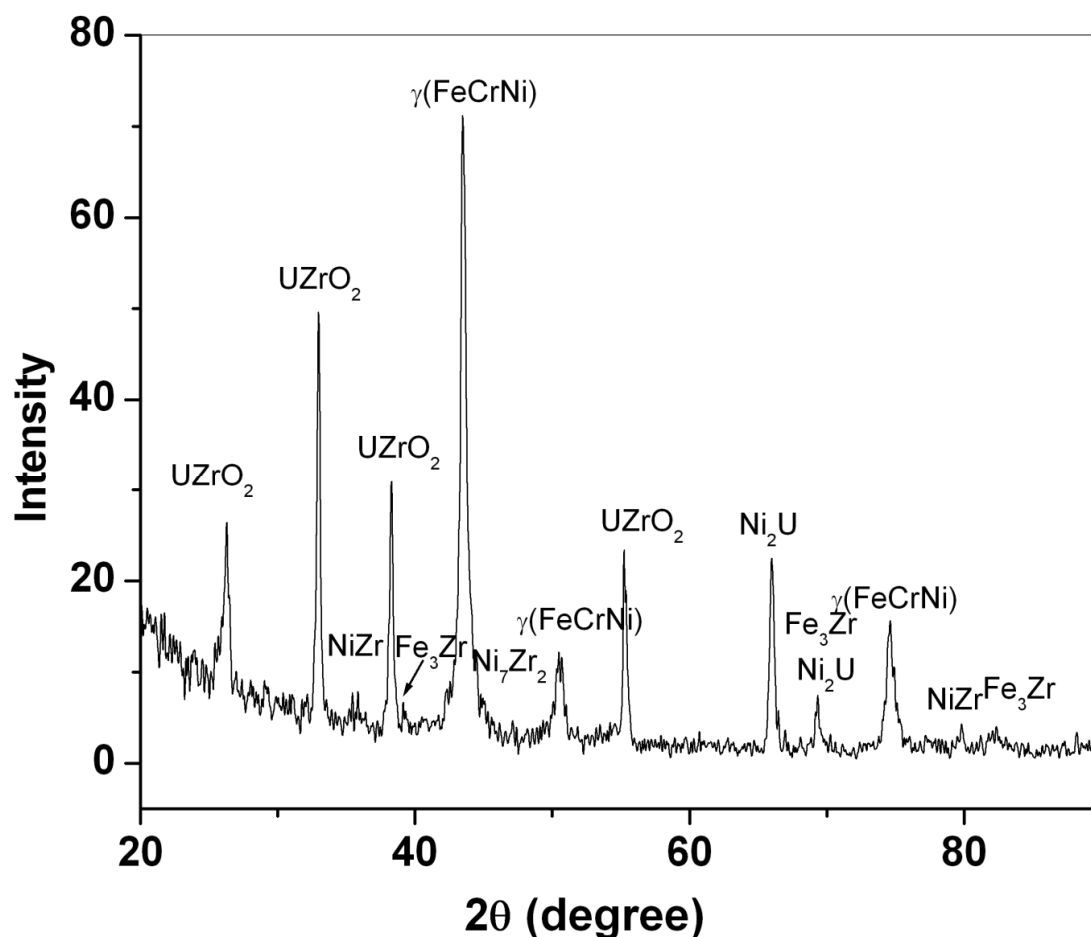


Fig. 7.18. XRD pattern of U added MWF alloy

7.3.2.4 Electrochemical corrosion testing

Different electrochemical corrosion methods including OCP, potentiodynamic polarisation and EIS were employed for evaluating the role of U in the corrosion behaviour of U added MWF alloy in simulated DM water at pH 5, KGW and RGW media.

7.3.2.4a OCP Monitoring

The OCP versus time plots of U added MWF alloy in different simulated media are shown in Figure 7.19. The OCP in DM water at pH 5 was nobler than other media. However,

in most of the simulated media OCP was found to move towards nobler direction with increase in time indicating the possibility of growth of stable oxide film which was responsible for shifting OCP towards nobler direction.

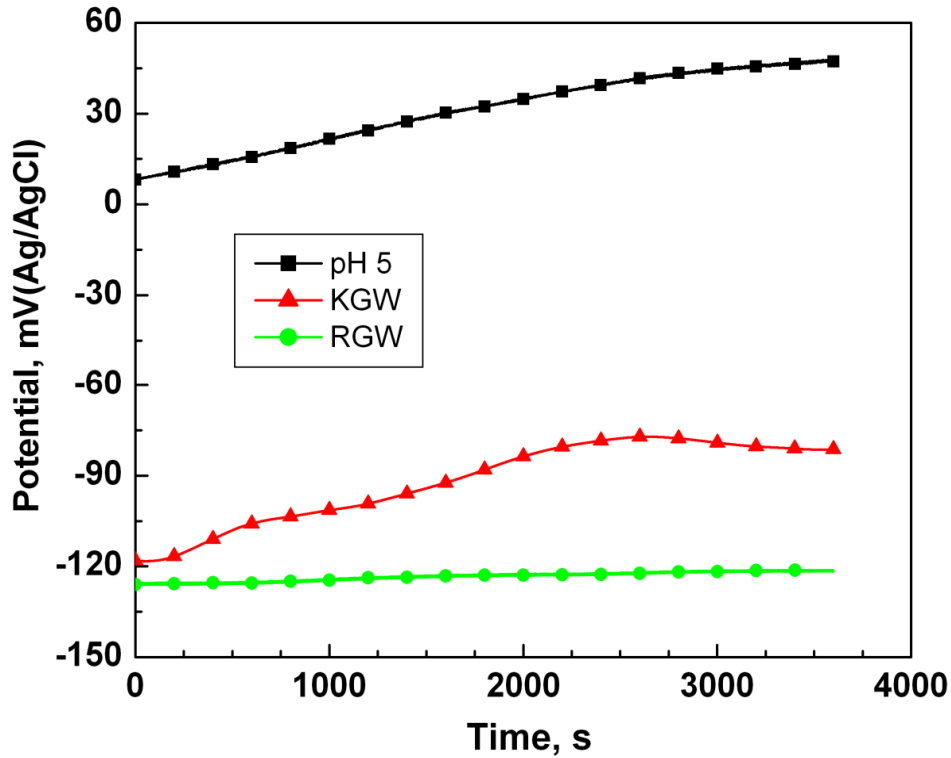


Fig. 7. 19. Variation of OCP with time of U added MWF-1NMFP alloys in DM water at pH 5, simulated KGW and RGW

7.3.2.4b Potentiodynamic Polarization study

The potentiodynamic polarization plot of U added MWF-1NMFP alloy in different simulated media is shown in Figure 7.20 and the polarization parameters E_{corr} , i_{pass} and E_{BP} are given at Table 7.12. Polarization results also showed active corrosion potential and higher passive current density in simulated KGW and RGW when compared to that in DM water at pH 5. However, in DM water at pH 5 and in simulated RGW this alloy showed wide range of passivation potential. The E_{BP} in KGW was found to be lower compared to DM water at pH 5 and RGW due to presence of higher concentration of chloride ion which was responsible for

pit initiation on the MWF surface. This alloy also showed steady state passivation behaviour without any noise which indicated the formation of stable passive film.

Table 7.12. Polarization parameters for U added MWF-1NMFP alloy in different simulated media.

Media	E_{corr} mV(Ag/AgCl)	i_{pass} $\mu\text{A}/\text{cm}^2$	E_{BP} mV(Ag/AgCl)
DM water (pH 5)	-215	1.25	1142
KGW	-553	8.33	452
RGW	-457	7.5	871

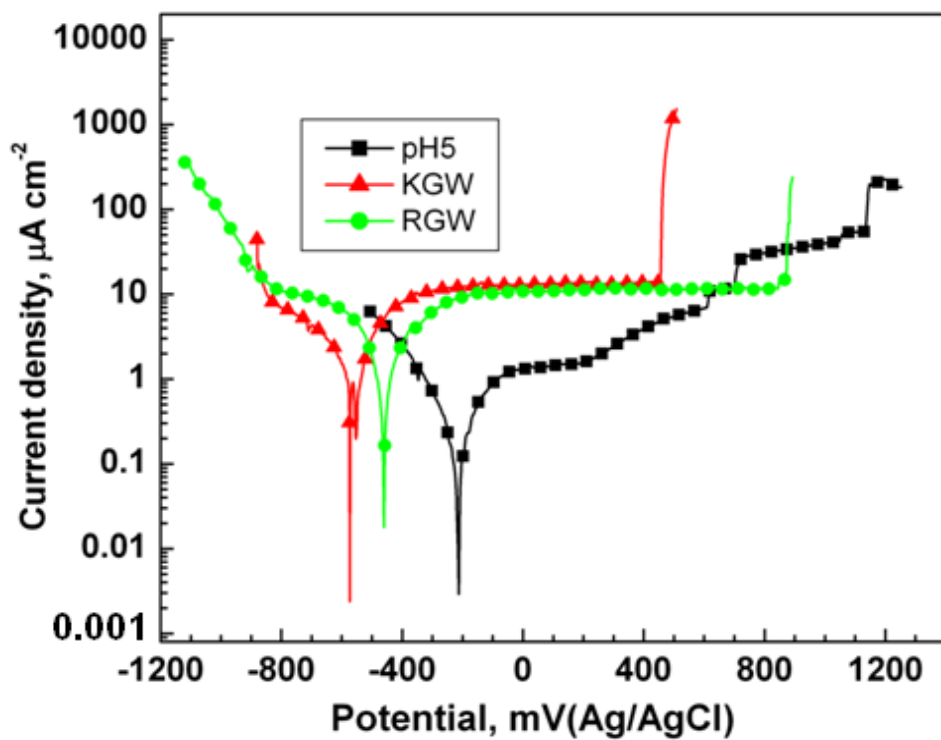


Fig. 7.20. Potentiodynamic polarization plot of U added MWF-1NMFP alloy in DM water at pH 5, simulated KGW and RGW

7.3.2.4c Electrochemical impedance spectroscopy

The EIS plots of U added MWF-1NMFP alloy in different simulated media are shown in Figure 7.21. and their corresponding fitting values are given in Table 7.13. In DM water at pH 5 the best fitting was obtained using the equivalent circuit model shown in Figure 3.10b with two time constants, whereas, in KGW and RGW media the best fitting values were obtained by employing equivalent circuit model shown in Figure 3.10a with one time constant. In DM water at pH 5 an additional adsorbed layer was found on the MWF surface as observed in the EIS study of NMFP added MWF-1NMFP alloys. The U added MWF alloy showed higher value of polarization resistance in all the simulated media indicating the formation of stable passive film in the metal solution interface even in Cl^- rich KGW medium.

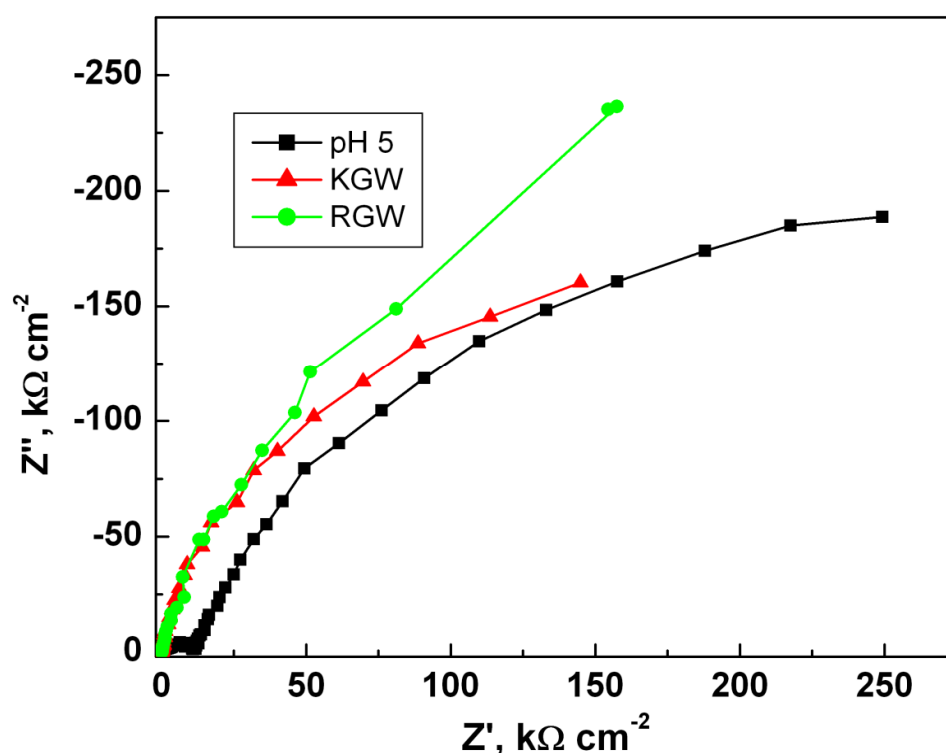


Fig. 7. 21. EIS plot of U added MWF-1NMFP alloy in DM water at pH 5, simulated KGW and RGW

Table 7.13. EIS fitted values of U added MWF-1NMFP alloy in different simulated media.

Media	R_s	R_a	CPEa-T	CPEa-n	R_p	CPEp-T	CPEp-n
	$(\Omega \text{ cm}^2)$	$(\Omega \text{ cm}^2)$	$(\text{F}/\text{cm}^2\text{S}^{-n})$		$(\text{k}\Omega \text{ cm}^2)$	$(\text{F}/\text{cm}^2\text{S}^{-n})$	
DM water (pH 5)	2.1×10^{-6}	11026	3.49×10^{-7}	0.63	555	1.9×10^{-5}	0.80
KGW	26.13	-----	-----	-----	368	4.6×10^{-5}	0.91
RGW	62.59	-----	-----	-----	664	2.8×10^{-5}	0.85

7.3.2.5 Surface morphology after polarization in different simulated media

The surface morphological changes in U added MWF-1NMFP alloy after polarisation in different simulated media are shown in Figure 7.22.

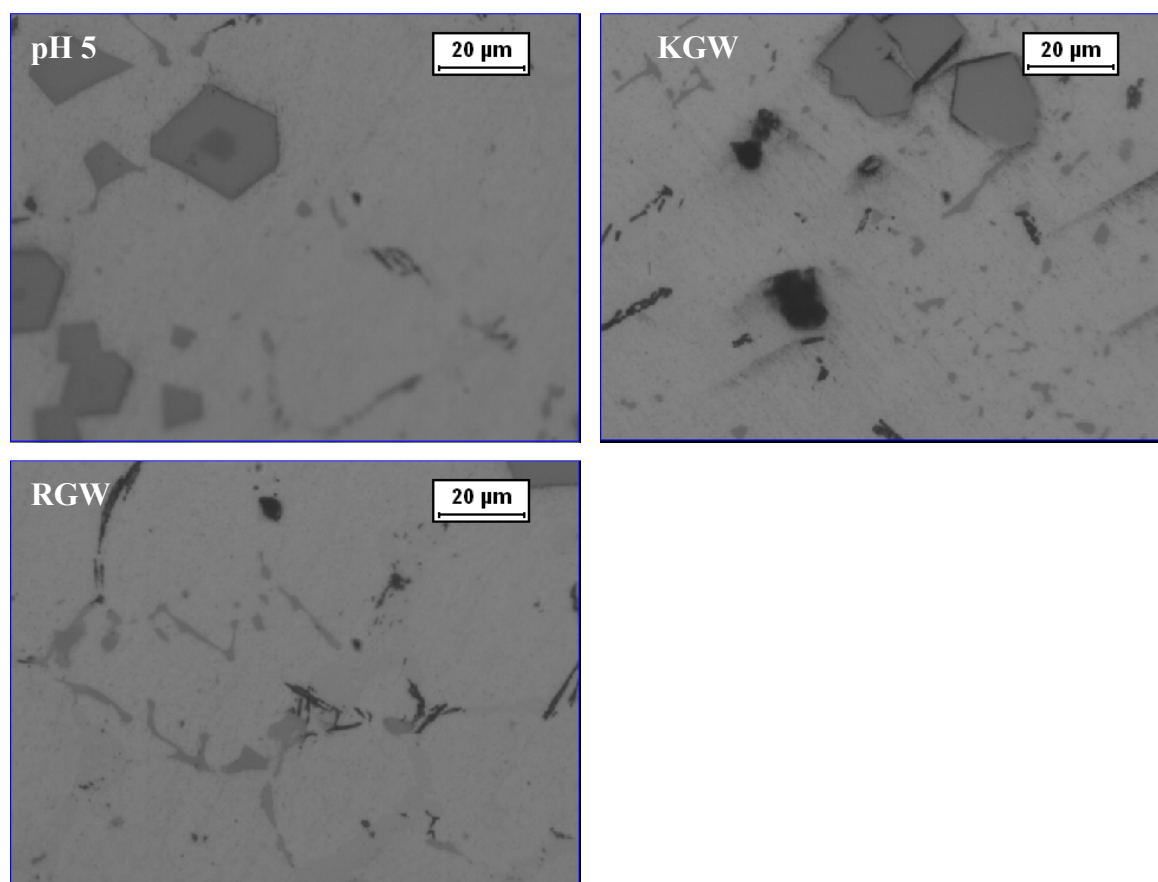


Fig. 7.22. Optical microscopic images of U added MWF-1NMFP alloys after polarization in different simulated media

No significant surface attack was observed after polarization in DM water at pH 5 and in simulated RGW media, whereas after polarization in simulated KGW pit formation was observed on the U added MWF-1NMFP alloy surface. Nevertheless, the pit was found on the Fe based solid solution matrix phase with no localized attack in the U bearing Zr rich intermetallic phases. This observation confirms the resistance of the MWF alloys towards radionuclide leaching even after polarization in chloride rich KGW medium.

7.4 Conclusions

The microstructural and corrosion behaviour of MWF alloys with the addition of NMFP and U were investigated to understand their influence on long term disposal issues in geological repository. Based on the above investigations the following conclusions could be drawn.

1. The hardness value of the MWF alloys increases gradually with the addition of NMFP and U.
2. Microstructure of NMFP added MWF alloys revealed the formation of Fe-based solid solution matrix and Zr-rich intermetallic phases similar to that observed in MWF alloys without NMFP. However, the NMFPs remained within the Zr-rich intermetallic phases.
3. Microstructure of U added MWF-1NMFP alloy also showed Zr-rich intermetallic phases and Fe-based solid solution matrix. Uranium was accommodated in the Zr-rich intermetallic phases.
4. XRD of NMFP added MWF alloys confirmed the existence of fcc Fe-based solid solution with Fe-Zr and Ni-Zr type Laves intermetallic phases. As the NMFP did not form any discrete phases it is confirmed that the NMFPs had completely dissolved in the Zr-rich intermetallic phases.

5. The phase analysis of U added MWF-1NMFP alloy by XRD showed the formation of fcc Fe-based solid solution, Ni-Zr and Fe-Zr type intermetallic phases and uranium bearing UZrO_2 and Ni_2U compounds.
6. NMFP added MWF alloys exhibited wide range of passivation behaviour with higher breakdown potential and polarization resistance indicating the formation of stable passive film on the metal solution interfaces.
7. Uranium added MWF-1NMFP alloy also showed high polarization resistance in the simulated repository media. Initiation of pit was observed at the Fe based solid solution phases in KGW medium. However, on the U bearing Zr rich intermetallic phases no significant localized attack was observed.
8. Leachability test of NMFP added MWF alloys in DM water at 90 °C for 90 days showed that the leaching of alloying elements was below the detection limit of the instrument. The surface morphology of the alloys also showed insignificant surface change.

The investigation on NMFP and U added MWF alloys revealed that the formation of Fe-based solid solution and Zr rich intermetallic phases. These Zr rich intermetallic phases serve as host matrix for the fission product and uranium. Corrosion investigations validated the appreciable corrosion resistance exhibited by these alloys in addition to the formation of stable passive film. The satisfactory performance of D9 SS-Zr-NMFP-U metal waste form alloys in different simulated water media had led to the conclusion that these MWF alloys are quite amenable for hosting the fission products and actinides by the way of providing good resistance to corrosion attack and selective leaching even in harsh environmental conditions.

CHAPTER 8

SUMMARY, CONCLUSIONS AND SCOPE FOR FUTURE WORK

CHAPTER 8

SUMMARY, CONCLUSIONS AND SCOPE FOR FUTURE WORK

This chapter summarizes the work carried out on the development and characterization of different D9 SS-Zr MWF alloys discussed in the entire thesis. Metal waste form, as per definition is the candidate metallic waste generated after pyrochemical reprocessing of spent nuclear fuel which entails cladding hulls, Zr from alloy fuel, NMFP and contaminated actinides. These metallic parts left over in the anode dissolution basket are melted together as consolidated volume and then packed as engineered barrier system for final disposal in geological repository. The actinides and NMFPs in the MWF alloy may retain their radioactivity for more than 100,000 years. To gain experience in the processing of metal waste and to optimise the process conditions, D9 SS-Zr MWF alloys were developed and characterized for microstructure, hardness, phase analysis, corrosion resistance and leachability.

8.1 Development of different MWF alloys

The casting and characterization of MWF alloys were carried out in three stages. To start with, D9 SS-Zr MWF alloys were investigated with different Zr content, followed by D9 SS-Zr- NMFP and finally D9 SS-Zr-NMFP-U alloy was developed. In the first stage, the development of D9 SS-Zr was carried out with five different contents of Zr from 5 to 17 wt.%. These alloys were subjected to rigorous examination for microstructure, phase identification, corrosion and selective elemental leaching behaviour and it was observed that MWF alloys of D9 SS with 8 to 12 wt.% Zr showed superior corrosion resistance and passive film stability. In the second phase three MWF alloys of D9 SS -10 wt.% Zr with 1, 2.5 and 4 wt.% NMFP (NMFP: Ru, Rh and Pd) were developed. These alloys were also characterized for their microstructure, compound phases, corrosion and selective elemental leaching

behaviour. In the third phase, one MWF alloy of D9 SS-10 wt.% Zr-1 wt.% NMFP-10 wt.% U was developed and characterized.

8.2 Characterization of alloy metallurgy of the MWF alloys

Metallurgical characterization of different MWF alloys was performed using Vickers hardness tester, SEM/EDS and XRD. The hardness values of the different D9 SS-Zr MWF alloys were gradually increasing with increase in Zr concentration. Further increase of hardness values was observed with the addition of NMFP and U. The microstructural analysis by SEM/EDS on different D9 SS-Zr MWF alloys revealed the formation of two phases: a dark Fe based solid solution matrix and bright Zr rich intermetallic precipitate phases. The XRD analysis validated the formation of Zr intermetallic compounds which were typically NiZr, Ni₅Zr, Ni₇Zr₂, FeZr₂ and Fe₃Zr type Laves intermetallic phases. These Zr rich intermetallic phases were stable at high temperature of 1173 K. The microstructure of NMFP added MWF alloys also showed the formation of two phases viz. the dark fcc Fe based solid solution matrix and the brighter Zr rich intermetallic phases. These intermetallic compounds also correspond to NiZr, Ni₂Zr, Ni₅Zr, Ni₇Zr₂, FeZr₂ and Fe₃Zr type Laves intermetallic compounds. The NMFPs were found to be accommodated within the Zr rich intermetallic phases and no discrete compounds phases containing NMFP were found. The microstructure of U and NMFP added MWF alloy also showed bright Zr rich intermetallic phases on the dark Fe based solid solution matrix. Uranium was found at the Zr rich intermetallic phases. Different compound phases formed in this alloy were fcc Fe based solid solution, Ni-Zr and Fe-Zr type Laves intermetallics and U bearing UZrO₂ and Ni₂U phases. This observation confirmed the stability of U in MWF matrix by combining with Zr and forming stable compound phases.

Thus, the alloy metallurgical study established the role of Zr in forming Zr rich Laves intermetallic phases and accommodating the NMFPs and U within the matrix as a host phase as well as providing stability to U by the way of forming highly stable compounds.

8.3 Corrosion and passive film behaviour of MWF alloys

The corrosion behaviour of the various MWF alloys was investigated in different simulated media like DM water at pH 1, 5 and 8, simulated KGW and RGW employing different electrochemical techniques including OCP, potentiodynamic polarization and EIS. The corrosion behaviour of the MWF alloys was assessed with respect to variation in Zr concentration as well as with variation of the repository environment. The stability and the morphology of the passive film on the MWF alloy (D9 SS-8.5 Zr) were investigated using XPS and AFM. For this purpose, the MWF alloy was passivated in DM water and the composition of the passive film was analyzed by XPS. Passive film topography of this alloy was evaluated by AFM after passivation and polarization in the entire investigated media.

The OCP and polarization studies indicated that D9 SS-Zr MWF alloys exhibited excellent corrosion resistance with wide range of passivation behaviour in simulated geological media like DM water at pH 5, pH 8, KGW and RGW. EIS study revealed that these MWF alloys exhibited higher polarization resistance by the formation of stable hydrated passive film at metallic interfaces. The MWF alloys with optimum Zr concentration (about 8 to 12 wt.%) exhibited appreciable passive film resistance in the most aggressive medium of DM water at pH 1 due to the combined effect of chromium oxide and zirconium oxide. After polarization, the surface morphological investigation of the MWF alloys showed insignificant dissolution in DM water at pH 5, pH 8 and RGW. Nevertheless, in KGW medium though corrosion dissolution was not significant, some dendritic salt deposition was noticed. Dissolution of Fe based solid solution matrix was observed after polarization in DM water at pH 1 but the Zr rich intermetallic phases were stable. The XPS analysis for the

passive film composition of MWF alloy surface showed the formation of oxide scale which was rich in chromium oxide and zirconium oxide. Zirconium oxide was present up to sufficient depth below the surface wherein the depletion of chromium oxide layer was observed. AFM topography of the MWF alloys passivated in simulated media showed surface deposition in KGW and RGW media. Pit formation was seen after polarization in DM water at pH 5 and 8, whereas in simulated KGW and RGW pits were observed along with salt deposition. The AFM topography of MWF alloys polarized in DM water at pH 1 showed the complete removal of Fe based solid solution matrix.

The NMFP added MWF alloys exhibited comparatively active corrosion potential due to their microstructural heterogeneity. These alloys showed higher resistance to localised corrosion with the existence of wide range of passivation potential and very high breakdown potential. The passive films formed in different simulated media for NMFP added MWF alloys were very stable due to the formation of an additional adsorbed layer on the metallic surface and displayed very high polarization resistance. The surface characterization of NMFP added MWF alloys showed insignificant corrosion dissolution in simulated DM water at pH 5 and KGW. Minor pitting attack was observed in DM water at pH 1. Unlike D9 SS-Zr MWF alloys, neither passive film dissolution nor salt deposition could be observed in NMFP added MWF alloys.

The corrosion investigation on U added MWF alloy also showed a similar trend of wide ranging passivation potential with the existence of stable passive film and higher polarization resistance just like NMFP added MWF alloys. The surface morphology of this alloy showed insignificant surface dissolution after polarization in DM water at pH 5 and in simulated RGW. However, in KGW medium a few pits were observed on the surface of Fe based solid solution phases, but the U bearing Zr intermetallic phases remained unchanged.

8.4 Selective elemental leaching and microbial induced corrosion behaviour

Selective radionuclide leaching as well as microbially induced corrosion behaviour of MWF alloys were investigated to understand the long term disposal issues. The selective elemental leaching of D9 SS-Zr MWF alloys were carried out as per ASTM standard material characterization centre (MCC) testing procedure. The MCC testing were carried out under dynamic condition known as MCC-5 at 90 °C for 260 days and in static condition known as MCC-1 at 90 °C and 200 °C for 90 days in DM water medium. MCC-1 testing was also carried out for D9 SS-Zr MWF alloy in simulated KGW and RGW media for 90 days at 90 °C. The selective elemental leaching behaviour of NMFP added MWF alloys were conducted as per MCC- 1 testing at 90 °C for 90 days. The above MCC testing revealed absolutely no selective leaching of the alloying elements from the MWF alloys. Instead, the surface of the MWF alloys were protected by the formation of stable and adherent Zr rich oxide scale due to long term exposure under high temperature conditions.

For investigating the microbially induced corrosion behaviour of the MWF alloys, two predominant biofilm forming bacterial species namely gram negative bacterium *Pseudomonas* species and a gram positive bacterium *Bacillus* species were considered. These bacterial species were cultured in simulated KGW and RGW individually and the MWF alloy specimens were exposed in the cultured solutions for 5 days and different post exposure studies were carried out with these specimens. The bacterial count (TVC) and epifluorescence microscopic studies confirmed good attachment of the bacterial species on the MWF surface. AFM and SEM studies showed that the bacterial species were preferentially attaching on the Zr rich intermetallic phases due to the biocompatible nature of Zr. The electrochemical corrosion investigation revealed that the bacterial species were responsible for active corrosion potential and higher passive current density due to corrosion dissolution. The hydrated passive film at the metal electrolyte interface also became very

weak due to the bacterial attachment which was validated from EIS study. The effect of microbially induced corrosion for *Pseudomonas* species was higher than that of *Bacillus* species owing to its higher attachment and slime formation on MWF surface.

8.5 Conclusions

Metal waste form alloys were developed, their microstructural characterization and corrosion behaviour in simulated water media were investigated for the purpose of acquiring knowledge as well as gaining confidence in processing the solid waste of pyrochemical reprocessing plants for safe disposal in geological repository. From the foregoing studies the following conclusions were made.

- The MWF alloys form secondary Zr rich intermetallic phases in their microstructure. These secondary Zr rich intermetallic phases act as host matrix for the actinide and fission products and form stable compound phases. These intermetallic phases have high temperature stability (more than 1173 K).
- The MWF alloys exhibit excellent resistance against corrosion. The stable and adherent ZrO_2 layer formed below the Cr_2O_3 on the surface protects the MWF alloys from localized attack. Though significant dissolution occurred in DM water at pH 1, the actinide and fission products bearing Zr intermetallic phase remained stable even in this aggressive medium.
- The MWF alloys showed admirable resistance against selective elemental leaching during prolonged exposure in high temperature aggressive simulated geological repository conditions. This is attributed to the formation of stable and well adherent ZrO_2 scale on the surface.

Based on the detailed investigations reported in this thesis it is inferred that the D9 SS- Zr based MWF alloys exhibit appreciable microstructural stability, corrosion resistance and retained their integrity against various issues that could arise during geological disposal.

Hence, these materials can be selected as the candidate MWF alloy for the long term disposal of radioactive solid waste generated in pyrochemical reprocessing plants deep in geological repository.

8.6 Scope for Future Work

8.6.1 Development and characterization of Chrome Moly - Steel - Zirconium MWF alloys

Modified 9Cr-1Mo steel has been proposed as the candidate clad material for metallic fuel in future Prototype Fast Breeder Reactors (PFBR) and the metal waste generated after pyrochemical reprocessing would be 9Cr-1Mo steel -Zr based alloys. Hence, it is worthwhile to develop 9Cr-1Mo steel-Zr MWF alloys and investigate:

- Microstructure and different compound phase formed
- Distribution of NMFPs and U in the microstructural phases
- Corrosion behaviour in different simulated environment
- Effect of NMFP and U on the corrosion behaviour
- Selective leaching of the alloying elements in simulated repository environments
- Passive film behaviour in simulated repository environments

8.6.2 Galvanic interaction of MWF alloys with canister materials

The MWF alloys will be poured inside the canister material during engineering sealing for final disposal. The canister materials will be either Ni or Cr based alloys which will have different alloy composition and properties when compared to MWF alloys. Hence, galvanic corrosion may become an issue during long term disposal period, and it is necessary to study the galvanic interaction and compatibility of MWF alloys with the canister material in different simulated repository environments.

8.6.3 Microbially induced corrosion

The microbially induced corrosion study (Chapter 6) revealed that the MWF alloys are susceptible to microbially induced corrosion due to the biocompatible nature of Zr. Therefore detailed microbial interaction with actinide and fission product added MWF alloys can be pursued and ways to to retard the attack by microbes can be explored.

8.6.4 Mott-Schottky analysis to evaluate semiconducting nature of passive film

During electrochemical studies of the noble metal added metal waste form alloys, significant changes of semiconducting nature in the passive film was observed. Hence the evaluation of the semiconducting behaviour of the MWF passive film can be evaluated in different simulated conditions by using Mott-Schottky analysis.

REFERENCES

REFERENCES

1. K.R. Rao, *Current Sci.*, 81 (2001) 1534-1546.
2. R. Chidambaram, C. Ganguly, *Current Sci.*, 70 (1996) 21-35.
3. M-S. Yim, K. Linga Murthy, *J. Metals*, 52 (2000) 26-29.
4. I. Johnson, *J. Nucl. Mater.*, 154 (1988) 169-180.
5. W.M. Nutt, R.N. Hill, D.B. Bullen, *Waste Management*, 15 (1995) 629-639.
6. M.I. Ojovan, W.E. Lee (Eds.), *An Introduction to Nuclear Waste Immobilisation*, Elsevier, U.K. (2005).
7. Baldev Raj, U. Kamachi Mudali, *Prog. Nucl. Energy*, 48 (2006) 283–313.
8. W.H. Hannum, J.E. Battles, T.R. Johnson, C.C. McPheeters, Actinide consumption: nuclear resource conservation without breeding in: *Proc. American Power Conf., Chicago, II, April 24-26, ANL/Cp-71359(1991)*.
9. P. Chiotti, S.J.S. Parry, Separation of various components from uranium by oxidation-reduction reactions in a liquid KCl-LiCl/Zinc system, Ames Laboratory Report IS-286 (1961).
10. R.K. Steunenberg, R.D. Pierce, I. Johnson, in: *Proc. Symp. on Reprocessing of Nuclear Fuels*, P. Chiotti(Ed.), *Nuclear Metallurgy*, Vol - 15, Conf.-690801, *Proc. Symp. on Reprocessing of Nuclear Fuels* (Aug. 1969), pp. 325–335.
11. K. Nagarajan, T Subramanian, B. Prabhakara Reddy, P.R. Vasudeva Rao, Baldev Raj, *Nucl. Technol.*, 162 (2008) 259-263.
12. M.F. Simpson, *Nucl. Technol.*, 162 (2008) 117.
13. H.P. Nawada, K Fukuda, *J. Phys. Chem. Solids*, 66 (2005) 647–651.

14. D.P. Abraham, J.J. Peterson, N.K. Katyal, D.D. Keiser, B.A. Hilton, Electrochemical corrosion testing of metal waste forms, Argonne National Laboratory Report, ANL/CMT/CP-100737 (2000).
15. D. Feron, D. Crussel, J.M. Grass, Corrosion, 65 (2009) 213-223.
16. D.D. Keiser Jr., D.P. Abraham, W. Sinkler, J.W. Richardson Jr., S.M. McDeavitt, J. Nucl. Mater., 279 (2000) 234-244.
17. N.R. Smart, Corrosion, 65 (2009) 195-212.
18. D.P. Abraham, S.M. McDeavitt, J. Park, Metall. Mater. Trans., 27A (1996) 2151-2159.
19. J.P. Ackerman, T.R. Johnson, L.S.H. Chow, E.L. Carls, W.H. Hannum, J.J. Laidler, Prog. Nucl. Energy, 31 (1997) 141-154.
20. D.P. Abraham, Corrosion testing of stainless steel - zirconium metal waste form, Report ANL/RAE/CP-97942 (1999).
21. S.M. McDeavitt, D.P. Abraham, J.Y. Park, J. Nucl. Mater., 257 (1998) 21-34.
22. S.M. McDeavitt, J.Y. Park, J.P. Ackerman, in: Actinide Processing: Methods and Materials, B. Mishra, W.A. Avrill (Eds.), TMS, Warrendale, Pennsylvania (1994), 305-319.
23. D.P. Abraham, L.J. Simpson, M.J. DeVries, D.E. Callahan, Corrosion behaviour of stainless steel - zirconium alloy waste forms, Argonne National Laboratory Report, ANL/CMT/CP-98181 (1999).
24. D.E. Janney, J. Nucl. Mater., 323 (2003) 81-92.
25. Performance of engineered barrier materials in near surface disposal facilities for radioactive waste, IAEA Tech. Doc., Austria, Nov. (2001).

26. L. Cederqvist and T. O'berg, *Reliability Engg. System Safety*, 93 (2008) 1491–1499.
27. X. He, D.S. Dunn, *Corrosion*, 63 (2007) 145-157.
28. ASTM C1174, Standard practice for prediction of the long-term behavior of waste package materials including waste forms used in the geologic disposal of high-level nuclear waste, ASTM International, West Conshohoken, PA (2007).
29. S.G. Johnson, D.D. Keiser, M. Noy, T. O'Holleran and S.M. Frank, Microstructure and leaching characteristics of a technetium containing metal waste form, Argonne National Laboratory report, ANL/NT/CP-96709 (1999).
30. F. King, *Corrosion*, 65 (2009) 233-251.
31. B. Little, P. Wagner, *Can. J. Microbiol.*, 42 (1996) 367-374.
32. Baldev Raj, *J. Nucl. Mater.*, 385 (2009) 142–147.
33. International Basic Safety Standards for Protection against Ionizing Radiation and for the Safety of Radiation Sources, Internatl. Atomic Energy Agency (IAEA), Vienna, Safety Series No. 115 (1996).
34. Internatl. Atomic Energy Agency, *Radiation, People and the Environment*, IAEA, Vienna (2004).
35. B.L. Cohen, *Rev. Mod. Phys.*, 49 (1977) 1–20.
36. C.M. Koplik, M.F. Kaplan, B. Ross, *Rev. Mod. Phys.*, 54 (1982) 269–312.
37. Requirements and Methods for Low and Intermediate Level Waste Package Acceptability, Internatl. Atomic Energy Agency (IAEA), Vienna, TECDOC-864, (1996).

38. Conditioning of Low and Intermediate Level Liquid Radioactive Wastes, Internatl. Atomic Energy Agency (IAEA), Vienna, Technical Report Series-222 (1983).
39. M. Atkins, F.P. Glasser, Waste Manage., 12 (1992) 105 – 131.
40. R. Kristulovich, P. Dabic, Cem. Concr. Res., 30 (2000) 693 – 698.
41. F.P. Glasser, J. Hazar. Mater., 52 (1997) 151 – 170.
42. R.E. Streatfield, A review of the BNFL cement formulation development programme for the immobilisation of the intermediate level wastes from magnox power stations, Proc. WM'01 Conf., February 25-March 1, Tucson, AZ, (2001).
43. Bituminization Processes to Condition Radioactive Wastes, Internatl. Atomic Energy Agency (IAEA), Vienna, Technical Report Series-352 (1993).
44. Handling and Processing of Radioactive Waste from Nuclear Applications, Internatl. Atomic Energy Agency (IAEA), Vienna, Technical Report Series - 402 (2001).
45. I.W. Donald, B.L. Metcalfe, R.N.J. Taylor, Review: J. Mater. Sci., 32 (1997) 5851–5887.
46. Characteristics of Solidified High-level Waste Products, Internatl. Atomic Energy Agency (IAEA), Vienna, Technical Report Series -187 (1979).
47. Design and Operation of High Level Vitrification and Storage Facilities, Internatl. Atomic Energy Agency (IAEA), Vienna, Technical Report Series -339 (1992).
48. N.P. Bansal, R.H. Doremus (Eds.), Handbook of Glass Properties, Academic Press, Orlando (1986).
49. M.J. Plodinec, Glass Technol., 41 (2000) 186 – 192.
50. A. Hespe, At. Energy Rev., 9 (1971) 195 – 207.

51. C.W. Kim, C.S. Ra, D. Zhu, D.E. Day, D. Gombert, A. Aloy, A. Mogus-Milankovic, M. Karabulut, J. Nucl. Mater., 322 (2003) 152–164.
52. W. Vogel (Ed.), Chemistry of Glass, American Chemical Society, Columbus, (1985).
53. M.J. Plodinec, J. Non-Cryst. Solids, 84 (1986) 206–214.
54. O.V. Mazurin, G.P. Roskova, V.I. Averyanov, T.V. Andropova, Two-phase glasses: Structure, properties and applications, Nauka, Leningrad (1991).
55. R.K. Brow, J. Non-Cryst. Solids, 263-264 (2000) 1–28.
56. D.S. Perera, E.R. Vance, R.L. Trautman, B.D. Begg, Current research on I-129 immobilization, Proc. WM'04 Conf., Tucson, Arizona (2004) WM- 4089.
57. C.C. Chapman, J.M. Pope, S.M. Barnes, J. Non-Cryst. Solids, 84 (1986) 226–240.
58. B.E. Burakov, E.B. Anderson, “Crystalline ceramics developed for the immobilization of actinide wastes in Russia”, Proc. ICEM'2001, Bruges, Belgium (2001) 39 - 121.
59. C. Adelhelm, C. Bauer, S. Gahlert, G. Ondracek, TiO₂ – a ceramic matrix, in: Radioactive Waste Forms for the Future, W. Lutze, R.C. Ewing (Eds.), Elsevier, Amsterdam (1988) 393–426.
60. B.E. Burakov, J.M. Hanchar, M.V. Zamoryanskaya, V.M. Garbuzov, V.A. Zirlin, Radiochim. Acta, 89 (2002) 95–97.
61. A. Jostsons, E.R. Vance, D.J. Mercer, V.M. Oversby, in: Scientific Basis for Nuclear Waste Management XVIII, T. Murakami, R.C. Ewing (Eds.), Mater. Res. Soc., Pittsburgh (1995) 775 - 782.

62. R. Roy, L.J. Yang, J. Alamo, E. R. Vance, in: *Scientific Basis for Nuclear Waste Management VI*, D.J. Brookins (Ed.), Elsevier, Amsterdam (1983).
63. *Handling, Conditioning and Disposal of Spent Sealed Sources*, Internatl. Atomic Energy Agency (IAEA), TECDOC-548 (1990).
64. M.I. Ojovan, W.E. Lee, I.A. Sobolev, O.K. Karlina, A.E. Arustamov, Metal matrix immobilisation of sealed radioactive sources for safe storage, transportation and disposal. Proc. WM'04 Conf., Tucson, Arizona (2004) WM-4085.
65. W. Lutze, R.C. Ewing (Eds.), *Radioactive Waste Forms for the Future*, Elsevier, Amsterdam (1988).
66. A.J.G. Ellison, J.J. Mazer and W.L. Ebert, Effect of glass composition on waste form durability: A critical review, Report No. ANL - 94/28 (1994).
67. H. Matzke, E. Vernaz, J. Nucl. Mater., 201 (1993) 295 - 319.
68. F. Pacaud, C. Fillet, N. Jacquet-Francillion, Mater. Res. Soc. Symp. Proc., 251 (1992) 155-162.
69. X. Feng, D.J. Wronkiewicz, J.K. Bates, N.R. Brown, E.C. Buck, M. Gong and W.L. Ebert, in: R.G. Post (Ed.), Proc. WM'04 Conf., Tucson, Arizona (2004) WM-1541.
70. S.M. McDeavitt, D.P. Abraham, D.D. Keiser Jr., J.Y. Park, in: *Extraction and Processing for the Treatment and Minimization of Wastes*, V. Ramachandran, C.C. Nesbitt (Eds.), The Minerals, Metals and Mater. Soc., Warrendale, PA (1996) 177.
71. S.M. McDeavitt, D.P. Abraham, D.D. Keiser Jr, J.Y. Park, in: *Internatl. Topical Meeting on Nuclear and Hazardous Waste Management*, Am. Nucl. Soc., LaGrange Park, IL, Vol. 3 (1996) 2477.

72. D.P. Abraham, J.W. Richardson Jr, S.M. McDeavitt, Mater. Sci. Eng. A, 239-240 (1997) 658 – 664.
73. Committee on Electrometallurgical Techniques for DOE Spent Fuel Treatment, National Research Council, Electrometallurgical Techniques for DOE spent Fuel Treatment: Final Report, National Academy Press, Washington, D.C. 2004.
74. D.P. Abraham, D.D. Keiser Jr, S.M. McDeavitt, Metal waste forms from treatment of EBR-11 spent fuel, Report No. ANL/CMT/CP-96406 (1999).
75. D. Arias, M.S. Granovsky, J.P. Abriata, in: Phase Diagrams of Binary Iron Alloys, H. Okamoto (Ed.), ASM International, Materials Park, OH (1993) 467-472
76. H. Okamoto, J. Phase Equilibria, 18 (1997) 316.
77. F. Stein, G. Sauthoff, M. Paim, J. Phase Equilibria, 23 (2002) 480 - 494.
78. D.P. Abraham, N. Dietz, Mater. Sci. Eng. A, 329 – 331 (2002) 610 – 615.
79. S.M. McDeavitt, D.P. Abraham, J.Y. Park, D.D. Keiser Jr., J. Metals, 49 (1997) 29 - 32.
80. D.D. Keiser Jr., D.P. Abraham, J.W. Richardson Jr., J. Nucl. Mater., 277 (2000) 333 -338.
81. Y. Liu, J.D. Livingston, S.M. Allen, Metall. Trans. A, 23 (1992) 3303 - 3308.
82. H. Fredriksson, Metall. Trans., 3 (1972) 2989 - 2997.
83. X.Y. Meng, D.O. Northwood, J. Less-Common Met., 125 (1986) 33 - 44.
84. S.M. McDeavitt, D.P. Abraham, D.D. Keiser Jr., J. Park, Proc. Conf. SPECTRUM '96, Seattle, Washington (1996) 2477.
85. F. Laves, Theory of Alloy Phases, ASM, Cleveland (1956) 124-198.

86. D.J. Thoma, J.H. Perepezko, J. Alloys Comp., 224 (1995) 330-341.
87. D.E Jenney, J. Nucl. Mater., 323 (2003) 81–92.
88. D.D. Keiser Jr., S.M. McDeavitt, in: DOE Spent Nuclear Fuel and Fissile Material Management, Am. Nucl. Soc., LaGrange Park, IL (1996).
89. Binary Alloy Phase Diagrams, T.P. Massalski (Ed.), ASM International, Materials park, OH (1990).
90. G. Okvist, K. Kalstrom, J. Nucl. Mater., 35 (1970) 316 - 321.
91. ASTM C1220, “Standard Test Method for Static Leaching of Monolithic Waste Forms for Disposal of Radioactive Waste”, ASTM International, West Conshohoken, PA (2010).
92. Baldev Raj, S. L. Mannan, P. R. Vasudeva Rao, M. D. Mathew, Sadhana, 27 (2002) 527–558.
93. F. Kozisek, Health Risks from Drinking De-mineralized water, WHO, Geneva, (2004).
94. C. Gurumurthy, P. Sasidhar, V. Arumugam, R. K. Mathur, Environ. Monit. Assess., 99 (2004) 211-222.
95. R. K. Tatawat, C.P. Singh Chandel, Appl. Ecol. Env. Res., 6 (2008) 79-88.
96. T. S. Rao, P. G. Rani, V. P. Venugopalan, K.V. K. Nair, Biofouling, 11 (1997) 265 – 282.
97. R. P. George, P. Muraleedharan, K. R. Sreekumari, H. S. Khatak, Biofouling, 19 (2003)1–8
98. N. R. Krug, J. G. Hold (Eds), Bergy’s Manual of Systematic Bacteriology, Volume 1. Williams & Wilkins, Baltimore (1984).

99. P. H. A. Sneath, S. Nicholas, M. Elizabeth Sharpe (Eds), Bergy's Manual of Systematic Bacteriology, Volume 2. Willams & Wilkins, Baltimore (1986).
100. S.H.Avner, Introduction to Physical Metallurgy, 2nd ed. Tata McGraw-Hill, India (2006).
101. Vickers Hardness Test, Surface Engineering Forum, Gordon England, U.K, www.gordonengland.co.uk.
102. Y. S. Han, J. B. Li, Y. J. Chen, Mater. Res. Bull. 38 (2003) 373-379.
103. J. Goldstein, D.E Newbury, D.C. Joy, C.E Lyman, P. Echlin, E. Lifshin, L.Sawyer, J.R. Michael, Scanning Electron Microscopy and X-ray Microanalysis, Plenum, New York (1981).
104. B.D. Cullity, Elements of X-ray Diffraction, Addison-Wesley Publishing Company, Inc. Massachusetts, USA (1956).
105. ASTM standard Cell, Radiometer Analytical SAS, France (2007).
106. Z. Ahmad, Principle of Corrosion Engineering and Corrosion Control, Ed: Zaki Ahmad, Elsevier, 2006.
107. G.T. Burstein, Corros. Sci., 47 (2005) 2858-2870.
108. ASTM G5, Standard Reference Test Method for Making Potentiostatic and Potentiodynamic Anodic Polarization Measurements, ASTM International, West Conshohoken, PA (2004).
109. R.G. Kelly, J.R. Scully, D.W. Shoesmith, R.G. Buchheit, Electrochemical Techniques in Corrosion Science and Engineering. Marcel Dekker, Inc. New York, 2003.
110. Gamry Instrument, Inc., EIS Manual, Basics of Electrochemical Impedance Spectroscopy, Application note, www.gamry.com.

111. J.R. Macdonald, *Impedance Spectroscopy, Theory, Experiment and Applications*. Evgenij Barsoukov, J.R. Macdonald eds. 2nd ed. John Wiley and Sons, Hoboken, New Jersey (1987).
112. D.A. Lo'pez, S.N. Simison, S.R. de Sa'nchez, *Corros. Sci.*, 47 (2005)735-755.
113. C.H. Hsu, F. Mansfeld, *Corrosion*, 57 (2001)747–748.
114. *Waste Form Technology and Performance, Final Report*, National Research Council of National Academies, The National Academic Press, Washington DC, 2011.
115. ASTM C1308, *Standard Test Method for Accelerated Leach Test for Diffusive Releases from Solidified Waste and a Computer Program to Model Diffusive, Fractional Leaching from Cylindrical Waste Forms*, ASTM International, West Conshohoken, PA (2008).
116. D. Briggs, M.P. Seah, *Practical Surface Analysis by Auger and X-ray Photoelectron Spectroscopy*, John Wiley and Sons, Chichester (1983).
117. K. Janssens, Chapter 2. X-Ray Photoelectron and Auger Electron Spectroscopy, Micro- and Trace Analysis Centre, Department of Chemistry, University of Antwerp, Belgium.
118. D.R. Baer, M.H. Engelhard, *J. Electron. Spectrosc. Relat. Phenom.*, 178–179 (2010) 415–432.
119. G. Binning, C. F. Quate, Ch. Gerber. *Atomic Force Microscope*. *Phys. Rev. Lett.*, 56 (1986) 930.
120. N. Frangis, A. Vilalta-Clemente, K. Gloystein, *Principles of Atomic Force Microscopy (AFM)*, Physics of Advanced Materials Winter School, Aristotle University, Thessaloniki, Greece (2008).
121. APHA, *Standard methods for the examination of water and wastewater*. Washington (DC), APHA (1989) 182–184.

122. J. Gopal, R.P. George, P. Muraleedharan, H.S. Khatak, *Biofouling.*, 20 (2004) 167 – 175.
123. T.C. Mah, G. A. O'Toole, Mechanisms of biofilm resistance to antimicrobial agents. *Trends. Microbiol.*, 9 (2001) 34–39.
124. K.B. Krauskopf, *Radioactive Waste Disposal and Geology*, Chapman and Hall, New York (1988)12-29.
125. N. Kazutoshi, S. Kazuyoshi, F. Tetsuya, N. Yasuhiro, Q. J. *Jpn. Weld. Soc.* 17 (1999) 59-68.
126. W. D. Callister, Jr, *Material Science and Engineering, an Introduction*, Wiley, India (2007).
127. E.P Abrahamson, S.L Lopata, *Trans. AIME*, 236 (1966) 76-87.
128. G.J. Zhou, S. Jin, L.B. Liu, H.S. Liu, Z.P. Jin, *Acta Metall. Sin.*, (Engl. Lett.) (2007) 398-402.
129. D.P. Abraham, J.W. Richardson, S.M. Mcdeavitt, *Scripta. Mater.*, 37 (1997) 239-244.
130. V.N. Svechnikov, A.T. Spektor, *Proc Acad Sci USSR, Chem Sect.*, 142 (1962) 231–233.
131. K. Mahdouk, J.C. Gachon, *J. Phase Equilibria.*, 17 (1996) 218-227.
132. L.N. Guse, T.O. Malakhova, *Metallofiz.*, (Kiev). 46 (1973) 111-113.
133. M. Sostarich, Y. Kha, Z. *Metallkd.*, 73 (1982) 706-709.
134. M. Matsuura, *J. Phys.*, F 15 (1985) 257-262.
135. Y.P. Liu, S.M. Allen, J.D. Livingston, *Metall. Mater. Trans.*, A 26 (1995)1107-1112.
136. F. Aubertin, U. Gonser, S.J. Campbell, H.G. Wagner, *Z. Metallkd.*, 76 (1985) 237-244.

137. Z.M. Alekseeva, V. Korotkovan, *Russ. Metall.*, 4 (1989) 197-203.
138. A.I. Zaitsev, N.E. Zaitseva, E.Kh. Shakhpazov, *Dokl. Phys.*, 46 (2001) 784–788.
139. A.J. Sedriks, *Corrosion of Stainless Steels*, Wiley, New York (1996).
140. H. Okamoto, *J. Phase Equilib. Diffus.* 28 (2007) 409.
141. V. Raghavan, *The Fe-Ni-Zr System, Phase diagram of ternary iron alloys, Part 6B*, Indian Institute of Metal, India (1992).
142. N.Tsoufanidis, R.G. Cochran, *Nucl. Technol.*, 93 (1991) 263–304.
143. H.M. McCullough, M.G. Fontana, F.H. Bech, *Trans. Am. Soc. Met.*, 43 (1951) 404-425.
144. J.R Myers, F.H. Beck, M.G Fontana, *Corrosion*, 21 (1965) 277-287.
145. G. Okamoto, *Corros. Sci.*, 13 (1973) 471-489.
146. K. Hladky, L. M Callow, J.L Dawson, *Br. Corros. J.*, 15 (1980) 20-25.
147. P. Kofstad, *High-Temperature Oxidation of Metals*, John Wiley, New York (1966).
148. C.L. McBee, J. Krueger, *Electrochim. Acta*, 17 (1972) 1337-1341.
149. T.P. Hoar, *J. Electrochem. Soc.*, 117 (1970) 17C.
150. R. C. Weast, *Handbook of Chemistry and Physics*, 5th ed., The Chemical Rubber Co, Cleveland (1974).
151. F. King, *Microbially Influenced Corrosion of Copper Nuclear Fuel Waste Containers in a Canadian Disposal Vault*. Atomic Energy of Canada Limited Report. AECL-11471. COG-94-519 (1996).
152. J.D. Ehrman, E.T. Bender, N. Stojilovic, T. Sullivan, R.D. Ramsier, B.W. Buczynski, M.M. Kory, R.P. Steiner, *Colloids Surf., B*, 50 (2006) 152-159.
153. B.W. Buczynski, M.M. Kory, R.P. Steiner, T.A. Kittinger, R.D. Ramsier, *Colloids Surf., B*, 30 (2003) 167-175.

154. C. Vreuls, G. Zocchi, G. Garitte, C. Archambeau, J. Martial, C. Van de Weerd, *Biofouling*, 26 (2010) 645-656.
155. D.H. Pope, E.A. Morris, *Mater. Perform.*, 34 (1995) 23-28.
156. T. H. Bauer, J. K. Fink, D. P. Abraham, I. Johnson, S. G. Johnson, and R. A. Wigeland, *Modeling Corrosion and Constituent Release from Metal Waste Forms*, Argonne National Laboratory report, ANL/RAE/CP-103572 (2001).
157. S. Langsrud, G. Sundheim, R. Borgmann-Strahsen, *J. Appl. Microbiol.*, 95 (2003) 874-882.
158. S. Ramya, R.P. George, R.V.S. Rao, R.K. Dayal, *Biofouling*, 26 (2010) 883-891.
159. Lipika Rani Bairi, S. Ningshen, U. Kamachi Mudali, Baldev Raj, *Corros. Sci.*, 52 (2010) 2291-2302.
160. Lipika Rani Bairi, S. Ningshen, U. Kamachi Mudali, Baldev Raj, *Corros. Eng. Sci. Tech.*, 46 (2011) 171-176.
161. B.J. Little, P.A. Wagner, O.J. Jacobus, *Mater. Perform.*, 27 (1988) 57-61.
162. B.J. Little, J. Lee, R. Ray, *How Marine Conditions Affect the Severity of MIC of Steels*, MIC-An International Perspective Symposium, Feb 14-15, Extrin Corrosion Consultants, Curtin University, Perth, Australia (2007).
163. S. Ningshen, U. Kamachi Mudali, S. Ramya, Baldev Raj, *Corros. Sci.*, 53 (2011) 64-70.
164. H.D. Cahan, C.T. Chen, *J. Electrochem. Soc.*, 129 (1982) 921-925.

PUBLICATIONS, AWARDS AND RECOGNITIONS



PUBLICATIONS, AWARDS AND RECOGNITIONS

I. In Journals

1. Lipika Rani Bairi, S. Ningshen, U. Kamachi Mudali and Baldev Raj, Microstructural analysis and corrosion behaviour of D9 stainless steel - zirconium metal waste form alloys, **Corrosion Science** 52 (2010) 2291-2302.
2. Lipika Rani Bairi, S. Ningshen, U. Kamachi Mudali and Baldev Raj, Corrosion issues related to disposal of 316SS-zirconium metal waste form under simulated repository conditions, **Corrosion Engineering Science and Technology** 46 (2011) 171-176.
3. Lipika Rani Bairi, S. Ningshen, U. Kamachi Mudali and Baldev Raj, Corrosion investigations on metal waste form of titanium modified 316 stainless steel - zirconium alloys in simulated ground water medium, **Corrosion** 68 (2012) 784-792.
4. Lipika Rani Bairi, G. Pannerselvam and U. Kamachi Mudali, High temperature phase stability and microstructural characterization of D9 stainless steel – zirconium metal waste form alloy, **Transaction of Indian Institute of Metal** 65 (2012) 333-341.
5. Lipika Rani Bairi, R.P. George and U. Kamachi Mudali, Microbially induced corrosion of D9 stainless steel- zirconium metal waste form alloy under simulated geological repository environment, **Corrosion Science** 61 (2012) 19-27.
6. Lipika Rani Bairi, Bhuvaneswari Gopal, S. Ningshen and U. Kamachi Mudali, Dynamic and static leachability studies and surface characterization of metal waste form alloys for geological disposal **Applied Surface Science** (under review).
7. Lipika Rani Bairi, C Mallika and U. Kamachi Mudali, Influence of noble metal fission product and actinide on the microstructural and corrosion behaviour of D9 SS-Zr metal waste form alloy, **Journal of Nuclear Materials** (Communicated)

8. Lipika Rani Bairi, C. Mallika and U. Kamachi Mudali, Distribution of noble metal fission product and its influence in corrosion behavior metal waste form alloy, **Corrosion** (Communicated)

II. Conference Proceedings and Oral Presentations

1. Lipika Rani Bairi, S. Ningshen and U. Kamachi Mudali, Electrochemical investigation to evaluate the corrosion behaviour of stainless steel –zirconium metal waste form alloys, Presented in the ‘14th Natl. Convention of Electrochemists (NCE-14)’, IGCAR, Kalpakkam, Dec. (2007).
2. Lipika Rani Bairi, S. Ningshen and U. Kamachi Mudali, Corrosion investigation on Ti modified 316SS- Zr metal waste form alloys in simulated ground water medium, Natl. Symp. ‘Electrochemical Science and Technology (NSEST-2009)’, Bangalore, India, July (2009).
3. Lipika Rani Bairi, Judy Gopal, S. Ningshen and U. Kamachi Mudali, Characterization of passive films on metal waste form alloys of D9 stainless steel containing zirconium, Internatl. Conf. on ‘Surface Modification Technologies (SMT-23)’, Mamallapuram, Nov. (2009).
4. Lipika Rani Bairi, S. Ningshen, U. Kamachi Mudali and Baldev Raj, Corrosion issues related to disposal of 316SS - Zr metal waste forms under simulated repository conditions, 4th Internatl. Workshop on ‘Long Term Prediction of Corrosion Damage in Nuclear Waste System (Long TermCor2010)’, Bruges, Belgium, June - July (2010).
5. Lipika Rani Bairi, Rani P. George and U. Kamachi Mudali, Electrochemical corrosion studies on metal waste form exposed to microbial environments, Chemistry Research Scholar Meet (CRSM-2011), IGCAR, Kalpakkam, July (2011).

6. Lipika Rani Bairi, G. Panneerselvam and U. Kamachi Mudali, High temperature microstructure characterization of D9 stainless steel - zirconium metal waste form alloys, 'Natl. Metallurgist Day - Annual Technical Meeting (NMD-ATM-2011)', Hyderabad, Nov. (2011).

III. Book Chapter

1. Lipika Rani Bairi, Judy Gopal, S. Ningshen and U. Kamachi Mudali, in: T.S. Sudarshan, U. Kamachi Mudali and Baldev Raj (Eds.), Characterization of Passive Films on Metal Waste Form Alloys of D9 Stainless Steel Containing Zirconium, Surface Modification Technology, First ed., Vol. 23, Valardocs, India (2010) pp. 529-536.

IV. Internal Report

1. **IGC annual report, 2008**, Development of Metal Waste Forms and their Characterization for Microstructure and Corrosion Behaviour, (Article No. IV B 3.2, pp. 154-155)

V. Award and Recognition

1. Best paper award for the paper "**Corrosion issues related to disposal of 316SS-zirconium metal waste form under simulated repository conditions**" by Lipika Rani Bairi, S. Ningshen, U. Kamachi Mudali and Baldev Raj in **Corros. Engg. Sci. Technol.**, 46 (2011) 171-176" from **Indian Institute of Metal**, Kalpakkam Chapter, May 4, 2012.
2. The AFM image of MWF alloys has been recognised as the cover page image in the book of "**Surface Modification Technology**", Vol. 23, Valardocs, India (2010).